Spectroscopic diversity of
Type Ia supernovae

by

Yi Chi Eric Hsiao
Bachelor of Science, University of Victoria, 2004
Bachelor of Applied Science, University of Toronto, 2002

A Dissertation Submitted in Partial Fulfillment of the
Requirements for the Degree of

DOCTOR OF PHILOSOPHY

in the Department of Physics and Astronomy

Spectroscopic diversity of
Type Ia supernovae

by

Yi Chi Eric Hsiao
Bachelor of Science, University of Victoria, 2004
Bachelor of Applied Science, University of Toronto, 2002

Supervisory Committee

Dr. Christopher J. Pritchet, Supervisor
(Department of Physics and Astronomy)

Dr. F. David A. Hartwick, Departmental Member
(Department of Astronomy)

Dr. Jon P. Willis, Departmental Member
(Department of Astronomy)

Dr. Colin Bradley, Outside Member
(Department of Mechanical Engineering)

Supervisory Committee

Dr. Christopher J. Pritchet, Supervisor
(Department of Physics and Astronomy)

Dr. F. David A. Hartwick, Departmental Member
(Department of Astronomy)

Dr. Jon P. Willis, Departmental Member
(Department of Astronomy)

Dr. Colin Bradley, Outside Member
(Department of Mechanical Engineering)

ABSTRACT

Type Ia supernovae (SNe Ia) are excellent tools in cosmology. Their intrinsic luminosities are found to vary systematically with the light-curve widths, providing an empirical calibration. This property, called the width-luminosity relation (WLR), is the basis of modern SN Ia cosmology and led to the unexpected discovery of the current accelerated rate of cosmic expansion. By examining the spectroscopic diversity of SNe Ia, this thesis aims to improve both the use of SNe Ia in cosmology and the physical understanding of the observed properties. Spectra of SNe Ia contain a wealth of information, but are difficult to organize. In this thesis, new methods are developed to consistently quantify and analyze the spectral features of supernovae. The efficacy of the methods is tested on a large library of observed spectra encompassing a wide range of properties. The spectroscopic diversity of SNe Ia enters cosmology through K-correction calculations. Before this work, K-correction was a major contributor of the systematic errors in cosmology. It is shown here that the systematic errors can be largely diminished by carefully quantifying the mean spectroscopic properties of SNe Ia. The remaining statistical errors are also quantified and shown to be redshift dependent. With the aid of principal component analysis (PCA), the multidimensional spectral information is reduced to a few components describing the largest variations in the spectral library. Using this tool, it is shown here that SN Ia intrinsic luminosity is the main driver of the spectroscopic diversity at maximum light, for *every*

spectral feature from the ultraviolet to the near-infrared. These spectroscopic sequences can potentially account for a large fraction of the K-correction statistical errors and even enable the use of SN Ia spectra as independent indicators of intrinsic luminosity and colors. The established relations will also disentangle the effects of demographic shift and true evolution in high-redshift SN Ia spectra. The temporal evolution of the spectral features is shown to exhibit the persistence of the spectroscopic sequences throughout other epochs. The effect is attributed to the more rapid spectroscopic temporal evolution of fainter SNe Ia. This conclusion supports the theory that WLR is primarily a spectroscopic effect, rather than a bolometric one.

Table of Contents

List of Tables

List of Figures

ACKNOWLEDGEMENTS

I would like to thank my supervisor, Chris Pritchet, for his guidance and for affording me plenty of freedom to be creative.

I would like to thank the "Toronto Postdocs," Alex Conley, Andy Howell and Mark Sullivan, who taught me so much of what I know in this field.

I would like to thank the people whom I have had the privilege to know in my professional life: Dave Balam, Russ Robb, Stephenson Yang, Melissa Graham, Don Neill, Mark Phillips, Chris Burns, Gaston Folatelli, Luis Boldt, Ray Carlberg, Richard Ellis, Howie Marion, József Vinkó, Sam Gooding, Saul Perlmutter, Nao Suzuki and Peter Nugent. Without their help along the way, this thesis would not have been possible.

I would like to thank my parents and my grandparents for always keeping an open mind and for patiently supporting me through years (decades!) of school.

I would like to thank my wife, Elaine, for her always unconditional love and support and my son, Ling, for being my constant reminder of what life is about.

DEDICATION

to Elaine, Ling, Mom and Dad

Chapter 1

Introduction

Type Ia supernovae (SNe Ia) are a remarkably homogeneous class of objects. Their peak luminosities are extremely bright and are found to vary systematically with the light-curve width. These properties make SNe Ia a powerful tool for cosmological studies and have led to the surprising discovery of the acceleration in the current cosmic expansion. The acceleration infers a previously unaccounted for component of the universe, named "dark energy" to reflect our ignorance. Dark energy comprises over half of the total matter-energy content of the universe, and poses a great challenge for fundamental physics.

The current generation of SN Ia surveys aims to constrain the nature of dark energy. This is achieved by the reduction of statistical errors with large sample sizes and the meticulous control of the systematic errors. One of the major sources of the errors arises from the spectroscopic diversity of SNe Ia. At first glance, the spectroscopic properties of SNe Ia are quite uniform. Yet exquisitely detailed observations of these objects have revealed not only subtle variations within the majority, but also some rare and truly peculiar events. Despite efforts in the observational and theoretical studies of SNe Ia, the origin of the variations remains unclear.

The effects of spectroscopic diversity have not been dealt with adequately in previous surveys. This thesis is primarily motivated by the potential to substantially improve SN Ia cosmology by examining the observed spectroscopic diversity. The same path will also lead to some insights which will help decipher some of the unanswered questions in SN Ia physics. There are thus two goals for this work: 1) to improve the use of SNe Ia as calibrated candles, and 2) to uncover the origin of the intrinsic variations in spectroscopic features of SNe Ia.

The thesis is organized as follows. In Chapter 2, the current status of our understanding of SNe Ia and the remaining unanswered questions are outlined. In Chapter 3, the standard

model of cosmology is developed on the foundation of the general theory, and the use of SNe Ia as calibrated candles to measure the cosmological parameters is also discussed. The library of spectra and the methods developed to quantify and analyze spectral features are described in Chapter 4. The effects of spectroscopic diversity on SN Ia cosmology and the efficacy of the proposed methods are examined in Chapter 5. In Chapter 6, the global trend of the spectral variation and the main drivers of the variation are identified. In Chapter 7, the spectroscopic properties of SNe Ia in the near-infrared are examined.

Chapter 2

Properties of Type Ia supernovae

Abstract   Type Ia supernovae (SNe Ia) are currently the most precise distance indicators, allowing for the direct measurement of the expansion history of the universe. SNe Ia display a range of intrinsic luminosities and are calibrated using the empirical width-luminosity relation (WLR). Because of their cosmological utility, there is pressing need for the physical understanding of the properties of SNe Ia. While there is general consensus that the progenitors of SNe Ia are carbon-oxygen white dwarfs (WDs) in binary systems, the nature of the donor stars is less certain. The explosion models depend on the total mass of the progenitor system and are thus also uncertain. Fortunately, in the study of the origin of WLR, the uncertainties in the progenitor systems and the explosion models are of little consequence. The primary driver of the intrinsic luminosity of SNe Ia is the amount of ^{56}Ni synthesized in the explosion. Most studies explain the WLR by relating the increase in the ^{56}Ni mass to the increase in the mean opacity and diffusion time. This is manifested as an increase in the widths of the bolometric light curves. However, recent work suggested that WLR is primarily a spectroscopic effect. The study of the spectroscopic temporal evolution of SNe Ia is needed to discern between the two possibilities. The evolution of SN Ia properties with redshift is also of great concern for cosmology. Current spectroscopic tests of evolution cannot distinguish between variations driven by demographic shift and true evolution. Established relations between SN Ia spectral features and intrinsic luminosity will help disentangle these effects.

2.1   Introduction

SNe Ia are the most precise distance indicators available for extragalactic astronomy. Their intrinsic luminosities in the optical are found to vary systematically with their light-curve widths, allowing them to be calibrated into standard candles. This empirical relation is the basis of modern SN Ia cosmology, and made possible the discovery of the current accelerated rate of cosmic expansion. Despite the successful applications, the physical origin of the empirical relation is not well understood. The SN Ia luminosity has also been found to correlate with host galaxy properties. As galaxy properties shift with redshift, supernova properties will also shift. The systematic difference between low-redshift and high-redshift SNe Ia may also affect cosmology. In this section, the observational properties and the current state of SN Ia physics are outlined. More importantly, the still unanswered questions and the approaches toward the solutions are also described.

2.2   Classification

Several important historical milestones led to the identification and the subsequent classification of supernovae. Lundmark (1925) was the first to suggest an "upper class" distinct from the regular novae. The new class was created for nova S Andromeda or SN 1885A, which was several magnitudes brighter than a sample of 21 regular novae in the Andromeda galaxy. Baade (1942) made the important connection between the historical supernova SN 1054 and its remnant, the Crab Nebula, M1. Minkowski (1941) introduced two subclasses for supernova based on their optical spectra. The classification system was then refined by Zwicky in 1965 and became the basis for modern classification of supernovae. For a review on the classification of supernovae, see Filippenko (1997) and Turatto (2003).

The classification of a SN is mainly based on its optical spectrum at maximum light (Figure 2.1). The presence or absence of hydrogen separates supernovae into Type II and Type I, respectively. When it became clear that a subset of Type I supernovae exhibit very red colors and lines of intermediate elements at late times (e.g. Filippenko & Sargent 1985; Panagia et al. 1986; Uomoto & Kirshner 1985; Wheeler & Levreault 1985), new subclasses were introduced. Type I supernovae which display the prominent Si II line near 6150Å are classified as Type Ia. The rest coincide with the subset of the unusually red supernovae and are further subdivided into Type Ib and Type Ic by the presence or absence of He lines, respectively.

Type II supernovae are also subdivided into Type IIP (for plateau) and Type IIL (for

linear) according to their optical light curves. Shortly after the light curve of a Type IIP supernova reaches the maximum, a plateau phase follows with an extraordinarily slow rate of decline, lasting for $2 - 3$ months. The light curve of a Type IIL supernova, on the other hand, shows linear decline after maximum light, much like Type I supernovae. Observations of Type IIP supernovae with extraordinarily short durations of the plateau phase suggest that there may be some continuity between the two subtypes. Progenitors of Type IIP supernovae are believed to have much more massive hydrogen envelopes than Type IIL supernovae.

A core-collapse supernova results from the gravitational collapse of the iron core of a massive star. The difference in the appearance of the spectra of these supernovae is thought to be determined by the amount of hydrogen envelope remaining in the massive star at the time of explosion (Nomoto et al. 1995). A regular star with a hydrogen layer would explode as a Type II supernova. A star which has lost its hydrogen envelope or both its hydrogen and helium envelopes, whether through stellar winds or binary interactions, would explode as Type Ib or Ic. The discovery of a hybrid Type IIb (e.g., Filippenko 1988) supports this picture. These objects start as Type II at early times and lose their hydrogen lines at late times and reveal He I lines characteristic of Type Ib supernovae. They make the important connection between Type II and Ibc supernovae. In the scenario of varying envelope mass manifesting as different observed properties, the subtypes of core-collapse supernovae can be placed in the sequence, types IIP-IIL-IIb-Ib-Ic, ordered by the decreasing envelope mass of the massive star undergoing the explosion (Figure 2.1).

Type Ia is believed to be the only supernova type that results from the thermonuclear disruption of a WD. It is thought that the progenitor of a SN Ia accretes mass until the carbon in the WD is ignited. This occurs when the WD reaches a mass of approximately 1% less than the Chandrasekhar mass. The carbon ignition leads to subsequent unregulated thermonuclear burning which unbinds and destroys the entire WD.

For a Type II supernova with its massive envelope intact, the envelope does not have to expand much for it to become sufficiently transparent for photons to escape. The light curve is powered by the shock energy from the explosion. This is not the case for the Type I family. The exploding objects of the Type I variety are compact, whether they are WDs, suspected for Type Ia, or bare cores of massive stars, suspected for Type Ibc supernovae. The expansion of the compact object after its explosion rapidly cools the ejecta. By the time the matter is transparent, the heat from the original shocks of the explosion has dissipated. The light curves of Type I supernovae are thus powered exclusively by the radioactive decay of the ^{56}Ni synthesized in the explosion.

Yet another class of objects, Type IIn supernovae, are identified by the prominent narrow hydrogen Balmer emission lines, in place of the broad P Cygni profile characteristic of normal Type II supernovae (Schlegel 1990). Other spectral features in these objects are weak. The prominent narrow Balmer emission line is typically superimposed on broader, weaker components. It is thought that these emission features are the results of the interaction between the supernova ejecta and a dense circumstellar medium (Chugai & Danziger 1994). The interaction between the fast moving ejecta and the slowly expanding circumstellar medium generates a forward shock in the circumstellar medium and a reverse shock in the ejecta. These shocks manifest as distinct components in the Balmer emission.

Some Type IIn supernovae, along with some Type Ibc supernovae, are suspected of being associated with gamma-ray bursts. The explosion energy produced in these events is generally high. Some have been shown to have kinetic energies $> 10^{52}$ ergs (e.g., Woosley et al. 1999). The extreme energies earn them the term "hypernova" (Iwamoto et al. 1998). These associations appear to group Type IIn with the core-collapse variety. However, recent discoveries of Type Ia/IIn hybrids, such as SN 2002ic (Hamuy et al. 2003) and SN 2005gj (Aldering et al. 2006; Prieto et al. 2007), revealed examples of what are presumed to be WDs exploding inside hydrogen envelopes and prompted the reexamination of some of these objects. The precise nature of these objects is still controversial (Benetti et al. 2006).

The spectroscopic properties of SNe Ia are quite uniform. Yet observations of Type Ia SN 1991bg (Filippenko et al. 1992a) and SN 1991T (Phillips et al. 1992; Filippenko et al. 1992b) revealed some peculiar spectral features which differ substantially from the norm. The spectra of normal SNe Ia are characterized by strong lines attributed to singly-ionized intermediate-mass elements. Around maximum light, SN 1991bg shows suppressed flux near 4200Å by strong Ti II features and a stronger than normal Si II line from the 5958, 5979Å doublet. The intrinsic luminosity of SN 1991bg is determined to be unusually low. On the other hand, SN 1991T exhibits essentially no absorption from the Ca II H&K and Si II 5958, 5979Å doublet, but prominent high-ionization features of Fe III in its early spectra. The intrinsic luminosity is determined to be brighter than normal. The subsequent discoveries of more objects like these prompted the further classification of spectroscopically peculiar objects into 1991bg-like and 1991T-like categories (Branch et al. 1993). Nugent et al. (1995) explains the diversity as an effect in the varying "effective temperature" of the ejecta, forming a sequence from the low-temperature 1991bg-like objects through the normal SNe Ia to the high-temperature 1991T-like objects.

More recently, the observations of SN 2002cx (Li et al. 2003) revealed peculiar properties which do not fit in either of the two peculiar subclasses described above. The premaxi-
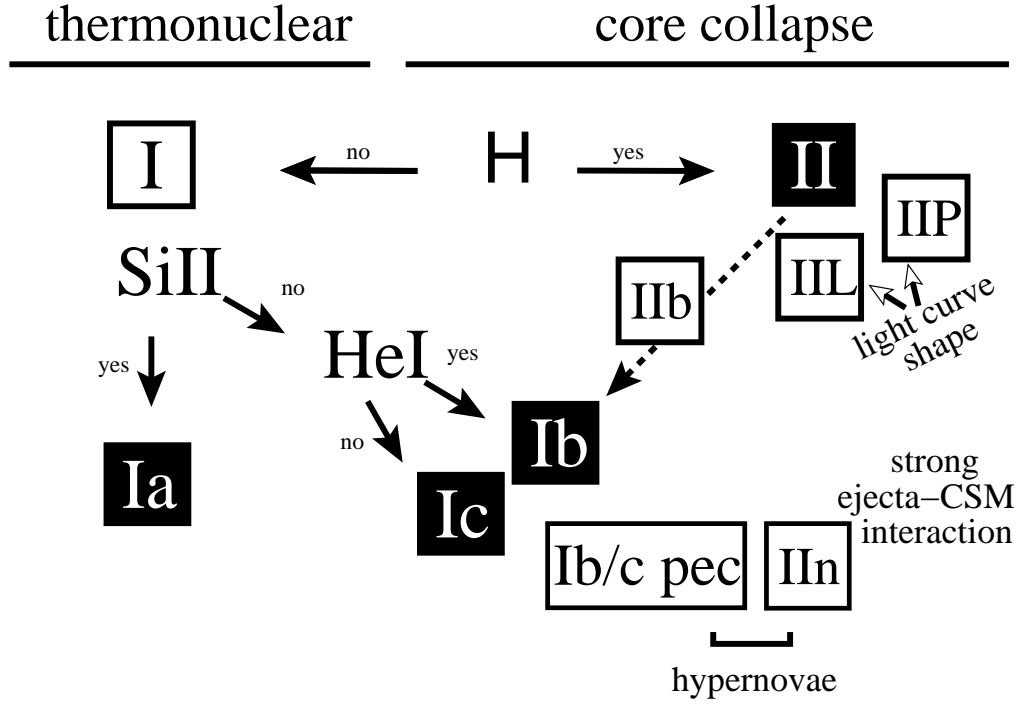
Figure 2.1: The classification scheme of supernovae. (source: Turatto (2003))

mum spectrum resembles overluminous 1991T-like objects, yet its low intrinsic luminosity resembles underluminous 1991bg-like objects. Discoveries of more objects with similar properties, such as SN 2005hk (Phillips et al. 2007) and SN 2008ha (Foley et al. 2009), have prompted yet another category of peculiar SNe Ia, 2002cx-like objects. Foley et al. (2009) estimate the rate of 2002cx-like objects to be as high as 10% of the total Type Ia supernova rate. To complicate the matter further, Valenti et al. (2009) claimed that members of this class of objects are not thermonuclear supernovae, but originate from the core collapse of the oxygen-neon cores of $7 - 9$ M$_\odot$ stars.

There are many more examples of these subclasses of peculiar SNe Ia, each with its own unique peculiarity. Among them are SN 1999aa (Garavini et al. 2004), SN 1999ac (Phillips et al. 2006), SN 2000cx (Li et al. 2001a), SN 2001ay (Howell & Nugent 2004), SN 2002bo (Benetti et al. 2004), SN 2003fg (Howell et al. 2006), and SN 2006gz (Hicken et al. 2007). As the extensive monitoring and exquisite observations of supernovae continue, the zoo of subclasses is sure to expand. The vast range of subclasses reflects the uncertainties in the theoretical models which describe these events, but at the same time provides insight into a more complete picture.

2.3 Progenitor systems

SNe Ia occur in all types of galaxies. In particular, SNe Ia occur in elliptical galaxies, while the others do not (van den Bergh et al. 2002, 2003, 2005). (However, it should be noted that a peculiar core-collapse event has recently been discovered in an elliptical galaxy (Kawabata et al. 2009).) This has given rise to the (incorrect) idea that the progenitors of SNe Ia are long-lived low-mass stars. The best candidate for the exploding object is a WD. A helium WD would yield compositions different from the observed ones (Nomoto & Sugimoto 1977). Accretion onto an oxygen-neon-magnesium WD is expected to lead to an accretion-induced collapse to a neutron star (Nomoto & Kondo 1991). The general consensus is therefore that a carbon-oxygen WD is the best progenitor candidate for a SN Ia.

The average WD mass is only about 0.6 $M_\odot$ (e.g., Ritter & Burkert 1986), and the Chandrasekhar limit is approximately 1.4 $M_\odot$ (Chandrasekhar 1931). The most sensible way to accumulate the mass necessary for an explosion is through a binary system. The question is: what types of companion stars would lead to a SN Ia? Despite the general agreement that the exploding object is a carbon-oxygen WD, there is no consensus on the donor star. For a review on the possible progenitor systems of SNe Ia, see Livio (2000, 2001).

One way for a WD to gain mass is to accrete hydrogen from a companion non-degenerate star (Whelan & Iben 1973; Nomoto 1982). In this scenario, only a narrow range of accretion rates is possible to allow for the stable burning of hydrogen required for the WD mass to grow (Nomoto 1982). The mass transfer rate must be rapid enough to prevent a nova explosion that ejects more mass and slow enough that the WD is not engulfed by hydrogen in a common envelope, displaying hydrogen in the spectrum (Yoon & Langer 2003). At this optimal transfer rate ($10^{-8} - 10^{-6}$ $M_\odot$/yr), the hydrogen will then gently burn to carbon and oxygen and settle onto the degenerate core. Promising candidates have been identified as supersoft X-ray sources, which display just the right transfer rate (Hachisu et al. 1996; Kahabka & van den Heuvel 1997).

Another possibility for a WD to gain the necessary mass for an explosion is through the merger of two WDs (Iben & Tutukov 1984; Webbink 1984; Paczynski 1985); the dissipation of orbital energy is accomplished through the emission of gravity waves. In this scenario, the less massive WD would fill its Roche lobe and swirl around the more massive WD in a thick disk. The total mass of the system is required to exceed the Chandrasekhar limit, and the orbital period is required to be short. It is unclear whether the system would

remain in this configuration, collapse to a neutron star (Saio & Nomoto 2004) or explode as a SN Ia.

Many routes have been explored in an attempt to determine whether single-degenerate scenario, double-degenerate scenario, or a combination of both best describe the progenitor systems of SNe Ia. Delay-time distributions, determined by the lag between the cosmic star formation rate and the SN Ia birth rate, have been used to deduce the progenitors. The results suggest that the single-degenerate scenario alone cannot explain the observed delay-time distribution (e.g., Mannucci et al. 2006; Pritchet et al. 2008; Totani et al. 2008). Observations of candidate binary systems containing carbon-oxygen WDs also yield constraints on the frequency of the progenitor scenarios. The recent survey of WD binary systems has identified many candidates for double-degenerate progenitors of SNe Ia (Napiwotzki et al. 2004). However, not one of the systems has both an orbital period short enough to merge in a Hubble time and a total mass that exceeds the Chandrasekhar limit. The dearth of promising double-degenerate systems led Parthasarathy et al. (2007) to conclude that single-degenerate systems produce most or perhaps all SNe Ia.

The detection or non-detection of material from the explosions themselves or from the companion stars gives clues as to whether or not the companions are degenerate stars. The single-degenerate scenario should lead to an enhancement in the density of the circumstellar material. Evidence of hydrogen in the spectra of SNe Ia, such as SN 2002ic (Hamuy et al. 2003) and SN 2005gj (Aldering et al. 2006; Prieto et al. 2007), presumably is a result of the interactions between the supernova ejecta and material from previous mass loss episodes of the companion stars. This supports the single-degenerate scenario; but the opposite has also been argued (Livio & Riess 2003). The ultra-violet flux of SNe Ia can also ionize circumstellar medium. The detections of Na I D lines in heavily reddened SNe Ia, such as SN 1999cl and SN 2006X, also favor single-degenerate progenitor systems for these SNe Ia (Patat et al. 2007; Blondin et al. 2009). The non-detection of SNe Ia at radio wavelengths excludes the case of accretion from a massive companion star (Panagia et al. 2006) and supports a low-mass non-degenerate or a degenerate companion star. The different types of companion stars lead to different explosion models and may lead to detectable differences in the amount of unburned carbon. Optical and infrared spectra have shown little or no carbon (Marion et al. 2006; Thomas et al. 2007). This is best matched by the delayed detonation in a single-degenerate scenario (Section 2.4). However, the unambiguous discoveries of super-Chandrasekhar-mass SNe Ia, such as SN 2003fg (SNLS-03D3bb; Howell et al. 2006) and SN 2006gz (Hicken et al. 2007), and the detections of unburned carbon in the outer layer, favor the double-degenerate scenario. Ruiz-Lapuente et al. (2004)

identified a possible companion star for Tycho Brahe's 1572 Type Ia supernova. The star is a type G0-G2 star, moving at more than three times the mean velocity of the stars at the same radial distance from the explosion. However, a more recent spectroscopic study of the star found this conclusion to be less certain (Kerzendorf et al. 2009).

It can be seen that these different methods lead to contradictory implications for the progenitor systems. However, most lines of evidence point to a combination of both degenerate and non-degenerate stars as donor stars for exploding WDs.

2.4   Explosion models

Explosion models of SNe Ia can generally be organized into three broad classes. All three classes involve the explosions of carbon-oxygen WDs, with varying mass conditioned by the progenitor systems. The first class of models describes the explosion of a WD with mass approaching the Chandrasekhar limit and accreted through the Roche-lobe overflow from an evolved companion star (Whelan & Iben 1973; Nomoto 1982). The explosion is then triggered by compressional heating near the center of the WD. The second class of models describes the explosion of a rotating configuration formed from the merger of two low-mass WDs (Webbink 1984; Iben & Tutukov 1984; Paczynski 1985). The merger is caused by the loss of angular momentum through gravitational radiation. The total mass of the system may be super-Chandrasekhar. The third class describes explosion of a low-mass sub-Chandrasekhar WD triggered by detonation of a helium layer (Woosley et al. 1980; Woosley & Weaver 1986, 1994). The sub-Chandrasekhar models have been ruled out for normal SNe Ia from the predicted light curves and spectra (Nugent et al. 1997). Here, we focus on the Chandrasekhar-mass models to develop an intuitive understanding of the process.

The thermonuclear runaway process in degenerate matter is considered the main mechanism for the explosion of SNe Ia (Hoyle & Fowler 1960). As the mass of the WD approaches the Chandrasekhar limit, any small mass increase results in substantial contraction of the star, compressing the material near the center. The compression ignites thermonuclear reactions and accelerates them with increasing temperature. Because the temperature increase does not affect the degenerate electron pressure and does not expand the star, the thermonuclear reactions continue in a runaway fashion. When the thermal and the degenerate electron pressures are comparable, expansion begins, but is too late to stop the thermonuclear reactions. The ignition starts a SN Ia explosion that lasts for approximately one minute. The network of thermonuclear processes begins from ^{12}C and ^{16}O and ends at

^{56}Ni where no more exothermic nuclear processes are possible. Vast quantities of partially processed intermediate-mass elements, such as Ne, Mg, Si, S and Ca, are also produced. The process releases energy on the order of 10^{51} ergs, most of which is transformed into kinetic energy that unbinds the star.

The thermonuclear reactions occur in a thin layer of thermonuclear flame that propagates from the center outwards. There are two modes of flame propagations in SNe Ia. "Detonation" describes burning velocities slightly above the local sound speed, where the reaction front is preceded by a shock wave. "Deflagration" describes burning well below the local sound speed. For pure supersonic burning, the flame would propagate through the entire WD before it has time to expand and convert the whole star into iron-peak elements. This is not what is observed; therefore, a pure detonation scenario can be ruled out.

In a pure deflagration scenario (Nomoto et al. 1984), significant amount of material remains unprocessed because the subsonic speed of the deflagration burning front is unable to catch up to the expansion of the WD near the surface. In multidimensional deflagration models, the burning front becomes turbulent and results in the large scale mixing of primordial and processed materials (Gamezo et al. 2003; Röpke & Hillebrandt 2005). Large pockets of unburned carbon and oxygen are expected to be found at various depths. This result contradicts the spectroscopic observations of normal SNe Ia, characterized by little or no unprocessed material and radially layered chemical structures. The pure deflagration scenario is also thought to provide insufficient energy for a normal SN Ia. The observations of the new class of 2002cx-like objects (Section 2.2) support them being pure deflagration supernovae.

The delayed-detonation models (Khokhlov 1991; Yamaoka et al. 1992) currently provide the best match to the observations of normal SNe Ia. These models start with a subsonic deflagration burning front. As described for the pure deflagration case, the turbulent nature of the burning front results in large scale mixing. The delayed-detonation models then introduce a transition from deflagration to detonation. The supersonic detonation front eradicates most chemical inhomogeneities, producing a radially stratified chemical structure and little unburned material at the surface, in agreement with observations of normal SNe Ia.

Despite the success of the delayed-detonation models at reproducing the observed properties of SNe Ia, how the deflagration-to-detonation transition occurs in the unconfined ejecta is still unclear (Gamezo et al. 2005; Zingale & Dursi 2007). A complete model also has to overcome other uncertainties, such as the nature of the progenitor systems, precise ignition conditions and the physics of the turbulent nuclear combustion. There is currently

no full theoretical description of the explosion mechanism of SNe Ia.

2.5   Light curve and spectra

As the compact exploding object is initially optically thick, most of the energy from the explosion is converted into kinetic energy (10^{51} ergs) to unbind the star. Another source of energy is required to produce the observed luminosity of a SN Ia. The natural end product of the thermonuclear process is ^{56}Ni. The observed luminosities of SNe Ia are powered entirely by the radioactive decay chain from ^{56}Ni through ^{56}Co and finally to the stable ^{56}Fe (Truran et al. 1967; Colgate & McKee 1969). The observed light curves and spectra are therefore fully determined by the density structure of the material synthesized during the explosion. The details in the explosion physics and the associated uncertainties are fortuitously of little consequence. This is perhaps the reason why SNe Ia, which seemingly originate from a range of different progenitor systems and explosion physics, can appear as a single family of objects.

The light curve of a SN Ia is determined by three competing effects: 1) the conversion of internal energy to kinetic energy to unbind the star, 2) the deposition of energy from radioactive decay, and 3) the escape of internal energy as the observed light curve. Before peak luminosity is reached, more internal energy goes into the expansion than escapes, trapping the photons from the radioactive decay. After peak luminosity, more energy escapes than is converted to kinetic energy, releasing the previous build up of trapped photons. Peak luminosity occurs when the product of the rising escape fraction and the decreasing deposition of energy reaches a maximum. Despite the more complicated details, Arnett (1979, 1982) demonstrated that the luminosity radiated at maximum light is approximately equal to the instantaneous rate of energy deposition by the radioactive decay and can be used to estimate the ^{56}Ni mass. "Arnett's Rule" has withstood the test of more detailed modeling and independent methods of obtaining ^{56}Ni mass and is verified to be a good approximation (Stritzinger et al. 2006b; Blinnikov et al. 2006).

A product of the radioactive decay induced by the weak force is gamma-ray photons. As mentioned above, these high energy photons do not immediately escape the SN Ia. They interact with the processed material and free electrons until they are redshifted to a wavelength region where the opacity is low enough to escape. In the fast differentially expanding envelope of a SN Ia, spectral lines block wide wavelength regions (Karp et al. 1977). The spectra of SNe Ia are therefore dominated by bound-bound transitions, forming characteristic feature shapes from a blend of P Cygni profiles.

The expansion of SN Ia ejecta is homologous, since the kinetic energy for the expansion (10^{51} erg) is orders of magnitude larger than the energy deposited by the radioactive decay (10^{49} erg). As the thermonuclear process lasts for 10^1 s and the expansion velocity is observed at 10^9 cm s^{-1}, the radius of the exploding WD (10^8 cm) is then negligible compared to the size of the supernova. Maximum light is on the order of 10^6 s past the explosion, which makes the observed properties of a SN Ia even less sensitive to the details of the explosion. Under these conditions, the velocity and radial coordinates are equivalent. The measurement of the expansion velocity of a spectral feature thus yields the layer in which it is formed. As time progresses, the "photosphere" recedes toward the center with respect to the comoving frame of the ejecta. Time series spectroscopic observations thus probe progressively deeper layers of the ejecta in time.

Around peak luminosity and during what is called the "photospheric phase," the observed spectra of normal SNe Ia are dominated by the P Cygni profiles of singly-ionized intermediate-mass elements, such as Mg II, Si II, S II and Ca II. These partially-processed elements are formed in the outer layer, where nuclear statistical equilibrium has no time to set in. At a later time, when the envelope becomes sufficiently transparent, the spectra enter the "nebular phase," where they are dominated by the emission lines of iron-group elements, such as Fe III, Fe II and Co II. Some of these are the decay products of ^{56}Ni. The rest are produced during the explosion in the inner layers where the density and temperature stay sufficiently high to establish a nuclear statistical equilibrium. A very thin outermost layer of unprocessed carbon is sometimes observed, but is not the norm (Section 2.3).

2.6   Width-luminosity relation

SNe Ia show a range of peak intrinsic luminosity in the optical. The light-curve width is found to vary systematically with intrinsic luminosity; fainter SNe Ia have narrower optical light curves, while brighter SNe Ia have wider ones. The relation is called WLR and is the basis of modern SN Ia cosmological studies. Because the WLR is used to make extraordinary claims in cosmology, it is ever more pressing to find its physical origin. The light curves of SNe Ia are powered entirely by radioactive decay. They are therefore fully determined by the composition and density structure of the explosion product. The uncertainties in the progenitor systems (Section 2.3) and in the explosion mechanism (Section 2.4) are of little consequence. The search for the origin of the WLR is a radiative transfer study. As seen in Arnett's Rule, the primary variable controlling the SN Ia luminosity is the amount of ^{56}Ni synthesized in the explosion. The question is: how does the variation of ^{56}Ni mass

lead to the observed WLR?

Most attempts at explaining the WLR involve relating the increase in the ^{56}Ni mass to the increase in the mean opacity. The increase in the mean opacity in turn leads to a longer diffusion time and broader bolometric light curves. The effect of temperature has been considered (Höflich et al. 1996, 2002). SNe Ia with higher amounts of ^{56}Ni have higher temperatures, shifting the photons toward the blue. As line opacity is also higher in the blue, the higher temperature leads to a higher mean opacity and longer diffusion time. The ionization state of the ejecta also affects the diffusion time (Pinto & Eastman 2000a,b, 2001). SNe Ia with higher amounts of ^{56}Ni have higher temperatures and are more ionized. Because fluorescence of blue photons toward longer wavelengths is less efficient in doubly ionized compared to singly ionized species of iron-group elements, more ionized material also leads to a longer diffusion time. The effect of ejecta composition has also been explored (Mazzali et al. 2001). SNe Ia with higher amounts of ^{56}Ni have higher abundances of iron-group elements. Because of the complex atomic structures of iron-group elements, the higher abundances also help to increase the mean opacity.

While all of the above explanations must operate at some level, Kasen & Woosley (2007) argued that the WLR is primarily a spectroscopic phenomenon, rather than a bolometric one. Past peak luminosity, spectra of SNe Ia are dominated by line blanketing from iron-group elements such as Fe II and Co II. The line blanketing effectively shifts the emissivity to the red, making the SN Ia redder. A SN Ia with lower ^{56}Ni mass has a lower temperature and experience an earlier onset of Fe III to Fe II recombination. This results in a more rapid ionization evolution and narrower optical light curves. Thus far, there is no strong evidence of correlation between bolometric light-curve width and luminosity (Contardo et al. 2000; Stritzinger et al. 2006b; Phillips et al. 2006), favoring a spectroscopic mechanism. In Chapter 6, we will also provide direct evidence from the temporal evolution of observed spectra to support this claim.

2.7   Host environment

The amount of ^{56}Ni synthesized in the explosion is the primary driver of the intrinsic luminosity of SNe Ia. In the previous section, some possibilities of how a range of ^{56}Ni mass can lead to the observed WLR are presented. Here, the possible variables controlling the yield of ^{56}Ni are outlined. For SNe Ia in external galaxies, it is not feasible to make direct measurements of the properties of the progenitor systems. The observations of SN Ia host galaxies have therefore been used as indicators of the progenitor environment. Early and

late-type galaxies have systematic differences in stellar age, metallicity and star formation rate, with significant overlaps across the types. These properties of the host galaxies have been considered in the search for the origin of the observed variation in the SN Ia intrinsic luminosity.

Hamuy et al. (1995, 1996b,c) first noted a correlation between SN Ia luminosity and host galaxy morphology. Intrinsically faint SNe Ia are preferentially located in early-type galaxies, while intrinsically bright objects are preferentially located in late-type galaxies. This result gives rise to the idea that the age of the progenitor is a key variable affecting the ^{56}Ni yield of SNe Ia (e.g., Howell 2001). Subsequent delay-time studies offer evidence that brighter SNe Ia come from a shorted-lived population with a delay time of at most a few hundred million years old, and fainter ones come from an old population with a delay time of at least several billion years (Mannucci et al. 2005; Scannapieco & Bildsten 2005; Sullivan et al. 2006).

The metallicity of the progenitors of SNe Ia has also been considered. In a SN Ia explosion, iron-peak elements are produced in the central regions. In a neutron-rich WD, more neutron rich and stable iron-peak elements, such as ^{58}Ni and ^{54}Fe, are produced compared to ^{56}Ni. Because a higher metallicity environment is expected to produce a more neutron-rich WD, it has been theorized that high-metallicity progenitors produce less ^{56}Ni and intrinsically faint SNe Ia (Timmes et al. 2003).

The determination of the metallicity of host galaxies is difficult. Many methods have been employed, such as using spectroscopic indicators (Hamuy et al. 2000; Gallagher et al. 2005, 2008), using galactocentric offsets and metallicity gradients (Wang et al. 1997; Ivanov et al. 2000; Gallagher et al. 2005), and using spectral energy distribution fits to the host galaxy photometry (Howell et al. 2009). Recent studies have shown that high-metallicity galaxies indeed host less luminous SNe Ia (Gallagher et al. 2008; Howell et al. 2009), but the variation can only account for a small fraction of the observed range of ^{56}Ni. Age appears to have a greater effect.

Using high-redshift SNe Ia, Sullivan et al. (2006) also found correlations between SN Ia properties and the star formation rate of the host. SNe Ia with wider light-curve widths preferentially exist in galaxies with recent star formation, while SNe Ia with narrower light-curve widths preferentially exist in galaxies with no ongoing star formation. As the cosmic star formation increases sharply with redshift, the mean SN Ia light-curve width is also expected to increase with redshift, as confirmed in high-redshift data (Howell et al. 2007).

A systematic difference between low-redshift and high-redshift SNe Ia is of great concern for SN Ia cosmology. As redshift increases, the demographic shift toward galaxies

with higher star formation causes the shift toward brighter SNe Ia at high redshifts. The demographic shift should not introduce a bias, if luminosities at high redshifts can be calibrated using the same WLR derived from nearby SNe Ia. The nearby sample of SNe Ia resides in host galaxies with a wide range of properties, which cover the range of properties of high-redshift hosts. It is therefore reasonable to believe in the validity of WLR over the redshift range currently probed by SNe Ia ($z \sim 0 - 1.5$).

Hubble diagrams for subsets of SNe Ia, which are based on host galaxy types, separately yield the same cosmology (Sullivan et al. 2003) and confirm the validity of the WLR across host types. The same result is found when comparing the cosmological fits using faint, low-redshift SNe Ia and bright, high-redshift SNe Ia (Howell et al. 2007). Any correlations between the Hubble diagram residuals and host properties could indicate true evolution in the intrinsic properties of SNe Ia. Gallagher et al. (2008) observed a correlation between the Hubble diagram residual and host metallicity, suggesting the influence of metallicity on luminosity is not fully corrected by the WLR. In an independent study, Howell et al. (2009) did not observe this effect and suggested that the difference may be caused by the different light-curve fitters used in the two studies.

Spectroscopic studies have also been conducted to test for evolution (Section 3.9). Recent studies have detected some systematic spectroscopic differences between low-redshift and high-redshift samples (Foley et al. 2008a; Sullivan et al. 2009). It is thus far unclear whether the differences are attributable to demographic shift, true evolution, or both.

2.8   Conclusion

While there is a general consensus that the exploding progenitors of SNe Ia are carbon-oxygen WDs in binary systems, the identities of the donor stars are less certain. Many approaches to identify the properties of the donor stars have been pursued. They sometimes lead to contradictory results, but mostly point to a combination of degenerate and non-degenerate donor stars. The explosion models depend on the total mass of the progenitor system and are thus also uncertain. The models that best match the observed properties of SNe Ia are the delayed-detonation models. They are characterized by the transition from subsonic to supersonic thermonuclear flame propagation. Despite their success, it is still unclear how the transition occurs in the unconfined ejecta.

Because of the cosmological utility of the empirical WLR, there is pressing need to understand its physical origins. Fortunately, the uncertainties in the progenitor systems and explosion models are of little consequence, as the observed light curves and spectra of

SNe Ia are fully determined by the density structure of the material synthesized during the explosion. The primary driver of the intrinsic luminosity of SNe Ia is the amount of ^{56}Ni synthesized in the explosion. Most studies explain the WLR by relating the increase in the ^{56}Ni mass to the increase in the mean opacity. The increase in the mean opacity in turn leads to longer diffusion time and broader bolometric light curves. However, recent work suggests that WLR is primarily a spectroscopic effect, associating a lower ^{56}Ni mass with a more rapid ionization evolution. The study of spectroscopic diversity presented in this thesis will offer evidence supporting this view.

SN Ia properties are found to correlate with their host environment. Evidence has been shown for the correlation between SN Ia luminosity and host stellar age, metallicity and star formation rate. The results give important clues about the origin of the variation in the ^{56}Ni yield. The existence of these correlations means that as host galaxy properties shift with redshifts, there would be systematically brighter SNe Ia at high redshifts compared to the low-redshift sample. As the evolution of SN Ia properties with redshift is of grave concern in cosmology, it is important to distinguish between the effects of demographic shift and true evolution. The work in this thesis will also help make this possible by identifying the variations in the spectral features of SNe Ia instigated by the change in the intrinsic luminosity.

Some of the still unanswered questions of SNe Ia have been outlined. The path to answering these questions and improving the use of SNe Ia in cosmology is one and the same. From the approach of examining the spectroscopic diversity of SNe Ia, we will attempt to do both in this thesis.

Chapter 3

Cosmology with Type Ia supernovae

Abstract   From the foundation of the general theory, cosmological parameters are shown to have direct links to observables, such as the apparent luminosities and redshifts of a set of standard candles. Type Ia supernovae (SNe Ia) are powerful stellar explosions with luminosities which can be observed at cosmological distances. Their optical peak luminosities are found to correlate with their light-curve widths. This empirical relation can then be used to calibrate SNe Ia to be standard candles. The cosmological studies using SNe Ia led to one of the most important discoveries in modern science. The universe is shown to be undergoing an accelerated rate of expansion. The repulsive energy driving the expansion constitutes over half of the matter-energy content of the universe and presents great challenges to fundamental physics. With meticulous control of systematic errors, SNe Ia can be further used to constrain the nature of this mysterious component of the universe. This thesis, in particular, is motivated by the potential for substantial improvement in SN Ia cosmology by studying the spectroscopic properties of SNe Ia.

3.1   Introduction

Our standard model of cosmology is built on the foundation of Einstein's general theory of relativity. The general theory is based on Einstein's insight that gravity is the manifestation of curvature in space-time created by matter and energy. The theory has been remarkably successful experimentally, explaining the precession of the perihelion of Mercury (Einstein 1916) and predicting gravitational redshift (Pound & Rebka 1959, 1960; Pound & Snider 1964), the deflection starlight by the sun (Dyson et al. 1920) and the Shapiro delay (Shapiro 1964).

When the assumption of an isotropic and homogeneous universe is made, Einstein's field equations from the general theory can be solved analytically. The solutions directly connect the matter-energy content of the universe, which governs the geometry of the universe, to observable quantities, such as redshifts and luminosities of astronomical objects. The solutions also show that, in general, the universe is dynamic. Einstein's preference for a static universe required that he add a cosmological constant of integration to the field equations to counter gravitating matter. This preference for a static universe was perhaps motivated more by aesthetics rather than by observational evidence. The Copernican principle states that we do not occupy a special position in space; by the same logic, we should not occupy a special position in time. The simplest way to establish both conditions is through a static universe infinite in both space and time. After Hubble (1929) demonstrated the expansion of the universe, the introduction of the cosmological constant was dubbed Einstein's "biggest blunder" (Gamow 1970).

Decades later, the potential to use SNe Ia as standard candles was being explored. SNe Ia have large luminosities which can be observed over cosmological distances. Their characteristic variability in both photometric and spectroscopic properties allows them to be securely identified. Their peak luminosities are found to correlate with light-curve widths, allowing them to be calibrated into very good standard candles. Fully expecting to find a decelerating rate of expansion in a universe full of gravitating matter, experiments using SNe Ia as cosmological probes found the surprising result that the current rate of expansion is accelerating. Einstein's cosmological constant is once again invoked to explain the acceleration. Even if the acceleration is indeed due to the cosmological constant, the physical origin is still unknown and presents great challenges to fundamental physics.

In this section, the steps from astronomical observables to the cosmological parameters are outlined, based on the general theory. The steps for calibrating the SN Ia peak luminosities are also discussed. Through careful identification and control of systematic errors, SNe Ia can be further used to falsify theories on what is causing the acceleration. The sources of these systematics and possible improvements are also described.

3.2   General theory

Einstein's general theory describes gravity as the manifestation of the curvature of space-time instigated by matter and energy. The geometry itself is described by the Einstein tensor G^{ik}. The distribution of matter and energy is specified by the energy-momentum tensor T^{ik}. The Einstein field equations equate the two tensors and establish a relation

between a specified matter energy distribution and the geometry of space-time.

The laws of physics must not depend on the frame of reference. This became Einstein's main motivation for using tensor calculus as the tool for the development of the general theory. In this framework, relations remain valid under the transformations of coordinate systems. In the absence of any matter or energy, the space-time interval ds is described by an analog to the familiar Pythagoras' theorem (in natural units, with $c = 1$): $ds^2 = dt^2 - dx^2 - dy^2 - dz^2$. More generally, the fundamental tensor g_{ij} describes the geometry of space-time with or without curvature as:

$$ds^2 = g_{ij}dx^i dx^j. \tag{3.1}$$

The Christoffel symbol is defined as a combination of fundamental tensors, where the partial derivatives are expressed in the shorthand form $_{,k} \equiv \frac{\partial}{\partial x^k}$:

$$\Gamma^l_{.ij} \equiv \frac{1}{2}g^{lk}(g_{ik,j} + g_{jk,i} - g_{ij,k}). \tag{3.2}$$

The Riemann tensor $R^i_{.jkl}$ arises when finding the change of a vector under parallel transport around a closed and infinitesimal path. In a curved space-time, the Riemann tensor yields non-zero components. It consists entirely of fundamental tensors:

$$R^i_{.jkl} \equiv \Gamma^i_{.jl,k} - \Gamma^i_{.jk,l} + \Gamma^i_{.rk}\Gamma^r_{.jl} - \Gamma^i_{.rl}\Gamma^r_{.jk}. \tag{3.3}$$

The differentiation of a tensor is done by a covariant derivative and is expressed in the shorthand form as $_{;k}$. The law of conservation of energy and momentum requires a null covariant derivative for the energy-momentum tensor:

$$T^{ik}_{;k} = G^{ik}_{;k} = 0. \tag{3.4}$$

The Einstein tensor is constructed by contracted Riemann tensors and the fundamental tensor in the fashion that produces a vanishing covariant derivative:

$$G^{ik} \equiv R^{ik} - \frac{1}{2}g^{ik}R. \tag{3.5}$$

The Einstein field equations (Einstein 1915) arise by recognizing that the matter and energy distribution specified by the energy-momentum tensor is the source of the space-time curvature described by the Einstein tensor:

$$G^{ik} + \Lambda g^{ik} = 8\pi G T^{ik}. \tag{3.6}$$

Note that the infamous cosmological constant Λ naturally arises here as a constant of integration. The covariant derivative of the term Λg^{ik} yields zero and does not disturb the conservation of energy and momentum.

3.3   Friedmann-Robertson-Walker Model

Observations have provided evidence that our universe is isotropic on scales larger than $\sim$ 150 Mpc from our vantage point. We are then justified to make the assumption of an isotropic universe. If the Copernican principle, sometimes referred to as the cosmological principle, is adopted, the assumption is made that we do not occupy a special place in the universe. The apparent isotropy observed from our vantage point should then be observed at any other place in the universe. The two assumptions thus imply homogeneity.

The most general homogeneous and isotropic fundamental tensor is in the form of the Robertson-Walker metric (Robertson 1935):

$$ds^2 = dt^2 - a^2(t)\left[\frac{dr^2}{1 - kr^2} + r^2(d\theta^2 + \sin^2\theta d\phi^2).\right] \tag{3.7}$$

The coordinates dr, $d\theta$ and $d\phi$ are comoving coordinates. A point which is at rest in the preferred frame of the universe has $dr = d\theta = d\phi = 0$. The scale factor $a(t)$ describes the relative sizes of the spatial surfaces. The scale factor can be re-normalized to obtain the values of +1, 0 or -1 for the constant k, representing cases of closed, flat and open spatial geometry of the universe, respectively.

If we choose to represent the universe on large scales with a perfect fluid, the energy-momentum tensor can be specified by energy density ρ and pressure p as follows:

$$T^{ik} = \text{diag}[\rho(t), -p(t), -p(t), -p(t)]. \tag{3.8}$$

Placing the fundamental tensors from the Robertson-Walker line element (Equation 3.7) and the energy-momentum tensor of a perfect fluid (Equation 3.8) in the Einstein field equations (Equation 3.6), the solutions for the scale factor $a(t)$ are known as the Friedmann equations (Friedman 1922). The first Friedmann equation characterizes the geodesic velocity:

$$\frac{\dot{a}^2 + k}{a^2} = \frac{8\pi G}{3}\rho + \frac{\Lambda}{3}, \tag{3.9}$$

where G is the gravitational constant. The second Friedmann equation characterizes the

geodesic acceleration:

$$\frac{\ddot{a}}{a} = -\frac{4\pi G}{3}(\rho + 3p) + \frac{\Lambda}{3}. \tag{3.10}$$

The knowledge of the relation between p and ρ, called the equation of state, is essential for the progress of cosmology, as the form of the energy-momentum tensor T^{ik} depends directly on it. In its simplest form, the equation of state relates p and ρ by a time-dependent scale factor w:

$$p = p(\rho) \equiv w\rho. \tag{3.11}$$

The energy density conservation law can be derived from Equation 3.9 and Equation 3.10:

$$\dot{\rho} = -3\frac{\dot{a}}{a}(\rho + p). \tag{3.12}$$

By integrating Equation 3.12, we obtain a power-law dependence of density ρ on the equation-of-state parameter w:

$$\rho \propto a^{-3(1+w)}. \tag{3.13}$$

3.4 Cosmological Parameters

The Hubble parameter is defined as $H(t) \equiv \dot{a}/a$. This convention is, of course, inspired by the linear Hubble law shown by Hubble (1929) for the local universe. The Hubble constant is expressed as the Hubble parameter at the present epoch t_0: $H_0 \equiv H(t_0)$. For the Euclidean geometry valid for the local universe, the relative distance and velocity between two objects can be expressed as $d = ar$ and $v = \dot{a}r$, where r is the comoving distance. The linear Hubble law then follows from these definitions:

$$v = H_0 d. \tag{3.14}$$

The non-zero and positive Hubble constant as a result of the observations of Hubble (1929) demonstrated that the universe is expanding and refuted Einstein's preference for a static universe. At large distances, the linear law is no longer valid.

The matter-energy content of the universe can be organized into four components: radiation, matter, curvature of space and the cosmological constant. The components are

characterized by their equation-of-state parameters w which take on the values 1/3, 0, -1/3 and -1 for the radiation, matter, curvature of space and the cosmological constant components, respectively. From Equation 3.13, each equation-of-state parameter then yields the characteristic dependence of the density on the scale factor. For example, the density of the matter and the cosmological constant components can be written as $\rho_M \propto a^{-3}$ and $\rho_\Lambda \propto constant$, respectively. This demonstrates that, as the universe expands, matter dilutes rapidly while the energy density from the cosmological constant stays the same.

Assuming $\Lambda = 0$, the critical energy density required for a spatially flat geometry ($k = 0$) at a given epoch can be defined from Equation 3.9:

$$\rho_c = \frac{3H^2}{8\pi G}. \tag{3.15}$$

We can then write the first Friedmann equation in terms of the dimensionless density parameters $\Omega_i \equiv \rho_i/\rho_c$, where each parameter specifies the contribution of the ith component to the critical density:

$$H^2 \equiv \left(\frac{\dot{a}}{a}\right)^2 = H_0^2 \left[\Omega_r a^{-4} + \Omega_M a^{-3} + \Omega_k a^{-2} + \Omega_\Lambda\right]. \tag{3.16}$$

The parameters Ω_r, Ω_M, Ω_k and Ω_Λ are measures of the present mean energy density contributions from radiation, matter, the curvature of space and the cosmological constant, respectively.

The redshift z of an object is an observational quantity. It is the fractional Doppler shift of its emitted light from radial motion, $z = \lambda_o/\lambda_e - 1$, where λ_e and λ_o are emitted and observed wavelength, respectively. The redshift of an object can be measured directly by identifying the source of a line in the spectrum and comparing the observed wavelength to that measured in the laboratory. The observed redshift is a combination of astrophysical effects, such as the cosmic expansion, peculiar velocities and gravitational redshift. If the observed redshift of an object is dominated by the effect of cosmic expansion, the object is said to be in the "Hubble flow." For an object in the Hubble flow, its redshift is directly related to the scale factor:

$$1 + z = \frac{a(t_0)}{a(t)} = \frac{\lambda_o}{\lambda_e}, \tag{3.17}$$

where t and t_0 specify the time of emission and observation, respectively. Equation 3.16 can then be expressed in terms of redshift:

$$\frac{H(z)^2}{H_0^2} = \Omega_r(1+z)^4 + \Omega_M(1+z)^3 + \Omega_k(1+z)^2 + \Omega_\Lambda. \tag{3.18}$$

The sum of the density parameters is defined to be unity. From observations, the matter density parameter Ω_M consists of baryon density Ω_b and dark matter density Ω_{DM} (e.g., Kirkman et al. 2003; Allen et al. 2008). The total density parameter is a measure of the flatness of space-time and is defined as:

$$\Omega_{total} \equiv \Omega_r + \Omega_M + \Omega_\Lambda. \tag{3.19}$$

A flat universe would have $\Omega_{total} = 1$.

A strictly isotropic and homogeneous universe will remain isotropic and homogeneous. To produce the structure observed in the universe, small deviations from homogeneity in the energy density are required. The density contrast is defined as:

$$\delta(t, \mathbf{x}) \equiv (\rho - \bar{\rho})/\bar{\rho}. \tag{3.20}$$

The Fourier transform of the density contrast in $\mathbf{k}$-space is written as:

$$\delta_{\mathbf{k}}(t) = \int d^3\mathbf{x}\delta(t, \mathbf{x}) \exp(i\mathbf{x} \cdot \mathbf{k}). \tag{3.21}$$

The power spectrum of the perturbations, averaged over a large volume, is then defined as:

$$P(\mathbf{k}, t) \equiv \langle |\delta_{\mathbf{k}}(t)|^2 \rangle. \tag{3.22}$$

The favored model for the origin of these fluctuations is based on the idea that if the very early universe went through an inflationary phase (Guth 1981), the quantum fluctuations of the field driving the inflation would then lead to energy density fluctuations (e.g., Hawking 1982). It is then possible to construct inflationary models described by a Gaussian random field, which is characterized by a power law spectrum (Harrison 1970; Zeldovich 1972):

$$P(\mathbf{k}) = A\mathbf{k}^n. \tag{3.23}$$

The parameters A and n specify the amplitude and the power law index of the initial fluctuation, respectively.

The modern standard cosmology is then fully specified by the five background parameters H_0, Ω_b, Ω_{DM}, Ω_Λ and Ω_r, and the two parameters A and n governing the conditions of the initial fluctuations (Narlikar & Padmanabhan 2001).

3.5 Luminosity distance

Suppose we have at our disposal a class of astronomical objects with the same absolute luminosity L, located at different redshifts. The observed fluxes f would then yield direct measurements of the cosmological density parameters. In this section, we outline the derivation relating the density parameters to the observables, redshift z and flux f.

The fundamental equation relating the bolometric flux f_{bol} received by the observer and the bolometric luminosity emitted L_{bol} is:

$$f_{bol} = \frac{L_{bol}}{4\pi(a_0 r)^2(1 + z)^2},$$ (3.24)

where $a_0 \equiv a(t_0)$ denotes the present day scale factor. The term $1/4\pi(a_0 r)^2$ is the inverse square law, accounting for the surface area over which the photons are diluted when they reach the observer. There are two factors of $(1 + z)$. One factor accounts for the fact that every photon is degraded in energy by $(1 + z)$ due to the redshift. The other deals with the dilution in the rate of photon arrival by $(1 + z)$ due to the stretching of the path length by the expansion.

The luminosity distance is defined as:

$$d_L \equiv \sqrt{\frac{L_{bol}}{4\pi f_{bol}}}.$$ (3.25)

From Equation 3.24 and Equation 3.25, we can then rewrite the luminosity distance in terms of the present day scale factor a_0, the comoving distance r and redshift z:

$$d_L = a_0 r(1 + z).$$ (3.26)

To find the relation between the luminosity distance d_L and the cosmological density parameters, we go back to the Robertson-Walker metric with the photon path of $ds^2 = 0$ and the choice a radial coordinate system, where $d\theta = d\phi = 0$:

$$\int_0^r \frac{dr'}{\sqrt{1 - kr'^2}} = \int_t^{t_0} \frac{dt'}{a(t')}.$$ (3.27)

Using the relation between redshift and the scale factor in Equation 3.17, the above equation can be rewritten as:

$$\int_0^r \frac{dr'}{\sqrt{1 - kr'^2}} = \frac{1}{a_0} \int_t^{t_0} (1 + z)dt'.$$ (3.28)

Obtaining the conversion between a time and a redshift integral dt/dz using Equation 3.17 and Equation 3.18, we can again rewrite the above equation as:

$$\int_0^r \frac{dr'}{\sqrt{1 - kr'^2}} = \frac{1}{a_0} \int_0^z \frac{dz'}{H(z')},$$

(3.29)

where $H(z)$ is defined in Equation 3.18. The integral on the left-hand side has the following solutions depending on the sign of k:

$$\int_0^r \frac{dr'}{\sqrt{1 - kr'^2}} = \begin{cases} \frac{\sin^{-1}(r\sqrt{k})}{\sqrt{k}} & \text{for } k = +1 \\ r & \text{for } k = 0 \\ \frac{\sinh^{-1}(r\sqrt{|k|})}{\sqrt{|k|}} & \text{for } k = -1 \end{cases} .$$

(3.30)

By solving the integral and using the definitions of the curvature density parameter $\Omega_k = -k/H_0^2 a_0^2$ and luminosity distance $d_L = a_0 r(1 + z)$, the luminosity distance can finally be expressed as a function of redshift and the cosmological density parameters:

$$d_L = (1 + z) \times \begin{cases} \frac{1}{H_0 \sqrt{|\Omega_k|}} \sin \left[H_0 \sqrt{|\Omega_k|} \int_0^z \frac{dz'}{H(z')} \right] & \text{for } \Omega_k < 0 \\ \int_0^z \frac{dz'}{H(z')} & \text{for } \Omega_k = 0 \\ \frac{1}{H_0 \sqrt{\Omega_k}} \sinh \left[H_0 \sqrt{\Omega_k} \int_0^z \frac{dz'}{H(z')} \right] & \text{for } \Omega_k > 0 \end{cases} .$$

(3.31)

For a summary of the various distance measures in cosmology, see Hogg (1999).

3.6 K-corrections

In astronomical observations, photons from an object are usually observed through a filter of fixed bandwidth. The expansion of the universe causes the spectral density distribution (SED) of the object to be redshifted and results in a change in the received flux through a fixed-bandwidth filter. To compare the magnitudes of objects at different redshifts, K-corrections are then required to convert the observed magnitude through a filter to that which would have been observed in the rest frame of that filter (Humason et al. 1956; Oke & Sandage 1968). The observed and rest-frame filters need not be the same. In fact, at high redshifts, one should take advantage of the overlapping of a redshifted rest-frame filter and a redder observed filter (Kim et al. 1996).

The K-correction K_{xy} converting the apparent magnitude m_y through the observed filter y to the absolute magnitude M_x through rest-frame filter x is defined as:

$$m_y = M_x + \mu + K_{xy},$$

(3.32)

assuming that the apparent magnitude is not affected by dust extinction along the line of sight. The distance modulus μ is defined by:

$$\mu \equiv 5 \log\left(\frac{d_L}{10 \text{ pc}}\right). \tag{3.33}$$

The apparent magnitude m_y comes from the SED $f_\lambda(\lambda)$ of the object observed through filter y in a particular magnitude system:

$$m_y = -2.5 \log\left[\frac{\int \lambda_o f_\lambda(\lambda_o) T_y(\lambda_o) d\lambda_o}{\int \lambda_o Z_\lambda^y(\lambda_o) T_y(\lambda_o) d\lambda_o}\right]. \tag{3.34}$$

The subscript λ for the SEDs denotes that they have the units of energy per unit time per unit area per unit wavelength. The term $T_y(\lambda)$ denotes the effective transmission function of the observed filter, and the term $Z_\lambda^y(\lambda)$ defines the idealized zero-magnitude SED for the magnitude system of the observed filter y. For a photon-based photometric system, such as the prevalent Johnson-Cousins system (Johnson & Morgan 1953), the extra λ terms are included in the integrals in Equation 3.34 to account for the λ/hc energy-to-photon conversion (see appendix of Nugent et al. 2002).

The absolute magnitude M_x is defined to be the apparent magnitude of the object if it is 10 pc away and not redshifted:

$$M_x = -2.5 \log\left[\frac{\int \lambda_e \frac{L_\lambda(\lambda_e)}{4\pi 10^2} T_x(\lambda_e) d\lambda_e}{\int \lambda_e Z_\lambda^x(\lambda_e) T_x(\lambda_e) d\lambda_e}\right]. \tag{3.35}$$

The term $T_x(\lambda)$ denotes the effective transmission function of the rest-frame filter, and the term $Z_\lambda^x(\lambda)$ defines the idealized zero-magnitude SED for the magnitude system of the rest-frame filter x.

As opposed to bolometric flux, the flux considered here is per unit wavelength. The relation between the observed flux and the emitted luminosity thus includes an extra term of $(1 + z)$ from Equation 3.17:

$$f_\lambda(\lambda_0) = \frac{1}{(1 + z)} \frac{L_\lambda(\lambda_e)}{4\pi d_L}. \tag{3.36}$$

Placing the above definitions of μ, m_y, M_x and f_λ in Equation 3.32, the K-correction term is then expressed as:

$$K_{xy} = -2.5 \log \left[\frac{1}{(1+z)} \frac{\int \lambda_o f_\lambda(\lambda_o) T_y(\lambda_o) d\lambda_o}{\int \lambda_o Z_\lambda^y(\lambda_o) T_y(\lambda_o) d\lambda_o} \frac{\int \lambda_e Z_\lambda^x(\lambda_e) T_x(\lambda_e) d\lambda_e}{\int \lambda_e f_\lambda((1+z)\lambda_e) T_x(\lambda_e) d\lambda_e} \right]. \qquad (3.37)$$

The above equation is written in terms of flux. Alternatively, it can also be written in terms of luminosity as:

$$K_{xy} = -2.5 \log \left[\frac{1}{(1+z)} \frac{\int \lambda_o L_\lambda(\lambda_o/(1+z)) T_y(\lambda_o) d\lambda_o}{\int \lambda_o Z_\lambda^y(\lambda_o) T_y(\lambda_o) d\lambda_o} \frac{\int \lambda_e Z_\lambda^x(\lambda_e) T_x(\lambda_e) d\lambda_e}{\int \lambda_e L_\lambda(\lambda_e) T_x(\lambda_e) d\lambda_e} \right]. \qquad (3.38)$$

For the detailed derivations of these definitions for K-correction, see Hogg et al. (2002).

Note that the K-correction term includes a $(1 + z)$ term from Equation 3.36. This extra $(1 + z)$ term accounts for the effective bandwidth shrinkage of the observed filter, as the SED of the distant object is redshifted and stretched. There was some controversy whether to include two or three terms of $(1 + z)$ in Equation 3.24, until it was settled by the rigorous derivation of Robertson (1938). The bandwidth term may have been the source of the controversy (Sandage et al. 1995). It is also interesting to note that Hubble's definition of the K term used in his galaxy count program (Hubble 1936) included the term accounting for the change in the region of the SED sampled by the observed filter, the $(1 + z)$ terms from Equation 3.24, but neglected the bandwidth term. The error was finally discovered by Humason et al. (1956). For the full account on this subject, see Sandage et al. (1995).

So far, the steps from observables of astronomical objects to the cosmological parameters have been outlined. For a set of perfect standard candles, their observed apparent magnitudes yield their luminosity distances. For objects in the Hubble flow, their luminosity distances and redshifts give direct measurements of the cosmological parameters. In the next section, the use of SNe Ia as standard candles is discussed.

3.7   Type Ia supernovae as cosmological probes

SNe Ia are powerful stellar explosions with luminosities which can be observed over cosmological distances. Their characteristic light curves and spectral features make them separable from other classes of variable objects. Their apparent uniformity in the peak brightness along with their large intrinsic luminosities make them an ideal candidate for use as standard candles for cosmological studies.

As early as the 1930's, Baade (1938) had noted that supernovae are more uniform than novae with a dispersion in peak magnitude of 1.1 mag. We now know that Baade's low dispersion sample only contained Type I supernovae, which are classified by the absence of hydrogen in their spectra (Section 2.2). The Hubble diagram of Kowal (1968) constructed using this class of supernovae showed a dispersion of 0.6 mag. Type Ia supernovae (SNe Ia) belong to a subclass of the type I supernovae and are classified by the presence of silicon features in their spectra. Subsequent studies using these objects yielded even smaller dispersion in the peak magnitude of $0.3 - 0.5$ and gave rise to the idea that they may be true standard candles (e.g., Branch & Bettis 1978; Sandage & Tammann 1982; Capaccioli et al. 1990; Tammann & Leibundgut 1990; Branch & Miller 1993; Sandage & Tammann 1993).

In the mean time, Pskovskii (1968, 1977, 1984) argued that the peak magnitudes of SNe Ia are not identical, but correlate with the decline rate of the optical light curves. The idea was generally not embraced by the community, as most of the light curves used by Pskovskii were derived from photographic photometry (Boisseau & Wheeler 1991). The first CCD light curves of a SN Ia were of SN 1986G (Phillips et al. 1987). The light curves were shown to declined significantly faster than the light curves of SN 1989B from photoelectric photometry (Buta & Turner 1983). Phillips (1993) confirmed the correlation between decline rate and peak magnitude, using a sample of nine well-observed SNe Ia with distance estimates from surface brightness fluctuations and Tully-Fisher methods.

Phillips (1993) introduced the parameter Δm_{15}, defined as the decline in B-band magnitude during the first 15 days past maximum. The correlation between the Δm_{15} parameter and peak absolute magnitude offers an empirical calibration of the peak luminosities of SNe Ia (Figure 3.1). As more SNe Ia were discovered and observed before maximum light, the peak absolute magnitude was shown to not only correlate with decline rate, but also with the overall width of the light curve. Perlmutter & et al. (1997) utilized this property to development a stretch parameter which linearly scales the time axis of a standard light-curve template to fit an observed light curve. This one-parameter parametrization of the peak absolute magnitude of SNe Ia is called the "width-luminosity relation" (WLR). For a review on the history and the techniques developed for using SNe Ia as distance indicators, see Phillips (2005).

A relation between the peak absolute magnitude and colors has also been reported (e.g., Riess et al. 1996; Tripp 1998; Tripp & Branch 1999; Parodi et al. 2000). Brighter SNe Ia are found to be systematically bluer; it is, however, unclear whether the relation is primarily driven by intrinsic colors of SNe Ia or by dust properties. Modern methods for calibrating SN Ia luminosities make use of both light-curve width and color information. Among the
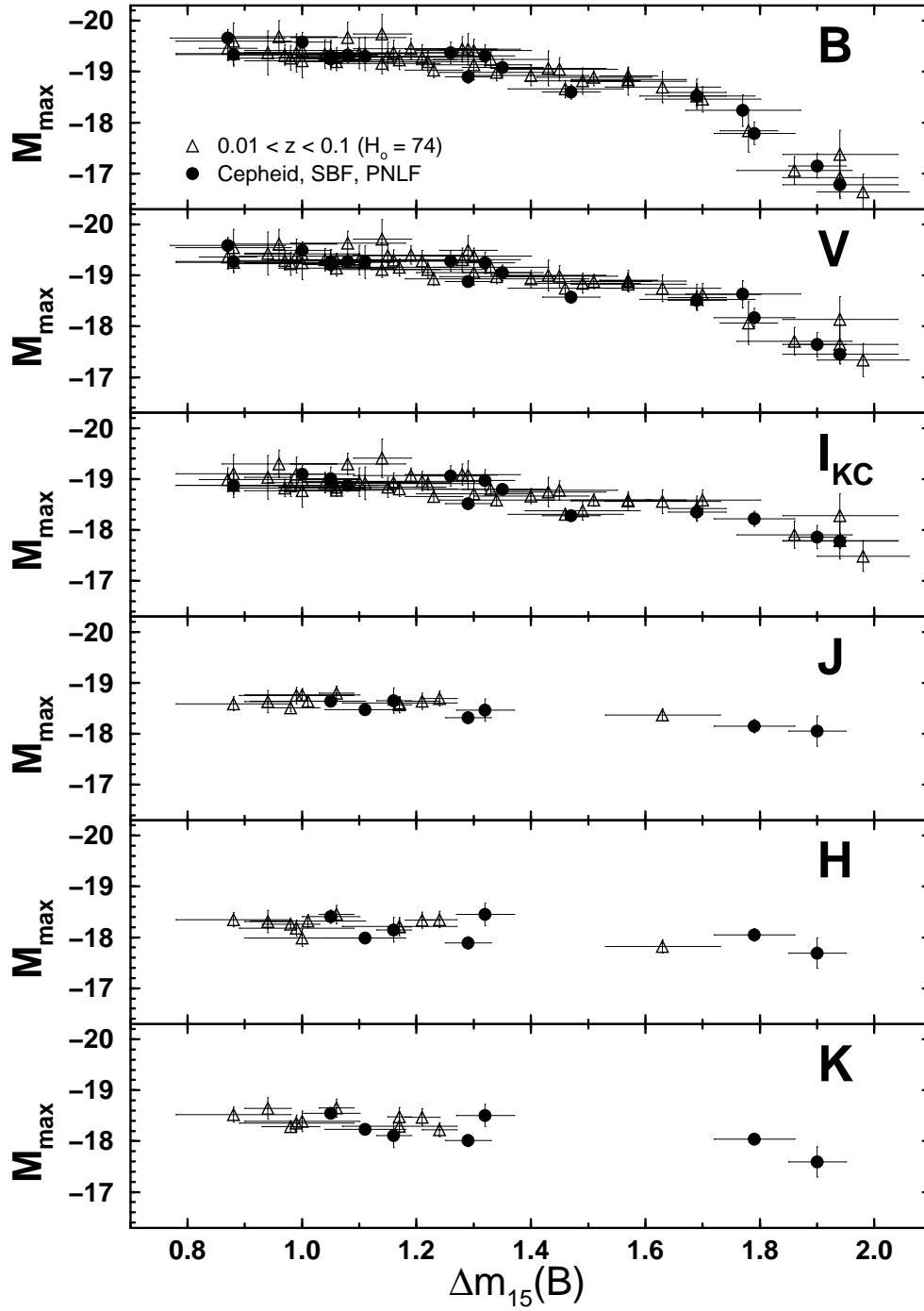
Figure 3.1: The decline rate relation in *BVIJHK*. The solid circles represent nearby SNe Ia with distances determined from Cepheids, surface brightness fluctuations or the planetary nebula luminosity function method. The open triangles represent SNe Ia in the Hubble flow with distances derived from the host redshifts. (source: Phillips (2005))

examples of these methods are multicolor light-curve shapes (MLCS; Riess et al. 1996, 1998; Jha et al. 2007), PRES (Prieto et al. 2006), spectral adaptive light-curve template (SALT; Guy et al. 2005, 2007) and SiFTO (Conley et al. 2008). These light-curve fitters are able to further reduce the intrinsic dispersion to ~ 0.15 mag, making SNe Ia the best known standard candles to date.

Even though WLR comes from the combination of several physical effects and the theory is not well understood (Section 2.6), a crude explanation can be formed from the effect of varying ^{56}Ni mass. The light emitted by a SN Ia is powered by the stored energy in the radioactive decay of ^{56}Ni through ^{56}Co to ^{56}Fe (Colgate & McKee 1969). From the estimates of the bolometric luminosities, SNe Ia are shown to produce different amounts of ^{56}Ni in the explosion (e.g., Stritzinger et al. 2006a). More nickel produced in the explosion means extra energy from radioactive decay and a brighter supernova. More nickel also keeps the expanding matter opaque for longer and the radiation takes longer to leak out, making a slower decay. The result is the observed WLR.

Figure 3.1 also demonstrates the difference between the photometric properties of SNe Ia in the optical and in the near-infrared (NIR). In the NIR J, H and K bands, the peak brightness is shown to be quite uniform and exhibits little or no correlation with light-curve width. While SNe Ia can be calibrated to make standard candles in the optical, they appear to be true standard candles in the NIR. Elias et al. (1981, 1985) first noted the uniform photometric properties of SNe Ia in the NIR and the potential for them to be used as distance indicators. Recent observations have demonstrated the efficacy of this proposal and reported a dispersion of only 0.16 mag in the H band without the aid of light-curve corrections (Krisciunas et al. 2004a; Wood-Vasey et al. 2008). Matching the photometric properties, the spectroscopic properties of SNe Ia in the NIR also show remarkable uniformity at maximum light (Chapter 7).

In the 1990's, two SN Ia surveys, the High-Z SN Search Team and the Supernova Cosmology Project, set out to search for high redshift SNe Ia and use them as calibrated candles to measure the state of the cosmic expansion (Perlmutter et al. 1998; Garnavich et al. 1998; Schmidt et al. 1998; Riess et al. 1998; Perlmutter et al. 1999; Knop et al. 2003; Tonry et al. 2003; Barris et al. 2004; Riess et al. 2004; Knop et al. 2003). It was fully expected that the expansion would slow down, because the universe appears to be filled with gravitating matter. Both teams, with independent sets of samples (Figure 3.2), found the surprising result that the SNe Ia were $\sim 20\%$ fainter than expected for a slowing expansion, implying that they are $\sim 10\%$ more distant. The results indicated that the expansion of the universe is accelerating, not decelerating. This was the first evidence that the expansion of

the universe is currently accelerating.

A repulsive gravity can manifest itself in the standard model of cosmology through a positive cosmological constant (Equation 3.10). For a large enough cosmological constant, the gravitating matter is overcome and the expansion begins to accelerate. Einstein's cosmological constant, originally introduced to maintain a static universe, is invoked here again as the possible explanation of the observed accelerated rate of expansion. The repulsive component is shown by the SN Ia data to comprise over half of the total matter-energy content of the universe. Whether or not the repulsive component is truly from a cosmological constant, it remains a challenge for current physics to explain its physical origin. This mysterious component of the universe became known as "dark energy" to reflect our lack of understanding as to its nature.

3.8   Dark energy

The determination of cosmological parameters using SNe Ia as calibrated candles is complemented by the results from other independent probes. These methods include cosmic microwave background anisotropies (e.g., Spergel et al. 2007), baryon acoustic oscillation (e.g., Percival et al. 2007), X-ray gas mass fraction of clusters (e.g., Allen et al. 2008) and primordial deuterium abundance (e.g., Kirkman et al. 2003). In particular, the cosmic microwave background method is sensitive to the sum of Ω_Λ and Ω_M, while the apparent magnitudes of SNe Ia are sensitive to the difference. The two methods combine to yield strict constraints on the values of Ω_Λ and Ω_M.

The results from the various methods show exquisite agreement and are consistent with a single picture of the universe characterized by a concordance model describing the present-day matter-energy contributions from the various components (Table 3.1). The universe is shown to be exquisitely flat ($\Omega_{total} \sim 1$). This can be shown to be a consequence of the exponential expansion, 10^{-36} seconds after the big bang, proposed by the inflationary theory. More than 90% of the matter-energy content of the universe consists of "material" unknown to current physics. While many feel that the identity of dark matter is within reach with the completion of the Large Hadron Collider, the same cannot be said about dark energy.

From observations, the contributions of the energy density from the curvature of space and radiation can be assumed to be zero. To test whether dark energy results from a pure cosmological constant, the luminosity distance from Equation 3.31 can be simplified and parametrized by the equation-of-state parameter of dark energy w:
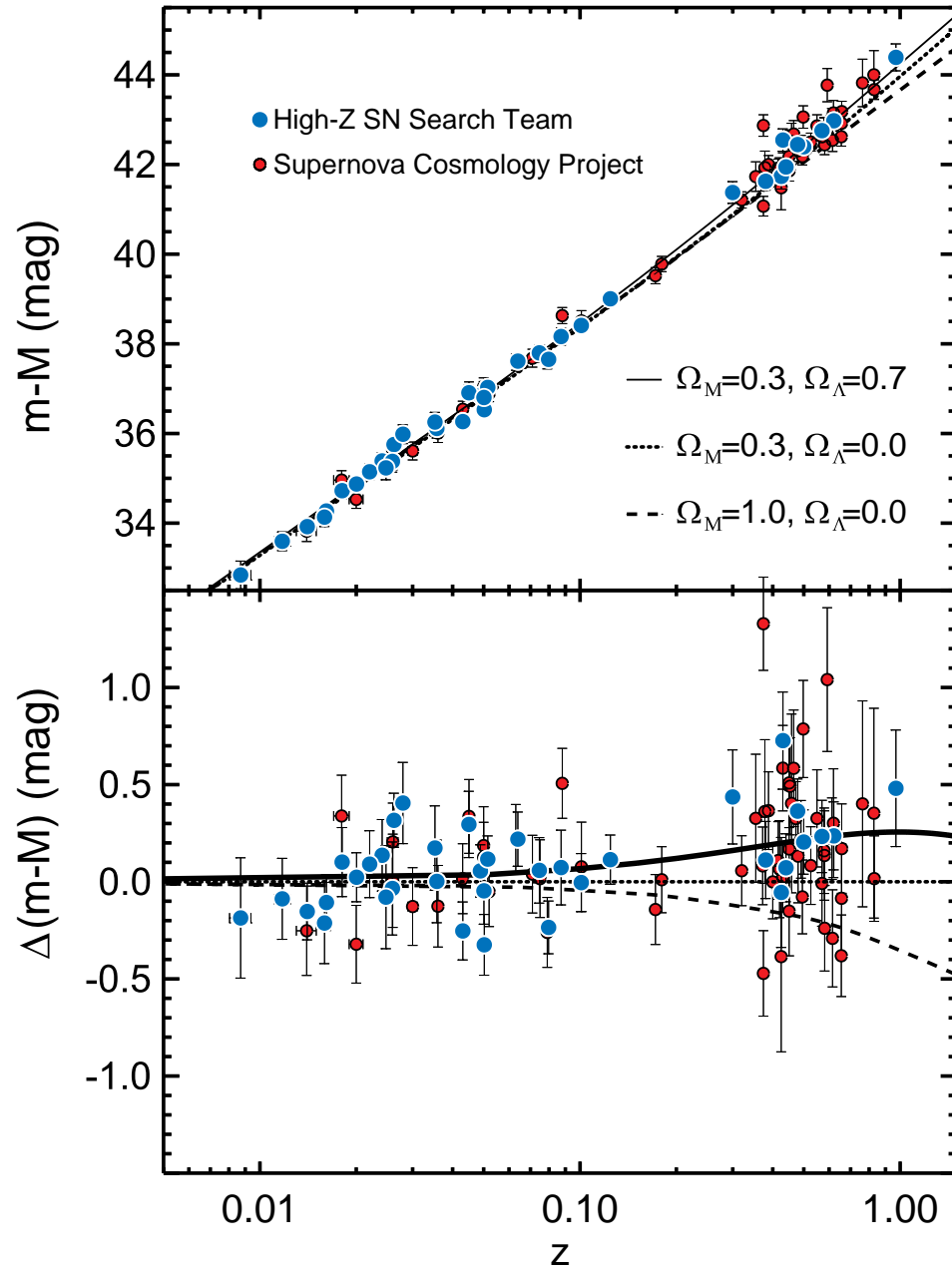
Figure 3.2: The Hubble diagram using independent samples from the High-Z SN Search Team (blue circles; Riess et al. 1998) and the Supernova Cosmology Project (red circles; Perlmutter et al. 1999) (source: Riess et al. (1998))

Table 3.1: The density parameters of the concordance model

density parameter	contribution
Ω_Λ	0.7
Ω_{DM}	0.26
Ω_b	0.04
Ω_r	5×10^{-5}
Ω_{total}	1

$$d_L = \frac{(1+z)}{H_0} \int_0^z \frac{dz'}{\sqrt{\Omega_M(1+z')^3 + (1-\Omega_M)(1+z')^{3(1+w)}}}. \qquad (3.39)$$

For the case of a cosmological constant, the equation-of-state parameter $w = -1$, and pressure p and density ρ are all independent of time.

The measurement of the equation-of-state parameter w can help to exclude certain theoretical models of dark energy (Huterer & Turner 2001). Two surveys, the Supernova Legacy Survey (SNLS; Astier et al. 2006) and Equation of State: Supernovae Trace Cosmic Expansion (ESSENCE; Wood-Vasey et al. 2007) aim to constrain the nature of dark energy with observations of hundreds of high-redshift SNe Ia. The key difference between this new generation of supernova surveys and previous surveys is the meticulous control of the systematic errors. This is accomplished through consistent instrumentation and reduction techniques.

Both teams have presented the equation-of-state parameter values close to $w = -1$ with ever decreasing uncertainties. The results are fully consistent with the idea that dark energy is the manifestation of the cosmological constant. The cosmological constant through the formulation of the general theory is the property of space itself. As seen previously in Equation 3.13, its density in empty space remains the same as the universe expands. Gravitating matter, on the other hand, is rapidly diluted by the expansion. Further observations of SNe Ia above redshift of 1 showed the apparent brightening of these high-redshift objects compared to an Einstein-de Sitter universe (Riess et al. 2004, 2007). This is interpreted to be evidence of past deceleration. The transition to a dark-energy-dominated universe is observed to take place at approximately 2/3 of the present age of the universe.

What is the physical origin of the cosmological constant? The inflationary nature of dark energy, and the fact that it infuses space, gives rise to the idea that dark energy is associated with vacuum energy introduced by quantum mechanical fluctuation. The energy

density expected from Planck units is on the order of $\rho_p \sim 10^{93}$ g cm^{-3}. From the observational value of Ω_Λ, the energy density of dark energy is on the order of $\rho_\Lambda \sim 10^{-30}$ g cm^{-3}. The discrepancy is on the order of 10^{123} requiring enormous fine tuning. This "fine-tuning problem" was dubbed "the biggest mistake ever made by physicists" by Steven Weinberg. Furthermore, there is also a lack of natural explanation for the observation that ρ_Λ/ρ_M is on the order of unity. This is called the "coincidence problem." The mysterious nature of dark energy has thus far generated an enormous number of theories in an attempt to address the above issues. A small fraction of them is outlined here.

Scalar fields   These theories utilize scalar fields coupled to gravity, such that ρ_Λ is nearly cancelled when the scalar field reaches equilibrium. An evolving scalar field with a chosen potential function can yield vacuum energy that varies with time. The free potential function can be chosen to produce any specified $H(z)$. Even if $w(z)$ is perfectly determined from observations, it is still difficult to falsify specific models. This class of models thus lacks predictive power. Furthermore, the scalar field potentials still require fine tuning in order to produce viable parameters (Weinberg 1989). This approach has thus been criticized of merely pushing the cosmological problems to another level (Padmanabhan 2006).

Inhomogeneity   Another class of theories examines whether the simplifying assumption of the Copernican principle is valid (Mustapha et al. 1997). The energy-momentum tensor of the real universe is inhomogeneous and anisotropic. The fundamental tensor describing the geometry of the universe at large scales should be obtained by averaging the exact solutions of the Einstein field equations over a suitably large range. Practically, the energy-momentum tensor is averaged first to obtain the solution for the Einstein field equations. In reality, the Einstein tensor is a nonlinear function of the fundamental tensor:

$$\langle G^{ik}(g) \rangle \neq G^{ik}(\langle g \rangle). \tag{3.40}$$

The Einstein field equations in Equation 3.6 can then be rewritten as:

$$\begin{aligned} G^{ik}(\langle g \rangle) \quad &= 8\pi G \langle T^{ik} \rangle + G^{ik}(\langle g \rangle) - \langle G^{ik}(g) \rangle \\ &\equiv 8\pi G[\langle T^{ik} \rangle + T^{ik}_{corr}]. \end{aligned} \tag{3.41}$$

If the correction term can mimic the cosmological constant at large scales, there will be no need for dark energy. In particular, an inhomogeneity in the form of a large void may also accomplish this effect (e.g., Leith et al. 2008). The probability of us living in such a special

place in the universe is unlikely but not impossible. SNe Ia in the redshift range $0.1 - 0.4$ may offer a way to test the validity of the Copernican principle (Clifton et al. 2008).

Anthropic principle There is also the distinct possibility that there is no natural way to explain the fine-tuning and coincidence problems from fundamental principles. The anthropic principle (Weinberg 1987) argues that we are here to observe the problems of dark energy precisely because we are in a universe with just the right conditions for intelligent life. This approach infers the existence of many universes or many disconnected sub-universes, with a range of different vacuum energy. The probability distribution of the observed values of vacuum energy is based on the likelihood of observers existing in these universes. Much like Darwin's theory of evolution by natural selection, our universe is selected because it has the right condition for galaxies to form. Universes with larger vacuum energy would produce the repulsive force before galaxies could form. Conversely, universes with negative vacuum energy would re-collapse before galaxies could form. Although not based on fundamental principles, the anthropic principle has the potential to provide a viable resolution for both the fine-tuning and coincidence problems.

3.9 Systematic errors

With the advent of large surveys producing data for hundreds of SNe Ia, the statistical uncertainties are lowered to the point where they are comparable to, or even surpassed by, the systematic uncertainties. Systematic errors are thus the current limiting factor in SN Ia cosmology. Systematic errors describe uncertainties which affect multiple SNe Ia in a correlated manner. To reduce the effects requires a deeper understanding of the sources of the errors, rather than a larger sample. A tremendous amount of work has been done to identify, model and reduce these effects and has helped the design of current and future surveys. A sample of the systematic errors which affect the SN Ia cosmology is outlined here.

Evolution The systematic uncertainties from evolution follow from our lack of understanding of SN Ia progenitors (Section 2.3). The effect is difficult to model with no quantitative predictions from current theories. Another effect to consider here is the demographic shift to brighter and bluer SNe Ia with increasing redshift. This is due to the demographic shift of the host galaxies (Section 2.7). This shift does not pose a problem to cosmology, as

long as the WLR, formed by low-redshift SNe Ia, can correct the shift in average luminosity at high redshifts. There is reason to believe this is the case, since the demographic shift of host galaxies over the redshift range considered is smaller than the variation of nearby host galaxies. Studies have used spectroscopic data in attempts to search for systematic differences between low-redshift and high-redshift SNe Ia. They use various indicators of spectroscopic properties, such as feature velocity, strength and flux ratios (Hook et al. 2005; Blondin et al. 2006; Garavini et al. 2007; Foley et al. 2008a; Bronder et al. 2008; Altavilla et al. 2009), ultraviolet spectra (Ellis et al. 2008; Sullivan et al. 2009) and temporal evolution (Foley et al. 2005; Blondin et al. 2008). The vast majority of the studies found no evidence of evolution. Foley et al. (2008a) found differences in the ultraviolet and optical Fe II features between low-redshift and high-redshift samples. Sullivan et al. (2009) found differences indicating lower abundances for intermediate-mass elements in the high redshift SNe. In both cases, they cannot rule out the possibility that the differences are driven by demographic shifts of host galaxies, rather than true evolution of SN Ia properties. Foley et al. (2008a) constrained the systematic error to be < 0.02 mag.

Malmquist bias   Flux-limited surveys suffer from Malmquist bias (Malmquist 1920). If after luminosity corrections based on WLR, SNe Ia are perfect standard candles, Malmquist bias would have no effect. Because there are additional dispersions after the corrections, Malmquist bias results in systematic errors. The effect should be negligible below intermediate redshifts where the sampling is complete. The effects at high redshifts can be modeled and accounted for. There is a related bias on the amount of time a SN Ia stays above the detection threshold. Brighter and slower declining SNe Ia would stay above the detection threshold longer, causing a change in the average brightness of SNe Ia in a redshift-dependent manner. The amount of bias in the nearby sample can be estimated by examining how early on in the light curve the SNe Ia are discovered. A data set with SNe Ia discovered at earlier epochs suffers less bias than one with SNe Ia discovered at later epochs.

Peculiar velocities   Systematic errors can arise with the assumption that the nearby SNe Ia are at rest in the cosmic microwave background frame, if there exists coherent large-scale local peculiar velocities (Hui & Greene 2006; Cooray & Caldwell 2006). Neill et al. (2007) presented corrections for this effect of the nearby sample using the density field of galaxies and different flow models. The remaining statistical errors can be further reduced with larger samples.

Gravitational lensing Gravitational lensing can magnify or de-magnify the observed flux. The expected probability distribution function is asymmetric about zero magnification. Systematic errors can arise from this asymmetry. Holz & Linder (2005) demonstrated that the effect decreases quickly with increasing sample size. The effect can then be treated as a statistical dispersion.

Gray dust Aguirre (1999a,b) suggested that an increase in the dust grain size can mimic the apparent dimming of SNe Ia brightness without producing observable reddening. However, the observations of SNe Ia at redshifts $z > 1$ by Riess et al. (2004, 2007) show the effect of the transition from a matter-dominated to a dark-energy-dominated universe. While the luminosities of SNe Ia are first found to be too faint for a matter-dominated universe, these higher redshift SNe Ia show an apparent brightening compared to a matter-dominated universe. The effect is difficult to explain using gray dust. Furthermore, for SNe Ia to become consistently dimmer, dust needs to be distributed throughout intergalactic space. Current observations have placed significant constraints on the amount of intergalactic dust (e.g., Petric et al. 2006).

Dust extinction The large extinction correction necessary in the optical magnifies any sources of systematic errors in the observed colors. The situation is further complicated by our lack of understanding of dust properties in distant galaxies. Using photometry in the NIR region, where the amount of dust extinction is much less compared to the optical, there is evidence that the dust along the line of sight to SNe Ia does not have the same average properties as dust in the Milky Way (Krisciunas et al. 2007; Wang et al. 2008; Elias-Rosa et al. 2008). Furthermore, the observed colors of SNe Ia include contributions from dust reddening and intrinsic colors, and the two effects cannot be separated easily. Modern light-curve fitters treat reddening differently. SALT2 (Guy et al. 2007) and SiFTO (Conley et al. 2008) fit for a color-luminosity relation with a slope β and do not distinguish between intrinsic colors and dust, while MLCS2k2 (Jha et al. 2007) attempts to separate the two effects using assumptions and redshift-dependent priors. Both approaches are susceptible to the shift in host properties with respect to redshift. Future surveys can reduce these errors by using complementary observations of NIR light curves (Krisciunas et al. 2000) or optical spectra (Chapter 6) as indicators of intrinsic colors. More recently, Wang et al. (2009b) demonstrated that the expansion velocities of the Si II 6355Å can be used to divide SNe Ia into groups of different dust properties, and in turn improve extinction correction.

Flux calibration   Nearby SNe Ia provide important comparison reference for cosmological studies. This requires the understanding of photometric calibrations of high-redshift data relative to the low-redshift sample. The current sample of low-redshift data is inhomogeneous with a range of qualities in flux calibration and bandpass knowledge. The use of this low-redshift data usually requires the calibration of SNe Ia onto the Landolt system (Landolt 1992) which is not well understood. Mismatch between actual instrumental passbands and those of the standard system causes uncertainties. Since passbands are shared across many observations, the errors are correlated between SNe Ia. Furthermore, Vega, which is used to define the zero points, is much brighter than the standard stars. The estimation of Vega's actual magnitudes in a photometric system that it has never been observed in introduces further systematic errors. Low-redshift data from ongoing surveys will allow cosmological studies to move off the Landolt system.

K-correction   The *K*-correction yields one of the largest sources of systematic errors as it directly affects the peak magnitude of a SN Ia (Section 3.6). *K*-correction errors have contributions from the uncertainties in the zero points and the passbands of the photometric system, the instrumental passbands, and the assumed SED for the object (Equation 3.37). The uncertainty in the zero points is related to the flux calibration. The indirect determination of the zero points from Vega can lead to systematic errors of a few percent (Fukugita et al. 1996). An instrumental passband is the wavelength-dependent throughput of the entire light path and includes transmission of the optics, mirror reflectivity, filter transmission, CCD quantum efficiency and atmospheric absorption. Examining the effects of bandpass shape on SN Ia cosmology, Davis et al. (2006) showed that for a typical deviation from the nominal filter shape, the *K*-correction error introduced is below 0.004 mag. Studying the effect of spectroscopic diversity on SN Ia cosmology, Hsiao et al. (2007a) demonstrated that the systematic errors from assuming an SED can be largely eliminated by using a mean spectral template time series. The remaining statistical errors are redshift dependent and are on average 0.02 mag (Chapter 5; Hsiao et al. 2007a; Foley et al. 2008a). The errors can be further reduced if the detailed shapes of the spectral features can be predicted using photometric information (Chapter 6).

3.10   Conclusion

SNe Ia can be used as standard candles to make direct measurements of the cosmological parameters. The apparent faintness of distant SNe Ia revealed a previously unaccounted

for dark energy. The discovery is significant as the existence of dark energy presents great challenges to fundamental physics. The current generation of supernova surveys produces observations for hundreds of SNe Ia. The statistical errors are reduced, while systematic errors become the limiting factor for SN Ia cosmology. With meticulous identification and control of systematic errors, SNe Ia can be further used to constrain the nature of dark energy.

This thesis is motivated by the potential for substantial improvement in cosmological studies by exploring methods to reduce systematic errors. In particular, the spectroscopic diversity of SNe Ia and its effect on SN Ia cosmology have not been studied in detail before this work. In the following sections, methods for quantifying spectral features of supernovae are developed. They are then used to identify the mean spectroscopic properties of SNe Ia; this eliminates the systematic errors associated with assuming a particular SED. Methods are also developed to search for correlations between spectral features and light-curve width. Established relations can further reduce the remaining statistical errors and even provide independent distance estimates.

Chapter 4

Quantifying spectral features

Abstract   The tools and the sample of observed spectra used to study the spectroscopic diversity of Type Ia supernovae (SNe Ia) are detailed here. A library of a statistically significant sample of observed spectra is presented. The spectra are from a wide variety of sources to cover a wide range of parameter space. Methods are thus developed to consistently quantify the spectral features from heterogeneous sources. A spectral template time series is constructed using the mean spectral properties of the library spectra. Using the mean spectral templates for K-correction calculations largely eliminates the systematic errors from assuming a particular SED. The procedures and formulation of principal component analysis (PCA) are also outlined. A set of spectroscopic data can be reduced into orthogonal principal components (PCs). Only the first few PCs are necessary to describe the bulk of the variations. They can then be used to correlate with other SN Ia properties to search for the origin of the observed variations.

4.1   Introduction

With the advent of modern surveys which yield observations for hundreds of SNe Ia, the precision and accuracy requirements for the K-corrections are only increasing. The diversities in the spectral features of SNe Ia become a major contributor of errors.

To study the spectroscopic diversity of SNe Ia, a statistically significant sample of observed spectra is needed. Our current library of spectra contains 1100 spectra of 183 SNe Ia. In order to obtain spectra which cover wide ranges of epoch, wavelength and light-curve width, the library is constructed using spectra from a variety of sources. Methods are thus developed specifically to quantify the spectral features of a heterogeneous data set

consistently.

SN Ia spectral features are formed by a blend of multiple lines enhanced by large Doppler broadening. The shapes of the spectral features are thus complex with no clear continuum. Methods are developed to standardize the broadband colors of the library spectra and to quantify their spectral features using artificial narrowband filters. The result is a consistent treatment of SN Ia spectra, without resorting to by-eye estimation of a "pseudo-continuum." A mean spectral template time series is built using the mean spectral properties of the large SN Ia sample. When used for K-correction calculations, the spectral template time series obviates the systematic errors resulting from assuming a particular SED.

PCA is a powerful statistical tool used to search for patterns and to reduce the dimensionality of a multidimensional data set. It is ideal for treating spectroscopic data. Instead of examining individual spectral features, PCA can pick out the dominant variations within a wavelength region and reduce the spectra into PCs. Once the largest variation is identified, the first few PCs describing the bulk of the observed variation can then be used to search for correlations between spectral features and other parameters, such as epoch and light-curve width. PCA will be adopted in Chapters 6 and 7 to identify the largest variations in the spectral features and to search for the origins of these variations.

In this thesis, particular sets of passbands are used for continuum adjustment and K-correction calculations. In the optical, the Bessell (1990) realization of the Johnson-Cousins $UBVRI$ passbands is adopted as rest-frame passbands. The MegaCam passbands, $g_M r_M i_M z_M$, are adopted as examples of observed passbands. MegaCam is a wide-field imager on the Canada-France-Hawaii Telescope (CFHT) on Mauna Kea. The MegaCam filters are closest to the US Naval Observatory (USNO) filters (Smith et al. 2002) and similar to the Sloan Digital Sky Survey (SDSS) filters (Fukugita et al. 1996). In the near-infrared (NIR), the $YJHK$ passbands of the Wide Field Infrared Camera (WIRC) on the 2.5 m du Pont telescope (Persson et al. 2002) are adopted. The methods developed here are general and are not restricted to these sets of filter bands.

4.2   Library of spectra

To study the spectroscopic diversity of an apparently uniform class of objects, it is important to use a statistically significant sample of observed spectra which spans a wide range of properties. We have constructed, and are continuing to update, a library of observed SN Ia spectra. The library currently includes 1100 spectra of 183 SNe Ia, including 117 nearby SNe Ia with complementary photometric information. The properties of the library

are illustrated in Figure 4.1, and the full list of library spectra is placed in Appendix A. Currently, the photometric data of approximately 300 low-redshift SNe Ia are cosmologically useful (Hamuy et al. 1996a; Riess et al. 1999; Jha et al. 2006; Hicken et al. 2009). The statistical significance of the spectroscopic data is rapidly approaching that of photometric data.

The observed spectra were gathered from heterogeneous sources with varying quality. A large fraction of the spectra was obtained from public resources, such as the SUSPECT[1] database and publications. Other spectra were supplied by past and ongoing supernova surveys, such as the Calán/Tololo Supernova Survey (Hamuy et al. 1996a), CfA Supernova Group (Matheson et al. 2008), Supernova Cosmology Project (Garavini et al. 2004, 2005; Lidman et al. 2005), Carnegie Supernova Project (Hamuy et al. 2006), Supernova Legacy Survey (Howell et al. 2005; Bronder et al. 2008) and Equation of State: Supernovae Trace Cosmic Expansion (Matheson et al. 2005).

Each observed spectrum is inspected by eye for quality. Spectra which have their spectral features dominated by noise are discarded. The edges of each spectrum are inspected and trimmed where the flux calibrations appear unreliable. The atmospheric telluric lines in the *I* band are removed using procedures described in Section 4.3.

The library spectra are overwhelmingly of low-redshift SNe Ia (top left panel of Figure 4.1). Spectroscopic observations of high-redshift supernovae are much more susceptible to host galaxy contamination, because the smaller supernova-host angular separations are observed through a fixed slit width. Observations of low-redshift SNe Ia generally yield higher signal-to-noise ratio than high-redshift ones, because of the larger apparent luminosities. On the other hand, high-redshift surveys produce spectra with better observations of the difficult ultraviolet (UV) region, which is crucial for *K*-corrections to *B* at high redshifts. Spectra from SNe Ia with redshifts up to 0.8 are included. For the making of the mean spectral template, the assumption is made that there is no significant evolution of spectral features between low-redshift and high-redshift supernovae (Section 3.9). Note that none of the high-redshift spectra have time series observations. The histograms in Figure 4.1 are separated by redshift at $z = 0.1$ to demonstrate the difference in characteristics between the two samples.

The library spectra mostly cover rest-frame *B* and *V* filter bands (bottom right panel of Figure 4.1). The *K*-correction analysis will be focused on corrections to the rest-frame *B* band, since it is the most important and commonly used band in current cosmological analysis. When the observed and the rest-frame *B* filter bands are misaligned, the spectral

---

[1]See http://bruford.nhn.ou.edu/~suspect/index.html.
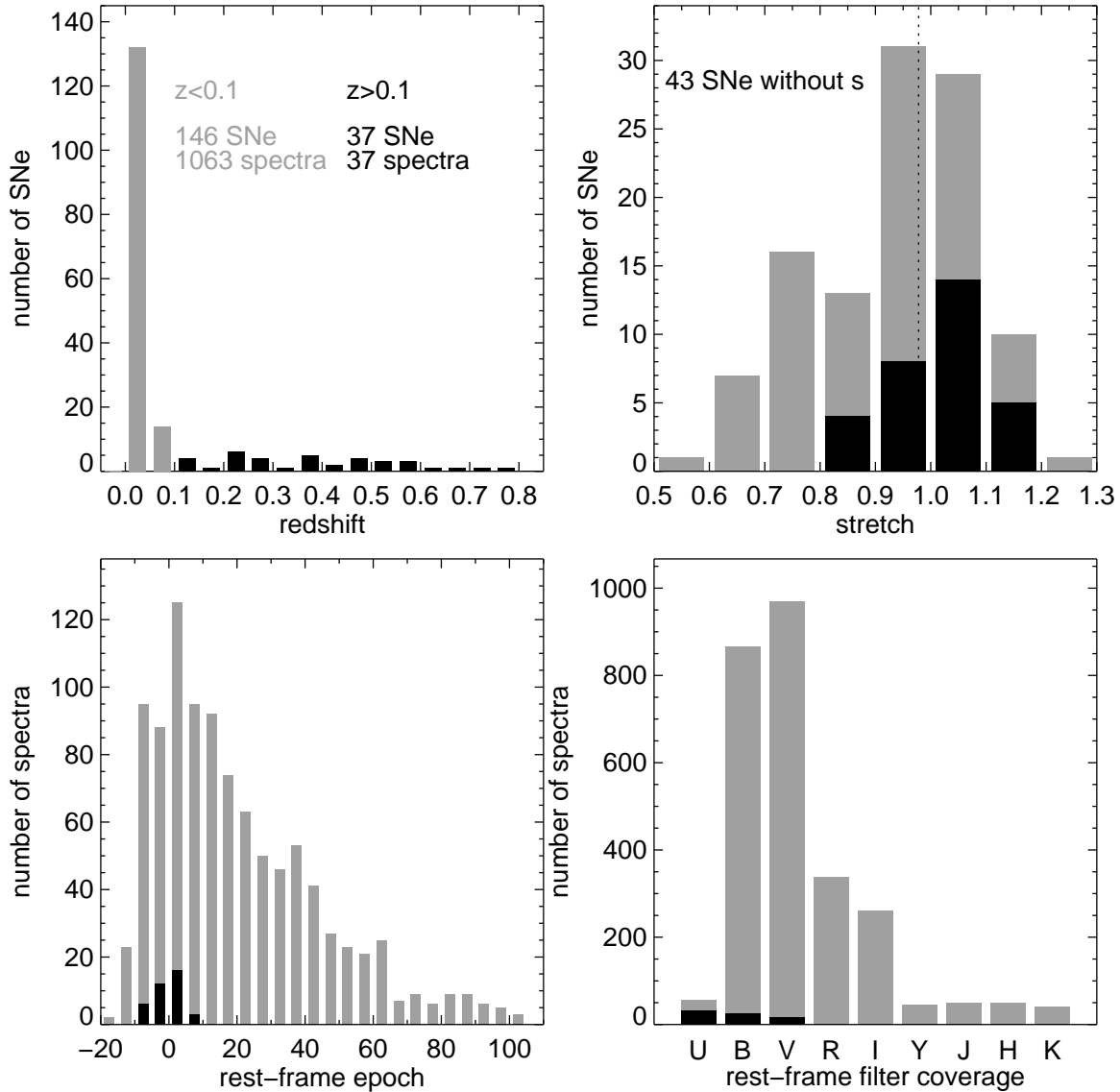
Figure 4.1: Characteristics of our current spectral library. The histograms are separated by redshift at $z = 0.1$ to demonstrate the difference in characteristics between the two samples (gray for $z < 0.1$ and black for $z > 0.1$). The top left panel plots the histogram of the redshifts of the library supernovae. The top right panel plots the histogram of the stretch factors of the library supernovae. Only supernovae with reliable photometry are included in this plot. The median stretch value for the combined sample is marked with a dotted vertical line. The bottom left and right panels plot the histograms of the rest-frame epoch relative to B-band maximum light and the rest-frame wavelength coverage of the library spectra, respectively.

features in the neighboring *U* and *V* filter bands are especially important. The relative shortage of UV spectra is slightly improved by the inclusion of high-redshift SNe Ia.

The rest-frame epochs of the spectra are relative to *B*-band maximum light and are obtained mainly from the light curves of the supernovae. When the photometry of a SN Ia is unavailable or unreliable, an estimate of the epoch is made by fitting the spectrum to other spectra of known ages. The distribution of the epochs peaks at maximum light (bottom left panel of Figure 4.1). The epochs are corrected for time-dilation with a factor $(1 + z)^{-1}$. They are also stretch-corrected by a factor s^{-1}. (This stretch correction procedure will be justified in Section 6.6.)

The light-curve shape is a useful parameter to characterize the diversity of the library SNe Ia. For each SN Ia with well sampled light curves, a stretch factor is measured using the SiFTO light-curve fitter (Conley et al. 2008). The stretch factor, *s*, linearly stretches or contracts the time axis of a template light curve around the epoch relative to maximum *B*-band light to best fit the observed light curve (Perlmutter et al. 1997, 1999; Goldhaber et al. 2001). The stretch factors of the library SNe Ia span a wide range of values with most of the supernovae around a stretch of unity (top right panel of Figure 4.1). The high-redshift sample has a slightly higher median stretch ($s = 1.039$) than the low redshift sample ($s = 0.964$). This is caused by the preferential selection of brighter (higher stretch) SNe Ia, which in general yield higher signal-to-noise ratios, at high redshifts. The median stretch factor for the combined sample is 0.978.

4.3 Telluric absorption correction

The atmospheric telluric absorption features are mainly caused by water vapor (Figure 4.2). The strengths, widths and central wavelengths of the telluric features depends on specific observing conditions, such as wind speed, pressure, temperature, humidity, air mass and the observer's elevation. Careful removal of telluric features requires the observation of a telluric reference star at a similar time and location in the sky as the observed object. The telluric features are then removed using templates of molecular absorption to match the features of the observed reference (Stevenson 1994) or by using the spectrum of the relative featureless A-type star directly as the telluric template (Vacca et al. 2003). Since the telluric absorptions only affect spectra at long wavelengths, telluric corrections are usually not applied for optical spectra of SNe Ia.

For SNe Ia at different redshifts, the telluric features are superimposed at different wavelength locations in the rest-frame of the SNe Ia. This is not desirable from the view point
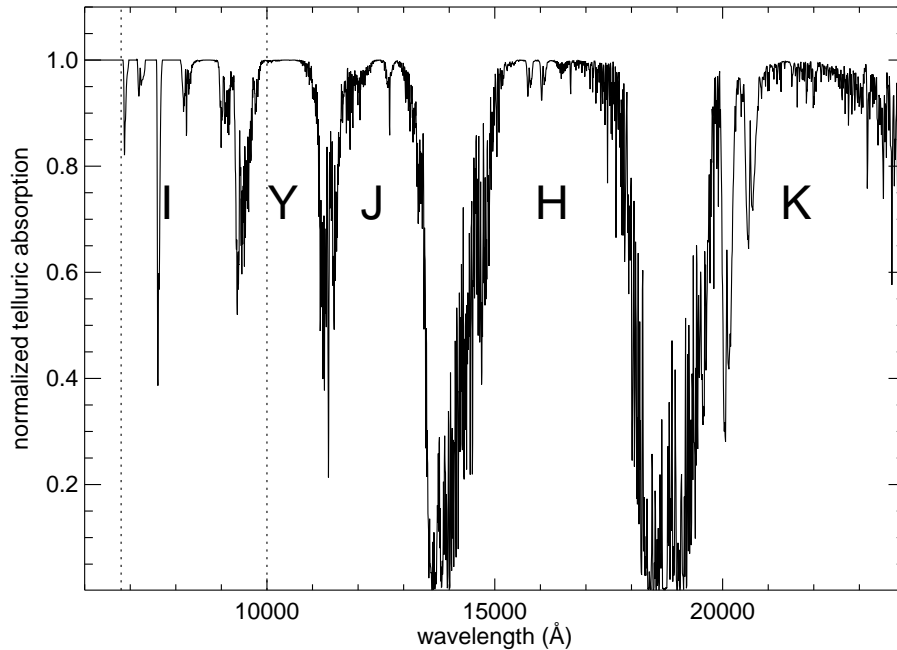
Figure 4.2: The atmospheric telluric absorption features. The locations of the *IYJHK* bands are noted. The dotted vertical lines mark the region where the telluric features are removed from the library spectra.

of *K*-correction, as the telluric absorptions should be included in the observed instrumental bandpasses. Steps are thus taken to remove the narrow telluric features in the *I* band (Figure 4.2). This will yield improvement to the spectral template in the *I* band for high-redshift NIR studies (Nobili et al. 2005; Freedman 2005) and for studying the spectroscopic diversity in the *I* band (Chapter 6).

It is obviously not possible to do the careful corrections described above for our heterogeneous data set. Instead, known host redshifts and the relative broadness of the supernova features compared to the telluric features are used to make the correction. The host redshifts are used to locate the telluric features. With low weights placed at the locations of the telluric features, Gaussian smoothing is used to extrapolate from regions without telluric contamination to determine what the flux level should be at the locations of the telluric features. Non-linear least-squares fitting (Markwardt 2009) is then used to determined the depths, widths and the central wavelengths of the telluric template which give the best fits to the observed telluric lines. Examples of these procedures on two SNe Ia at two different epochs are shown in Figure 4.3.

During the building of a set of mean spectral templates, wavelength regions of the
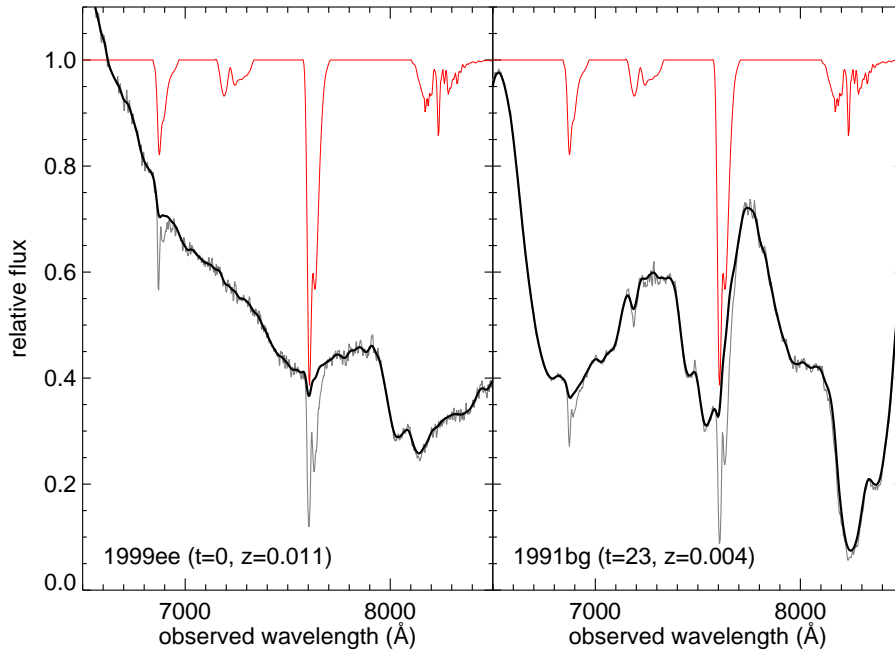
Figure 4.3: Two examples of telluric feature removal from supernova spectra. The left and right panels show spectra of SN 1999ee at maximum light (Hamuy et al. 2002) and SN 1991bg at 23 days past maximum light (Turatto et al. 1996). The normalized telluric template is plotted as red curve. The library spectra before and after telluric correction are plotted as gray and black curves, respectively.

spectra which had the telluric correction are again assigned lower weights to minimize the impact from the uncertainties in the above procedures (Section 4.7). By using SNe Ia from a range of different redshifts, it is possible to obtain a good representation of the true SN Ia flux at every wavelength.

Note that for the 52 NIR library spectra, the prominent telluric absorptions were corrected using the observations of flux standards. These library spectra are discussed in Section 7.3. The procedures for their telluric corrections are detailed by Maiolino et al. (1996) and Vacca et al. (2003). The spectral features which are heavily affected by the prominent telluric lines between the NIR $YJHK$ bands are not included in the analysis of spectroscopic diversity in Chapter 7.

4.4   *K*-corrections and broadband colors

K-corrections of SNe Ia rely on the SED of the supernova. Since high signal-to-noise spectrophotometry of high-redshift SNe Ia at multiple epochs is currently not feasible, it is necessary to assume a set of spectral template time series.

K-correction calculations also depend on the supernova redshift through the alignment of the rest-frame and the observed filter bands. The observed filter band progressively shifts towards bluer parts of the spectrum as a supernova is redshifted to progressively longer wavelengths (from top to bottom panel of Figure 4.4). When the observed and rest-frame filter bands are misaligned, as in the top and the bottom panels of Figure 4.4, the *K*-corrections are more reliant on the assumed spectral template.

K-corrections are largely driven by the broadband colors of a SN Ia and are thus sensitive to anything that affects the continuum of the SED, such as the Milky Way and host galaxy extinction, and the intrinsic colors of the supernova. When a spectral template is used as an assumed SED for the supernova, its continuum must be adjusted to have the same colors as the supernova before the *K*-corrections can be determined. Nugent et al. (2002) demonstrated that two SNe Ia with very different spectral features can yield similar *K*-corrections when the spectra of the SNe Ia are adjusted to the same broadband colors. Adjusting the colors of the spectral template to match those of the particular SN Ia significantly improves the accuracy of the *K*-correction (Nugent et al. 2002). However, it is not generally true that two SNe Ia with identical broadband colors share identical SEDs. The diversity in individual spectral features between SNe Ia must also affect *K*-correction calculations.

These effects are illustrated in Figure 4.5. The *K*-corrections are calculated using individual library spectra. The spectrum colors are determined from synthetic photometry on the actual observed spectrum. Colors from the spectra themselves are used instead of photometric colors for the following reasons. Most of the library spectra are not spectrophotometric; therefore, using colors from photometry introduces errors which do not originate from supernova feature inhomogeneity. This choice was also made for practical reasons as the photometry of the library supernovae is sometimes unavailable or unreliable.

In Figure 4.5, the relation between the *K*-correction and broadband color is shown at two redshifts. At a redshift of 0.75 where the B and i_M bands are aligned (middle panel of Figure 4.4), *K*-corrections are largely independent of the colors of the supernovae (top panels of Figure 4.5). At $z = 0.9$, the filter bands are misaligned (bottom panel of Figure 4.4), and the *K*-corrections show a strong dependence on broadband colors with a
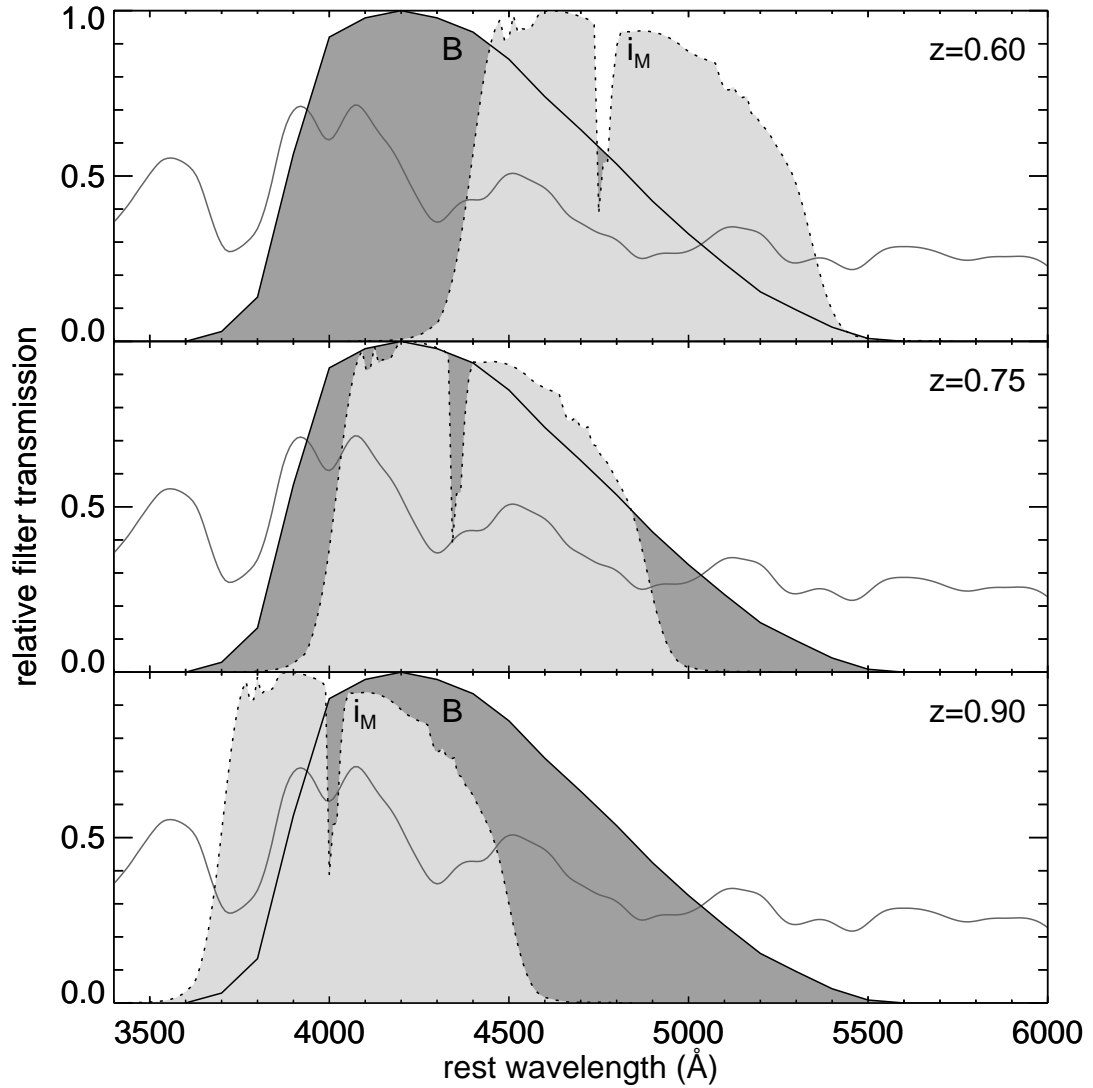
Figure 4.4: The pairing of observed filter i_M and rest-frame filter B at redshifts 0.6 (top panel), 0.75 (middle panel) and 0.9 (bottom panel). The solid curves are the transmission of B band, and the dotted curves are the transmission of the de-redshifted i_M band. The filter bands are misaligned at $z = 0.6$ and $z = 0.9$. The K-corrections at these redshifts depend heavily on the assumed spectral template.
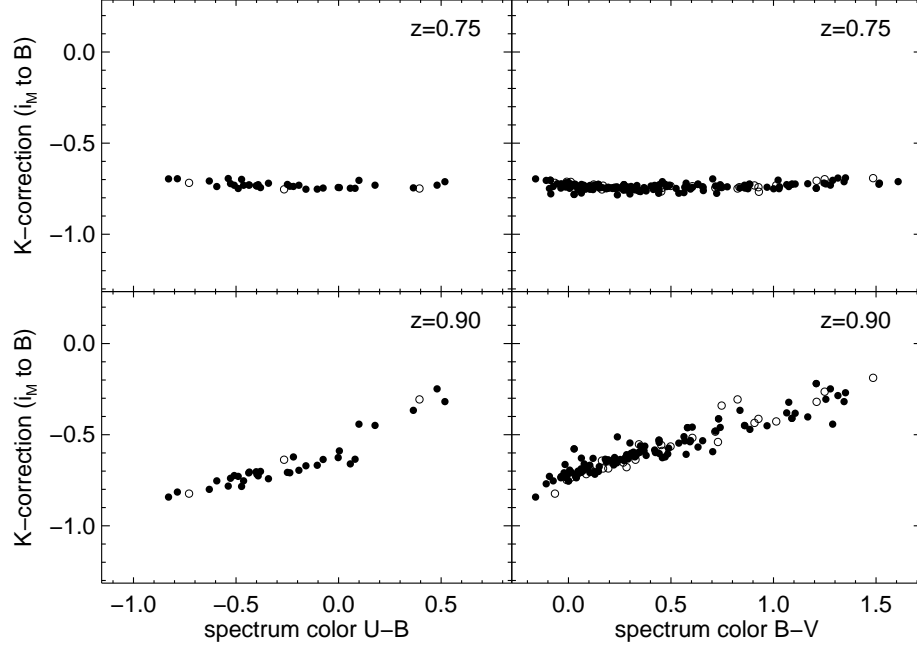
Figure 4.5: *K*-corrections from observed i_M band to rest-frame *B* band as a function of broadband colors, $U - B$ (left panels) and $B - V$ (right panels). The *K*-correction-color relations are plotted at the redshifts $z = 0.75$ (top panels) and $z = 0.9$ (bottom panels). The i_M and *B* filter bands are aligned at $z = 0.75$ and misaligned at $z = 0.9$. All the library spectra with adequate wavelength coverage are included. Each point represents one library spectrum. Filled and open circles represent normal and spectroscopically peculiar SNe Ia, respectively. The diversity in colors mostly reflects the time evolution of supernova colors. The scatter reflects the differences in the spectral features.

larger scatter around the trend (bottom panels of Figure 4.5). At these misaligned redshifts, the *K*-correction involves larger extrapolations and hence is more reliant on the details of the SED. The colors of the SED describe the bulk of the relation. The remaining scatter can be attributed to the inhomogeneity in spectral features, which will be the focus of this thesis.

How should one allow for color variations when calculating *K*-corrections? Previous studies have utilized the reddening law of Cardelli et al. (1989) to perform the color correction on the spectral template (e.g., Riess et al. 1998; Nugent et al. 2002; Tonry et al. 2003). This choice is based on the observation that SN Ia color relations roughly follow the reddening law. The correction applies a slope as a function of wavelength to the spectral template in order to obtain the desired $B - V$ color.

Modern surveys, such as the Supernova Legacy Survey, produce well sampled multi-
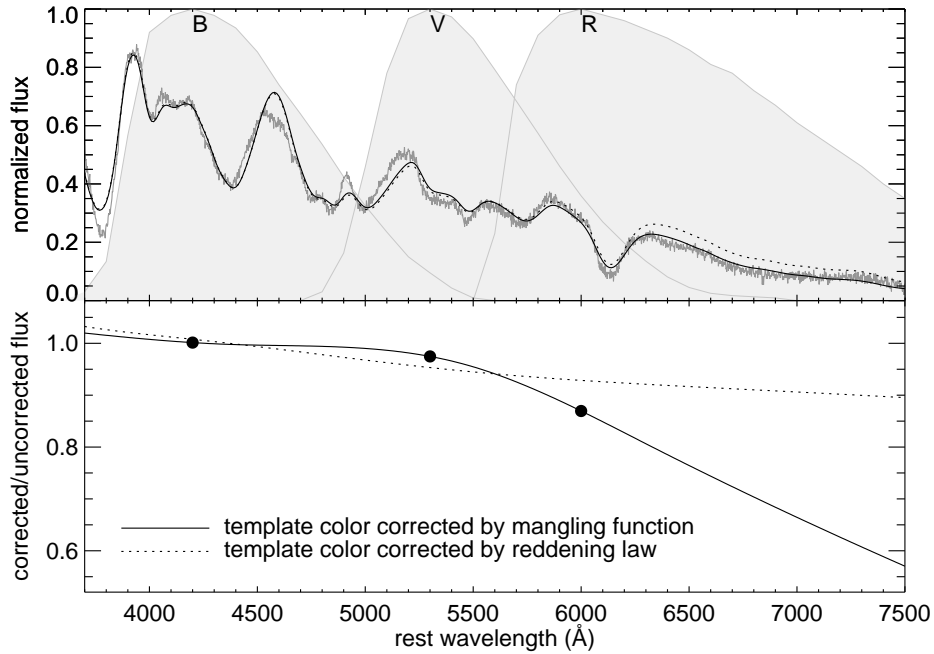
Figure 4.6: An example of color correction which contrasts the two color-correction methods: reddening law slope correction and the mangling function. The spectral template is color corrected to match the colors of an observed spectrum. The top panel shows three spectra: the observed spectrum (gray curve), the spectral template corrected by the mangling function (black solid curve) and the spectral template corrected by the reddening law (black dotted curve). The bottom panel shows the color-correction scale for the mangling function (black solid curve) and for the reddening law (black dotted curve). The black filled circles locate the spline knots for the mangling function. The mangling function adjusts the continuum using all the color information supplied, $B - V$ and $V - R$.

filter light curves and in turn produce multi-color information for most SNe Ia. To utilize fully the multi-color information, a "mangling function" is developed in lieu of the reddening law slope correction. It defines a spline as a function of wavelength, with knots located at the effective wavelengths of the filters. Non-linear least-squares fitting (Markwardt 2009) is used to determine the spline which smoothly scales the spectral template to the correct colors.

Figure 4.6 shows an example of color correction which contrasts the mangling function and the slope correction of the reddening law. The two methods exhibit similar behavior between the B and V filter bands. When the $V - R$ color information is included, the scale in the R band determined by the mangling function diverges from a slope correction to incorporate the extra color information. The mangling function anticipates the possibility

that the reddening law does not completely characterize all the colors of a SN Ia; it effectively pieces together segments of slope corrections smoothly to satisfy the multi-color information.

The variations in large features, such as the Ca H&K feature in the UV, can significantly alter the colors of the supernovae. It is difficult to disentangle color and feature variations in these cases; however, the results of the analysis here are unaffected as long as the distinctions between the effects of colors and features are consistently defined. Before spectra are compared with one another, they are color-corrected to the same broadband colors using the mangling function. This procedure consistently defines an effective "continuum" for all spectra and enables the study of the effect of spectral features on K-corrections independent of colors, whether the color differences are caused by extinction, intrinsic colors or observational effects.

Returning to Figure 4.5, this figure illustrates not only the general trend of K-correction in terms of supernova colors, but also the scatter around the trend which is caused by the diversity of spectral feature shapes. The scatter becomes more significant as the rest-frame filter band is redshifted away from the observed filter band (from top to bottom panels of Figure 4.5) showing the heavier reliance on the spectra and the inhomogeneity of the spectral features. The goal now is to construct a mean spectral template time series that is representative of the observed SN Ia spectral features and to characterize the errors associated with the spectral inhomogeneity shown in the scatter.

4.5 Measurements of feature strengths

A set of artificial non-overlapping narrowband filters are defined for measuring the spectral feature strengths (Figure 4.7). A trade-off needs to be considered when setting the bandwidths of the narrowband filters. A smaller bandwidth captures more details of the spectral feature shapes, but the signal-to-noise ratio is reduced. Here, we take advantage of the large expansion velocities of SNe Ia. The bandwidths of the narrowband filters are set to be on the order of the sizes of supernova features to maximize the signal-to-noise ratio without sacrificing the details of the spectral features.

The bandwidths of the narrowband filters are logarithmic in wavelength, and the ratio of $\Delta\lambda/\lambda = 0.03$ is adopted. This ratio corresponds to an expansion velocity of ~ 9000 km s^{-1}, which is on the low end of the observed expansion velocities in SN Ia features. The large expansion velocities of SNe Ia mean that the bandwidth of the narrowband filters can be set large enough that modest noise in observed spectra has minimal effect on the
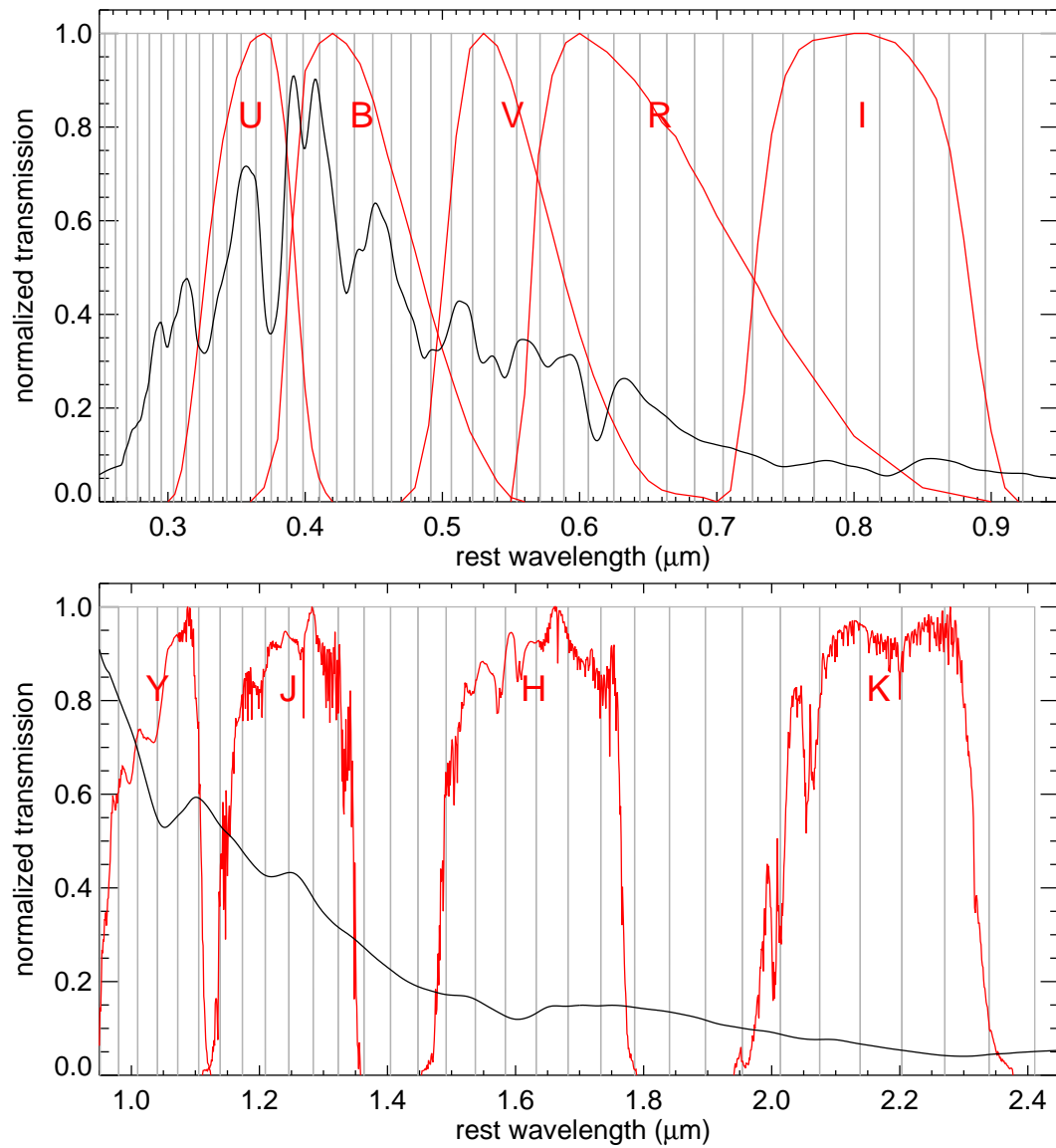
Figure 4.7: The defined narrowband filters for the measurement of spectral feature strengths. The narrowband filters are defined to have logarithmic bandwidths with a ratio of $\Delta\lambda/\lambda = 0.03$ and are plotted as gray lines. Broadband filters *UBVRIYJHK* are plotted as red curves. The spectral template at maximum light is plotted as a black curve to show the widths of the spectral features.

measurements of feature strengths.

The narrowband measurement approach also effectively lowers the resolutions of all spectra to a standard one. This is especially important for our heterogeneous data set which is obtained from a wide range of instruments and reduced with different techniques. A lowered resolution will help keep the heterogeneous nature of the data set from entering the signals which are intrinsic to the SNe Ia.

Before the feature strengths are measured, each library spectrum is color-corrected using the mangling function (Section 4.4) to a set of light-curve templates with a set stretch value (conventionally $s = 1$). It is worth noting that the procedure presented here for calculating K-corrections is independent of any established photometric relation, such as the stretch-color relation. Even though the stretch-color relation for a particular stretch value is used here to yield the standard colors for the library spectra, the spectral template later has to be color-corrected to match the colors of the particular SN Ia in question. The color-correction procedure removes any dependence on color varying factors, such as stretch, extinction and flux calibration. The spectral diversity of the library SNe Ia can then be adequately quantified independent of broadband colors.

4.6   Mean spectral template time series

The spectra of normal SNe Ia are remarkably uniform in the time evolution of their spectral features (Branch et al. 1993), but some differences do exist. Some of these differences are associated with the variation in light-curve shapes (e.g., Nugent et al. 1995, Chapter 6), while the origins of others remain unknown (e.g., Hatano et al. 2000; Benetti et al. 2005).

Nugent et al. (2002) introduced a spectral template time series that is based on one well-observed supernova spectrum for each epoch and wavelength interval. The template is constructed by assembling well-observed spectra in a two-dimensional grid of flux as a function of epoch and wavelength. The temporal gaps are then filled with a simple interpolation.

The spectral features of the templates used for K-correction calculations of a particular set of SNe Ia should be representative of that population. The templates constructed by the method outlined in Nugent et al. (2002) can cause systematic errors if the spectra used represent the extremes in spectral features. In this section, a prescription for constructing a mean spectral template time series with representative spectral features is described.

Simply averaging a large number of spectra tends to broaden and weaken the spectral features, when there exists a range of feature velocities. Instead, we adjust the features

of a base template to the weighted mean of the measured feature strengths from a large sample of observed spectra. The procedures of building the spectral template time series have been built into a fully automated IDL program. The program can incorporate new additions to the library, adjust the grid size accordingly and create a new spectral template. The procedures are summarized as follows:

1. Assign a two-dimensional grid of epoch and wavelength bins.

2. Color-correct each library spectrum to the same broadband colors in each epoch bin.

3. Measure the feature strength in each wavelength bin of each library spectrum.

4. Assign weights to each feature strength of each library spectrum.

5. Determine an effective epoch for each epoch bin.

6. Determine a weighted mean feature strength for each grid element.

7. Build a base template time series from a subset of library spectra at the effective epochs.

8. Adjust the base template time series to the weighted mean feature strengths using the mangling function.

The library spectra are first divided into epoch bins. When assigning an epoch bin, two competing factors affecting the bin sizes must be considered. First, a statistically significant sample size of spectra in each epoch bin is required to obtain representative characterizations of the spectral features; larger bin sizes yield more spectra per bin. Second, the temporal evolution of the spectral features within each bin should be kept as small as possible; small epoch bin sizes are preferred in this case. The most direct way to improve the situation is to increase the number of library spectra such that the epoch bin sizes can be narrowed without sacrificing the generality of the sample in each bin. For the current sample size, it is not sensible set a bin size of one day for all epochs. Instead, variable bin sizes are adopted.

The temporal evolution of spectral features is illustrated in Figure 4.8. The SEDs at different epochs are normalized to the same *B*-band flux to emphasize the evolution of the spectral features. The spectrum of a SN Ia evolves rapidly from the time of explosion to around 20 days past maximum light. These epochs are also the most important when fitting light curves. The epoch bin sizes for these epochs are kept small such that the effects of
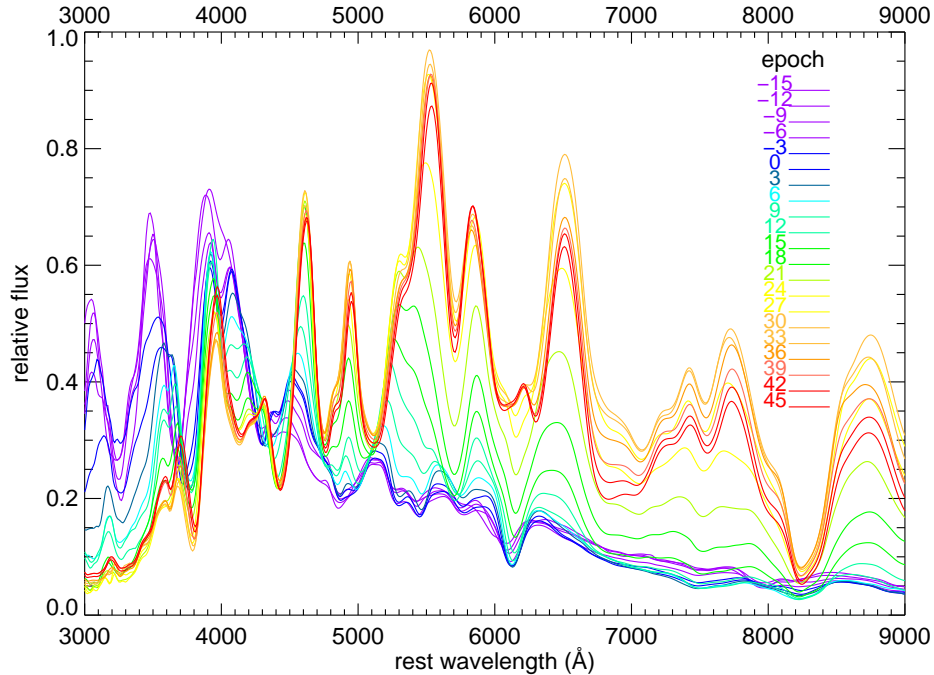
Figure 4.8: An illustration of the time evolution of spectral features of SNe Ia. A spectral template time series is plotted from $t = -15$ to $t = 48$ relative to B-band maximum. Template spectra at different epochs are normalized to the same B-band flux to emphasize the evolution of the spectral features. Spectral features of SNe Ia evolve rapidly around maximum light and slow down past $t = 30$. This emphasizes the importance of small epoch bins near maximum light.

temporal evolution on spectral features are minimized. The temporal evolution of feature shapes in the B and V bands slows down considerably beyond the age of 30 days. At these epochs, larger bin sizes are adopted to compensate for the small number of spectra. Table 4.1 lists the epoch bins adopted for the current library.

The relative spectral feature strengths of a library spectrum are measured as narrowband colors, as described in Section 4.5. Note that measuring relative feature strengths eliminates the need for the absolute fluxes of the spectra. The narrowband colors are organized in a two-dimensional grid of wavelength and epoch. The sizes of the grid elements are defined by narrowband filter bandwidths and epoch bins. Figure 4.9 illustrates a schematic of the grid and specifies the number of narrowband measurements for each grid element. A typical grid element in the B and V filter bands yields approximately 40 measurements from the current library.

Before the narrowband colors are averaged in each grid element, they are weighted to

Table 4.1: The assignment of epoch bins for the mean spectral template time series

Lower epoch	Upper epoch	Bin size	Effective epoch	Number of spectra
-15	-9	6	-10.8	34
-9	-7	2	-7.9	39
-7	-5	2	-6.0	51
-5	-3	2	-3.8	37
-3	-1	2	-2.0	44
-1	1	2	-0.0	71
1	3	2	2.0	51
3	5	2	3.9	38
5	7	2	6.0	39
7	9	2	7.9	39
9	11	2	10.0	38
11	13	2	12.1	34
13	16	3	14.4	56
16	19	3	17.4	42
19	22	3	20.5	47
22	25	3	23.4	32
25	29	4	27.0	40
29	33	4	30.9	38
33	38	5	35.7	50
38	42	4	39.9	38
42	50	8	45.5	51
50	57	7	53.6	33
57	68	11	62.1	42
68	81	13	74.8	18
81	91	10	85.6	16
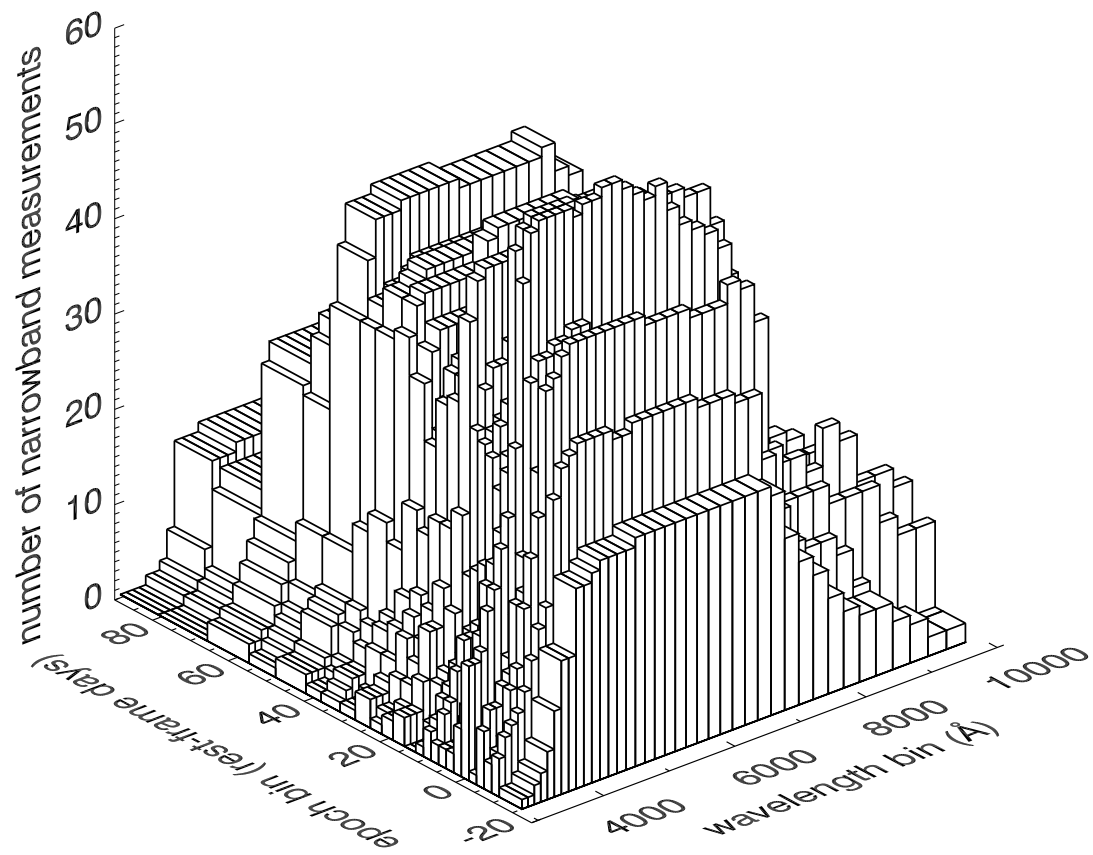
Figure 4.9: A schematic of the two-dimensional grid defined by the epoch bins and the narrowband filters. The number of narrowband color measurements in each grid element is plotted in the third dimension.

account for the heterogeneous nature of the data set. The weights are designed to yield feature measurements which are truly representative of the mean of SNe Ia. They ensure that the final mean spectral template time series is not dominated by peculiar spectra, supernovae with multiple observations or supernovae with extreme stretch values. The details of the weighting schemes are described in Section 4.7. The weighting schemes yield an effective epoch for each epoch bin. The base template time series is then built at these effective epochs.

As the narrowband filters degrade the resolutions of the library spectra, it is important to start with a set of base template spectra with the correct feature shapes. The steps for building the base templates are similar to those for building the spectral templates of Nugent et al. (2002). A subset of library spectra with high signal-to-noise ratios is selected. The coverage in epoch and wavelength is kept below three spectra per day per wavelength to avoid broadening the spectral features with a range of expansion velocities. Each library spectrum is given a Gaussian spread in epoch, centered on its rest-frame stretch-corrected epoch, with a standard deviation the size of the associated epoch bin. The base template time series is then produced by averaging the Gaussian weighted fluxes at each effective epoch. The Gaussian spread allows the smooth time evolution of the spectral features and also helps to fill the gaps in epoch and wavelength space where observations are rare.

The grid of weighted mean narrowband colors as a function of wavelength and epoch is now used as the input color information for the mangling function described in Section 4.4. Each spectral feature of the base spectrum is adjusted by the mangling function to have the weighted mean strength of the library spectra. The adjusted template at the effective epochs is then smoothly interpolated to an integer epoch grid from $t = -19$ to $t = 85$ at each wavelength.

Finally, the spectral template is color-adjusted to a light-curve template. Note that adjusting the flux and the colors of the spectral templates to a particular set of template light curves is optional for the following reasons. The constant of normalization for the template SED is cancelled when performing a K-correction calculation. Furthermore, the broadband colors of the spectral template would later have to be adjusted to match the colors of the SN Ia in question. Here, the mean spectral templates are adjusted to a set of template light curves to allow for a more natural interpolation of flux between epochs.

The resulting spectral template at maximum light is shown in Figure 4.10. To illustrate that the spectral template is indeed the mean of the library spectra, spectral templates are also built using 100 bootstrapped samples of library spectra. The bootstrapped templates also show the size of the dispersion at each wavelength. The spectral features in the U
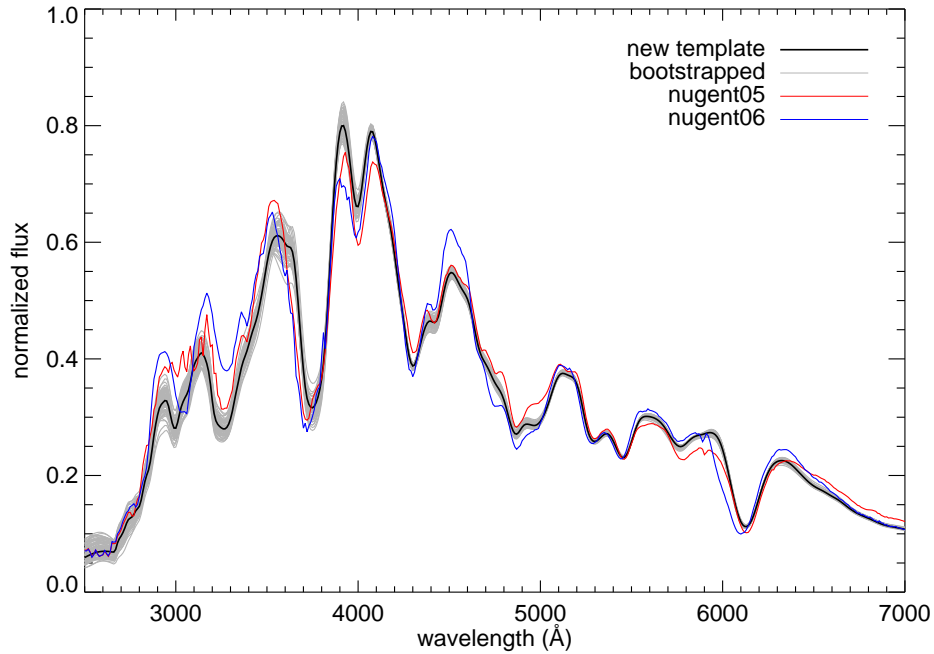
Figure 4.10: The comparison of spectral templates at maximum light. The mean spectral template is plotted as a black curve, while the templates from bootstrapped samples are plotted as gray curves. The revised templates of Nugent et al. (2002) from 2005 and 2006 are plotted as red and blue curves, respectively.

band exhibit much larger dispersion around the mean than those in the *V* band. The mean spectral template is also compared with the revised templates of Nugent et al. (2002). Figure 4.10 shows that the Nugent templates are not representative of the library spectra and can cause significant systematic errors. The resulting systematic errors will be quantified in Chapter 5.

The mean spectral template time series provides an excellent reference for the spectral features of a typical SN Ia and has a wide range of applications. The current spectral template time series covers epochs from -19 to 85 days past *B*-band maximum and wavelengths from 0.1 μm to 2.5 μm. It has been adopted as the spectral model for the SiFTO light-curve fitter (Conley et al. 2008). Because of the wide wavelength baseline, it has also been adopted to estimate the bolometric luminosities, and in turn the ^{56}Ni masses, of SNe Ia (Howell et al. 2009).

4.7   Weighting of narrowband measurements

The heterogeneous nature of our library means that the differences between the spectra need to be considered carefully. Before the narrowband colors are averaged in each grid element, some simple weighting schemes are applied to each spectrum to ensure that the resulting template is not dominated by peculiar spectra, supernovae with multiple observations or supernovae with extreme stretch values. Weights as a function of wavelength are also assigned to deal with the differences in the spectral coverage and in the locations of the telluric lines.

We chose to include spectroscopically peculiar SNe Ia for the following reasons. Including peculiar spectra in the template and the analysis gives a more complete description of the population of the SNe Ia. Moreover, peculiar SNe Ia tend to receive more attention and yield more detailed observations. Including these spectra helps to increase the number of spectra in wavelength and epoch intervals which are rarely covered. To adequately include these peculiar spectra in the spectral template, we adopt the weight, w_{type}. For the peculiar spectra, we chose a relative weight of one fifth that reasonably characterizes the intrinsic fraction of peculiar supernovae in the SN Ia population (Branch 2001; Li et al. 2001b). For a grid element with N_{normal} normal spectra and N_{peculiar} peculiar spectra, the weight for the type of spectra is:

$$w_{type} = \begin{cases} 1/N_{\mathrm{normal}} & \text{for normal SNe Ia} \\ 1/5N_{\mathrm{peculiar}} & \text{for peculiar SNe Ia} \end{cases}. \tag{4.1}$$

For a SN Ia with N narrowband color measurements in a grid element, the measurements are averaged and weighted as one measurement:

$$w_{\mathrm{multiplicity}} = 1/N. \tag{4.2}$$

Narrowband color measurements at the edges of a library spectrum are assigned less weight than the measurements at the center. This step goes beyond the edge trimming, described in Section 4.2, in minimizing the effects of miscalibration at the edges of observed spectra. It also gives higher weights to library spectra which have wider wavelength coverage and thus have their continua better adjusted by the mangling function. The weight for the filter coverage, w_{coverage}, is a triangular or trapezoidal function in wavelength space with a value of unity at the effective wavelengths of the available bands and one fifth at the ends of the spectrum.

Even though the telluric features for each spectrum taken at ground-based telescopes

are removed, lower weights at the location of the telluric features are applied to account for the errors associated with this procedure. The diversity of redshifts in our library means that most of the grid elements would have at least a few feature strength measurements uncontaminated by telluric features. The weight assigned for telluric line contamination, w_{telluric}, is inversely proportional to the equivalent width of a telluric feature template inside the two adjacent narrowband filters in question.

To ensure that a grid element is not dominated by supernovae of extreme stretch values, the narrowband color measurements are weighted such that the weighted mean of the stretch values in each grid element is close to a representative stretch value $s_{\text{effective}}$ (conventionally unity). A normal distribution centered on the effective stretch $s_{\text{effective}}$, with a standard deviation of $\sigma_s = 0.2$, is used to define the weight for stretch:

$$w_{\text{stretch}} = \exp\left[\frac{(s_{\text{SN}} - s_{\text{effective}})^2}{2\sigma_s}\right]. \tag{4.3}$$

For SNe Ia without stretch factors, the mean weight for stretch is adopted for each grid element.

An effective epoch, $t_{\text{effective}}$ is determined for each epoch bin using the rest-frame, stretch-corrected epochs of the library spectra, t_i, and their weights, w_i':

$$t_{\text{effective}} = \frac{\sum_i w_i' t_i}{\sum_i w_i'}. \tag{4.4}$$

The letter i denotes the ith spectrum of the epoch bin in question. The weight, w_i' is the product of the weights for supernova type, multiplicity, wavelength coverage, telluric features and stretch. The resulting effective epochs for our current library are listed in Table 4.1. Within an epoch bin, library spectra with epochs t_{SN} closer to the effective epoch are then assigned higher weights. A normal distribution is again used to define the weights. It is centered on the effective epoch, $t_{\text{effective}}$, with a sigma, σ_t, corresponding to the size of the epoch bin:

$$w_{epoch} = \exp\left[\frac{(t_{\text{SN}} - t_{\text{effective}})^2}{2\sigma_t}\right]. \tag{4.5}$$

The total weight for the ith library spectrum can then be written as:

$$w_i = w_{\text{type},i} \times w_{\text{multiplicity},i} \times w_{\text{coverage},i} \times w_{\text{telluric},i} \times w_{\text{stretch},i} \times w_{\text{epoch},i} \tag{4.6}$$

Assuming that the spectral features of SNe Ia depend on the stretch parameter (Chapter 6), weighting the feature strength measurements in terms of epoch and stretch helps us

to disentangle the two effects on spectral features in an epoch bin of finite size.

The weighted mean of the narrowband measurements, f, is determined for each grid element (in epoch and in wavelength) using the total weight, w_i, and the narrowband color measurements f_i for the ith spectrum:

$$f = \frac{\sum_i w_i f_i}{\sum_i w_i} \tag{4.7}$$

The grid of weighted mean narrowband colors in epoch and wavelength now characterizes the mean spectral features of the desired SN Ia spectral template time series.

4.8   Principal component analysis

PCA is a statistical technique useful for reducing the dimensionality and identifying patterns in a set of multi-dimensional data. PCA has been employed for analyzing astronomical spectra in a wide variety of applications (e.g., Ronen et al. 1999; Kong & Cheng 2001; Madgwick et al. 2003; Ferreras et al. 2006; Suzuki 2006). In Chapter 6 and Chapter 7, the method will be used to search for correlations between spectral features and factors which drive the variations in spectral features, such as time evolution and photometric properties.

The simplifying "bra ket" notation of Suzuki (2006) is adopted here for the formulation of PCA. PCA in this case is applied to the narrowband measurements of a set of supernova spectra. Each spectrum is denoted here by $|f_i\rangle$ and is characterized by n narrowband color measurements. First, the mean spectrum (mean narrowband measurements) $|\mu\rangle$ is computed and removed from the data set. The covariance matrix is then computed to determine how strongly a spectral feature is correlated with the others. For this n-dimensional data set, the covariance matrix is an $n \times n$ symmetric matrix.

The eigenvectors and eigenvalues of the covariance matrix are obtained using internal IDL routines which utilize Householder reductions and the QL method (Press et al. 1992). The resulting eigenvectors form an $n \times n$ matrix. Each of the n PCs, denoted here by $|\xi_j\rangle$, are simply each of the n n-dimensional column vectors of the eigenvectors. In this formulation, the PCs are renormalized to be unit vectors. They are further ranked by the eigenvalues which provide a measure of the amount of variation in the spectra that the PCs describe. The fractional variance for a PC is the ratio of the eigenvalue of the PC over the sum of all the eigenvalues. The first PC points in the direction of maximum variance in the n-dimensional data space, and the rest of the PCs are orthogonal vectors:

$$\langle \xi_i | \xi_j \rangle = \delta_{ij}. \tag{4.8}$$

The projection of a spectrum $|f_i\rangle$ on a PC $|\xi_j\rangle$ can then be computed as:

$$p_{ij} = \langle f_i - \mu | \xi_j \rangle. \tag{4.9}$$

This projection for the ith spectrum and the jth PC, denoted here by p_{ij}, gives a measure of how much the spectral features of the spectrum $|f_i\rangle$ vary in the direction of the PC $|\xi_j\rangle$ in the n-dimensional data space. Because the PCs are unit vectors, the projections have the units of narrowband magnitude. PCA searches for patterns in the spectroscopic data independent of any information about the spectrum or the supernova. The projections p_{ij} can thus be used to search for correlations between the spectral features and any factors which may cause the observed variation.

The set of spectra used in PCA can be represented as the sum of all of its PCs and the mean spectrum:

$$|f_i\rangle = |\mu\rangle + \sum_{j=1}^{n} p_{ij} |\xi_j\rangle. \tag{4.10}$$

The set of spectra can also be reconstructed using only the first few PCs. If these PCs constitute a large fraction of the overall variations, the reconstructed spectra will be representative of the actual data.

4.9   Conclusion

A library of a statistically significant sample of observed spectra is presented. The spectra are from heterogeneous sources to cover a wide range of parameter space in epoch, wavelength and photometric properties. New methods for continuum adjustment and flux measurement are developed, such that the spectral features from the heterogeneous data set can be consistently quantified.

A mean spectral template time series is constructed by consistently quantifying the spectral features of the large sample of library spectra and carefully incorporating the measurements with weighting schemes which account for the wide variations in properties of the library spectra. The resulting templates are shown to have the mean properties of SNe Ia. The revised spectral templates of Nugent et al. (2002) are shown to have unrepresentative spectral features which will result in systematic errors in cosmological studies. These

errors will be quantified in Chapter 5.

The procedures and formulation of PCA have been outlined. A set of spectroscopic data can be reduced into orthogonal PCs. Only the first few PCs are necessary to describe the bulk of the variations. These PCs are then used to search for correlations between spectral features and factors which drive the variations of spectral features, such as light-curve width and time evolution. PCA will be adopted in Chapter 6 and Chapter 7 to identify the origins of observed variations and to construct template spectroscopic sequences to gain insight on how the spectral features vary with light-curve width.

Chapter 5

Impact of spectroscopic diversity on cosmology

Abstract The mean spectral template time series is shown to eliminate the systematic errors in K-corrections which arise from assuming the spectral energy distribution (SED) of a particular Type Ia supernova (SN Ia). The remaining statistical errors are redshift dependent, with minima at redshifts where the rest-frame filter band and the observed filter band are aligned. Because the broadband colors of the spectral templates are adjusted to match those of the SNe Ia, the errors are attributed to the inhomogeneity in the spectral features. As these errors directly affect the magnitudes of the SNe Ia, it is important to incorporate the redshift-dependent effect in cosmology. The effect of filter coverage on the K-correction errors is also examined. Spectral templates which are not adequately constrained by the color information of the SN Ia are shown to cause significant errors in the K-correction, emphasizing the importance of the choice of filter bands in survey designs. A first attempt is made at measuring the correlation of K-correction errors between epochs. The effect of partial correlation of spectral features between epochs is approximately a factor of two increase in the errors of the peak magnitudes from those estimated assuming uncorrelated errors.

5.1 Introduction

K-correction calculations require the SED of the SN Ia. As high signal-to-noise, time series spectroscopic observations of high-redshift SNe Ia are currently not feasible, a spectral template time series is usually assumed. This is justified by the existence of remarkable

homogeneity in the observed optical spectra of "normal" SNe Ia (Branch et al. 1993).

The dependence of K-corrections on the spectral template is large at redshifts where the observed and the rest-frame filter bands are misaligned. While the observed spectra of "normal" SNe Ia are apparently uniform, subtle differences in feature strengths and velocities do exist (e.g., Nugent et al. 1995; Hatano et al. 2000). How well the spectral template represents the SED of the SNe Ia becomes especially important at the misaligned redshifts.

Previous papers on K-corrections of SNe Ia presented methods which made it possible to use SNe Ia for the determination of cosmological parameters. Hamuy et al. (1993) explored the possibility of using SNe Ia as distance indicators and presented single-filter K-corrections for supernovae out to redshift $z = 0.5$ using spectroscopic observations of SN 1990N, SN 1991T and SN 1992A. At high redshifts, considerable extrapolation is required for single-filter K-corrections. Kim et al. (1996) developed the cross-filter K-correction to take advantage of the overlap at high redshifts of a rest-frame filter band and a redder observed filter band. Nugent et al. (2002) presented a SN Ia spectral template time series and a recipe for determining K-corrections. The importance of broadband colors was particularly emphasized.

While K-corrections are largely driven by SN Ia colors, it is shown here that the diversity in spectral features of SNe Ia can also be important. In this section, we investigate the effects of SN Ia inhomogeneity on the determination of K-corrections and cosmology, paying close attention to the effects of the diversity in the spectral features.

5.2   Quantifying K-correction errors

For a high-redshift supernova, the light through a rest-frame filter band is redshifted to longer wavelengths and is observed through an observed filter band that overlaps, but is not identical to, the redshifted rest-frame filter band. The cross-filter K-correction (Kim et al. 1996), K_{xy}, allows one to transform the magnitude in the observed filter, y, to the magnitude in the rest-frame filter, x:

$$K_{xy}(t, z, \vec{c}) = -2.5 \log \left(\frac{\int \lambda T_x(\lambda) Z(\lambda) d\lambda}{\int \lambda T_y(\lambda) Z(\lambda) d\lambda} \right) + 2.5 \log \left(\frac{\int \lambda T_x(\lambda) S(\lambda, t, \vec{c}) d\lambda}{\int \lambda T_y(\lambda) \left[\frac{S(\lambda/(1+z), t, \vec{c})}{(1+z)} \right] d\lambda} \right). \quad (5.1)$$

The K-correction, K_{xy}, is a function of the epoch t, the redshift z, and a vector of pa-

rameters $\vec{c}$, which affect the broadband colors of the SN Ia, such as light-curve width and dust reddening. $S(\lambda)$ designates the SED of the supernova. $T_x(\lambda)$ and $T_y(\lambda)$ denote the effective transmission of the x and y filter bands, respectively. $Z(\lambda)$ denotes the SED for which the reference $x - y$ color is precisely known. Note that the normalization of the SED is arbitrary.

K-correction dispersions are quantified here as the differences between the K-correction calculated using a particular observed spectrum $S^S(\lambda)$ and that calculated using an assumed template spectrum $S^T(\lambda)$, where the continuum of $S^T(\lambda)$ is adjusted with the mangling function to have the same broadband colors as $S^S(\lambda)$ (Section 4.4). From Equation 5.1, the K-correction dispersions can be expressed as:

$$\Delta K_{xy} \equiv 2.5 \log \left(\frac{\int \lambda S^S(\lambda) T_x(\lambda) d\lambda}{\int \lambda S^T(\lambda) T_x(\lambda) d\lambda} \right) - 2.5 \log \left(\frac{\int \lambda S^S(\lambda/(1+z)) T_y(\lambda) d\lambda}{\int \lambda S^T(\lambda/(1+z)) T_y(\lambda) d\lambda} \right). \tag{5.2}$$

This definition of K-correction dispersions removes the dependence on the zero points and focuses on the effects of an assumed spectral template and the alignment of the rest-frame and observed filters. The first term in Equation 5.2 provides the normalization such that the two spectra have the same flux under the rest-frame filter band. The second term then yields the magnitude difference caused by the spectroscopic differences between the supernova spectrum and the template.

The library spectra are used here to quantify the K-correction errors. The library spectra are artificially redshifted from $z = 0$ to $z = 1.2$ to determine the K-correction as a function of redshift. The K-correction difference between each library spectrum and the appropriate template is then determined for all redshifts with various combinations of rest-frame and observed filter bands. The statistical error is then defined as the K-correction dispersions added in quadrature at each redshift, and the systematic error is defined as the average of the K-correction dispersions at each redshift.

When a relation between light-curve shape and color (e.g., Riess et al. 1996) is used, one has available the predictions of multiple rest-frame color information from the fit to the observed light curve. The spectral template can be color-corrected using the predicted rest-frame colors in this case. On the other hand, when multi-color observations of a SN Ia are available, one may choose to use the more empirical approach of correcting the spectral template directly to the observed colors. The K-correction errors calculated from both color-correction options are examined in the following subsections.

5.3 Color correction using model rest-frame colors

First, the case where the colors of the spectral templates are corrected by the rest-frame colors is examined. When determining the K-correction to a rest-frame filter, the neighboring spectral regions become important when the rest-frame and observed filter bands are misaligned. Library spectra which have U, B and V rest-frame filter band coverage (approximately 9% of the library spectra) are selected to characterize the errors in K-correction from the observed filters to the rest-frame B filter band. The selected library spectra range in epoch from $t = -15$ to $t = 65$. The rest-frame colors of the library spectra are measured by synthetic photometry. Before calculating the K-correction difference between a library spectrum and the corresponding template, the template spectrum is color corrected to have the same $U - B$ and $B - V$ colors as the library spectrum.

To ensure that the sample of library spectra used to build the spectral templates and the one used to measure the K-correction errors are independent of each other, the selected library spectra are randomly split in half. One half of the selected spectra and the library spectra which did not meet the wavelength coverage criterion are used to build a set of spectral templates. The other half is then used to compute the K-correction dispersions. The random selection process was repeated 100 times. The K-correction errors are also calculated using the revised templates of Nugent et al. (2002). The Nugent templates are assumed to be independent of the selected library spectra. The resulting statistical and systematic errors for K-corrections going from observed $g_M r_M i_M z_M$ bands to the rest-frame B band are plotted in Figure 5.1.

Note that the errors presented here are for individual observations. Combining multiple data points on a light curve to derive overall light-curve parameters should reduce these errors. This will be examined in Section 5.6. The statistical errors follow the pattern of a minimum at the redshift where the observed and the rest-frame filter bands are aligned and two maxima where the two filter bands are misaligned. The pattern repeats as a function of redshift and as one observed filter is switched to another. At a redshift where the filter bands are misaligned, the K-correction error for a single observation is important at the 0.04 mag level. Because the spectra are compared with consistent broadband colors, we argue that the 0.04 mag error is primarily due to the inhomogeneity in spectral features of SNe Ia.

The right panel of Figure 5.1 shows that the new mean templates cause lower systematic errors than the Nugent templates. This is because the mean templates have more representative spectral features for the selected spectra considered here. This implies that
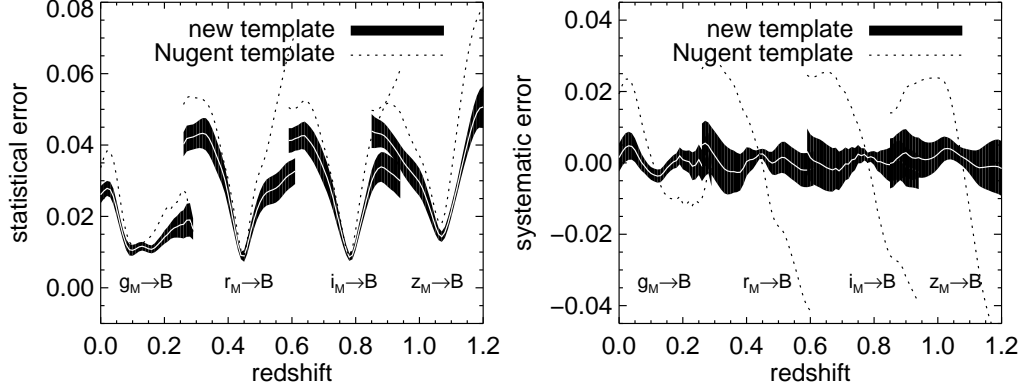
Figure 5.1: *K*-correction errors to the rest-frame *B* band, for the case where the template spectra are color corrected with rest-frame colors. The errors of the new template and the revised template of Nugent et al. (2002) are represented with solid black and dotted curves, respectively. The statistical errors are plotted in the left panel, and the systematic errors in the right panel. The thickness of the black solid curve shows the dispersion from the random selection process and the thin white curve is the mean. The errors presented here are for individual observations of a light curve.

the Nugent templates are only representative for the handful of spectra used to make it. The method presented in Section 4.6 allows for the inclusion of a large sample of spectra for building the mean templates. Assuming that our current library is a more representative sample than the sample used by Nugent et al. (2002), the mean template will largely eliminate the systematic errors caused by spectral features. An ideal spectral template for this particular population of spectra would yield distributions centered on zero at all redshifts and epochs. The deviation from zero for the mean templates reflects the particularity of the smaller sample used for the *K*-correction estimate.

When a SN Ia lies at a redshift where the observed and rest-frame filter bands are misaligned, all the observations on the light curve would have larger *K*-correction errors. The larger errors are attributed to the larger extrapolation and the heavier reliance on the spectral templates. Multiple epochs may reduce the errors, but the redshift dependent nature remains. SNe Ia at different redshifts would have different *K*-correction errors. This redshift-dependent feature of the *K*-correction error must be considered in the determination of cosmological parameters.
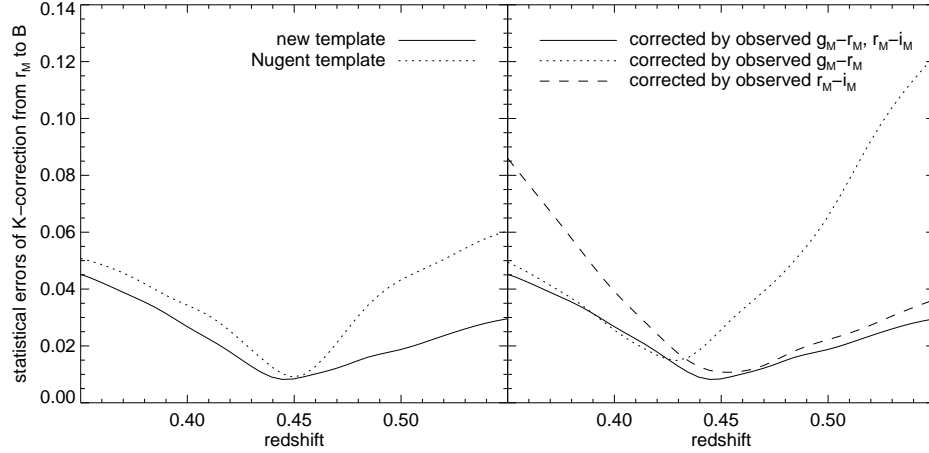
Figure 5.2: Statistical errors of K-corrections from the observed i_M band to rest-frame B band, for the case where the template spectrum is color-corrected with "observed" colors. The observed colors are from synthetic photometry using the observed $g_M r_M i_M$ filter bands. The left panel compares the errors of the revised Nugent templates and the mean spectral templates. Both sets of templates are color corrected by observed $g_M - r_M$ and $i_M - r_M$ colors before the calculation. The right panel shows the effect of the availability of observed colors on the errors. The solid, dotted and dashed curves represent the errors of the mean templates corrected by both $g_M - r_M$ and $r_M - i_M$ colors, $g_M - r_M$ color alone, and $r_M - i_M$ color alone, respectively.

5.4 Color correction using observed colors

Here, the same error analysis as above is performed, but the template spectra are color-corrected using "observed" colors. The observed colors are obtained from synthetic photometry using de-redshifted g_M, r_M and i_M observed filter bands. As the redshift of a supernova spectrum increases, the observed filter bands cover progressively bluer regions of the spectrum. The locations of the spline knots for the mangling function are thus not fixed as in the previous subsection, but instead depend on the redshift of the supernova.

Because the observed filter bands are shifted as a function of redshift, spectra with wide wavelength coverage are required for the analysis. There are 12 spectra with adequate wavelength coverage from seven SNe Ia: SNe 1981B, 1989B, 1990N, 1990T, 1991T, 1991bg, and 1992A, covering ages from -14 to 37 days relative to B-band maximum light. The spectral templates built for this analysis exclude these 12 spectra, such that the spectral template is independent of the library spectra used for the analysis. An example of K-correction from the observed r_M band to rest-frame B band is plotted in Figure 5.2.

The left panel plots the comparison of statistical K-correction errors calculated using

the revised Nugent templates and the mean spectral templates. The result is similar to that of Figure 5.1. Since the spline knots are placed at different locations for the two methods of color correction, the similarity between the results gives us confidence that the method of constructing spectral templates presented in Section 4.6 is largely independent of the way in which the spectra are color corrected.

Color correction using observed colors has the advantage of being independent of an assumed stretch-color relation, but the K-correction errors depend on the availability of observed colors. The effects of the availability of observed colors are shown in the right panel of Figure 5.2. We consider three cases where the mean spectral templates are color-corrected by 1) both observed $g_M - r_M$ and $r_M - i_M$ colors, 2) by observed $g_M - r_M$ color, and 3) by observed $r_M - i_M$ color. They illustrate the point that in the treatment of K-correction, the errors should also reflect the availability of observed colors. For example, the K-correction error is increased considerably for a SN Ia missing $g_M - r_M$ observed color at $z = 0.36$ (dashed curve of the right panel of Figure 5.2). A similar effect is also observed for a SN Ia at $z = 0.54$ missing $r_M - i_M$ (dotted curve of the right panel of Figure 5.2).

At redshifts where the observed and rest-frame filter bands are misaligned, the observed color which straddles the rest-frame filter band is the most important. This is illustrated in Figure 5.3. For a SN Ia that is at a misaligned redshift, and missing this observed color information, the associated K-correction error arises not only from inhomogeneity of SNe Ia spectral features, but also from the missing color information.

The filter coverage of modern SN Ia surveys is simulated to get a more realistic description of the statistical errors. The observed filter bands and the surveys considered here are *RI* bands for Equation of State: Supernovae Trace Cosmic Expansion (ESSENCE; Miknaitis et al. 2007; Wood-Vasey et al. 2007), *gri* bands for the Sloan Digital Sky Survey-II Supernova Survey (SDSS II; Sako et al. 2008; Frieman et al. 2008), *griz* bands for the Supernova Legacy Survey (SNLS; Astier et al. 2006), and *YJ* bands for the Carnegie Supernova Project (CSP; Freedman 2005). CSP uses near-infrared photometry, as well as optical photometry from other surveys, to compute K-corrections to rest-frame *I* band. Here we compute K-corrections to the rest-frame *B*, *V* and *I* bands. At each redshift, all the library spectra with adequate wavelength coverage to perform color corrections are included. The results are plotted in Figure 5.4.

The redshift-dependent nature of the K-correction errors should be incorporated into cosmological analysis to fully account for the effects of feature inhomogeneity and filter coverage. Figure 5.4 also illustrates the importance of the choice of filter bands in survey design. For the case of ESSENCE, there is reasonable overlap between the observed *R*
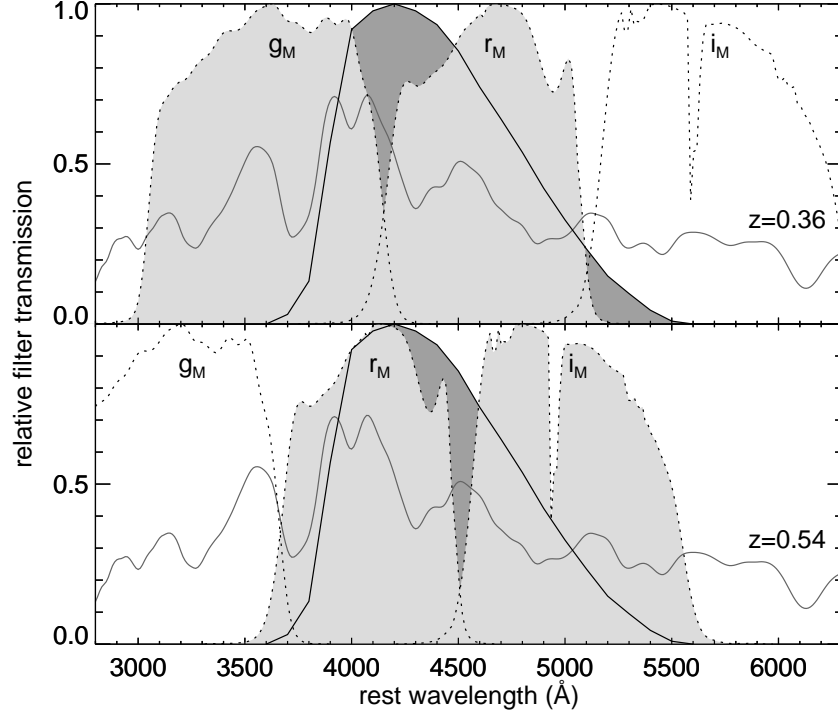
Figure 5.3: The locations of the observed filters at redshifts $z = 0.36$ (top panel) and $z = 0.54$ (bottom panel). The same example of K-correction as in Figure 5.2 is considered. The solid curves represent the rest-frame B band, while the dotted curves represent the observed $g_M r_M i_M$ bands. At redshifts where the observed and rest-frame filter bands are misaligned, the observed color which straddles the rest-frame filter band (highlighted for each plot) is the most important.

band and the rest-frame B band in the redshift range $z = 0.2 - 0.4$. However, there is no filter band on the blue side of the R filter to constrain the color of the spectral template in the rest-frame B-band region. As a result, B-band based cosmology is expected to have larger scatter in this redshift range (top-left panel of Figure 5.4).

5.5   Spectral templates from the minimization of errors

In Section 4.7, two constants are chosen for the weighting schemes, constants for w_{type} and w_{coverage}, in order to ensure that the spectral templates produced are not dominated by an extreme of the SN Ia population. A constant of 0.2 was chosen for w_{type} to simulate the fraction of peculiar supernovae in the SN Ia population. A constant of 0.2 was chosen for w_{coverage} to deweight the edges of the spectra. Alternatively, these constants can be quan-
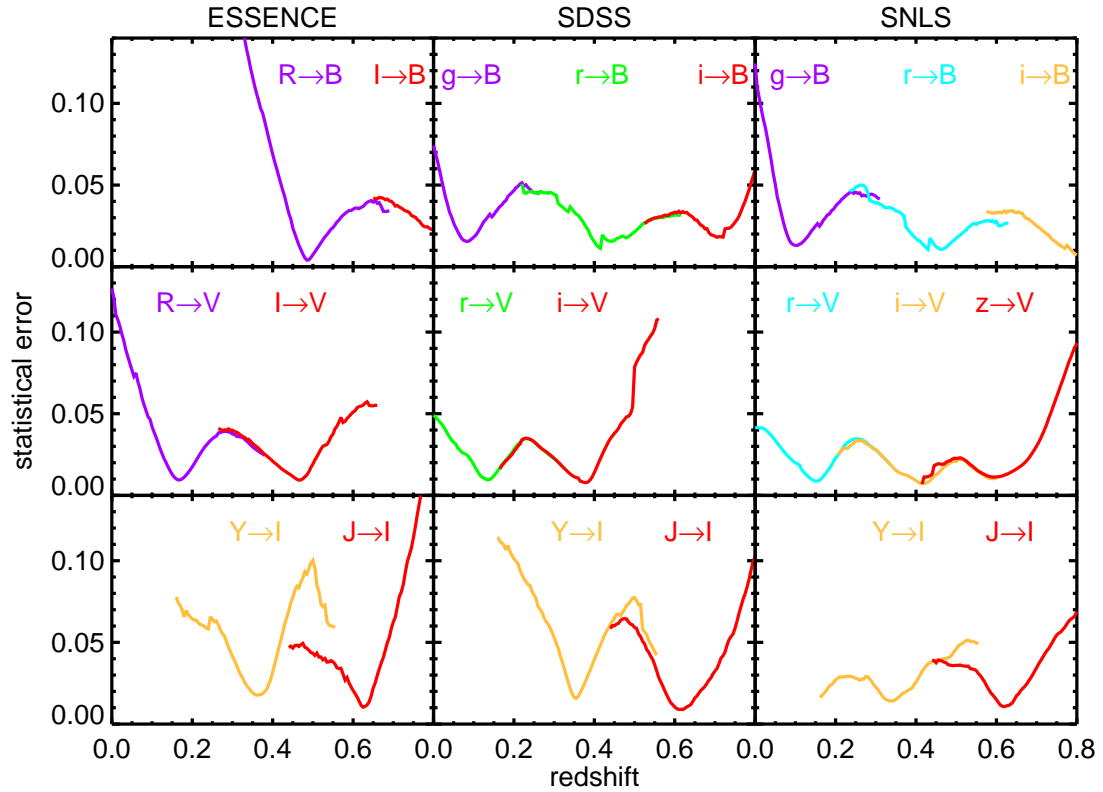
Figure 5.4: Realistic models of *K*-correction statistical errors for ESSENCE, SDSS II, SNLS and CSP. *K*-corrections to rest-frame *B* (top panels), *V* (middle panels) and *I* bands (bottom panels) are considered. The *K*-correction errors are computed using spectral templates color corrected with the observed filter bands of ESSENCE (left panels), SDSS II (center panels) and SNLS (right panels). CSP uses near-infrared photometry, as well as optical photometry from other surveys to compute *K*-corrections to rest-frame *I* band (bottom panels).
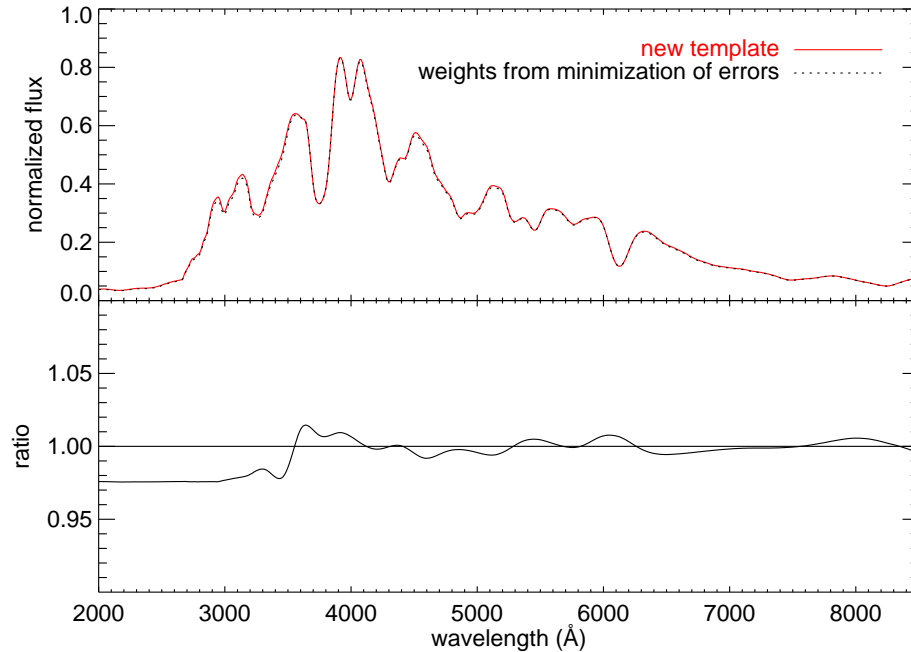
Figure 5.5: Comparison between the spectral templates built using weights determined by minimizing the *K*-correction errors, and templates built using preselected weights. The templates at maximum light are shown. The template building process is largely insensitive to the way these constants are determined. The largest *K*-correction (to *B*) difference between the two templates is 0.004.

titatively determined by minimizing the systematic *K*-correction errors of a set of library spectra.

The constants for w_{type} and w_{coverage} are now set as parameters free to vary between 0 and 1. All of the library spectra which have enough wavelength coverage to allow for accurate mangling are used to determine the systematic errors in redshift, as discussed in Section 5.3. The parameters are determined by minimizing these errors using non-linear least-squares fitting (Markwardt 2009). At each iteration, a spectral template is produced from the entire spectral library with the specified parameters, and the averages of the *K*-correction differences between this template and the library spectra are taken as the systematic errors in redshift to be minimized.

By minimizing the systematic errors, the optimal constants for w_{type} and w_{coverage} were determined to be 0.244 and 0.498, respectively. The constant for w_{type} roughly reflects the fraction of peculiar spectra in the sample. The larger constant for w_{coverage} reflects the fact that the edges of the library spectra are also used to determine the errors at redshifts where

the filters are misaligned.

The spectral templates produced by using the quantitatively determined parameters show very little difference from the mean spectral template presented in Section 4.6. The templates at maximum light are compared in Figure 5.5. The largest K-correction (to B) difference between the two templates is 0.004. Even when the two constants are set as their maximum value of unity, the maximum K-correction difference is still less than 0.01. The spectral template building process is therefore largely insensitive to the way these constants are determined.

The statistical error estimates remain on the order of 0.01 at the redshifts where the filters are aligned and 0.04 at the redshifts where the filters are misaligned. The minimization of the systematic error represents an improvement of ~ 0.0005 at the misaligned redshifts and has no effects on the shape of the systematic errors in redshift. The insensitivity to these parameters is mostly due to the fact that our spectral library is large and encompasses SNe Ia which span a wide range of properties.

Despite the fact that the template building process is largely unaffected by the choice of these parameters, the weights determined from the minimization of errors depend on the characteristics of the sample used for the error estimates. To use the method presented in this section, one should ensure that the sample of spectra has good spectral and epoch coverage and is reasonably representative in properties such as the stretch and the fraction of peculiar spectra. Using an unrepresentative sample of spectra has the potential to skew the template toward a particular extreme of the SN Ia population.

5.6   Impact of K-correction errors on cosmology

In the preceding sections, the K-correction errors for individual observations are quantified. Since one generally observes a supernova at multiple epochs, it is natural to ask what the final effect of these errors will be on the derived light-curve parameters, such as the peak magnitude in B.

This question is currently difficult to answer. The critical issue is how correlated the K-correction error is at different epochs. If the errors were completely uncorrelated, as is often assumed in the literature, then the final error would be approximately reduced by $1/\sqrt{N}$, where N is the number of observations. Alternatively, if the K-correction errors were perfectly correlated, then there would be no reduction in the final error from multiple observations.

In reality, we are somewhere between these extremes. It is easy to understand why
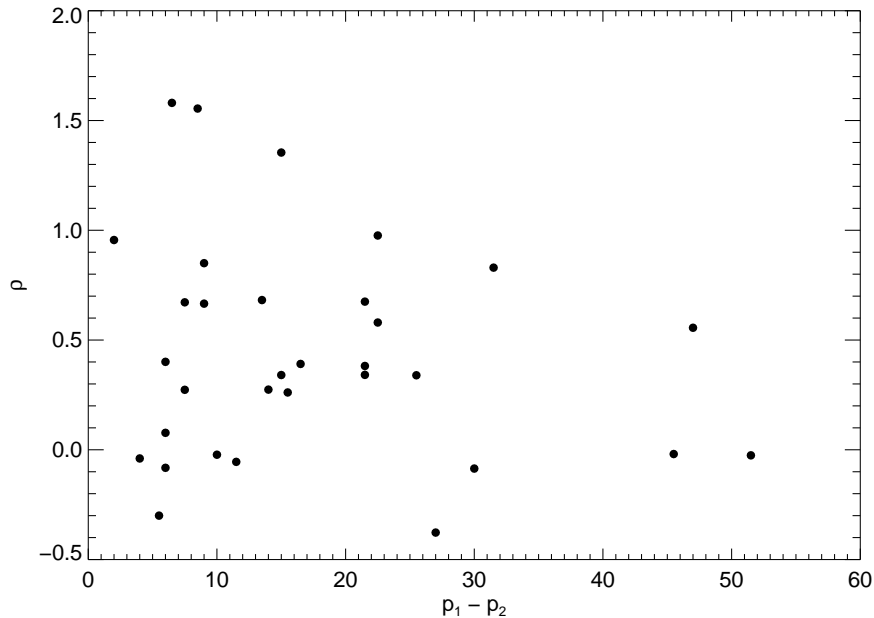
Figure 5.6: Estimated correlation coefficients for the ∼ 10% of the off-diagonal elements of the K-correction covariance matrix that we can currently measure plotted against the difference between the two epochs. Here the $z = 0.8$ i_M to B is shown. At this redshift the filters line up fairly well. Note that some of the correlation coefficients are greater than one, which is unphysical, and results from the fact that many of these bins have only one SN Ia in them.

observations at different epochs could be correlated. For example, imagine a supernova at a redshift where a particular feature is barely outside a given observed filter for a normal SN Ia. If this supernova has unusually high expansion velocities, then the feature might be shifted just inside the observed filter and affect the K-correction. Since a supernova with a high expansion velocity is likely to also have a high expansion velocity at a later date, the same effect will occur when the supernova is observed several days later. Thus, the errors in the K-correction will be correlated between different observations.

What is needed to determine the level of correlation is SNe Ia with spectra obtained at many epochs. One can then calculate the K-correction errors for the same supernova at different epochs and form the covariance matrix. Unfortunately, at the current time, there are not nearly enough SNe Ia with multiple published spectra. New data samples such as those which should be provided by the Carnegie Supernova Project (Hamuy et al. 2006), Katzman Automatic Imaging Telescope (Li et al. 2000) and the Supernova Factory (Wood-Vasey et al. 2004) will help address this issue.

Nonetheless, we can try to develop a feel for the importance of this effect with the current data, although this will necessarily be highly speculative. All of the SNe Ia with multiple spectra which have wide enough wavelength coverage to allow for accurate mangling are included in the analysis. Their K-correction errors are computed as discussed in Section 5.3. A covariance matrix in epoch is then formed by taking the appropriate products. This covariance matrix has 275 unique off-diagonal elements (from 25 epoch bins defined in Table 4.1). The current data set provides information for only 10% of these, many of which have entries from only one SN Ia.

Clearly, with only 10% of the elements specified, some assumptions on the empty elements are required to compute the final errors. The distribution of correlation coefficients for the K-correction from i_M to B at $z = 0.6$ is shown in Figure 5.6, plotted against the epoch difference between the two bins. Note that some of the correlation coefficients are larger than 1, which is non-physical and is related to the fact that there is only one supernova in that bin from which to estimate the covariances. There are no clear trends visible, which is not surprising given the paucity of data.

For the lack of a better model, the mean correlation coefficient is computed (~ 0.5) and used for all of the unknown off-diagonal elements. The calculations are carried out at three redshifts, 0.6, 0.7 and 0.8, in all cases calculating the error in the K-correction from i_M to B. The alignment between B and i_M is the best at $z = 0.8$. To get the typical cadence, the Supernova Legacy Survey (SNLS) i_M observations of three SNe Ia at three different redshifts are adopted: SNLS-03D4dy at $z = 0.604$, SNLS-04D1si at $z = 0.701$, and SNLS-04D1ks at $z = 0.798$. SNe Ia at higher redshifts tend to have slightly more frequent measurements due to time dilation.

The expected error in the peak B magnitude is then computed in three different ways: 1) assuming that the errors are completely uncorrelated, 2) using only the covariance matrix elements with actual measurements (i.e., with 10% of them non-zero), and 3) using the above model for the unknown coefficients. The results are summarized in Table 5.1. Roughly speaking, the errors in the final magnitudes are a factor of 2 or so larger than one would expect in the absence of correlations. It must be emphasized that these numbers are tentative, but they should be a considerable improvement over the assumption that the K-correction errors at different epochs are uncorrelated.

The differences between local and high-redshift SNe Ia are also of interest in cosmology. The possible systematic differences between spectra of nearby and distant SNe Ia have been studied extensively (Section 3.9). For the building of the spectral template time series, it has been assumed that the effect of the evolution in redshift is negligible compared

Table 5.1: The approximate effects of including correlations between K-corrections at different epochs on the peak magnitude in B

	z=0.6	z=0.7	z=0.8
1) Uncorrelated	0.011	0.011	0.004
2) Partially correlated	0.013	0.011	0.006
3) Correlations model	0.023	0.018	0.010

to the intrinsic variations in spectral features between SNe Ia at the same redshift. A basic test is performed on the impact of including both low-redshift ($z < 0.2$) and high-redshift samples in the template building process. A spectral template time series is built using only low-redshift spectra to compare with the mean spectral template time series built using the full sample of library spectra (Figure 5.7). The largest difference is seen in U, where most of the high-redshift spectra are observed. The difference between the two templates primarily reflects the higher average stretch of the high-redshift sample and the differences in wavelength coverage. The difference in K-corrections between the two spectral templates is small (typically 0.01 to rest-frame B band).

5.7 Conclusion

A method for quantifying the K-correction errors is developed to examine the impact of the observed spectroscopic diversity on SN Ia cosmology. The mean spectral template time series described in Chapter 4 is built to have the mean spectroscopic properties of SNe Ia. The mean spectral template time series is shown to eliminate the systematic errors in K-correction, which arise from assuming the SED of a particular supernova.

The remaining statistical errors are redshift dependent, with minima at redshifts where the rest-frame filter band and the observed filter bands are aligned. At redshifts where the filters are misaligned, the statistical errors are measured to be 0.04 mag for one observation on the light curve. Because the broadband colors of the spectral templates are adjusted to match those of the SNe Ia, the errors are attributed to the diversity in the spectral features. As these errors directly affect the magnitudes of the SNe Ia, it is important to incorporate the redshift-dependent effect in cosmology.

The effect of filter coverage on the K-correction errors is also examined. Spectral templates which are not adequately constrained by the color information of the SN Ia are shown to cause significant errors in K-correction. The effect is also illustrated with the simulation
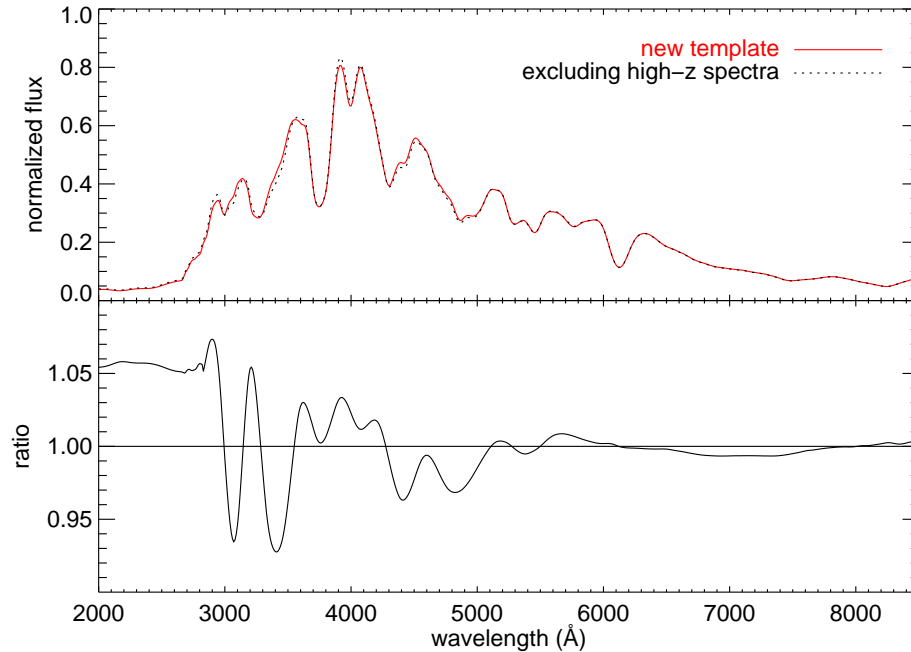
Figure 5.7: Comparison between the spectral template built with the full sample of library spectra (solid curve) and the spectral template built with only low-redshift spectra (dotted curve). The templates at maximum light are shown. The difference in K-corrections between the two spectral templates is small and mostly reflects the difference in the wavelength coverage of the two samples rather than true evolution.

of K-correction statistical errors using the observed bands of current high-redshift SN Ia surveys.

There is not enough time series spectroscopic data to perform a full analysis, but a first attempt is made at measuring the correlation of K-correction errors between epochs. This represents a significant improvement from the assumption of completely uncorrelated errors, where the errors are reduced by approximately $1/\sqrt{N}$ with N observations. The effect of the partial correlation is approximately a factor of two increase in the errors in the peak magnitudes from those estimated assuming uncorrelated errors.

Chapter 6

Spectroscopic sequence

Abstract   The relations between the spectral features of Type Ia supernovae (SNe Ia) and the light-curve width are investigated. Principal component analysis (PCA) is performed on the narrowband measurements of the spectral features of a large number of spectra. The methods are specifically designed to quantify the spectral features consistently, while retaining the detailed information on the diversity of the spectral shapes. At maximum light, light-curve width is shown to be the main driver of the observed diversity for every spectral feature from U band to I band, even for features which have been previously reported to show little or no correlation. There is also evidence of the persistence of the spectroscopic sequences throughout other epochs. This is shown to originate from the more rapid temporal evolution of fainter objects than that of their brighter counterparts.

6.1   Introduction

SNe Ia have provided the most direct measurements of the expansion history of the universe and, in turn, the most direct evidence for the existence of a cosmic acceleration. SNe Ia are found to have a spread of B-band peak luminosities. After the correction for extinction, the spread is thought to be instigated by the range of ^{56}Ni mass synthesized in the explosions. Standardizing the luminosities of SNe Ia is made possible through the width-luminosity relation (WLR; Phillips 1993) which describes SNe Ia as a one parameter family. Brighter objects have wider light-curve widths and thus have slower temporal evolution than the dimmer ones.

Matching the photometric behavior, corresponding spectroscopic sequences have also been found near maximum light. The ratio of the depth of two Si II absorption features near

0.58 μm and 0.615 μm were found to correlate with the width of the light curve (Nugent et al. 1995). Subsequent studies also detected correlations between spectral features and light-curve width using a variety of indicators, such as the slopes of the UV continuum (Foley et al. 2008b), the flux ratio of the regions which form the boundaries of the Ca II H&K feature (Bongard et al. 2006), the pseudo equivalent width measurements of the Si II feature at 0.40 μm (Arsenijevic et al. 2008), the Fe II feature at 0.48 μm, the S II feature at 0.54 μm and the O I feature at 0.75 μm (Hachinger et al. 2006).

While many of the optical spectral features at maximum light have been found to vary systematically with light-curve widths, other spectroscopic properties were reported to have weak dependence on light-curve widths or no dependence at all. Hachinger et al. (2006) noted large scatters in the relations between the light-curve decline rates and the pseudo equivalent widths of the Fe II feature centered at 0.48 μm and the Si II feature centered at 0.615 μm. Benetti et al. (2005) found that for the Si II feature at 0.615 μm, the time rates of change of the velocities divide the SNe Ia into three distinct groups. There also has been little attention paid in the literature to spectroscopic sequences at epochs other than at maximum light. All this seems to suggest that the one-parameter description of the spectral features of SNe Ia is inadequate and other unknown drivers have significant contributions to the observed diversity in the spectral features.

Spectroscopic data of SNe Ia provides a wealth of information, such as ionization evolution and chemical composition and structure. However, because the nature of the expanding medium, it is difficult to organize. SN Ia spectral features are formed by a blend of multiple lines enhanced by large Doppler broadening. The shapes of the spectral features are thus complex with no clear continuum. This makes the spectral features difficult to quantify. Previous studies have often relied upon by-eye estimations of the boundaries of a spectral feature and methods which do not retain information on the complexity of the spectral shapes. The methods developed here are specifically designed to quantify spectral features consistently and to study the diversity without sacrificing the details of the spectral features. These methods are then used to investigate the relations between spectral features and light-curve widths.

PCA is a statistical technique useful for reducing the dimensionality and identifying patterns in a set of multi-dimensional data. PCA has been employed for analyzing astronomical spectra in a wide variety of applications (e.g., Ronen et al. 1999; Kong & Cheng 2001; Madgwick et al. 2003; Ferreras et al. 2006; Suzuki 2006). We also adopt the method described by Hsiao et al. (2007a) to systematically quantify the spectral features of observed spectra using artificial narrowband filters. The broadband colors of the spectra are

first standardized to a single set of light curve templates. The flux ratios of neighboring spectral features are then measured as narrowband colors. PCA is then performed on these measurements to detect the largest variations of spectral features among the observed spectra.

The spectra of low-redshift ($z < 0.1$) SNe Ia from the library of observed spectra described in Section 4.2 are used for the analysis. The *B*-band stretch parameters (Goldhaber et al. 2001) are also adopted as a measure of the width of the light curve. The technique is based on the linear scaling of the time axis of a light curve to fit a fiducial template. The scale is then taken as the stretch parameter. Most of the stretch values of the low-redshift SNe Ia are derived using the SiFTO light-curve fitter (Conley et al. 2008). For supernovae which only have Δm_{15} values available, they are converted to stretch values using a relation similar to that described by Garnavich et al. (2004).

At maximum light, the results of the PCA are used to detect a spectroscopic sequence for every spectral feature across the optical wavelengths and to construct template spectroscopic sequences. The template spectroscopic sequences will allow us to visualize in unprecedented detail how the spectral features vary with the light-curve width. Light-curve width will indeed be shown to be the main driver of the spectroscopic diversity observed in SNe Ia, even for features which have been previously reported to have little or no dependence. Evidence of the persistence of the spectroscopic sequences throughout other epochs will also be presented. Similar to the photometric WLR, the spectroscopic properties of fainter objects will be shown to have more rapid temporal evolution than those of brighter ones.

The WLR provides the basis for the modern empirical calibration techniques for SNe Ia in cosmological studies. The physical origin of the relation is, for this reason, of great interest. Kasen & Woosley (2007) argued that WLR reflects the faster spectroscopic evolution for fainter SNe Ia, rather than a bolometric effect due to the overall diffusion time. The methods developed here allow the quantitative examination of spectroscopic temporal evolution throughout wavelength and time. We will provide evidence that the spectroscopic properties of fainter SNe Ia, independent of the established photometric relations, indeed have faster temporal evolution than their brighter counterparts.

6.2 Systematic measurement of spectral feature strengths

The methods described by Hsiao et al. (2007a), and in Section 4, are adopted to quantify the spectral features across a spectrum. These methods are specifically designed to incorporate
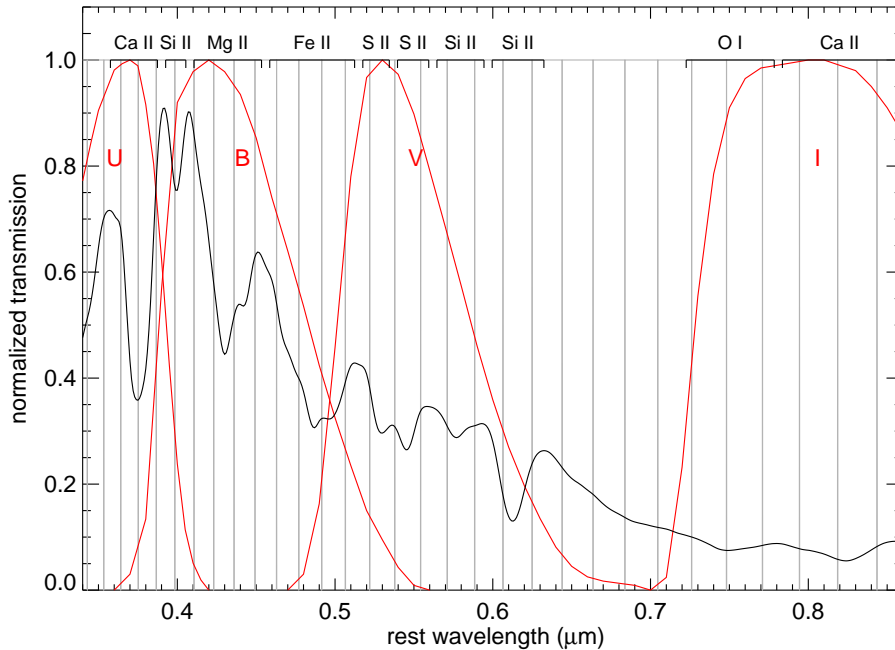
Figure 6.1: Narrowband filters for the measurements of spectral feature strengths. The spectral template of SN Ia at *B*-band maximum light is also plotted to compare spectral feature sizes with the chosen bandwidths. The most dominant species responsible for each spectral feature is also noted.

a large number of spectra from a wide variety of sources. First, the broadband colors of each spectrum are adjusted to a set of light-curve templates. A set of artificial narrowband filters is defined to have bandwidths on the order of the widths of the supernova spectral features. The relative feature strengths of neighboring spectral features are then measured as narrowband colors.

The broadband colors of the spectra are adjusted using the mangling function described in Section 4.4. It defines splines as a function of wavelength, with knots located at the effective wavelengths of the filters. Non-linear least-squares fitting (Markwardt 2009) is used to determine the spline which smoothly scales the spectral template to the correct colors. This step consistently defines and removes an effective "continuum" for each spectrum.

The vast majority of the spectra in our library are not spectrophotometric. To adequately study the patterns in the spectra, their broadband colors need to be adjusted. (It should however be noted that recent spectrophotometric data from the Nearby Supernova Factory allows the study of spectral features with accurate broadband properties (Bailey et al. 2009).) We chose to correct their broadband colors to a set of template light curves

instead of correcting them to the observed colors. This choice was made so that the most dominant patterns detected by the PCA will be from the variations of the spectral features instead of established photometric relations, for example, the stretch-color relation. Because each spectrum is color adjusted to a single set of light curves, the focus of our analysis is placed on the spectral features of the spectra.

There is a trade-off to consider when setting the bandwidths of the narrowband filters. A smaller bandwidth captures more details of the spectral feature shapes, but the signal-to-noise ratio is reduced, making it more difficult to identify the patterns in the data. To maximize the signal-to-noise ratio without sacrificing the details, we set the bandwidth of the narrowband filters to be logarithmic in wavelength and on the order of the width of supernova spectral features. The value adopted for this exercise is $\Delta\lambda/\lambda = 0.03$. It corresponds to an expansion velocity of ~ 9000 km s^{-1}, on the same order of magnitude as the expansion velocities of SNe Ia. The narrowband filters are plotted in Figure 6.1 and compared with the spectral features of a SN Ia at *B*-band maximum light.

The narrowband measurement approach also effectively lowers the resolutions of all spectra to a standard resolution. This is especially important for our heterogeneous data set which is obtained from a wide range of instruments and reduced with different techniques. A lowered resolution will help keep the heterogeneous nature of the data set from entering the signals which are intrinsic to the SNe Ia.

The method used here for characterizing the spectral features has several advantages over the "pseudo equivalent width" method (Folatelli 2004) widely adopted for measuring feature strengths of SNe Ia (e.g., Hachinger et al. 2006; Garavini et al. 2007; Bronder et al. 2008; Foley et al. 2008a; Arsenijevic et al. 2008). The spectral features of a SN Ia are formed from a blend of multiple P-Cygni features with large Doppler broadening. At later epochs, the emission features of iron group elements from forbidden transitions dominate the spectrum and further complicate any attempts at quantifying the spectral feature. It is thus not possible to identify the true continuum of a SN spectrum. The pseudo equivalent width method relies on locating the edges of the spectral features by eye. It is thus inconsistent and prone to errors. Our approach, on the other hand, consistently removes the broadband tilt in the spectra and consistently quantifies the spectral features. The method can also be easily extended to measure spectral features in all wavelengths and epochs.
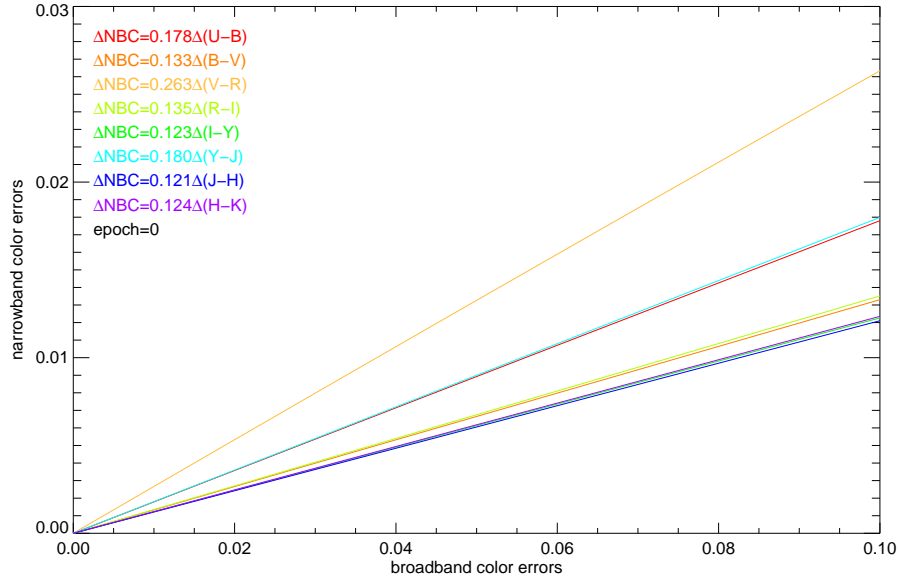
Figure 6.2: Wavelength dependent relations at maximum light between narrowband and broadband color errors. The relations are linear with the slopes noted. The broadband tilt of a spectrum generally has a small effect on the narrowband measurements.

6.3 Determination of errors in the projections

In order to establish relations between the spectral features and the stretch parameter or epoch, appropriate errors need to be assigned to the projections on the PCs. The formulation of the PCA performed here is outlined in Section 4.8.

First, the errors in the narrowband measurements are considered. The dominating errors for the narrowband measurements come from the uncertainties in the broadband color adjustment. Even though all the spectra at the same epoch are corrected to the same broadband colors, many factors may cause the spectra to tilt in different ways. These factors include, for example, the intrinsic colors of SNe Ia, dust reddening, host contamination and atmospheric differential refraction.

The dependence of narrowband color errors on errors in broadband colors is simulated using the spectral template of Hsiao et al. (2007a). The wavelength dependent relations at maximum light between narrowband and broadband color errors are plotted in Figure 6.2. The narrowband color errors increase linearly with broadband color errors. The narrowband errors vary between 1/8 and 1/4 of the associated broadband color errors, depending on the wave bands. This suggests that the broadband tilt of a spectrum generally has a small effect on the narrowband measurements.
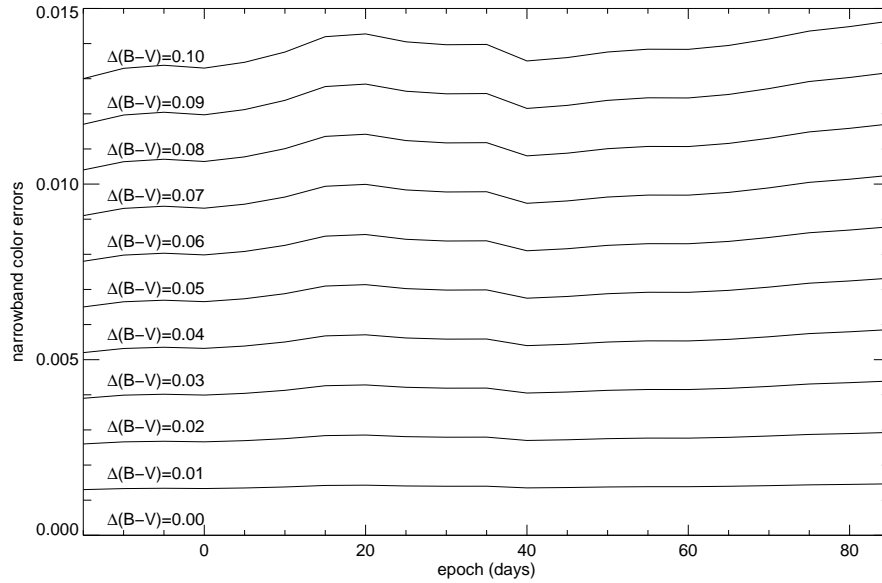
Figure 6.3: The relation between narrowband color error and epoch. Epochs and spectral features have small effects on the narrowband error estimates.

The simulation is also done across epochs, forming a grid of scaling factors between narrowband and broadband errors across wave bands and epochs. The result is shown in Figure 6.3. The epoch has mild effects on the narrowband color errors. The small variations across the wide variations of spectral features in epoch suggest that these error estimates are largely independent of the spectral features.

The narrowband color errors of a particular spectrum are then determined by two factors: 1) the amount of broadband color adjustment (difference between the spectrum colors and the light-curve template), and 2) the wavelength coverage of the spectrum. The broadband color error is set to be equal to the amount of broadband color adjustment. In cases where there is inadequate wavelength coverage for broadband color adjustment, three times the error is assigned. The factor of three is a liberal estimate, and is based on the study of the effects of the availability of photometry on K-correction errors (Hsiao et al. 2007a, Figure 5.2 in Section 5.4).

Once the narrowband color errors of a particular spectrum are determined, a normally-distributed random population of displacements is generated with standard deviations equal to the narrowband color errors. The random displacements are added to the mean subtracted narrowband color measurements, $|f_i - \mu\rangle$, and the projection p_{ij} of this data on each PC $|\xi_j\rangle$ is computed. This step is repeated until a reliable standard deviation can be determined from the distribution of the projections for each PC. The standard deviation is then taken
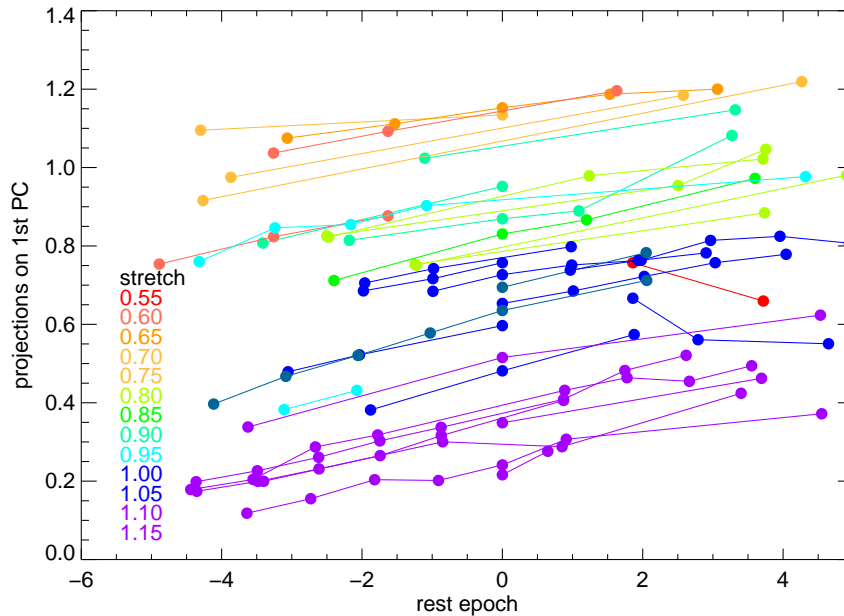
Figure 6.4: An example of temporal evolution of projections on a PC. This plot shows in particular the projections of *V* band spectral features on the first PC of a set of spectra around *B*-band maximum light. Lines connect projections from the same SNe Ia. The plot is color coded using the stretch parameters of the SNe Ia.

as the error in the determination of the projection p_{ij} for the *i*th spectrum and the *j*th PC.

For cases where the projections on a spectrum at a particular epoch (for example, at *B*-band maximum light) are desired, epoch corrections to the projections are applied. The corrections are determined using SNe Ia in the library with spectra at multiple epochs around the desired epoch. These spectra are projected on the PC in question, yielding the evolution of projections in epoch. The assumption is made that even though the projections from different SNe Ia would vary widely in magnitude, the instantaneous changes of projections around the desired single epoch are similar between SNe Ia and that the slopes do not correlate with stretch. An example of this claim is shown in Figure 6.4. This assumption will be shown to be false in Section 6.6. However, for a small correction within a timescale of a few days, the assumption is reasonable. For a particular PC, the median of the slopes is adopted for epoch correction. The standard deviation of the slopes is used to generate the errors associated with the correction, such that spectra at epochs further from the desired epoch are assessed higher correction errors. Finally, the correction errors are added in quadrature with the projection errors to form the final errors on the projections.

6.4 Detection of spectroscopic sequences at maximum light

In this section, the subtle relations between the spectral features and the stretch parameter at *B*-band maximum light are examined using the technique of PCA on the narrowband measurements, outlined in Chapter 4.

For this analysis, the narrowband measurements are divided into four wavelength regions. They approximately cover the regions of *U*, *B*, *V* and *I* bands, and are summarized in Table 6.1. There are two main reasons for such divisions. First, PCA on only a handful of spectral features would yield larger signals than it would on a large segment of the observed spectra. Second, observed spectra have limited wavelength coverage. It is rare for an observed spectrum to cover all four bands considered here. By dividing the analysis into smaller segments in wavelength, more spectra can be included in the analysis. The number of narrowband measurements and the number of spectra for each region are tabulated in Table 6.1.

Table 6.1: Wavelength regions for the PCA at maximum light

Band	Lower wavelength	Upper wavelength	Lower epoch	Upper epoch	Number of measurements	Number of spectra
U	$0.348\,\mu m$	$0.405\,\mu m$	-3	3	5	34
B	$0.381\,\mu m$	$0.546\,\mu m$	-2	2	12	71
V	$0.499\,\mu m$	$0.654\,\mu m$	-2	2	9	74
I	$0.694\,\mu m$	$0.937\,\mu m$	-3	3	10	22

All the epochs are corrected for time dilation with a factor of $1/(1+z)$ (Riess et al. 1997; Foley et al. 2005; Blondin et al. 2008), where z is the supernova redshift. The corrections for the low-redshift objects in our sample around maximum light are quite small. All the epochs are also stretch corrected with a factor of $1/s$, where s is the stretch factor. This correction is also small around maximum. At later epochs, the stretch corrections become significant and are the focus of our study in Section 6.6.

In Table 6.1, the lower and upper epochs used to select the library spectra are also specified. The epoch intervals are set large enough that a statistically significant number of spectra can be included and small enough that the epoch corrections are insignificant compared to the magnitudes of the variations in the data.

PCA is performed on the narrowband measurements in each wavelength region to yield the PCs. Each library spectrum is then projected on the PCs (Equation 4.9). The projec-
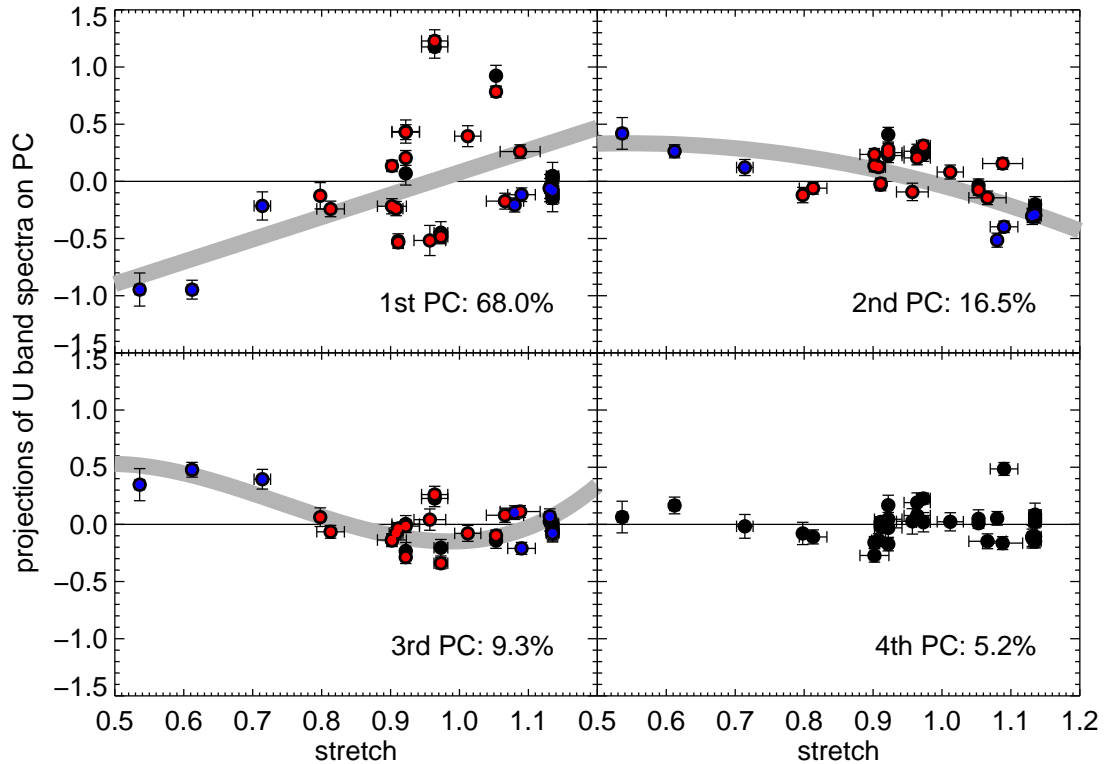
Figure 6.5: Projections of *U* band spectra on the PCs. The fractional variance is noted for each PC and is a measure of how much the spectral features vary in the direction of the PC. Polynomial fits are done on a subset of the data which contains one data point per SN Ia. These data points are marked as red dots. Spectroscopically peculiar SNe Ia are denoted with blue dots.

tions are then used to search for correlations between the spectral features and the stretch parameters. The results for the first few PCs in the bands *U*, *B*, *V* and *I* are plotted in Figure 6.5, Figure 6.6, Figure 6.7 and Figure 6.8, respectively.

It is immediately apparent that the projections of the spectral features on the PCs correlate strongly with the stretch parameter, with significant dispersions only observed in the *U* band. The individual spectral features will be discussed in detail in Section 6.5.

Spectroscopically peculiar, 1991bg-like and 1991T-like SNe, are marked as blue dots in Figure 6.5, Figure 6.6, Figure 6.7 and Figure 6.8. Garnavich et al. (2004) noted that while the $B - V$ colors at maximum is continuous between 1991bg-like and normal SNe Ia, a sharp change of slope is observed at the transition. In the analysis of spectroscopic properties, such a sharp transition is not observed. While it is true that spectroscopically peculiar SNe Ia anchor the extreme ends of the stretch range in these observed trends, the
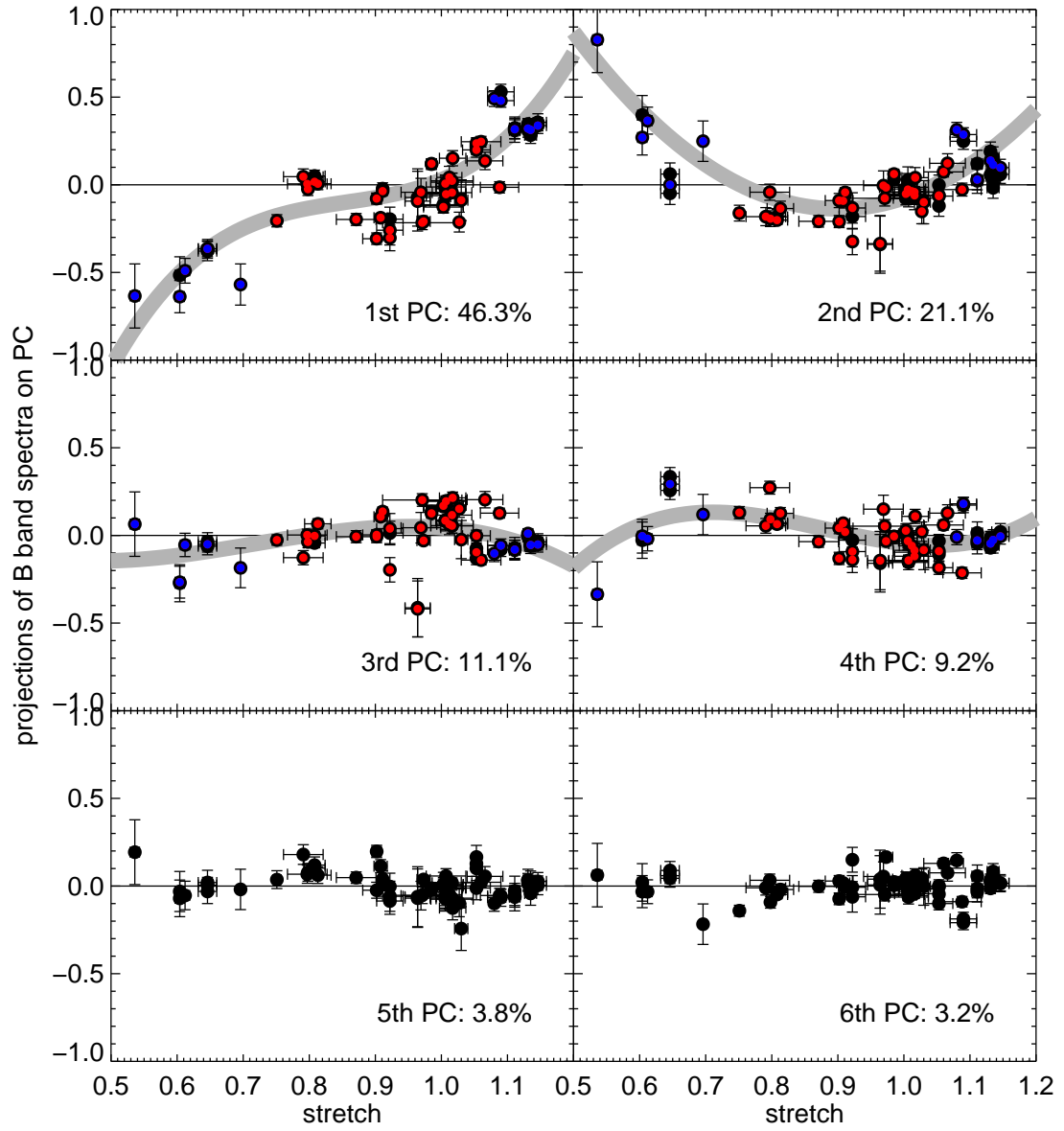
Figure 6.6: Same as Figure 6.5 in the *B* band.
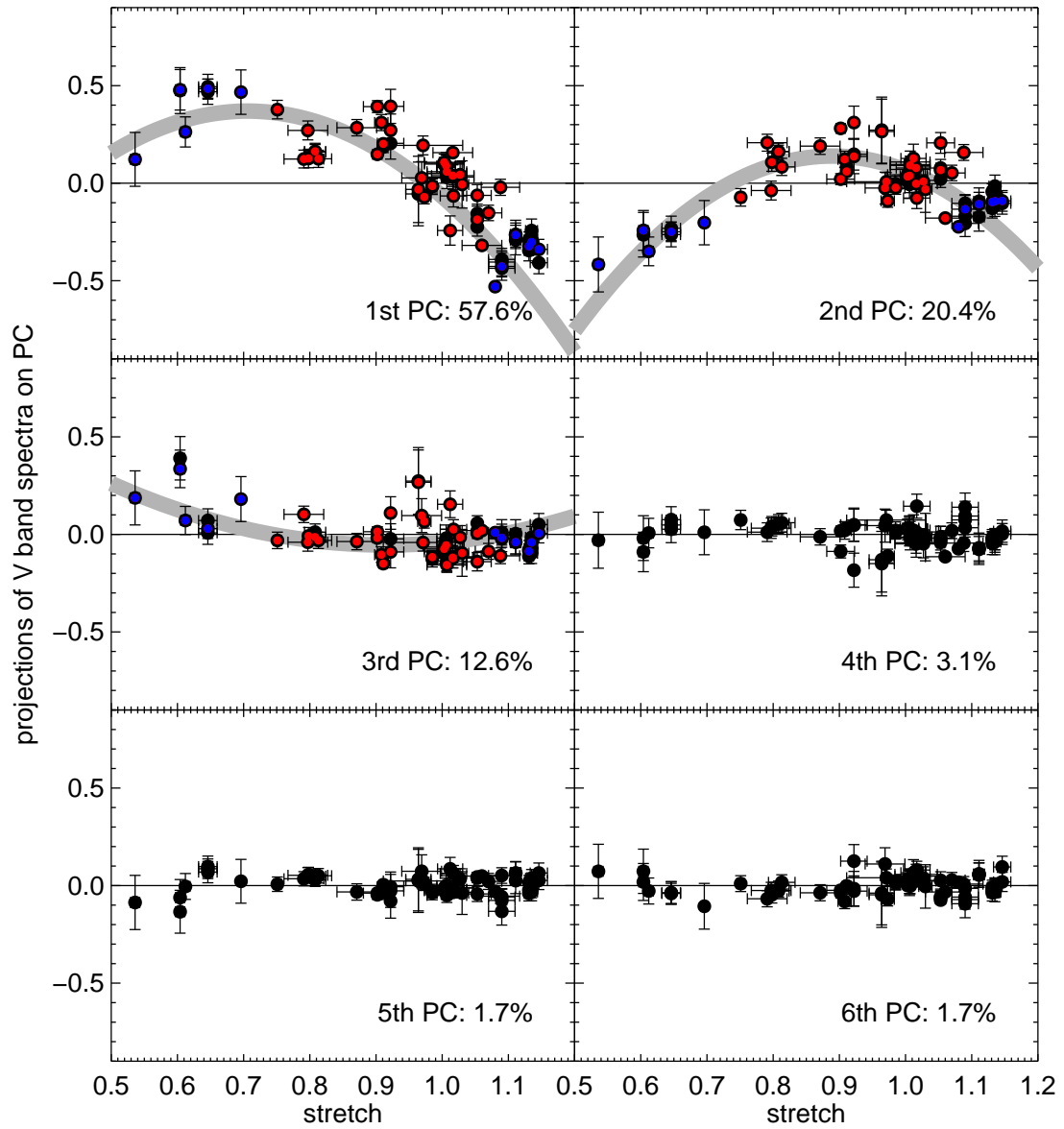
Figure 6.7: Same as Figure 6.5 in the *V* band.
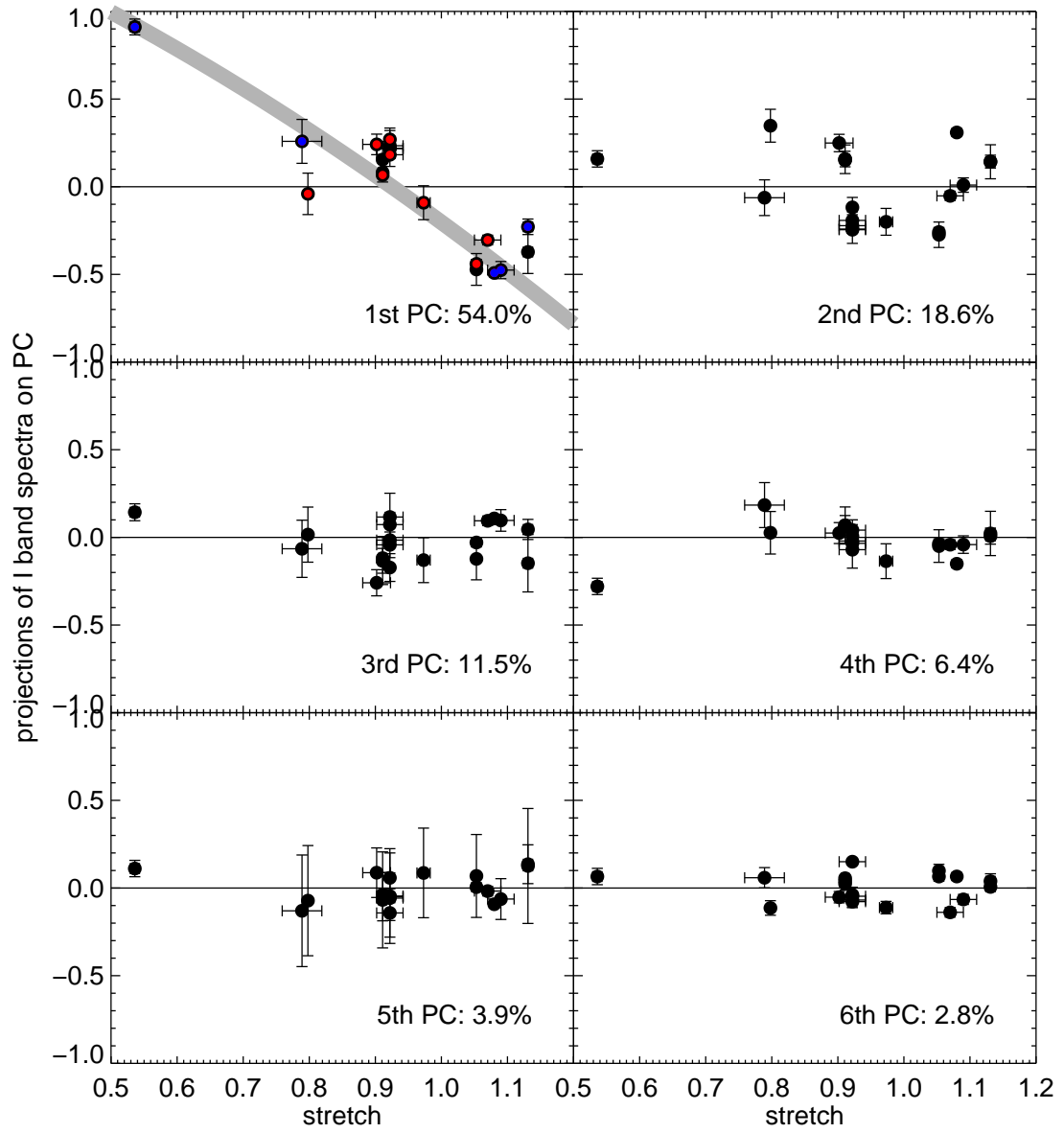
Figure 6.8: Same as Figure 6.5 in the *I* band.

spectra of normal SNe Ia also show strong trends with respect to stretch. Furthermore, spectroscopically peculiar and normal SNe Ia appear to be following the same relations, suggesting a continuous shift in the shapes of the spectral features from peculiar to normal objects. Although, the dearth of spectroscopic data in the stretch range where the transition between peculiar 1991bg-like to normal SNe Ia occur may conceal a sharp boundary between the two populations.

We comment here on a truly peculiar SN 2000cx in our data. SN 2000cx has asymmetric light curves, which rise faster and decline slower than a typical SN Ia. Li et al. (2001a) found that when the full range of the B-band light curve was used to obtain a stretch value, the fit was poor. The fits are better when only premaximum or only post-maximum data is included. From our analysis, it is clear that SN 2000cx has spectral features associated with high-stretch objects in all four wavelength regions. When the stretch value of $s = 1.09$, using only post-maximum data (Li et al. 2001a), was adopted, the spectra of SN 2000cx agree with the relations formed by other SNe Ia. If the stretch of $s = 0.89$ derived from the whole light curve is used, SN 2000cx would be a clear outlier in these trends.

A simple approach of polynomial fits was taken to establish one-to-one relations between the projections and stretch. This is done for the first few PCs which describe the bulk of the variations in the spectra and show strong correlations with stretch. For each of the SN Ia with multiple spectra in the epoch interval, one spectrum closest to maximum light is selected so that these SNe Ia are not weighted more than other SNe Ia. The data points used for the polynomial fits are marked as red dots in Figure 6.5, Figure 6.6, Figure 6.7 and Figure 6.8.

With these projection-stretch relations, template spectroscopic sequences can be constructed. These sequences will reveal the details of how the spectral features vary with stretch which may have been missed by using pseudo equivalent width measurements. They will also provide a set of stretch-dependent spectral templates for further improvement of K-corrections in cosmological studies.

6.5 Reconstruction of spectroscopic sequences at maximum light

Equation 4.9 gives the definition of projections for the ith library spectrum and the jth PC. The polynomial fits in Section 6.4 then yield projections as a continuous function of the stretch parameter, s:

$$p_j = p_j(s). \tag{6.1}$$

With these projection-stretch relations, a continuous sequence of spectral templates can be constructed with respect to stretch:

$$|f(s)\rangle = |\mu\rangle + \sum_{j=1}^{m} p_j(s)|\xi_j\rangle, \tag{6.2}$$

where m is the number of PCs used for the reconstruction and is smaller than, or equal to, the number of narrowband measurement n. The value chosen for m and the total fractional variance accounted for in the selected PCs are tabulated in Table 6.2.

Table 6.2: Number of PCs used for sequence reconstruction and their total fractional variance

Band	m	Fractional variance
U	3	0.939
B	4	0.876
V	3	0.906
I	1	0.540

The resulting sequences $|f(s)\rangle$ are a continuous set of narrowband colors as a function of stretch. The narrowband colors are converted into template sequences using the same method as the one used to build a mean spectral template described by Hsiao et al. (2007a), and in Section 4.6. We start with the mean spectral template of Hsiao et al. (2007a) and use the mangling functions to scale the spectral features of the template to the desired narrowband colors as prescribed by $|f(s)\rangle$.

The template sequences are compared to the actual library spectra used to create them. The library spectra are first placed in stretch bins to accent the differences in spectral features between SNe Ia with different stretch values. For each stretch bin, the mean of the bootstrapped sample of spectra is then determined. The process is repeated to get a fair representation of the spectral features in each stretch bin. We now discuss the results in each wavelength region as follows:

U **band**   The U-band region focuses on the deep spectral feature attributed to Ca II H&K. From Figure 6.5, the projections to the first PC exhibited large dispersions with respect to stretch, although a trend is still clearly visible. It is likely that stretch is not the only driver
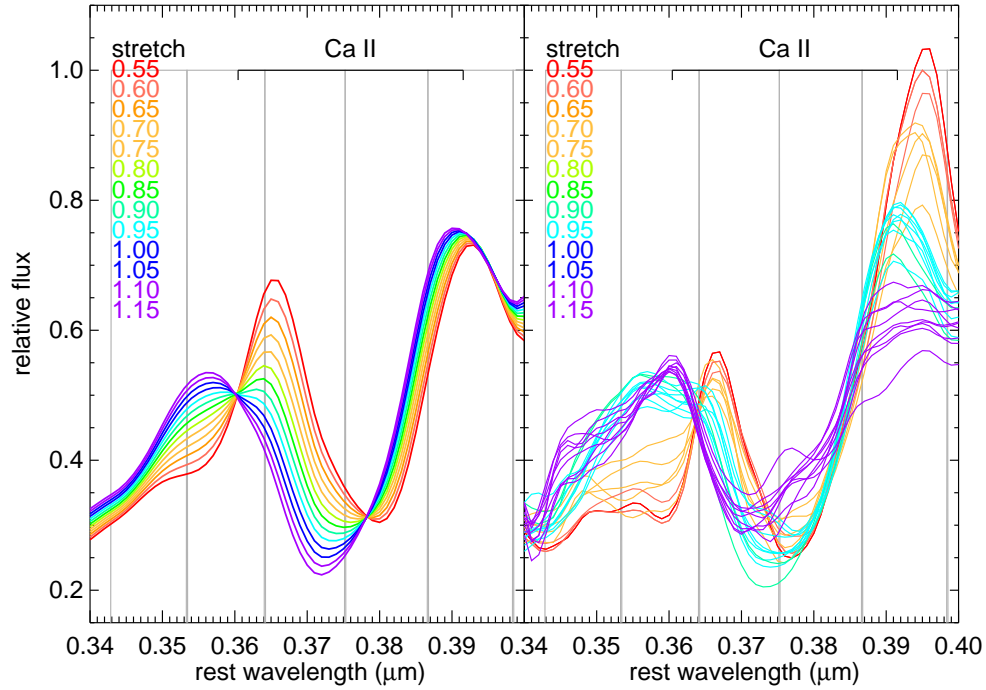
Figure 6.9: The template spectroscopic sequence in the *U* band at maximum light from the first PC. The template spectroscopic sequence (left panel) is compared to the means of bootstrapped samples of library spectra (right panel). The bootstrapped samples are binned in stretch intervals to emphasize the differences between SNe Ia of different stretch. The mean spectra are color coded using the mean stretch values of the bootstrapped samples. The narrowband filters used to quantify the features are plotted as gray lines. The dominant species responsible for each spectral feature in the region is also noted.

of the variations described by the first PC, and that other factors, such as the progenitor metallicity (Höflich et al. 1998; Lentz et al. 2000), may play a role.

The first PC describes the range of expansion velocities of the Ca II feature, especially on the blue edge (Figure 6.9). This correlation with the expansion velocity of the Ca II was first noted by Wells et al. (1994). The large dispersion for the projections on this PC, and the fact that this PC accounts for the largest variation, suggests that there exists significant variation in the velocities of the Ca II feature in SNe Ia and that the velocities correlate with stretch, but with large dispersion.

The second PC detects the flux variation on the red edge of the Ca II feature, while the third PC detects that on the blue edge (Figure 6.10 and Figure 6.11). These two PCs describe the flux difference across the Ca II feature described by Nugent et al. (1995) and the Ca II luminosity indicator examined by Bongard et al. (2006).
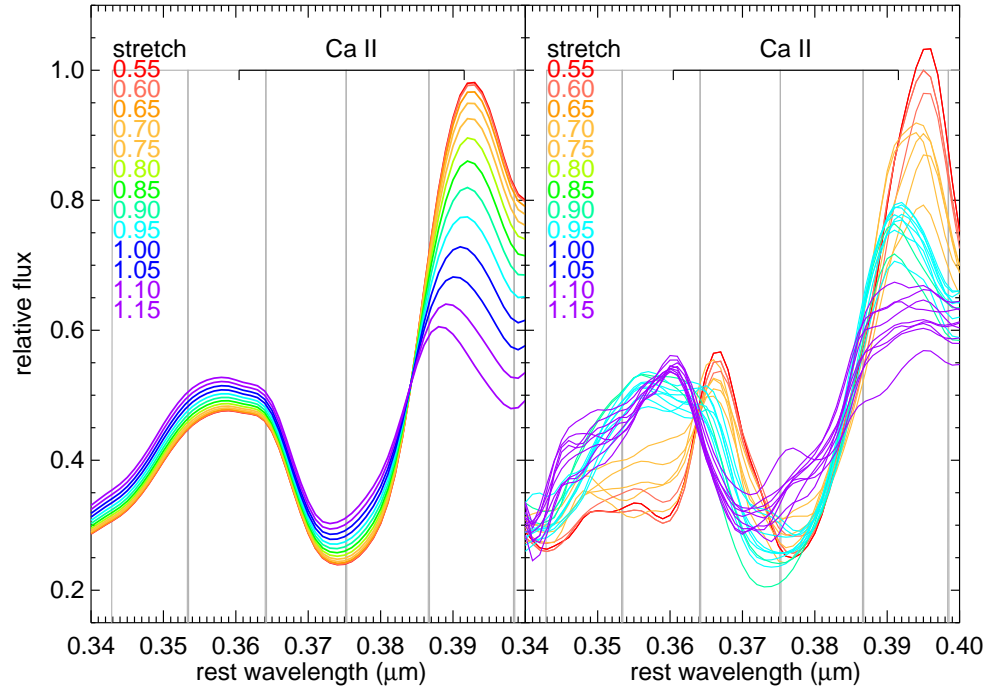
Figure 6.10: Same as Figure 6.9 in the *U* band from the second PC.

The final template sequence, with contributions from all three PCs, is plotted in Figure 6.12. The template sequence is shown to match the observed spectra fairly well. From Figure 6.12, it is clear that a consistent definition of the blue edge of the Ca II H&K feature is difficult. Bongard et al. (2006) used flux integrals of fixed wavelength regions to define the boundaries of the feature This method may soften the impact of the large dispersion on the large velocity shifts, but is arbitrary and may miss the blue edges of high-stretch objects.

B **band**　The spectral features examined in the *B*-band region are the Si II feature centered at 0.40 *μm*, the Mg II triplet and Fe II/Fe III blend centered at 0.43 *μm* and the Fe II/Fe III blend centered at 0.48 *μm*. The first two PCs detect variations over the entire *B*- band region (Figure 6.13 and Figure 6.14). The most prominent variations originate from the contributions of the low-stretch objects, such as, SN 1991bg (Filippenko et al. 1992a) and SN 1999by (Garnavich et al. 2004). For these objects, strong Ti II lines dominate the Si II lines at 0.40 *μm* and the Mg II lines at 0.43 *μm* and dramatically alter the shapes of these spectral features.

In the first PC plot of Figure 6.6, a cluster of data points in a tight stretch range of

Figure 6.11: Same as Figure 6.9 in the *U* band from the third PC.
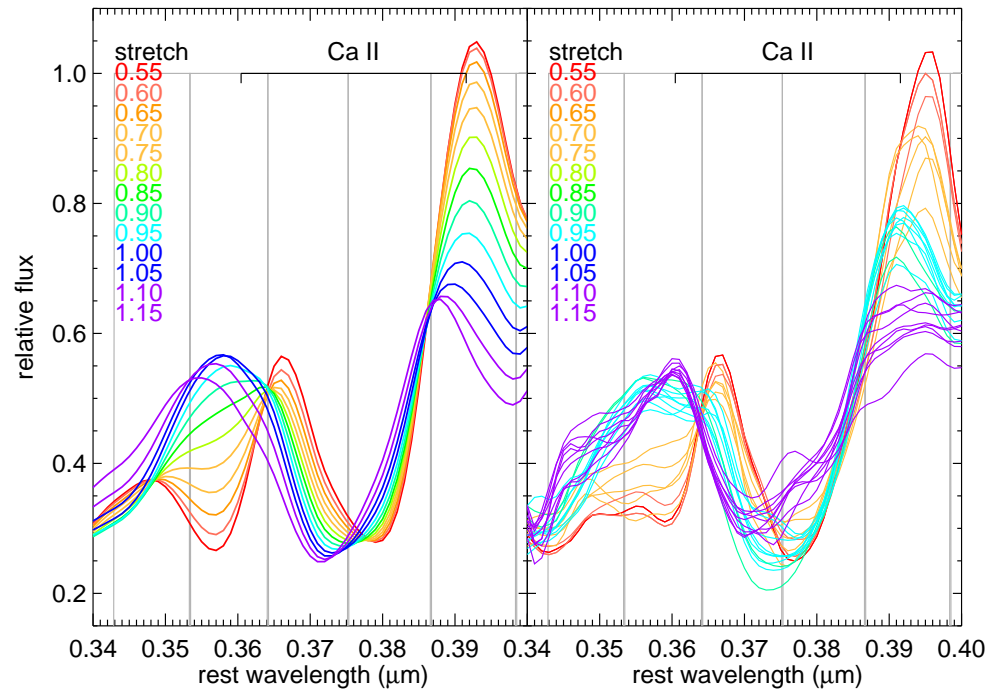
Figure 6.12: Same as Figure 6.9 in the *U* band from the first three PCs.

$s = 0.79 - 0.82$ is observed to lie $\sim 1\sigma$ off the polynomial fit. The same is also observed in the first PC in the *V* band. The cluster contains SNe 1992A, 1992bl, 1999cc, 1999ej, 2004ef. The spectra of the five SNe Ia all appear to be unremarkable. The spectroscopic properties of the five SNe Ia are also quite uniform, forming tight clusters in most PCs. The tight cluster may be just an aberration caused by the dearth of spectra in the stretch range. However, it creates a noticeable kink in an otherwise smooth relation in the current data set. As these SNe Ia lie close to the stretch where the transition between 1991bg-like and normal SNe Ia occurs, they may hold the clues as to whether the transition is abrupt.

The third and fourth PCs describe diminishing variations among the spectra (Figure 6.15 and Figure 6.16). In particular, the third PC probes the variation of the flux between the Mg II and Fe II features. An outlier in the third PC plot of Figure 6.6 is SN 1999cl (Matheson et al. 2008) with a normal stretch of $s = 0.964$. The spectrum was reported to have unusually broad absorption features and evidence of heavy extinction (Garnavich et al. 1999). The spectra of SN 1999cl around maximum light exhibit exaggerated flux between the Mg II and Fe II. As described by the first PC (Figure 6.13), this enhanced flux is most often accompanied by the characteristic Ti II features associated with low-stretch objects. This is not the case for SN 1999cl, causing it to show up as an outlier in the third PC. The PCA method can perhaps be used to identify heavily extincted objects like SN 1999cl and SN 2006X (Patat et al. 2007; Wang et al. 2008; Blondin et al. 2009).

The final template sequence, with contributions from all four PCs, is plotted in Figure 6.17. Hachinger et al. (2006) found no significant trend using the equivalent width measurements of the Fe II feature at 0.48 μm with respect to Δm_{15}. From Figure 6.17, it is obvious that this result is not due to the lack of correlation between the spectral features and the light-curve parameters. The equivalent width measurements in this case removed the details of the spectral feature shapes. A dependence of the shapes on the light-curve was thus not detected with this method.

The variations described by this sequence appear drastic, but it is mostly accounting for the low-stretch objects. As is evident in Figure 6.6, the variation in the spectral features for the stretch range of "normal" SNe Ia ($s \sim 0.8 - 1.1$) is actually quite small. This is not the case in for the spectral features in the *V* band.

V **band**   The *V*-band region includes the S II features centered at 0.54 μm. It also includes the Si II features centered at 0.58 μm and 0.615 μm, the ratio of which form the well known spectroscopic sequence noted by Nugent et al. (1995). The first PC, which describes more than half of the variations in this region, indeed pick up the Si II spectroscopic sequence

Figure 6.13: Same as Figure 6.9 in the *B* band from the first PC.

Figure 6.14: Same as Figure 6.9 in the *B* band from the second PC.

Figure 6.15: Same as Figure 6.9 in the *B* band from the third PC.

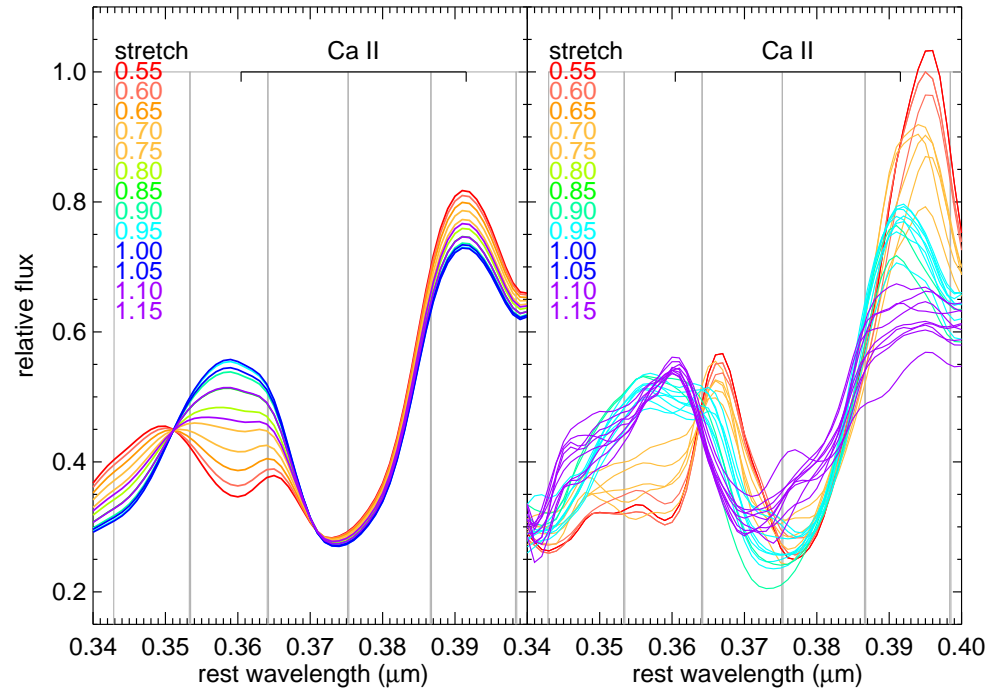Figure 6.16: Same as Figure 6.9 in the *B* band from the fourth PC.

Figure 6.17: Same as Figure 6.9 in the *B* band from the first four PCs.

(Figure 6.18). The second and third PCs also detect variations in the S II features along with those in the Si II features (Figure 6.19 and Figure 6.20).

The final template sequence, with contributions from all three PCs, is plotted in Figure 6.21. The Si II feature at 0.58 *μm* exhibits the most prominent spectroscopic sequence, perhaps of all the sequences, deepening as the stretch value decreases. Garnavich et al. (2004) suggested that the variation is due to contribution of Ti II lines in fainter objects, while Hachinger et al. (2008) claimed that the variation is due to the higher Si II/Si III ratio in the fainter objects. The depth of the Si II feature at 0.615 *μm* appears to reach its maximum at a stretch value of *s* ∼ 0.8, and decreases slightly in strength for objects with lower stretch values. Hachinger et al. (2008) explains this behavior as Si II line saturation for the fainter objects.

Hachinger et al. (2006) shows large dispersion for the equivalent width measurements of the Si II feature at 0.615 *μm* at a decline rate of Δm_{15} ∼ 1.2, which correspond to a stretch value of *s* ∼ 0.9. Figure 6.7 does not show especially large dispersions around this stretch value. This may reflect the differences in the samples or in the methods used to quantify the features.

Hachinger et al. (2006) also reported parabolic trends for equivalent measurements of
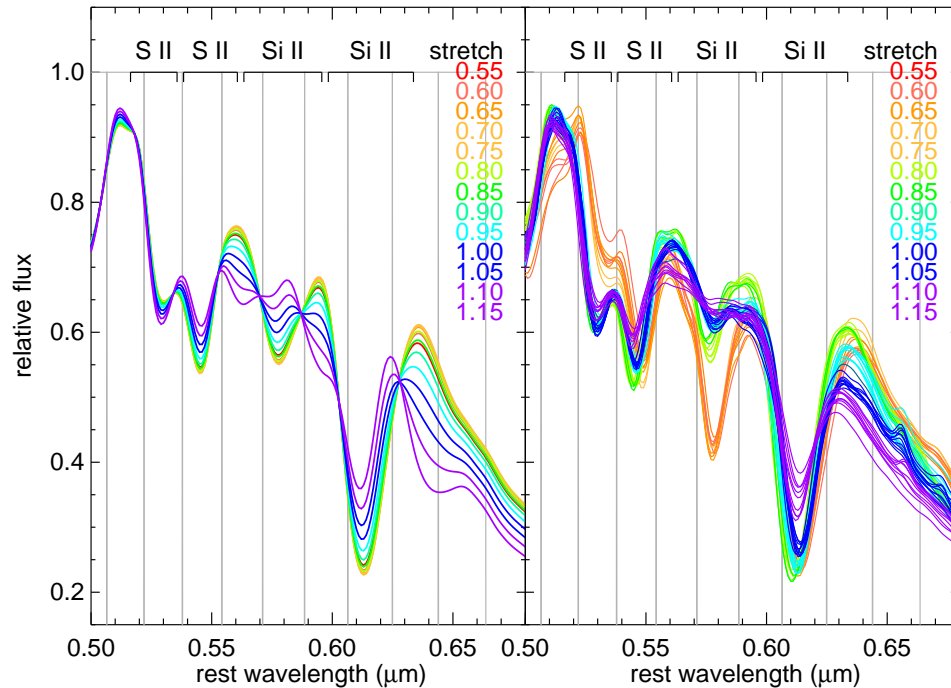
Figure 6.18: Same as Figure 6.9 in the *V* band from the first PC.

both the S II features and the Si II at 0.615 *μm*, indicating that low-stretch and high-stretch objects have similar equivalent widths. From Figure 6.21, it is apparent that although the equivalent widths of low-stretch and high-stretch objects may be similar, the shapes of the spectral features are quite different.

Also note that the library spectra from Figure 6.21 show subtle differences in the expansion velocities between SNe Ia of different stretch parameters in nearly all of the spectral features in the *V* band. While the PCA can detect expansion velocity shifts on the order of the widths of the narrowband filters, such as the range observed in the Ca II H&K feature (Figure 6.12), the subtle differences in the *V* band are not detected. The expansion velocity of the Si II have been used by previous studies to show evidence of substantial diversity between SNe Ia (e.g., Hatano et al. 2000; Benetti et al. 2005; Hachinger et al. 2006) and remains an important diagnostic. Here, the focus is placed on flux ratios.

I **band**   In the *I* band, the spectral features examined are the O I feature centered at 0.75 *μm* and the large Ca II triplet feature centered at 0.83 *μm*. In this region, only the first PC was used to construct the template sequence, as the projections on the other PCs show little trend with respect to stretch (Figure 6.8).
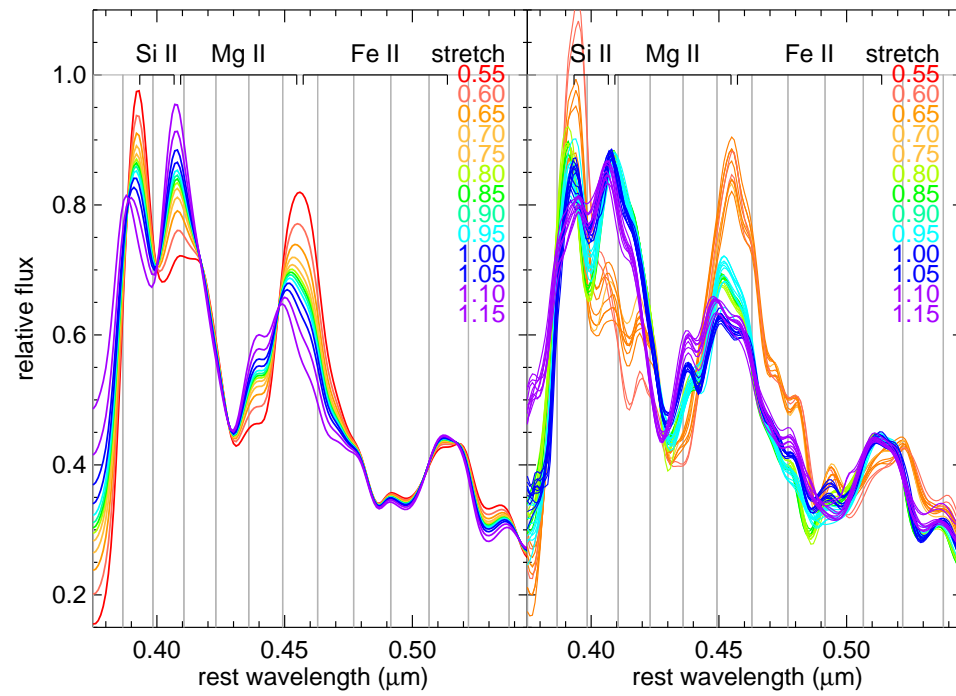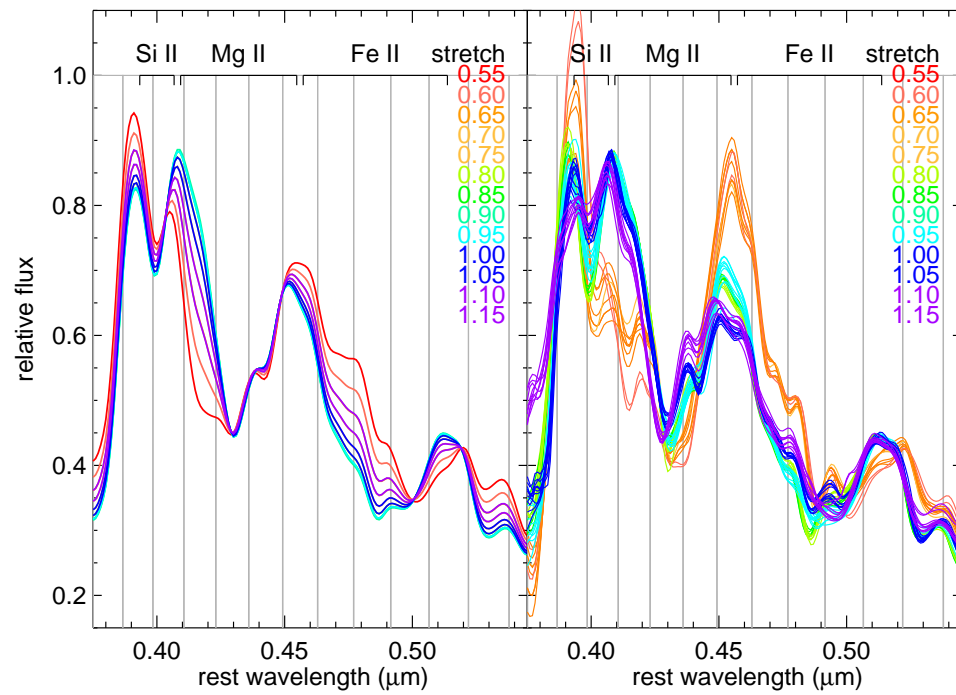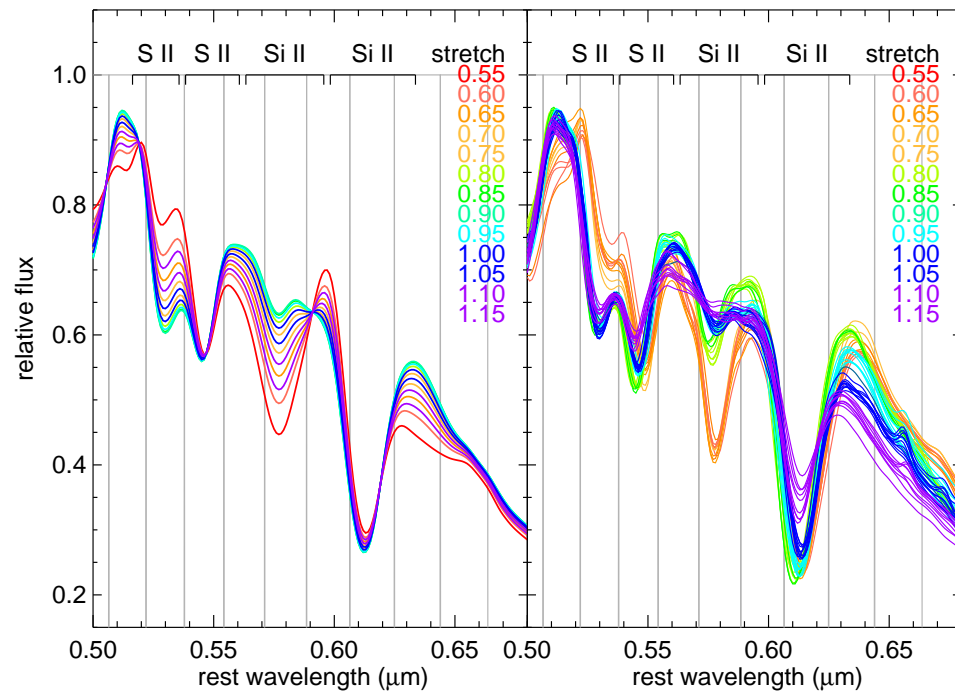
Figure 6.19: Same as Figure 6.9 in the *V* band from the second PC.
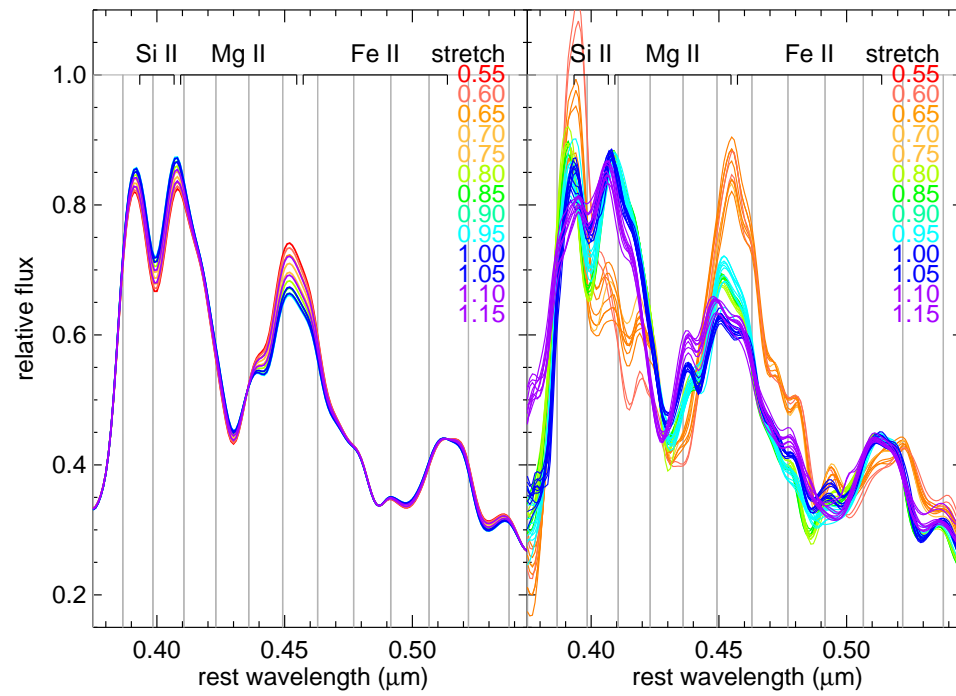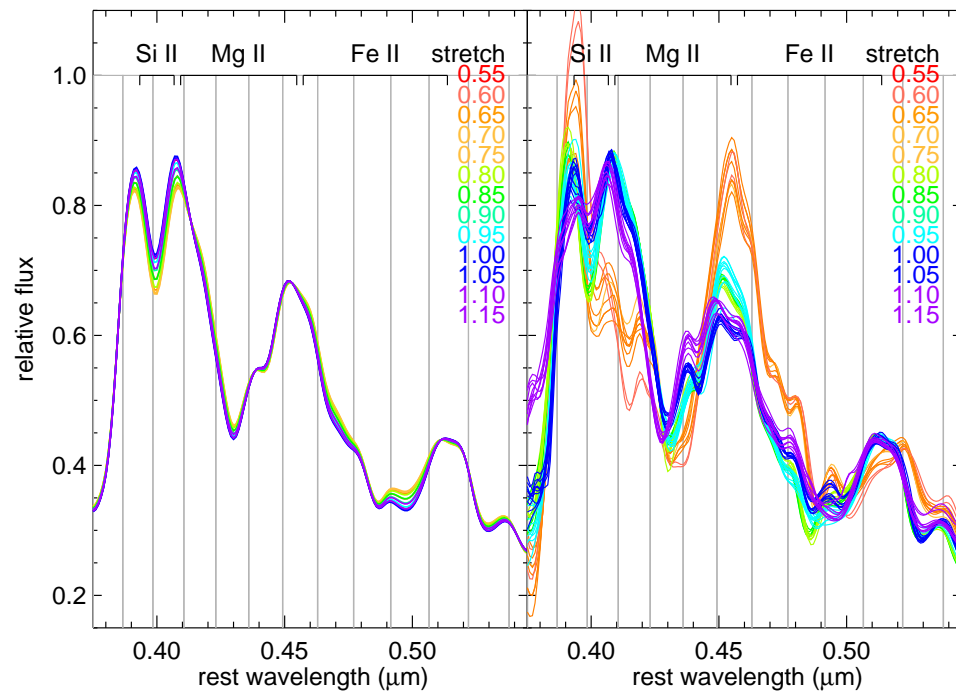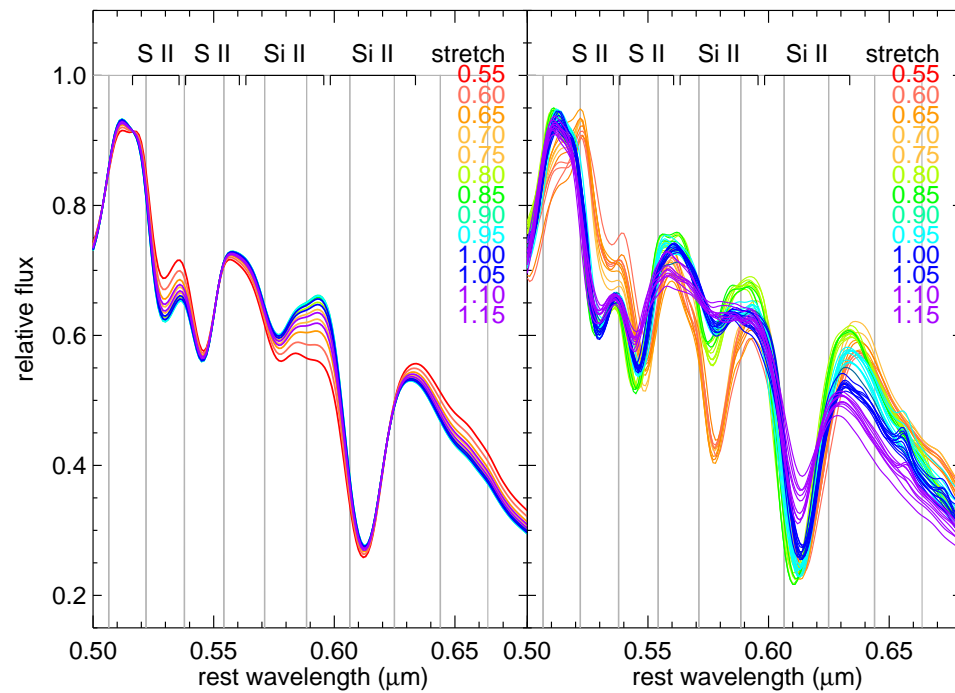

Figure 6.20: Same as Figure 6.9 in the *V* band from the third PC.

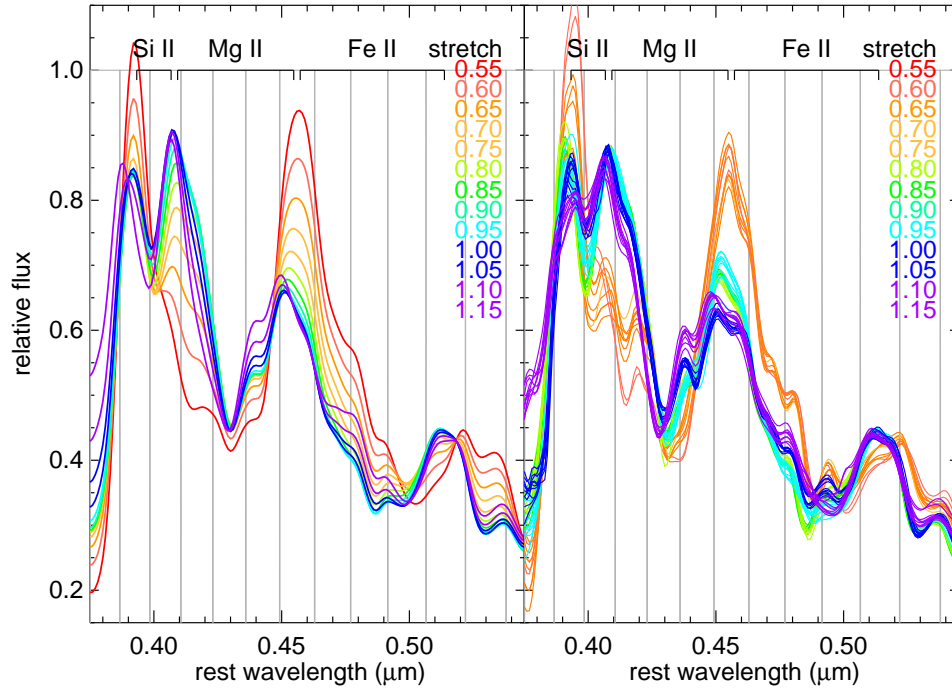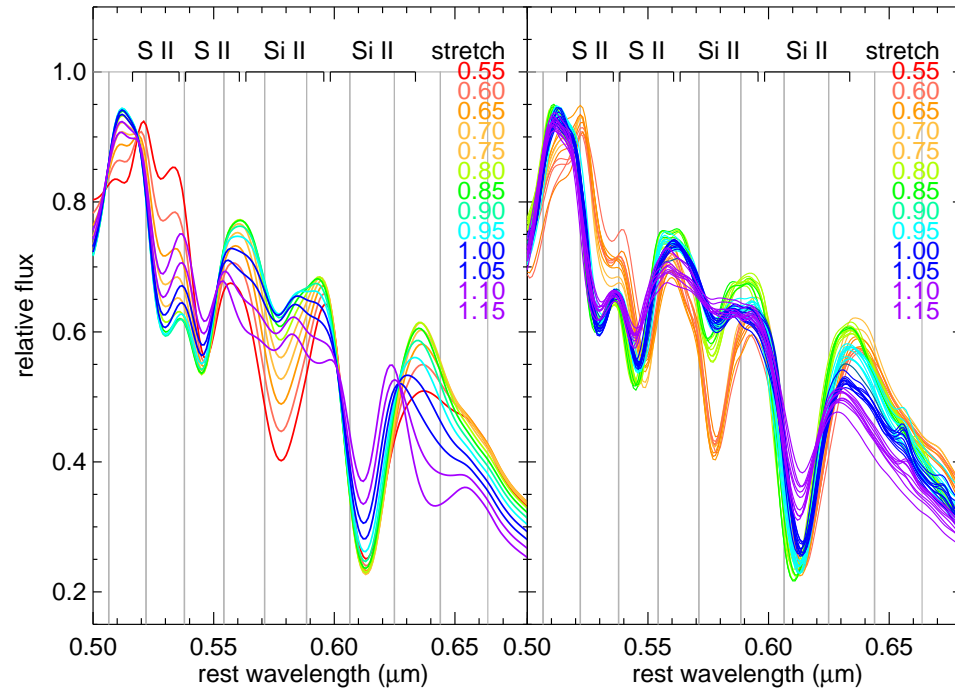Figure 6.21: Same as Figure 6.9 in the *V* band from the first three PCs.
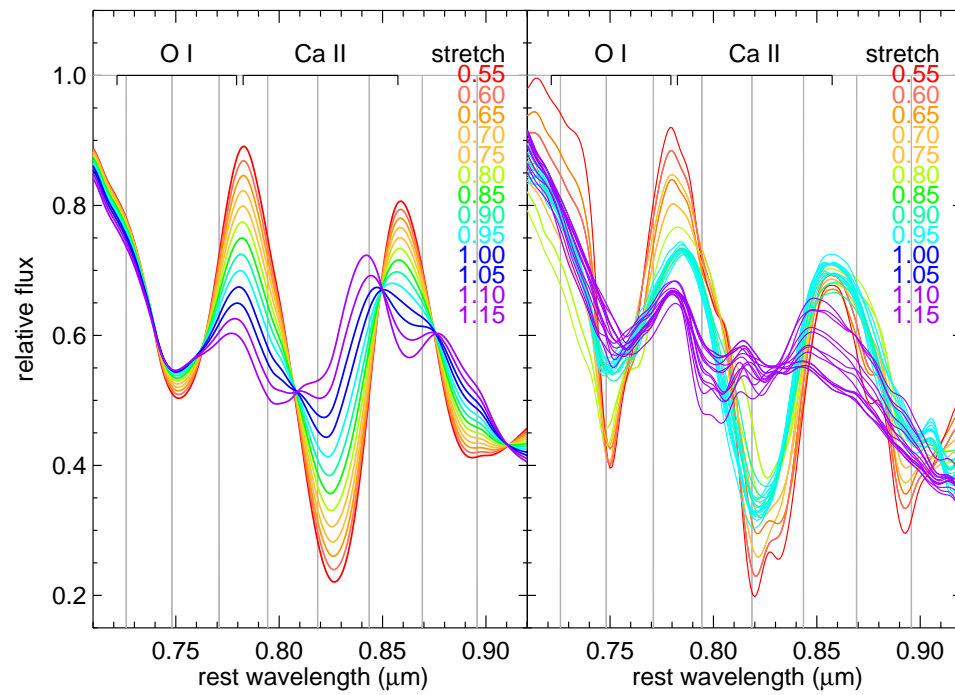
Figure 6.22: Same as Figure 6.9 in the *I* band from the first PC.

The first PC accounts for over half of the variations and shows a clear trend with a relatively small number of data points. The first PC describes the variations in both of the spectral features (Figure 6.22). It detects the deepening of the O I and Ca II triplet features as stretch decreases. It also picks up the detached high-velocity component of the Ca II feature which has been previously reported (e.g., Li et al. 2001a; Kasen et al. 2003; Mazzali et al. 2005a,b; Marion et al. 2006). In our template sequence, the detached high-velocity feature is associated with high-stretch SNe Ia.

Note that because only the first PC was used to construct the template sequence, the sequence does not match the observation as well as in the B and V regions. For majority of the SNe Ia in this low-redshift sample set, a strong and narrow telluric feature coincides with the O I feature. Our attempts to remove this feature described in Section 4.2 may be a significant cause of the scatter observed beyond the first PC (Figure 6.8). It may also be driven by another yet unidentified factor. A homogeneous spectroscopic data set with careful and consistent telluric removal may be necessary to identify the source of the remaining 46% of the variation.

At maximum light, every spectral feature examined exhibits a strong correlation with stretch, even ones which have been previously reported to show little or no correlation. The lack of trend found using the equivalent width method is not caused by the lack of a spectroscopic sequence. Rather, it is caused by the fact that the equivalent width method does not retain information on the shapes of the spectral features. Two spectral features with very different shapes can yield the same equivalent width.

6.6   Temporal evolution of spectroscopic sequence

As mentioned in Section 6.4, all the epochs of the spectra considered in the previous sections are corrected for time dilation with a factor of $1/(1 + z)$, where z is the supernova redshift, and stretch corrected with a factor of $1/s$, where s is the stretch factor of the supernova. In this section, we present the justification for the step of stretch correction and show that it originates from the persistence of a spectroscopic sequence not only at maximum light, but throughout a supernova's evolution in epoch.

For photometric observations of SNe Ia, the stretch parameter gives a measure of the width of a light curve. Fainter SNe Ia have a faster rise and decline in their optical light curves and hence narrower light curves and a smaller stretch parameter. Taking advantage of the ability of PCA to reduce the dimensionality of spectroscopic data, we can

show whether or not the spectral features of fainter SNe Ia also evolve faster than brighter ones. To accomplish this, the temporal evolutions of spectral features using timescales with stretch correction ($t_{\mathrm{Bmax}}^{\mathrm{s}}$) and without stretch correction (t_{Bmax}) are compared.

The time of B-band maximum light has some physical relevance, as it is close to the time when the luminosity is equal to the rate of energy deposition by radioactive decay (Arnett 1979, 1982). Labeling epochs relative to the time of B-band maximum light (t_{Bmax}) is also convenient observationally, but there is no prior evidence to suggest that this choice of reference point is superior over the others. For this reason, the epochs are also labeled using the time of explosion as the reference point ($t_{\mathrm{explosion}}$). The rise time from Conley et al. (2006) of $t_{\mathrm{rise}} = 19.58$ is adopted. The time of explosion is then estimated to be st_{rise} prior to time of B-band maximum. The effects of performing stretch correction on the temporal evolution of spectral features are then examined in both cases.

Note that there is evidence which suggests that there may be a range of SN Ia rise time (Strovink 2007). We do not explore this possibility here, but focus mostly on the time evolution past maximum light. In future studies, the method of PCA on relative flux measurements adopted here may be used to determine whether the spectroscopic temporal evolution on both the rising and declining parts of the light curve is well described by a single stretch parameter.

The epochs with various options of corrections and reference points are summarized as follows:

$$t_{\mathrm{Bmax}} = \frac{t(\mathrm{observation}) - t(\mathrm{Bmax})}{1 + z} \tag{6.3}$$

$$t_{\mathrm{Bmax}}^{\mathrm{s}} = \frac{t(\mathrm{observation}) - t(\mathrm{Bmax})}{s(1 + z)} \tag{6.4}$$

$$t_{\mathrm{explosion}} = \frac{t(\mathrm{observation}) - t(\mathrm{Bmax}) - st_{\mathrm{rise}}}{1 + z} \tag{6.5}$$

$$t_{\mathrm{explosion}}^{\mathrm{s}} = \frac{t(\mathrm{observation}) - t(\mathrm{Bmax}) - st_{\mathrm{rise}}}{s(1 + z)} \tag{6.6}$$

The same wavelength regions are used to divide the spectra into four segments. PCA is again performed on the observed spectra to reduce the dimensionality in the wavelength direction and to examine the relation between spectral features and epochs. We select an epoch interval for each wavelength region where the largest temporal evolution of spectral features is observed in the direction of the first PC. This is done to amplify the effect of

stretch correction on the relation between spectral features and epoch. The epoch intervals are tabulated in Table 6.3.

Table 6.3: Epoch intervals for the temporal evolution analysis and the dispersions from the linear fit of timescales with various options of reference points and stretch corrections

Band	Lower epoch	Upper epoch	Number of spectra	Dispersions from linear fit			
				t_{Bmax}	$t_{\mathrm{explosion}}$	$t^{\mathrm{S}}_{\mathrm{Bmax}}$	$t^{\mathrm{S}}_{\mathrm{explosion}}$
U	-10	10	96	0.415	0.504	0.404	0.403
B	5	20	165	0.298	0.586	0.189	0.192
V	3	22	232	0.200	0.435	0.180	0.183
I	-20	30	90	0.262	0.339	0.255	0.253

In each wavelength region, a linear fit is done for the temporal evolution of the spectral feature projections on the first PC with respect to the stretch-corrected epochs. The data points are weighted by the errors in the epochs and in the projections. The data points are also weighted by the stretch values, such that SNe Ia with stretch values further from the mean value are weighted less. This step ensures that the linear fits through points which require the smallest stretch corrections. The resulting projections of the spectral features on the first PC are plotted in Figure 6.23, Figure 6.24, Figure 6.25 and Figure 6.26 for the U, B, V and I wavelength regions, respectively.

In all four wavelength regions considered, there is evidence that high-stretch objects tend to lie on one side of the linear fit, while low-stretch objects tend to lie on the opposite side. The trends also support the idea that low-stretch objects have a more rapid evolution in their spectral features than high-stretch ones. After the timescale is stretch corrected, the dispersions of the projections around the linear fit seem to decrease. The effects are most dramatic when the timescales are taken with respect to the time of explosion, because of the larger magnitudes of stretch corrections. To confirm the dependence of the directions and the magnitudes of the dispersions on the stretch parameter, the dispersions of the projections from the linear fits are plotted in Figure 6.27, Figure 6.28, Figure 6.29 and Figure 6.30 for the U, B, V and I wavelength regions, respectively.

In each of the four bands, there is evidence of a trend between the dispersions from the linear fit and the stretch parameters, when the timescale is not stretch corrected. After the stretch corrections, the trend mostly disappears. Although there is not enough spectroscopic data to confirm a spectroscopic sequence at each epoch, our method here has shown evidence that spectral features correlate with stretch throughout these epochs and that spec-
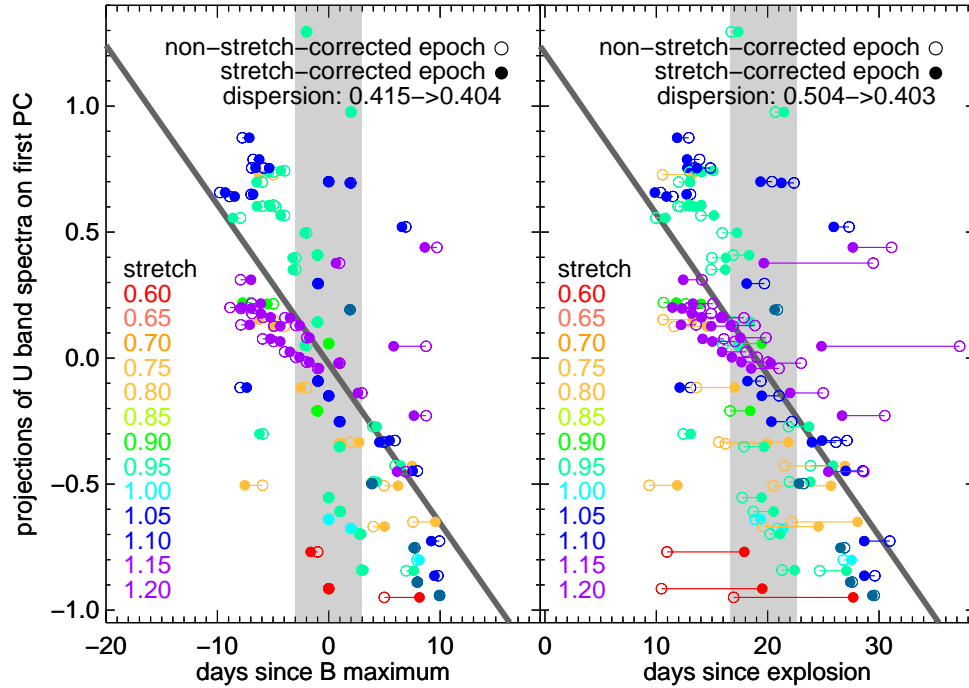
Figure 6.23: The time evolution of the projections of *U*-band spectral features on the first PC. The left panel shows epochs with respect to *B*-band maximum, and the right panel shows epochs with respect to time of explosion. The epochs with stretch corrections are represented by solid dots, and epochs without stretch corrections are represented by open dots. For each spectrum, epochs with and without stretch corrections are connected with a horizontal line. The quadrature sums of the dispersions of the linear fit are also noted from before to after stretch corrections to the timescales. The error bars are omitted for clarity.

tral features evolve faster for low-stretch objects than for high-stretch ones. After stretch correcting the timescale, the sequences largely disappear.

The dispersions from the linear fits are summed in quadrature over all the spectra at the epoch intervals considered and are tabulated in Table 6.3. The scatters indeed decrease when stretch corrections are applied to the timescale. Table 6.3 also shows that the total dispersions show very small differences between adopting timescales with respect to time of *B* maximum and time of explosion. For our data set, there is not a preferred choice of reference point between the two options.

When a spectral template time series is used for cosmological analysis, it is common practice to use the stretch corrected timescale of the observed SN to select the epoch of the spectral template. Before this study, there was no evidence to suggest that this step was necessary, except for parallels drawn from the photometric behavior of SNe Ia. Because the
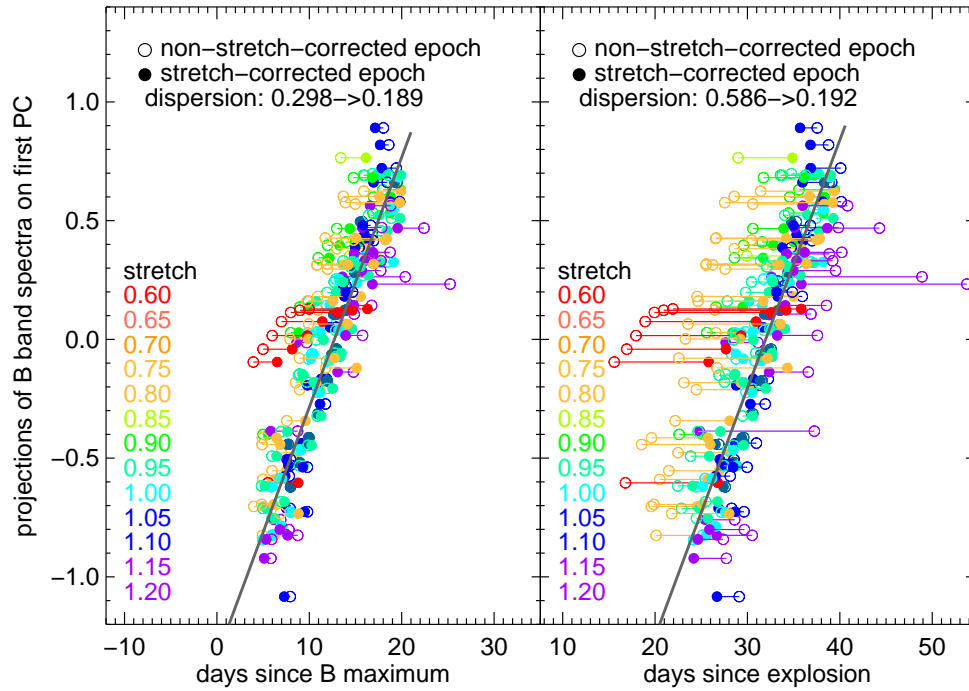
Figure 6.24: Same as Figure 6.23 in the *B* band.
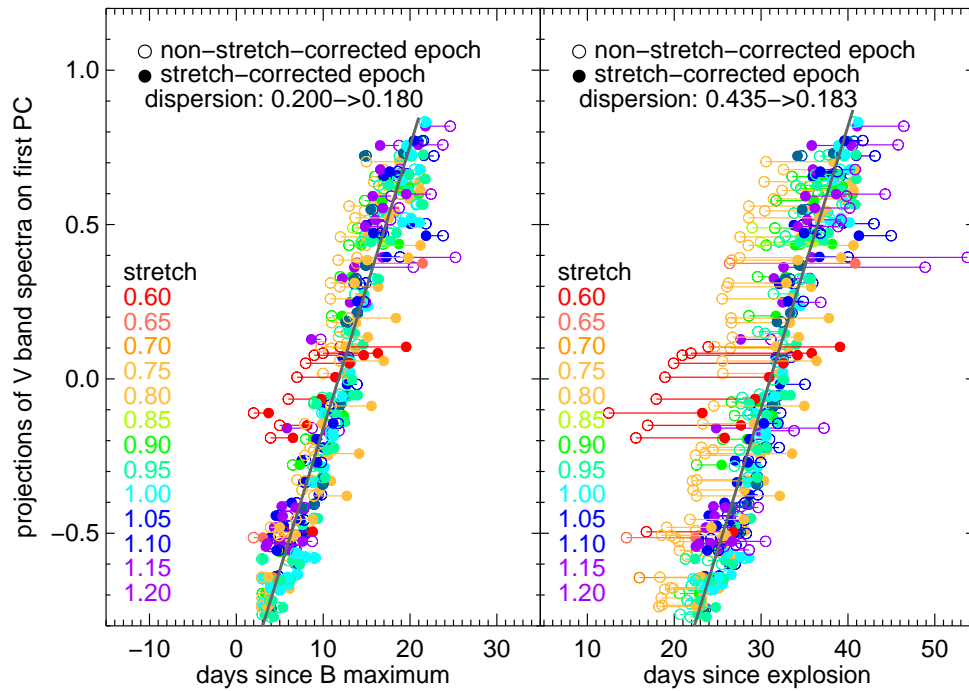
Figure 6.25: Same as Figure 6.23 in the *I* band.
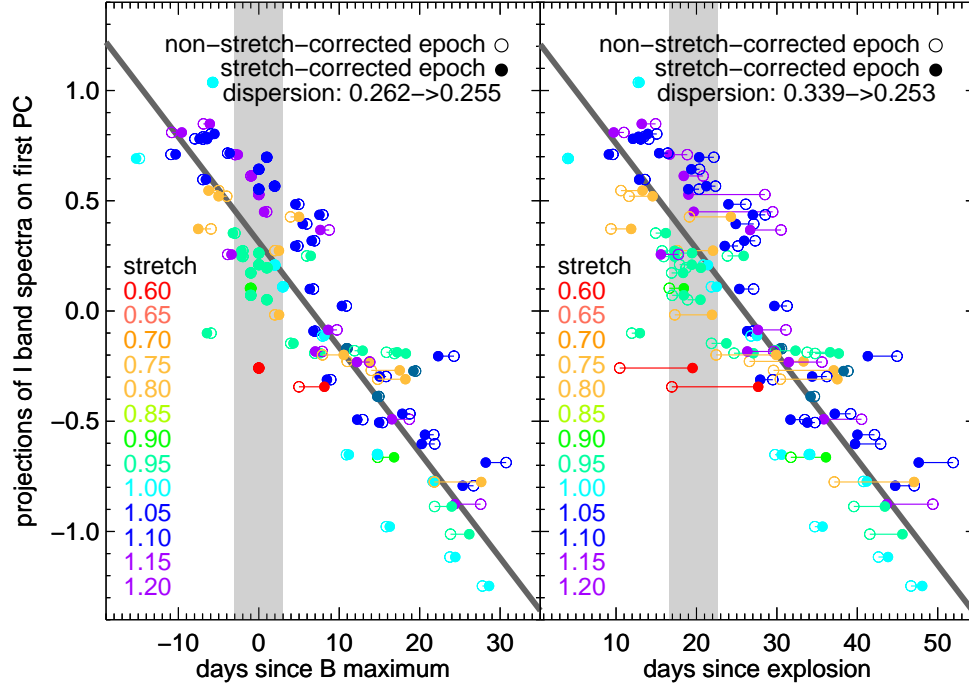
Figure 6.26: Same as Figure 6.23 in the *I* band.

spectral template usually has features which are representative of a SN Ia with stretch close to unity (e.g., Hsiao et al. 2007a), it is shown here that using stretch-corrected timescale indeed reduces the dependence of spectral features on stretch and the scatters caused by this effect. It is also true that even after stretch corrections, the spectroscopic sequences around maximum light still exist, regardless of which reference point is used for the timescale. The construction of template sequences described in Section 6.5 provides an improvement to the use of spectral templates near maximum light.

In the above analysis, the resemblance between the spectral features of a stretch *s* SN Ia at time *t* and those of a typical *s* ~ 1 SN Ia at time *s* × *t* is used to infer the existence of spectroscopic sequences throughout the epochs. This is also used to show that the spectral features of low-stretch SNe Ia evolve faster than those of high-stretch ones. The claims can be further tested by directly measuring the time rate of change of the projections using SNe Ia with time series observations.

The time rates of change of the *V*-band projections are examined, using the timescales before stretch corrections to see if the spectral evolution of low-stretch objects is indeed faster. The analysis is limited to SNe Ia in the library with four or more time series obser-vations covering epoch intervals of five or more days in order to obtain secure estimates of
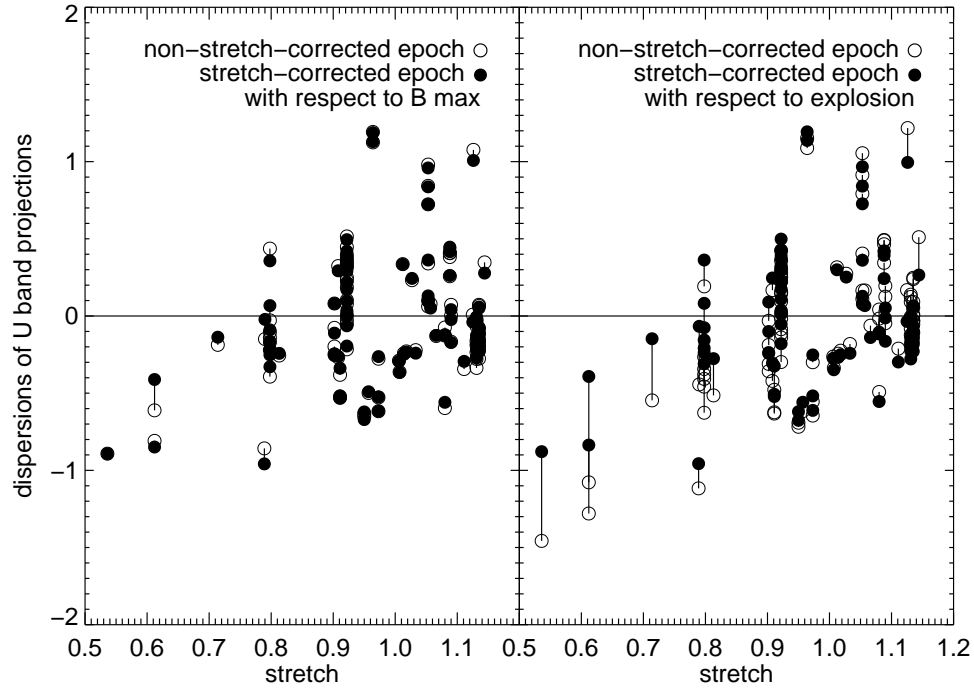
Figure 6.27: Dispersions of *U*-band projections from the linear fit against stretch. The left panel shows the case of epochs with respect to *B*-band maximum, and the right panel shows the case of epochs with respect to time of explosion. The epochs with stretch corrections are represented by solid dots, and epochs without stretch corrections are represented by open dots. For each spectrum, epochs with and without stretch corrections are connected with a vertical line.

the speed of the evolution. The results are plotted in the upper panel of Figure 6.31. Except for one outlier, there is a clear trend of decreasing time rate of change of the projections with respect to stretch. For the epoch intervals specified, the linear fit in Figure 6.25 is assumed to be a reasonable description of the time evolution of the projections for a SN Ia with stretch value equal to the mean of the sample. In the scheme of WLR and linear projection evolution, the time rate of change can be written as:

$$\dot{p}_1(s) = \frac{\dot{p}_1(s=1)}{s}, \tag{6.7}$$

where p_1 denotes the projections of the library spectra on the first PC. The fainter objects are expected to evolve faster than the brighter ones in this fashion. This derived time rate of change with respect to stretch is plotted as a gray curve in the upper panel of Figure 6.31 for comparison. The WLR scheme and the linear approximation are shown to provide a
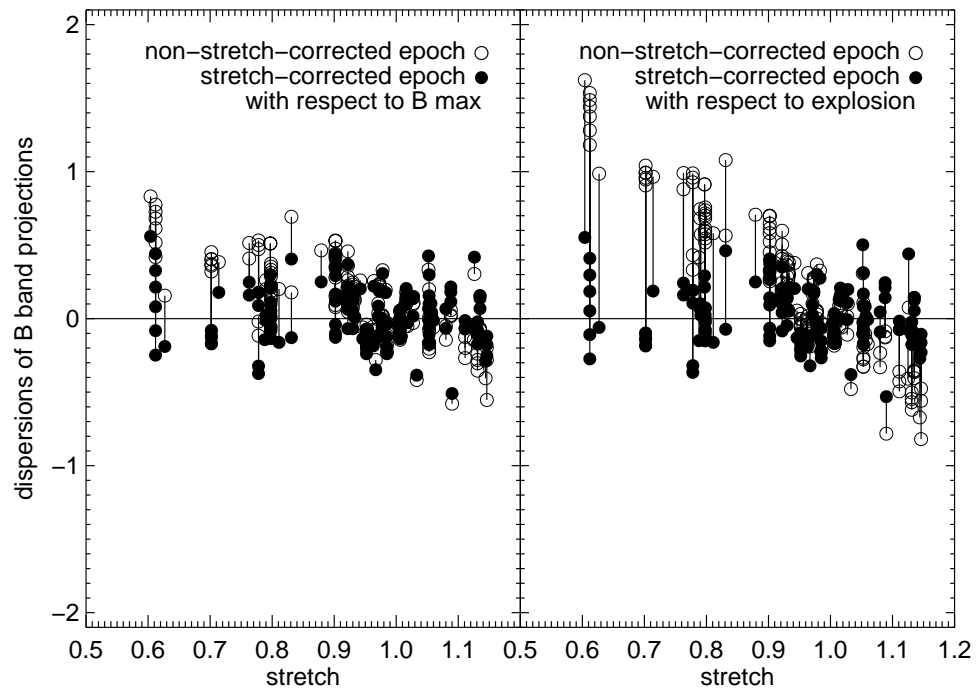
Figure 6.28: Same as Figure 6.27 in the *B* band.
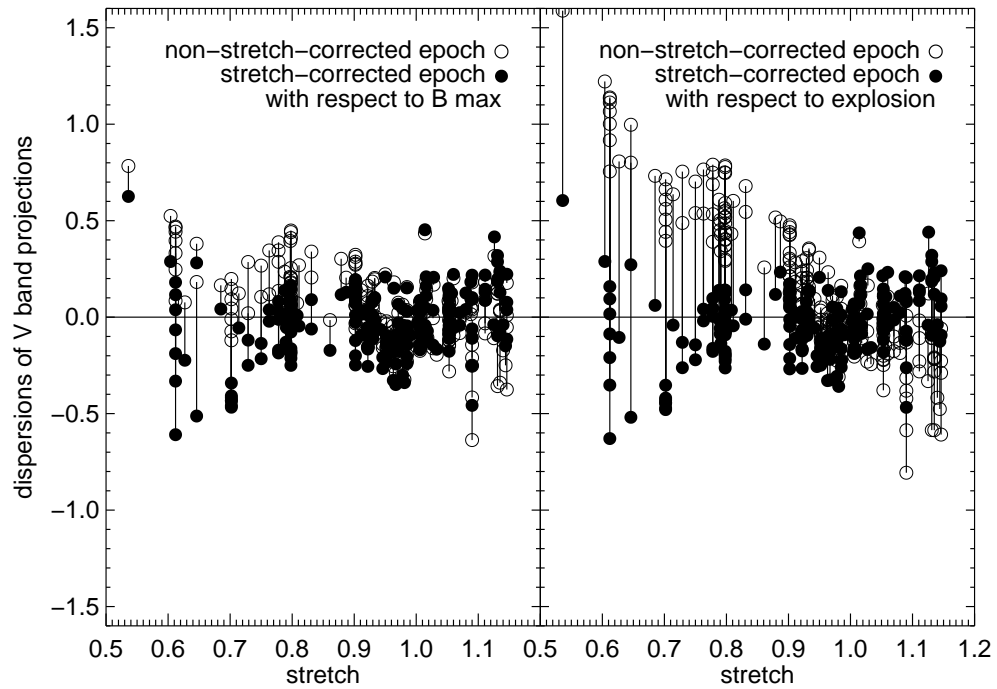
Figure 6.29: Same as Figure 6.27 in the *V* band.
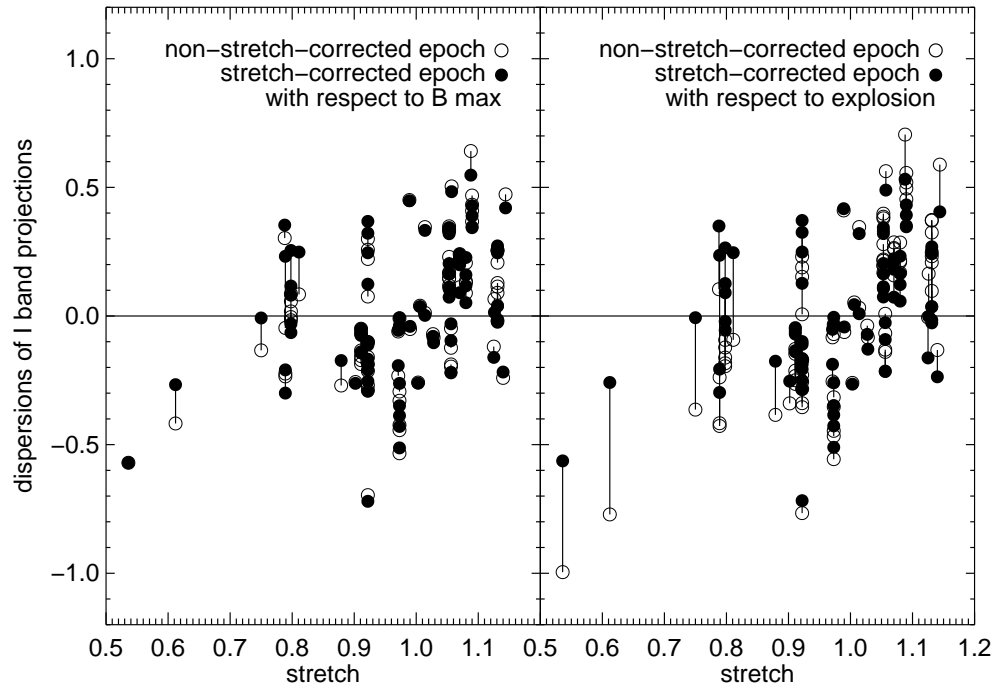
Figure 6.30: Same as Figure 6.27 in the *I* band.

decent description for the speed of the spectral evolution.

In the upper panel of Figure 6.31, SN 1999by (Garnavich et al. 2004) is an outlier because of its exceptionally low rate of change in the projections. To examine the source of this mismatch, the projections of SN 1999by and a normal SN 1997do from Figure 6.25 are isolated and plotted in the lower panel of Figure 6.31. It is clear that the data points of SN 1999by are not well described by the linear fit and thus do not have a constant rate of change. The projections of SN 1999by flatten and enter into a plateau phase much earlier than a normal SN Ia like SN 1997do. This is expected in the scheme of WLR. What is not expected is the low projections of SN 1999by compared to those of SN 1997do when they enter the plateau phase. With the lack of time series spectroscopic data for 1991bg-like objects, it is difficult to tell whether this peculiarity is a common feature among them. The stretch corrections indeed reduce the scatter from the linear fit. There is therefore no doubt that their spectroscopic temporal evolution is faster than normal at earlier phases.
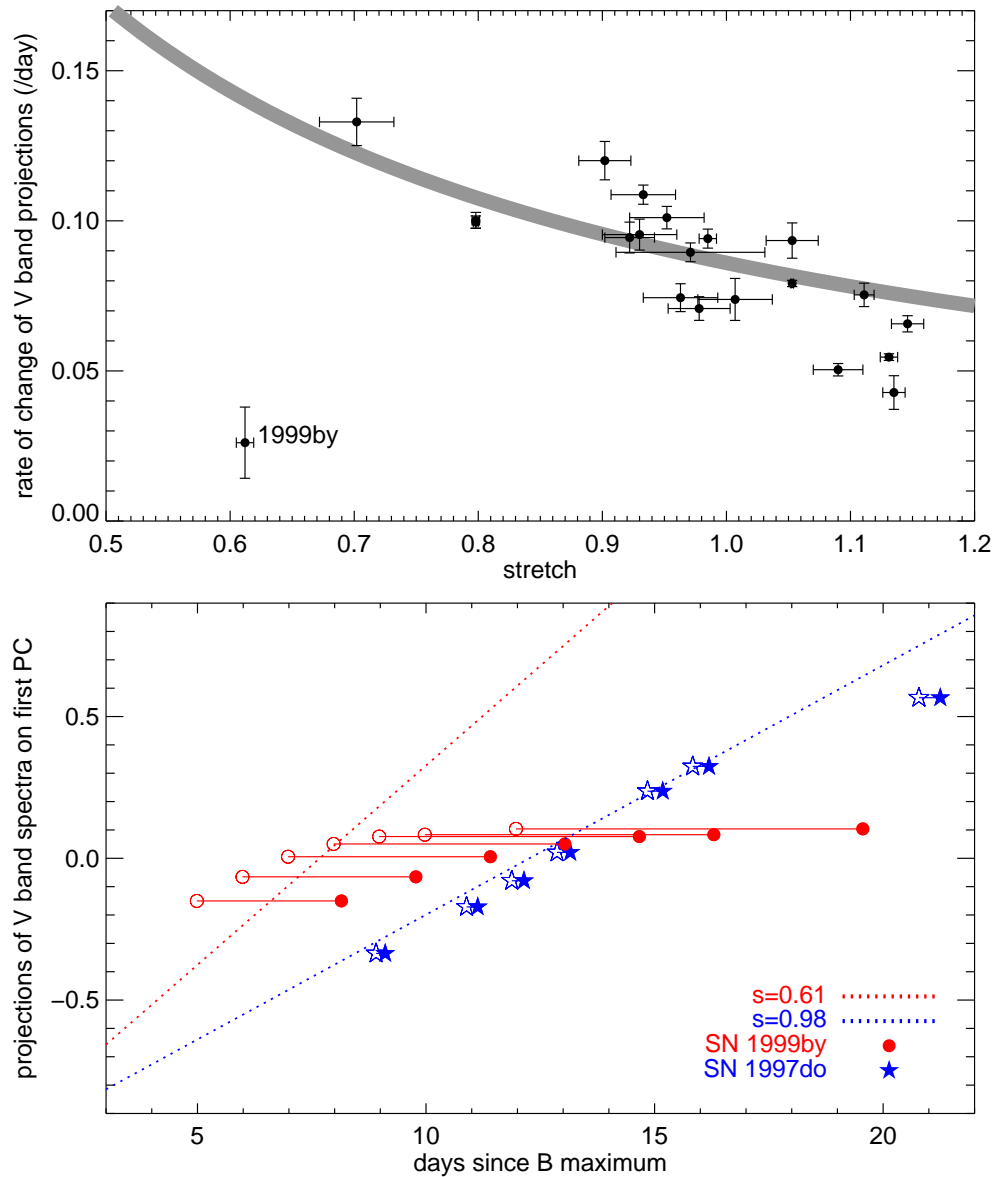
Figure 6.31: The time rate of change of *V*-band projections on the first PC with respect to stretch (upper panel) and the projections of SN 1999by and SN 1997do with respect to time (lower panel). In the upper panel, the timescale used is with respect to *B* maximum, corrected for time dilation, and before stretch correction. The thick gray line corresponds to the time rate of change expected from the WLR scheme and the linear fit from Figure 6.25. In the lower panel, the timescale is with respect to *B* maximum and corrected for time dilation. The open and filled symbols represent timescales before and after stretch corrections, respectively. The red and blue dotted lines represent the expected temporal evolution, before stretch correction, from the WLR scheme and the linear fit from Figure 6.25 for SN 1999by (s=0.61) and SN 1997do (s=0.98), respectively.

6.7 Conclusion

At maximum light, the detection of a strong correlation between spectroscopic properties and light-curve widths is reported for every spectral feature from *U* band to *I* band. The detections are made even for spectral features which have been previously shown to have little or no correlations using the equivalent width method. The lack of detections from previous studies is attributed to the inability of the equivalent width method to retain information on the detailed spectral shapes. In a Chandrasekhar-mass model, brighter SNe Ia produce more ^{56}Ni and therefore have fewer intermediate-mass elements. Brighter SNe Ia also have higher temperature ejecta in general. The snapshots of SN Ia spectral features at maximum light reflect both the effect of different temperatures on ionization and the effect of different compositions.

Steps have been taken to remove the broadband tilts of the spectra. Furthermore, the narrowband measurements of the spectral features have been shown to have a weak dependence on the broadband tilt. Thus, the PC projections reflect solely the diversity of spectral features, independent of any established photometric behaviors. A large fraction of the information in the spectral data can be retained using only the first few PCs, even when large gaps exist in the stretch parameter space of the data. The descriptions of the sequences from PCA show in unprecedented detail how spectral features vary with stretch. They also show great promise for improving the use of spectral template time series in cosmological studies, by including an extra dimension of light-curve width along with wavelength and time.

These methods provide a straight-forward application for using spectral features as distance indicators. They can also be extended to search for correlations between spectral features and intrinsic colors. As there is evidence that intrinsic colors also correlate with peak luminosity, the spectral features are expected to correlate with intrinsic colors. Established relations between spectral features and intrinsic colors will help disentangle the degeneracy between dust reddening and intrinsic colors in the observed colors of SNe Ia.

Evolution of SN Ia properties with respect to redshift is also of great concern in cosmology. Recent spectroscopic studies detected systematic spectroscopic differences between low-redshift and high-redshift SNe Ia (Foley et al. 2008a; Sullivan et al. 2009). However, it was unclear whether the differences were caused by the effects of demographic shift or true evolution. As the cosmic star formation density increases with redshift, the mean light-curve width of SNe Ia, which depends on the star formation rate of the host galaxy, also increases with redshift. With the relations between spectral features and light-curve width

established here, the effect of demographic shift on the spectra of SNe Ia can be pinpointed. If there are remaining variations in the spectral features of SNe Ia with the same light-curve width at different redshifts, they may be signs of true evolution.

The time evolution of spectral features is also shown to correlate with stretch across the optical wavelengths. In particular, low-stretch SNe Ia show a more rapid evolution in their spectral features than high-stretch ones. The speed of the evolution is also shown to be well characterized by the stretch parameter. These results lend support to the idea that the origin of the WLR is predominantly a spectroscopic phenomenon, rather than a bolometric one (Kasen & Woosley 2007). As fainter SNe Ia are cooler and have earlier recombination of iron-group elements, the more rapid spectroscopic temporal evolution of fainter SNe Ia reflects the faster ionization evolution of iron-group elements. Our study of spectroscopic temporal evolution also offers, for the first time, empirical evidence that using stretch-corrected epochs when selecting the epochs of the mean spectral template time series reduces the scatter instigated by stretch.

There is evidence that the one-parameter description may not completely account for the observational diversity in the spectral features, such as the spectral features in the U band and the feature velocities in the V band. Nevertheless, stretch, and in turn, the luminosity of a SN Ia, is shown here to be one of the dominant, if not *the* most dominant, driver of time-dependent spectroscopic diversity observed in SNe Ia at optical wavelengths.

Chapter 7

Spectroscopic diversity in the near-infrared

Abstract   While Type Ia supernovae (SNe Ia) can be calibrated into standard candles in the optical, they appear to be true standard candles in the near infrared (NIR). Matching the photometric behavior, the spectroscopic properties of NIR spectra around the NIR maxima are shown here to be exceptionally uniform with very slow temporal evolution. The first mean spectral template time series of SNe Ia in the NIR is presented. The spectral template is shown to minimize the K-correction systematic errors caused by using individual spectra. Principal component analysis (PCA) is performed the NIR spectra to search for relations between the spectral features and light-curve widths. Around the NIR primary maximum, a spectroscopic sequence is detected in each of the Y, J, H and K bands. These systematic variations are perhaps too small to enter into broadband photometric observations. The rapidly evolving and prominent H-band feature also shows evidence of a spectroscopic sequence. Because the sequences are formed by only $8 - 9$ spectra for each analysis, more NIR spectra are required to confirm or refute these trends.

7.1   Introduction

NIR observations of SNe Ia are challenging both because of the strong absorption features due to the Earth's atmosphere, and the low intrinsic luminosities of SNe Ia in the NIR. The benefits of observing in the NIR, however, outweigh the challenges. Light is less extincted by dust along the line of sight, with the extinction originating from the host galaxy, the intergalactic medium and the Milky Way. The standard Galactic dust law of Cardelli et al.

(1989) shows that the extinction in the NIR is less than 30% of that in the optical. As we move toward longer wavelengths, the extinction corrections become less dependent on our assumptions on the properties of dust and the intrinsic colors of SNe Ia.

In recent years, extensive monitoring of nearby SNe Ia in the NIR has become more common, producing statistically significant samples of well observed photometry (e.g., Jha et al. 1999; Meikle 2000; Hernandez et al. 2000; Valentini et al. 2003; Candia et al. 2003; Krisciunas et al. 2001, 2003, 2004b,c, 2006, 2007; Benetti et al. 2004; Elias-Rosa et al. 2006, 2008; Hamuy et al. 2006; Phillips et al. 2006; Pastorello et al. 2007a,b; Prieto et al. 2007; Stritzinger & Sollerman 2007; Wang et al. 2008, 2009a; Taubenberger et al. 2008; Pignata et al. 2008; Wood-Vasey et al. 2008; Foley et al. 2009) and spectra (e.g., Meikle et al. 1996; Bowers et al. 1997; Rudy et al. 2002; Hamuy et al. 2002; Höflich et al. 2002; Marion et al. 2003, 2006; Krisciunas et al. 2007). Elias et al. (1981, 1985) first noted the small dispersion in the peak absolute magnitudes of SNe Ia in the NIR and the potential for them to be used as distance indicators. Considering theoretical models with ^{56}Ni mass range $0.4 - 0.9 M_{odot}$, Kasen (2006) found similar small dispersions at the NIR primary maximum.

Krisciunas et al. (2004a) demonstrated the efficacy of using NIR primary maxima of SNe Ia as distance indicators. They found that the stretch technique provides good fits to the observed light curves in the range $-12 - 10$ days with respect to B-band maximum. This range includes the primary NIR maximum, but excludes the secondary peak. They also found no obvious relation between light-curve shape and maximum brightness. Heavily reddened or peculiar objects in the optical are also shown to be good standard candles in the NIR. While SNe Ia are standardizable candles in the optical, they appear to be true standard candles in the NIR.

Crucial for the study of the NIR photometric properties of SNe Ia is an accurate and expansive set of spectral templates which covers the range of wavelengths and epochs of observed SNe Ia. Previous studies of NIR photometry have relied on the time series spectra of a single SN Ia for the determination of K-corrections (e.g., Krisciunas et al. 2004b). This method has been shown to cause significant systematic errors in the optical (Hsiao et al. 2007a). The methods presented by Hsiao et al. (2007a), and in Chapter 4, are adopted to build the first mean spectral template time series of SNe Ia in the NIR. The K-correction errors from the spectroscopic diversity of observed spectra are quantified and shown to be reduced from the previous method of using the spectra of a single SN Ia.

In Chapter 6, the light-curve width as an indicator of the luminosity of a SN Ia is shown to be the main driver of the diversity observed in optical spectra. Here, the spectroscopic

properties of SNe Ia in the NIR are examined, using 52 NIR spectra gathered from the literature and through private communications. PCA is performed on the spectral features of the NIR spectra to identify the vectors pointing toward the largest variations in the data space. The projections of the library spectra on the resulting vectors are correlated with the light-curve widths. The relations are examined to see if NIR spectral features vary systematically with the light-curve widths, even when the photometric properties appear to show no such correlations.

7.2   Color curves

To build a mean spectral template time series, a representative set of light-curve templates which cover a wide range of epochs for the NIR $IYJHK$ bands are required. Such a set of light-curve templates is not yet available in the literature. In this section, a set of NIR light-curve templates are built from available photometry and light-curve templates in the literature. The purpose here is not to build accurate light-curve templates for the use of cosmological analysis or the study of photometric properties, but to build representative and expansive light curves to scale the colors of the spectral templates smoothly with time.

The primary purpose for a mean spectral template is for K-correction calculations. The absolute flux of a SN Ia is normalized away for K-corrections, and the broadband colors of a SN Ia play an important role for K-corrections. For these reasons, the focus is placed on building template color curves in the NIR.

Our color curves include contributions from two light-curve templates presented by Krisciunas et al. (2000) and Wood-Vasey et al. (2008). Also included are the photometry of SNe 1980N, 1981B, 1981D (Elias et al. 1981, 1985), 1986G (Frogel et al. 1987), 1989 (Kidger et al. 1989; Wells et al. 1994), 1998bu (Mayya et al. 1998; Jha et al. 1999; Hernandez et al. 2000), 2001el (Krisciunas et al. 2003) and 2004S (Krisciunas et al. 2007). Even though the library spectra are not spectrophotometric, the colors obtained by performing artificial photometry on the spectra are also used for the determination of the color curves. The different contributions are then combined by appropriate weighted mean at each epoch to create the final template color curves.

The template color curves are plotted in Figure 7.1 and compared with other light-curve templates, photometry from individual SNe Ia and colors from the library spectra. The temporal evolutions of the broadband colors of SNe Ia are shown here to be quite uniform. The colors of the library spectra also match the template color curves well. For this reason, the library spectra require small color corrections when their broadband tilts are standardized
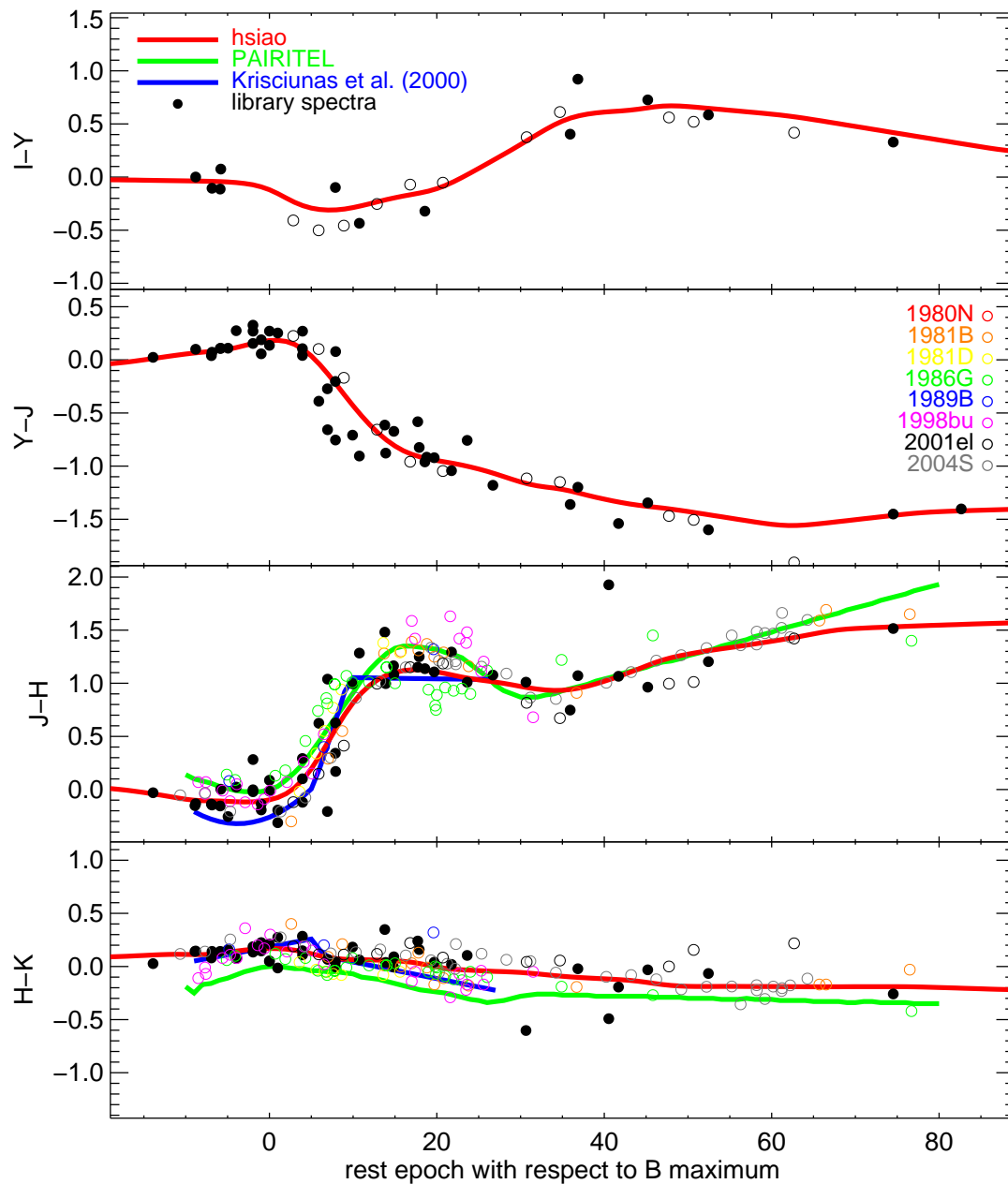
Figure 7.1: The NIR template color curves for the mean spectral template. The epochs are with respect to *B*-band maximum. The light-curve templates are plotted as solid lines. The photometry from individual SNe Ia is plotted as open circles. The colors of the library spectra obtained from artificial photometry are plotted as solid circles.
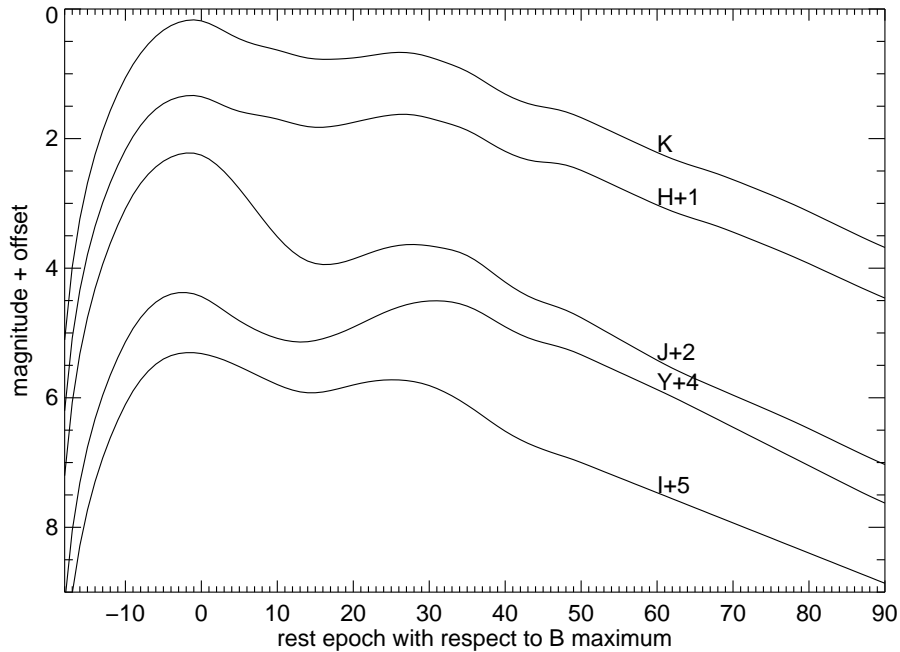
Figure 7.2: The NIR light-curve templates with respect to time of *B*-band maximum.

to this set of color curves. The narrowband measurements of their spectral features will thus be less susceptible to uncertainties in the broadband colors and the process of color corrections.

The final NIR light-curve templates are plotted in Figure 7.2. The double-peaked characteristics of NIR light curves are present for the templates in all five bands. The primary maximum occurs a few days before *B*-band maximum. The secondary peaks in the *I* band are found to occur later in time and have higher intensities for the more luminous objects (Hamuy et al. 1996a; Nobili et al. 2005). This photometric behavior is found to be connected to the ionization evolution of iron group elements (Kasen 2006). Here, we do not study the dependence of photometric properties of SNe Ia on their brightness, but focus on the spectroscopic properties instead. Our template light curves should be similar to the light curves of a typical $s = 1$ SN Ia.

7.3   Library spectra

Despite the recent surge in NIR observations of the SNe Ia, the number of NIR spectra is still relatively low compared to the number of optical spectra. 52 NIR spectra of 30

SNe Ia are gathered for this study. All of the spectra are of low-redshift nearby SNe Ia, reflecting the challenging observing conditions in the NIR. Approximately half of the SNe Ia have complementary optical photometric observations available to derive *B*-band stretch parameters (Goldhaber et al. 2001). These stretch values are used as measures of the widths of the optical light curves and as indicators of the luminosity of the SNe Ia. The full list of library NIR spectra and the available stretch values are listed in Table 7.1.

Most of the spectra are from Marion et al. (2003, 2009) and currently form the largest set of NIR spectra of SNe Ia. The spectra were obtained using the 3-meter telescope at the NASA Infrared Telescope Facility (IRTF) with the SpeX medium resolution spectrograph (Rayner et al. 1998). The data was reduced using IDL routines developed by Cushing et al. (2004). The prominent telluric absorption features in the NIR were removed using techniques developed by Vacca et al. (2003).

Also included in the library are the NIR spectra of SN 1999ee published by Hamuy et al. (2002). These 11 spectra constitute the largest sample of time series observations of a SN Ia in the NIR. The telluric features are removed using the flux calibration technique described by Maiolino et al. (1996). A single NIR spectrum from SN 2004S, published by Krisciunas et al. (2007), is also included in the library.

Table 7.1: The full list of library NIR spectra. The epochs are with respect to the time of *B* maximum. The stretch parameters are obtained from *B*-band light curves.

Name	Epochs	Stretch	References
1999ee	-9, 0, 1, 4, 8, 15, 19, 22, 27, 31, 41	1.053	Hamuy et al. (2002)
2000dk	6, 7	0.763	Marion et al. (2003)
2000dm	0	0.885	Marion et al. (2003)
2000dn	-6	1.140	Marion et al. (2003)
2000do	7		Marion et al. (2009)
2001bf	4	1.140	Marion et al. (2003)
2001bg	10	0.993	Marion et al. (2003)
2001br	-2	1.060	Marion et al. (2003)
2001dl	-1	1.140	Marion et al. (2003)
2001en	-2, 20	0.935	Marion et al. (2009)
Continued on the next page...			

Table 7.1 – Continued

Name	Epochs	Stretch	References
2002bo	83	0.922	Marion et al. (2009)
2002cr	-7, -5		Marion et al. (2009)
2002ef	11		Marion et al. (2009)
2002fb	8		Marion et al. (2009)
2002fk	-14, 42	0.940	Marion et al. (2003)
2002ha	8		Marion et al. (2003)
2002hw	-1		Marion et al. (2003)
2003W	-7, -6		Marion et al. (2009)
2003cg	37		Marion et al. (2009)
2003du	1, 75	1.056	Marion et al. (2009)
2004E	37		Marion et al. (2009)
2004S	15		Krisciunas et al. (2007)
2004ab	18		Marion et al. (2009)
2004bk	19		Marion et al. (2009)
2004bl	-2		Marion et al. (2009)
2004bv	-5, 53		Marion et al. (2009)
2004bw	-9		Marion et al. (2009)
2004ca	46		Marion et al. (2009)
2004da	4, 14, 18, 24		Marion et al. (2009)
2005am	-4, 0, 7, 14	0.729	Marion et al. (2009)

A sample of the library spectra is plotted in Figure 7.3. Immediately apparent from the plot is the uniformity in the temporal evolution of the spectral features. Even though time series observations are lacking in our sample, the large scale temporal evolution of the spectral features appear to be similar between different SNe Ia.

Early spectra are relatively featureless and appear to have very slow temporal evolutions. The deep absorption trough centered near 0.82 μm is the Ca II triplet feature which was examined in Chapter 6. The feature near 1.05 μm can be attributed to Mg II triplet (Wheeler et al. 1998; Marion et al. 2003). There is also evidence for an emission feature due to Fe III near 1.25 μm (Rudy et al. 2002). The P Cygni-like feature near 1.6 μm is
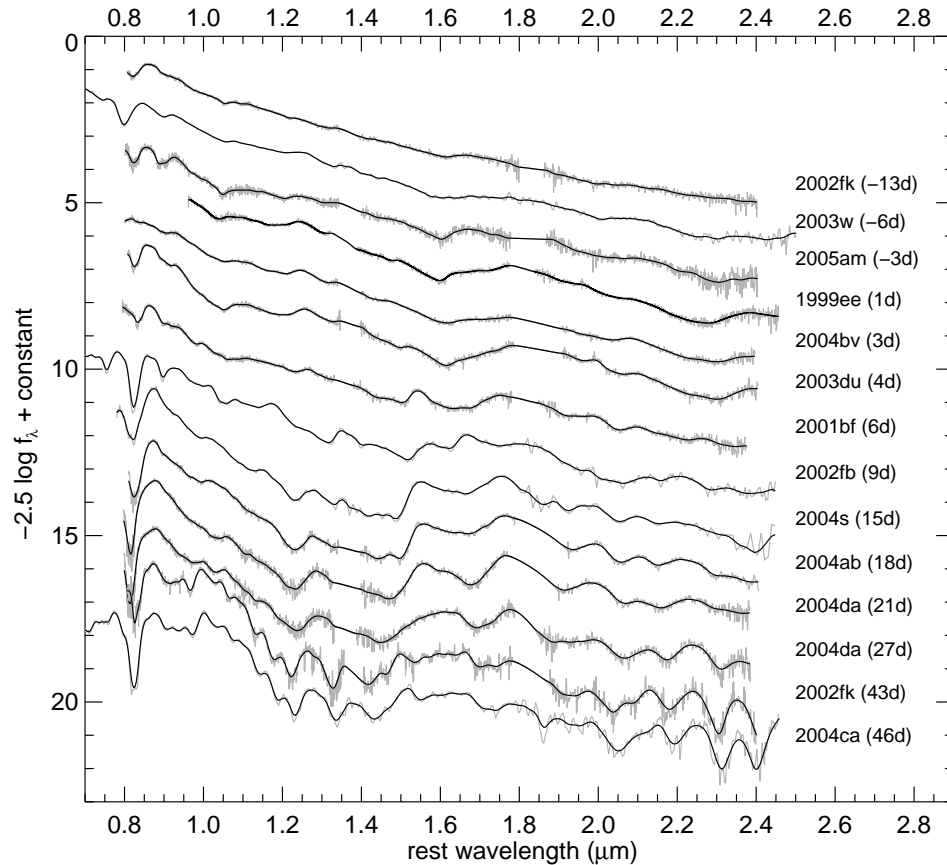
Figure 7.3: A sample of NIR library spectra. The spectra are plotted in log scale with offsets. The library spectra are plotted in gray. The Gaussian smoothed spectra are plotted on top to aid the comparison. The names of the SNe Ia are noted along with the epochs of the spectra with respect to the time of *B*-band maximum.

attributed to a blend of Si II and Mg II lines (Wheeler et al. 1998; Marion et al. 2003). These feature become more apparent with time during the early phases.

At around five days past *B*-band maximum, the NIR spectra rapidly form a wide and prominent feature stretching from 1.50 μm to 1.80 μm. This feature is produced by line blanketing from thousands of Co II, Fe II and Ni II lines (Wheeler et al. 1998; Marion et al. 2003). The result is a pseudo-emission feature with flux about twice as large as the adjoining continuum. After its quick development, this feature stays prominent for weeks. The abrupt development of this feature marks the transition from partial to complete silicon burning in the expanding envelope (Marion et al. 2003).

From approximately two weeks past *B*-band maximum, a group of emission features begin to appear between 2.1 μm and 2.4 μm. The features appear to grow more prominent

with time and can be attributed to Fe II, Si II, Co II and Ni II.

7.4 Temporal evolution of spectral features

Here, the temporal evolution of the NIR spectral features is examined using PCA. PCA is a statistical tool which searches for patterns in a multidimensional data set, and in effect, reduces the dimensionality of the data set. PCA is performed on the narrowband measurements of library spectra, using the methods described in Section 6.2 and Section 4.8. The analysis is done over a wide bandwidth, which spans from 1.0 μm to 2.3 μm and covers rest-frame filters Y, J, H and K. It consists of 39 library spectra which have the specified wavelength coverage and 28 narrowband spectral feature measurements. The resulting projections of the library spectra on each principal component (PC) are plotted in Figure 7.4.

A detailed comparison between the temporal evolutions of fainter and brighter objects, like ones done in the optical bands (Section 6.6) is difficult. First, the number of spectra is relatively small compared to the optical sample. Furthermore, half of the library SNe Ia do not have complementary light curves available to yield the stretch parameters. When the spectra with complementary stretch information are used to exam to temporal evolution, it is not clear whether stretch correcting the timescale reduces or increases the scatter. Therefore, the epochs specified here are all rest epochs, corrected for time dilation only.

The projections of our library spectra on the first 3 PCs, which account for over 70% of the spectral variance, show remarkable uniformity in their temporal evolution. The time line has been divided into four evolutionary stages based on the following observations.

The early spectra, before around three days past B-band maximum, are remarkably uniform for all PCs. This section of the time line includes the NIR primary maximum which occurs a few days before B-band maximum. The third PC picks up the temporal evolution for this stage and quantifies the magnitude of evolution to be relatively small compared to the other evolutionary stages. This reflects the slight strengthening of the broad features in the early and largely featureless library spectra.

The second evolutionary stage is dominated by the rapid development of the most prominent spectral feature in the NIR, the pseudo-emission feature in the H band produced by line blanketing from Fe II, Co II and Ni II lines. The feature is shown in the second PC to reach its peak strength at approximately two weeks past B-band maximum. This evolutionary stage also shows the largest dispersion, suggesting that the temporal evolution of the prominent H-band feature is less uniform.

The third evolutionary stage reflects a slight weakening of the prominent H-band fea-
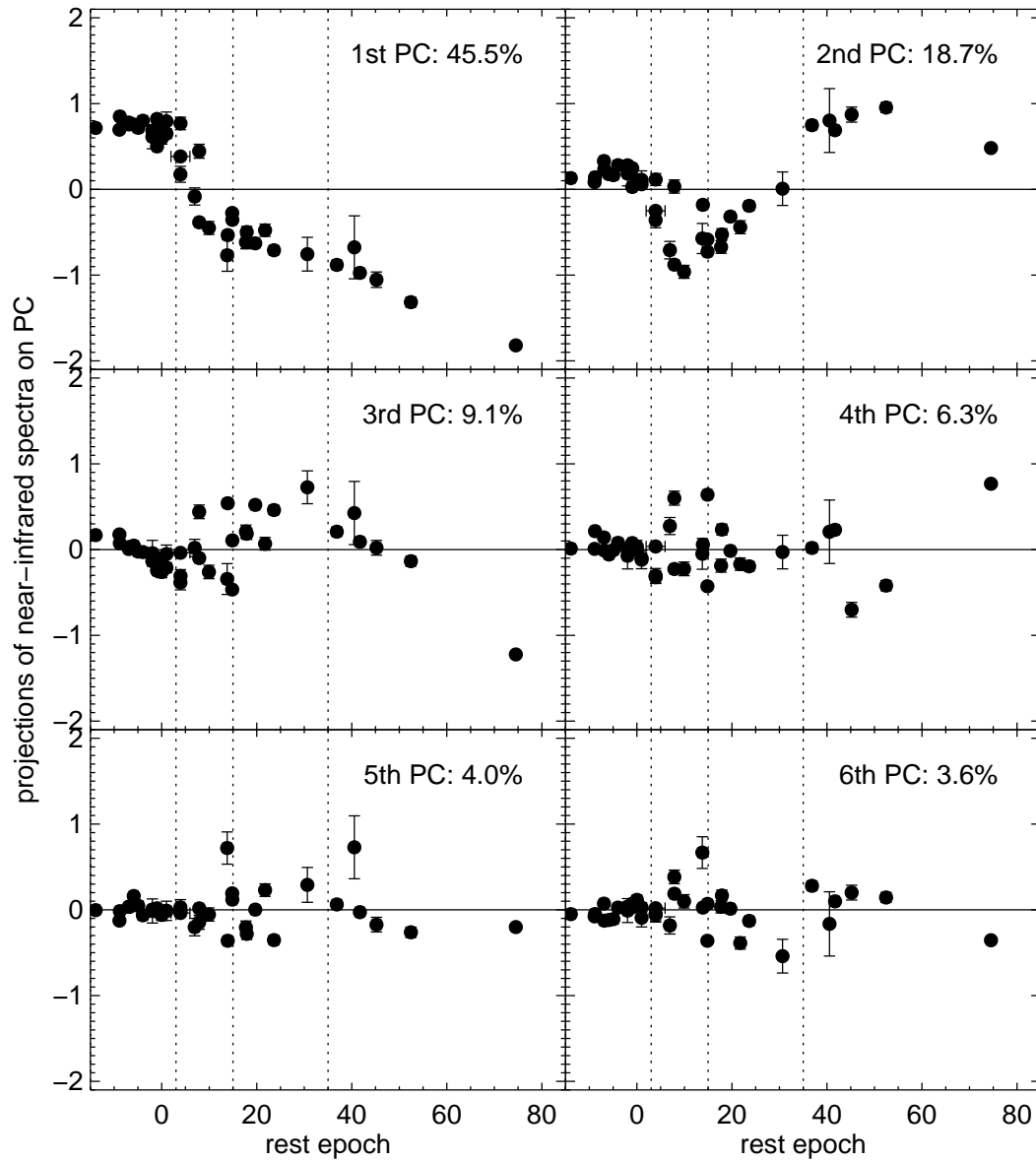
Figure 7.4: The temporal evolution of the projections of NIR spectral features on the PCs. The fractional variance for each PC is noted. The epochs are corrected for time dilation and are with respect to *B*-band maximum. The vertical dotted lines specify the epoch divisions.
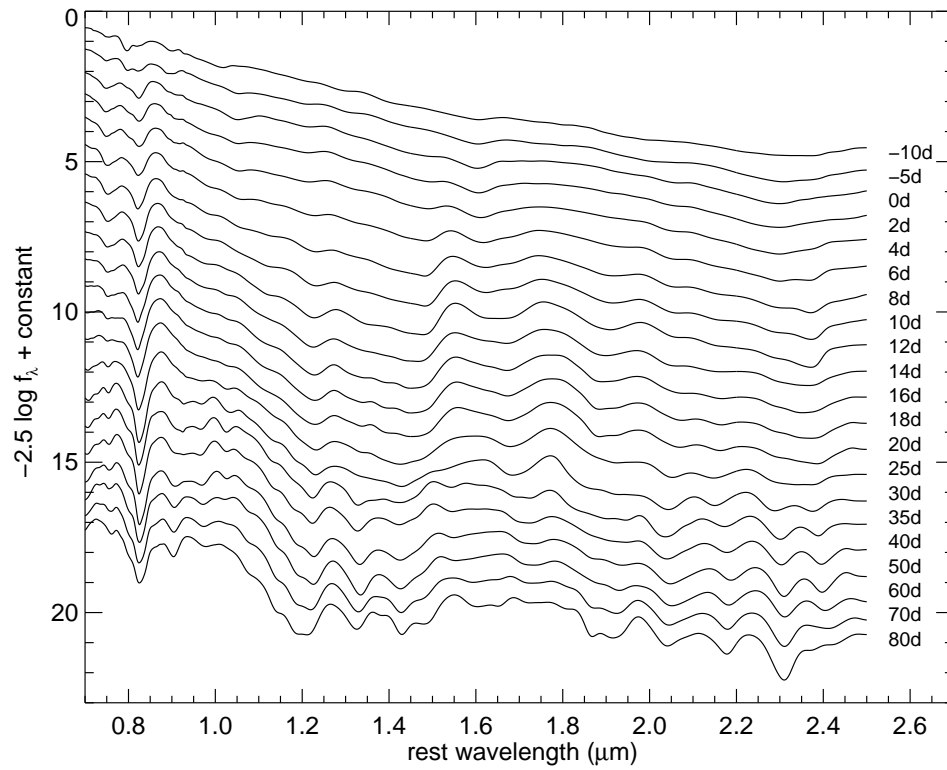
Figure 7.5: The NIR spectral template time series. The template spectra are plotted in log scale with offsets. The epoch with respect to *B*-band maximum for each spectrum is also noted.

ture, while the fourth stage exhibits the strengthening of the emission features in the *K* band, attributed to Fe II, Si II, Co II and Ni II. From the small number of spectra in these epochs, the temporal evolution appears to be uniform, with smaller dispersion than observed in the second stage.

7.5 Spectral template time series

In this section, a mean NIR spectral template time series, built from the 52 NIR library spectra listed in Table 7.1, is presented. The spectral templates are built using the methods presented by Hsiao et al. (2007a), and in Chapter 4. The library spectra are first color corrected to the template color curves presented in Section 7.2. The spectral features of each spectrum are then quantified using artificial narrowband filters. The narrowband measurements are then placed in epoch bins and averaged with appropriate weights. The resulting

spectral template is presented in Figure 7.5.

Even though the number of NIR spectra is quite small compared to that of optical spectra, the 52 library spectra provide excellent temporal coverage. The majority of the spectra are taken around maximum light and during the development phases of the prominent H-band feature. This provides good descriptions of the temporal evolution of the spectral features during these epochs. At later epochs, even though the epoch bins are wider, the construction of the templates often has to relies on one or two spectra per epoch bin. There is clearly room for improvement at these phases.

The spectral template time series in Figure 7.5 nicely resembles the library spectra in Figure 7.3. For a more detailed comparison, we separate the library spectra into the four evolutionary stages described in Section 7.4 and compare them with spectral templates at corresponding epochs. They are presented in Figure 7.6.

The first stage includes the largest number of spectra, but shows the least amount of dispersion. This illustrates both the remarkable uniformity in the evolution of the spectral features and the relative slow evolution at this stage. The second stage is dominated by the abrupt formation of the prominent H-band feature. The strengthening of this feature is most striking on the blue edge of the feature. The spectral templates are shown in Figure 7.6 to track this evolution closely. For the third and fourth evolutionary stages, because the construction of the spectral templates rely on only one or two spectra per epoch bin, the spectral templates are expected to be very similar to the library spectra.

At the second evolutionary stage, there is also a curious feature near 1.66 μm at which the library spectra show diversity. This spectral feature falls right in the center of the prominent H-band feature. Because this feature from our low-redshift sample falls well within the H band, the contamination from telluric features should be negligible, suggesting that the diversity originates from differences in the SNe Ia. The feature does not follow the temporal evolution of the spectral templates. The diversity of this feature therefore does not appear to be driven by temporal evolution. The spectral feature will be examined in detail in Section 7.8.

There is also evidence of diversity in the spectral features around the blue and red edges of K band. Since these features are either close to the telluric absorption features or close to the edges of the observed spectra, they are not examined here.
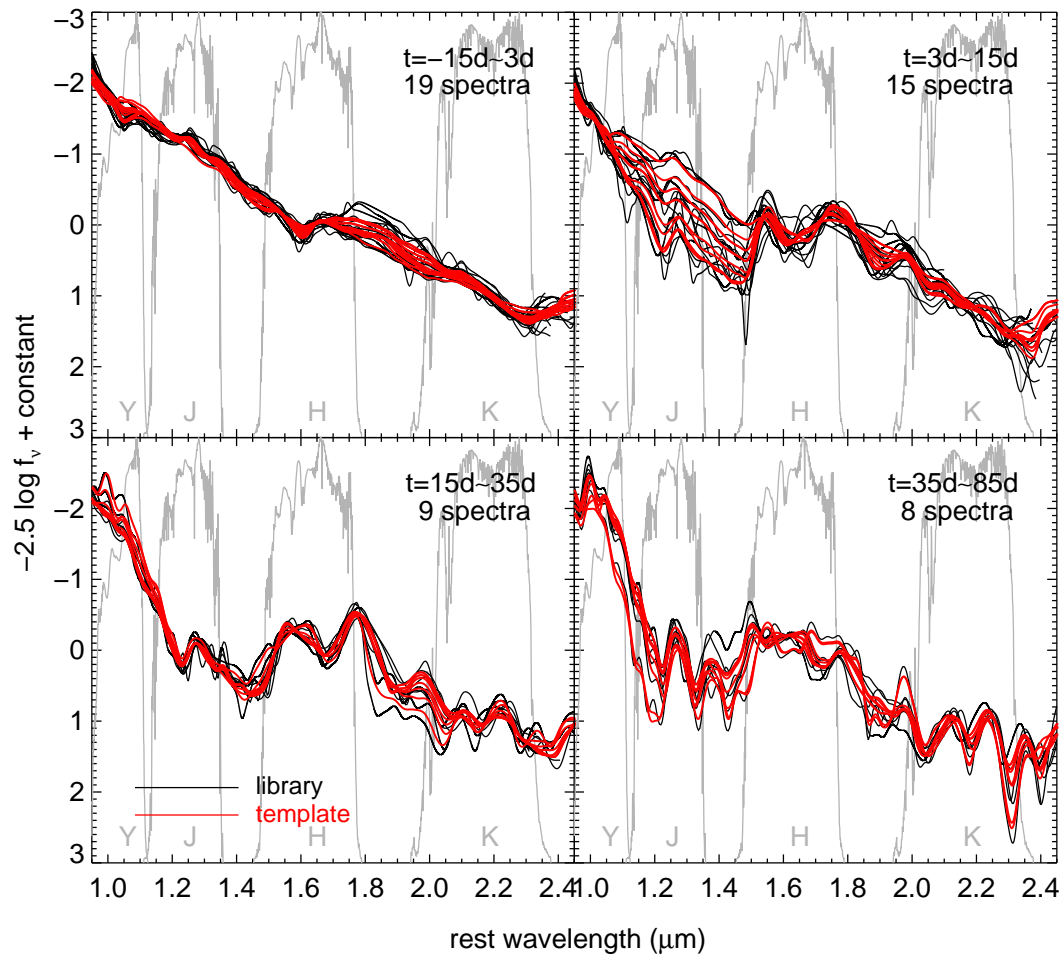
Figure 7.6: The comparison between NIR library spectra and the spectral template time series. The library spectra (black curves) are divided into four evolutionary stages described in Section 7.4 and compared with spectral templates (red curves) of corresponding epochs. The epoch range and the number of library spectra included are also noted for each evolutionary stage.

7.6   *K*-correction

The primary motivation for building a set of mean spectral templates is for *K*-correction calculations. Even though *K*-corrections for nearby objects are small, there is the risk of incurring significant systematic errors by calculating *K*-corrections using individual spectra.

To illustrate this effect, the *K*-corrections calculated using the mean spectral templates are compared to those calculated using individual library spectra. A typical redshift of 0.02 for a nearby SN Ia is adopted for this analysis. As described in the *K*-correction calculation procedures presented by Nugent et al. (2002), we make broadband color corrections such that the colors of the spectral template match those of the SN Ia. In practice, these color corrections are done on the spectral templates such that the colors of the templates match the observed colors of the SN Ia. Here, library spectra are color corrected to match the template color curves, such that the *K*-corrections can be presented in a single plot. As shown in Section 7.2, NIR colors exhibit small dispersions. This color correction step should have minimal effects on the determination of *K*-correction.

The resulting *K*-corrections and the differences from the *K*-corrections of the spectral template are plotted in Figure 7.7. Previous studies often derived *K*-corrections from a single SN Ia. The *K*-correction values published by (Krisciunas et al. 2004b), determined using time series spectra of SN 1999ee, are also plotted for comparison.

First thing to notice from Figure 7.7 is the remarkably small *K*-correction errors around the NIR primary maximum. This corresponds to the first evolutionary stage described in Section 7.4, where the temporal evolution of the NIR spectral features is slow and uniform. Larger *K*-correction errors begin to occur past *B*-band maximum, where the use of a representative spectral template becomes important.

From Figure 7.7, our NIR spectral templates yield essentially the mean of the *K*-corrections at each epoch. The systematic errors from assuming a set of spectral templates are therefore largely diminished. On the other hand, the use of individual spectra for the determination of *K*-corrections is shown to cause, in some cases, significant systematic errors. The *K*-correction values published by (Krisciunas et al. 2004b) exhibit especially large differences from the mean spectral templates past *B*-band maximum light. The dispersions may have contributions from both the differences in the broadband colors and truly unrepresentative spectral features.

The dependence of *K*-correction errors on redshift is also examined. The *K*-correction errors are taken as the difference in *K*-corrections between the spectral templates and the
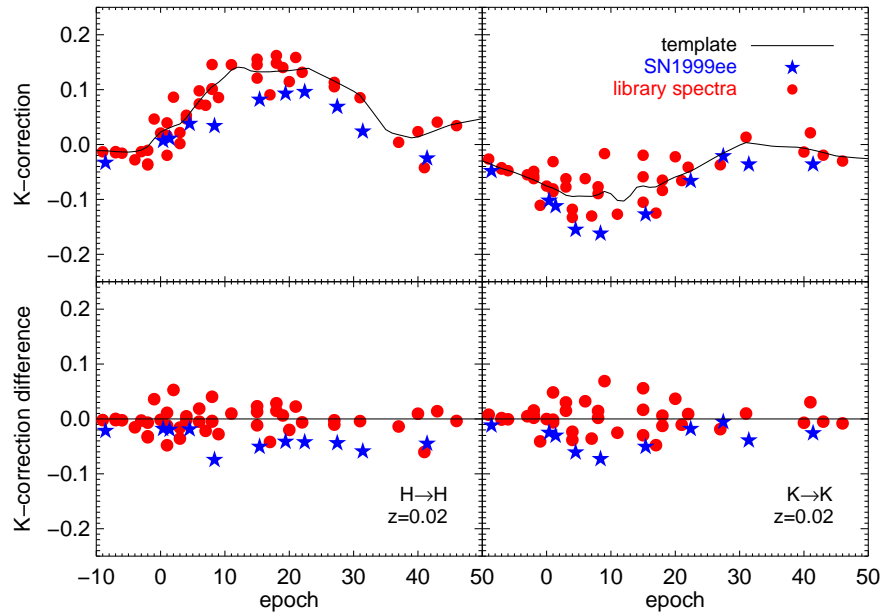
Figure 7.7: The comparison of *K*-corrections calculated using our mean NIR spectral templates and library spectra. They are calculated assuming a redshift of 0.02. The epochs are rest epochs with respect to *B*-band maximum. The upper panels show the *K*-corrections, and the lower panels show the *K*-correction differences from those of the spectral templates. The left and right panels show *K*-corrections for the *H* and *K* band, respectively. The *K*-corrections of the spectral templates and library spectra are plotted as black curves and red dots, respectively. The *K*-correction values published by (Krisciunas et al. 2004b) are plotted as blue stars for comparison.
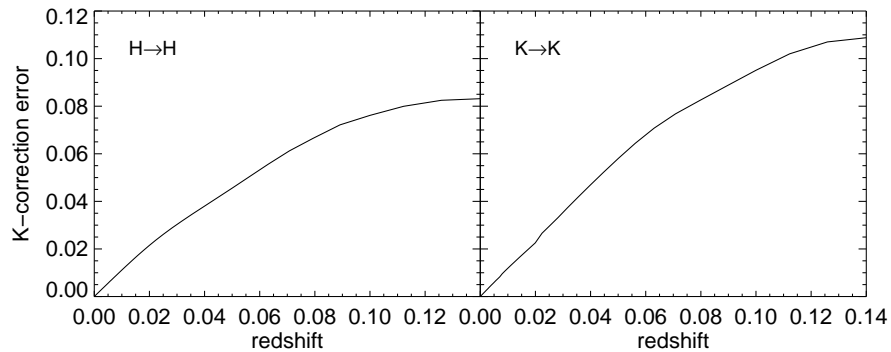
Figure 7.8: The dependence of *K*-correction errors on redshift. The left and right panels show the errors in the *H* and *K* bands, respectively.

library spectra. They are then summed in quadrature. The results are plotted in Figure 7.8 for a large redshift range. The typical redshifts for nearby studies are between 0.01 and 0.03. In this redshift range, the *K*-correction errors scale roughly linearly with redshift and coincidentally have similar values as the redshifts. These error estimates include all epochs. The errors around the NIR primary maximum are expected to be much smaller.

7.7   Spectroscopic sequence around NIR primary peaks

Krisciunas et al. (2004a) tested the efficacy of using the NIR primary maximum of SNe Ia as a distance indicator. In the range between -12 and 10 days with respect to *B*-band maximum, the light curve shapes in the *J*, *H* and *K* bands can be standardized by stretch correcting the time axis using stretch parameters derived from *B*-band light curves. The resulting NIR peak absolute magnitudes were shown to have indeed small dispersions and have little or no correlation with the light-curve widths.

In the optical bands, the peak absolute magnitudes vary systematically with the light-curve widths. In Chapter 6, the optical spectroscopic features at peak brightness are also shown to vary systematically with light-curve widths, matching the photometric behavior. Here, we examine whether the same parallels can be drawn between photometric and spectroscopic properties in the NIR.

The first evolutionary stage, described in Section 7.4, covers epochs ranging from -15 to 3 days past *B*-band maximum and includes the primary NIR maximum. The spectral features in this epoch range exhibit very small dispersion and relatively slow temporal evolution (Figure 7.4). We will attempt to search for any correlations between spectral features and light-curve widths within the small diversity shown in these early spectra.

The analysis is divided into four wavelength regions. The regions correspond to the NIR bands *Y*, *J*, *H* and *K*. The NIR filters are strategically placed between the prominent telluric features. Having the wavelength regions similar to the wavelengths covered by the NIR filter bands prevents the telluric features from entering the signals intrinsic to the SNe Ia. Each wavelength region covers six narrowband measurements of spectral features. All the library spectra with stretch values available are included in the analysis. The information for each wavelength region is listed in Table 7.2.

Because of the small number of spectra available, analysis at a single epoch, as done in the optical band, is not possible. The sample size of time series spectroscopic data in the NIR is also small. We therefore do not attempt to correct the projections of the library spectra on the PCs to a single epoch. Because of the wide epoch range considered and the

Table 7.2: Wavelength regions for the NIR PCA

Band	Lower wavelength	Upper wavelength	Number of measurements	Number of spectra	Sequence variance
Y	0.937 μm	1.122 μm	6	8	43.5%
J	1.122 μm	1.343 μm	6	9	11.8%
H	1.426 μm	1.708 μm	6	9	17.8%
K	1.925 μm	2.305 μm	6	9	31.0%

mild temporal evolution observed in Figure 7.4, it is important to identify which PCs are detecting spectral variations instigated by temporal evolution. The projections on the six PCs are plotted against rest epoch in Figure 7.9, Figure 7.10, Figure 7.11 and Figure 7.12 for the *Y*, *J*, *H* and *K* wavelength regions, respectively.

In the *Y* band, there is no clear sign of temporal evolution within this epoch range for the first PC. A mild trend in the projections on the second PC may indicate some temporal variation with large scatter. The projections on the first PC in the *J*, *H* and *K* bands all exhibit trends which suggest that the variations are driven by temporal evolution. The projections on the second PC in these three bands appear to have no correlation with epoch.

The projections are then plotted against stretch to search for any spectroscopic sequence in the NIR. The results are presented in Figure 7.13, Figure 7.14, Figure 7.15 and Figure 7.16, for the *Y*, *J*, *H* and *K* wavelength regions, respectively. Focus is placed on the PCs which do not appear to be detecting temporal evolution and constitute significant fractions of the overall variation.

In the *Y* band, the projections on the first PC exhibit little sign of a correlation with epoch (Figure 7.9), but a trend against stretch (Figure 7.13). The projections on the second PC exhibit a hint of a trend against epoch, but no correlation with stretch. Similar behaviors are observed for the *J*, *H* and *K* bands. For these three bands, the variations driven by temporal evolution in the epoch range considered is larger than those driven by stretch. For all four of the NIR bands and for the epoch range considered, epoch and stretch appear to be the two most dominant drivers of the spectral variation. PCA is able to separate the contributions from these two factors into the two orthogonal vectors.

Weak correlations with stretch are observed for all four NIR bands in PCs which show little time dependence. For these cases, polynomial fits are done to derive one-to-one and continuous relations between projections and stretch. The relations then yield a continuous set of narrowband measurements. The narrowband measurements are converted into
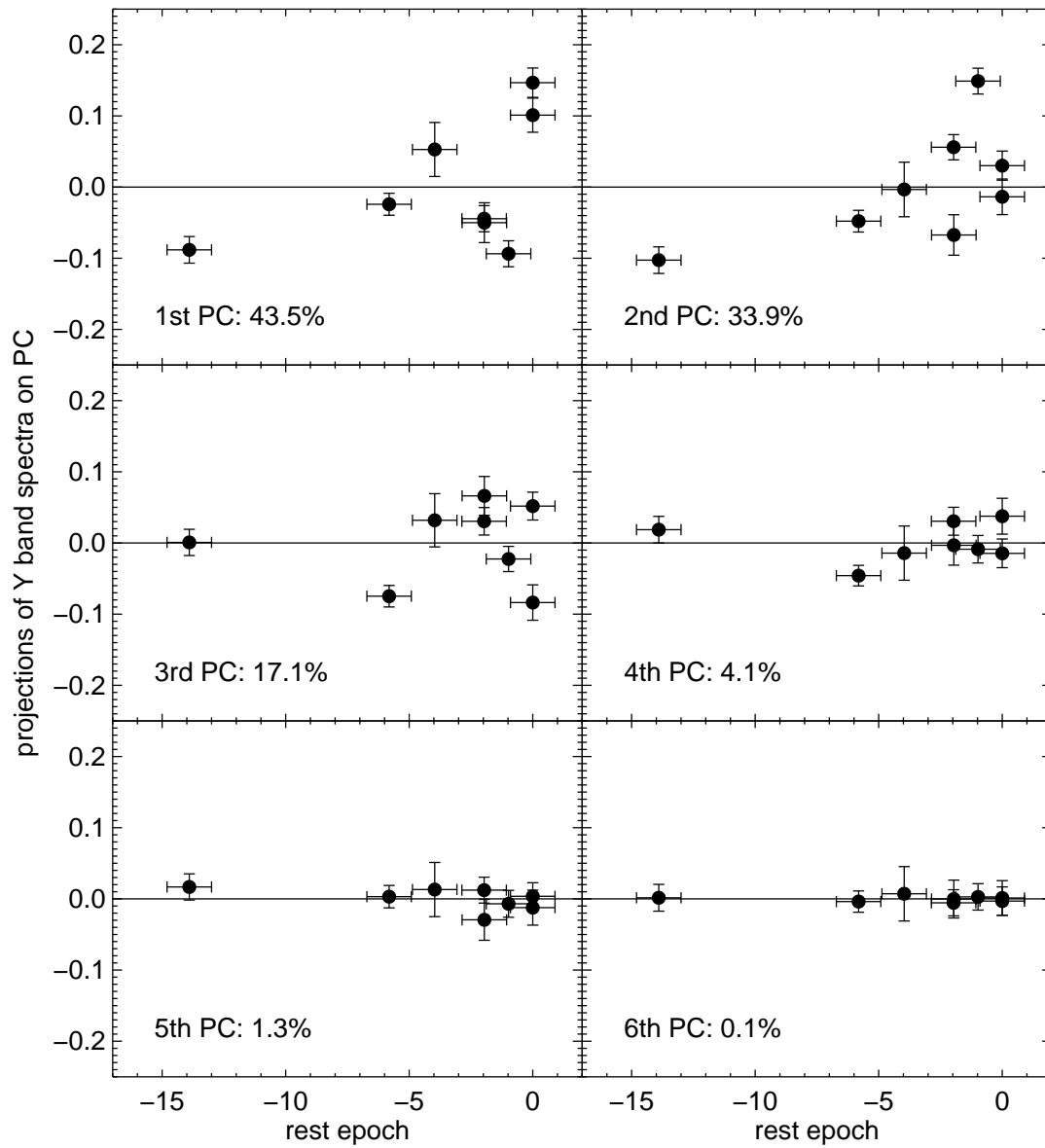
Figure 7.9: The projections of library spectra in the *Y* band on the six PCs with respect to epoch. The fractional variance for each PC is also noted. The epochs are corrected for time dilation and are with respect to *B*-band maximum.
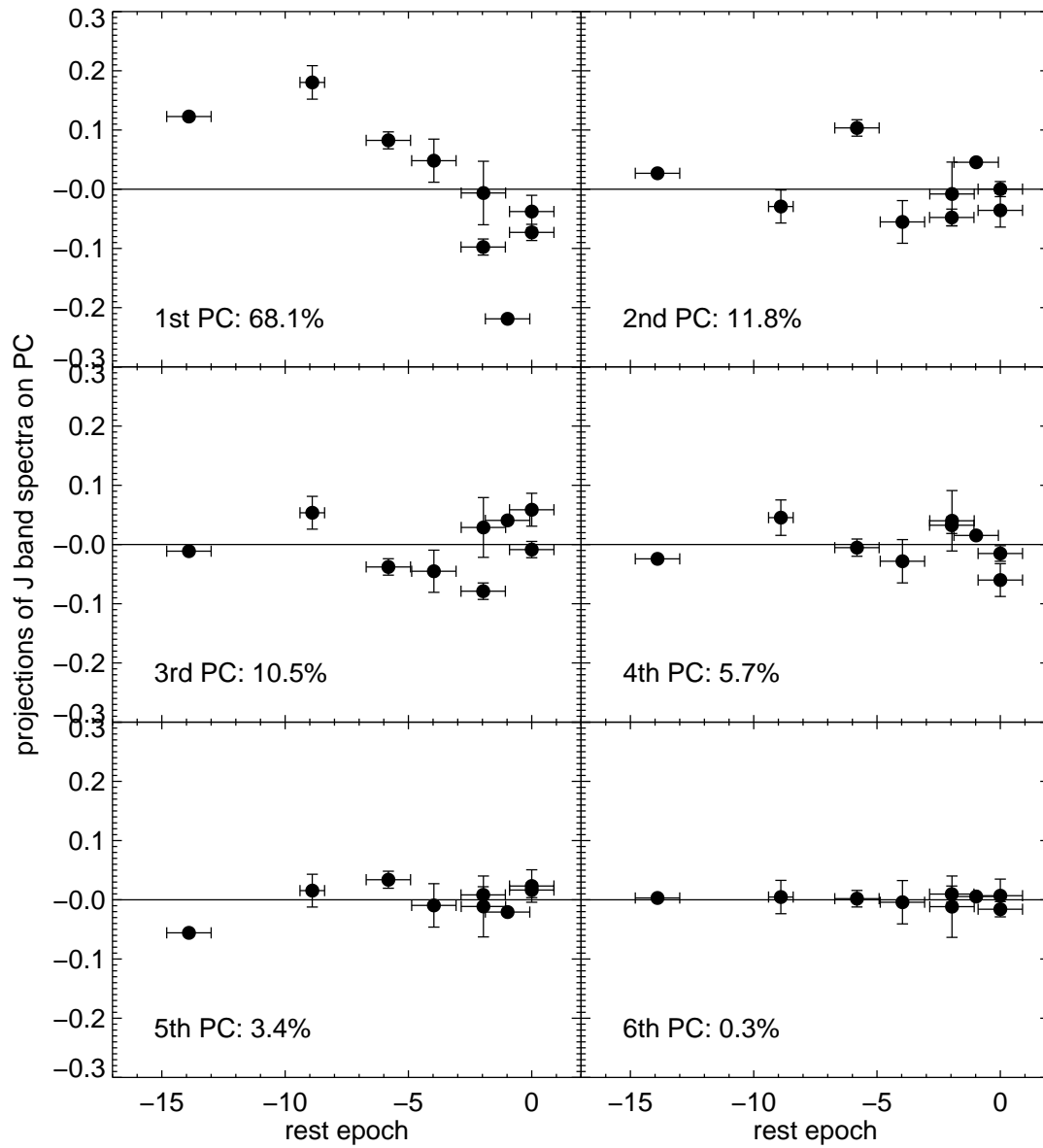
Figure 7.10: Same as Figure 7.9 in the *J* band.
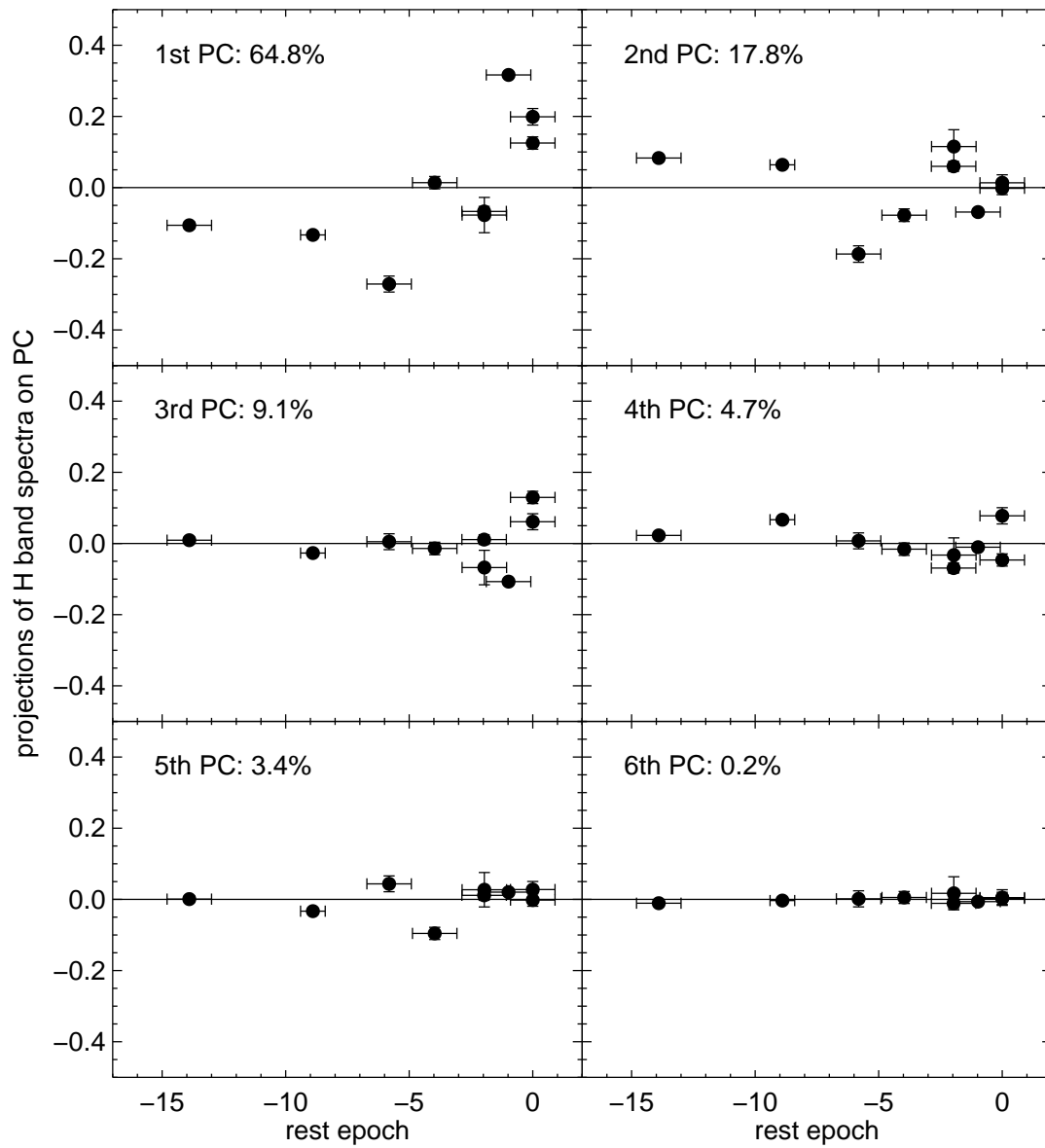
Figure 7.11: Same as Figure 7.9 in the *H* band.
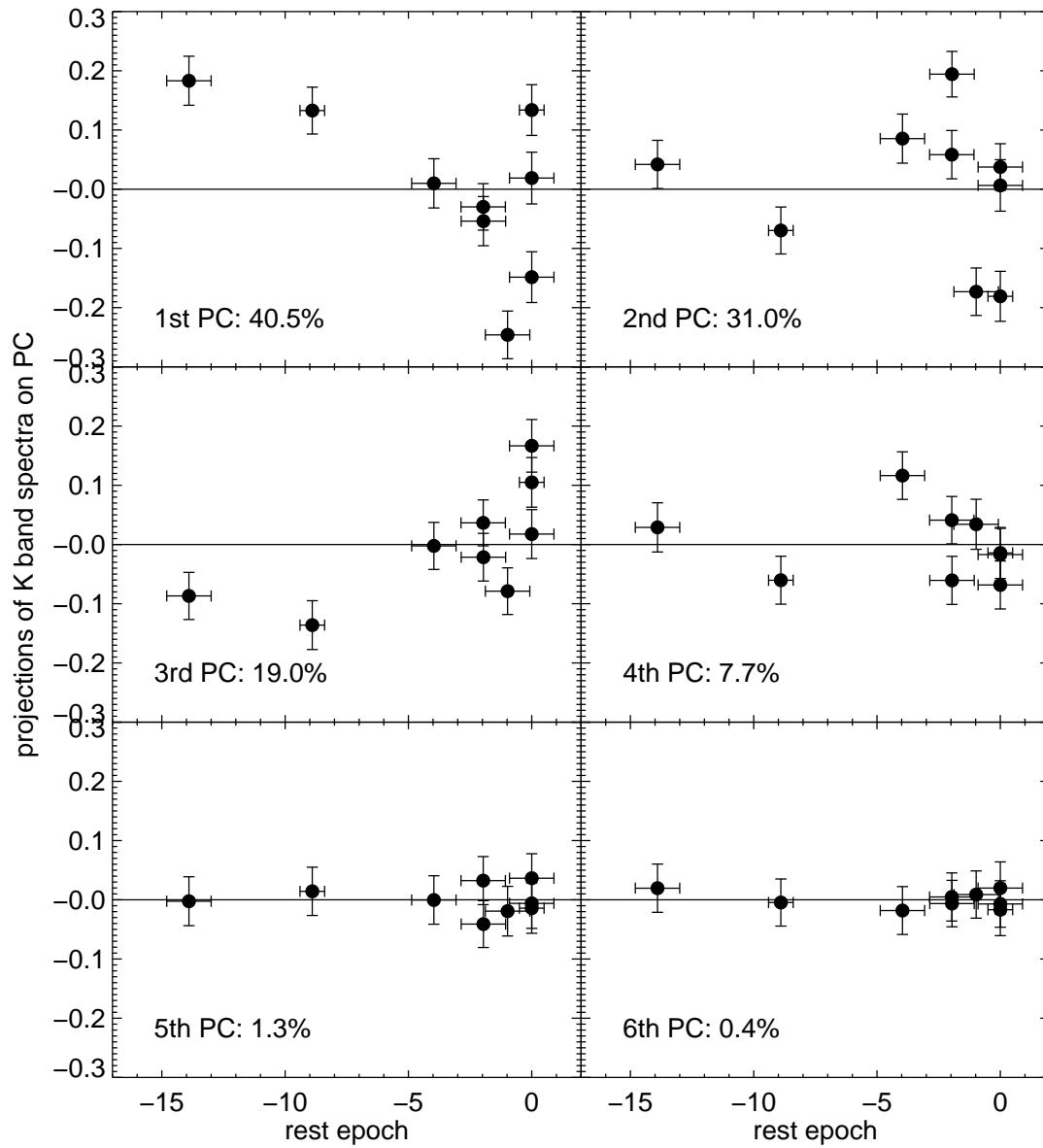
Figure 7.12: Same as Figure 7.9 in the *K* band.
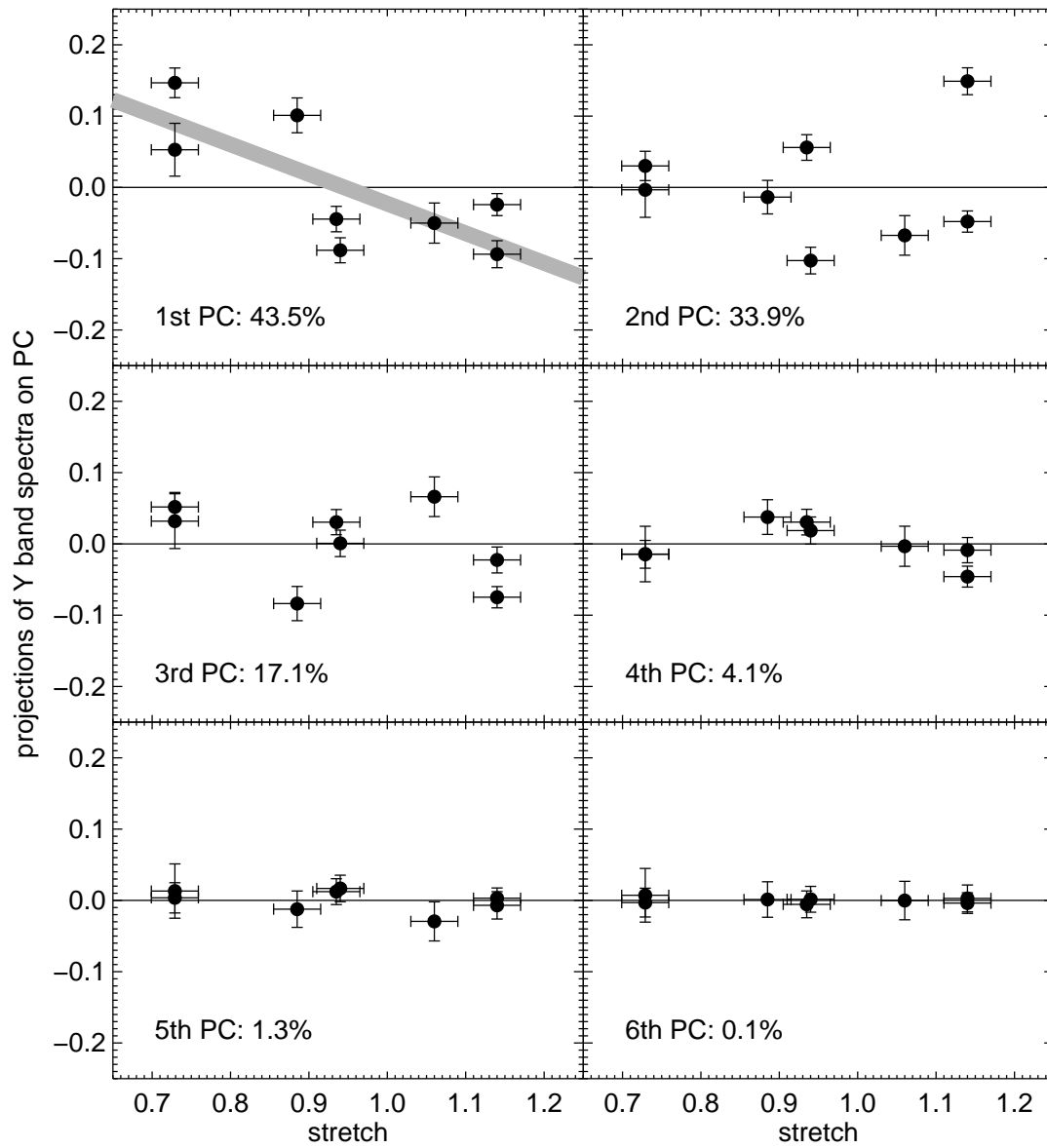
Figure 7.13: The projections of library spectra in the Y band on the six PCs with respect to stretch. The fractional variance for each PC is also noted. For cases where possible spectroscopic sequences are detected, polynomial fits are plotted as gray curves.
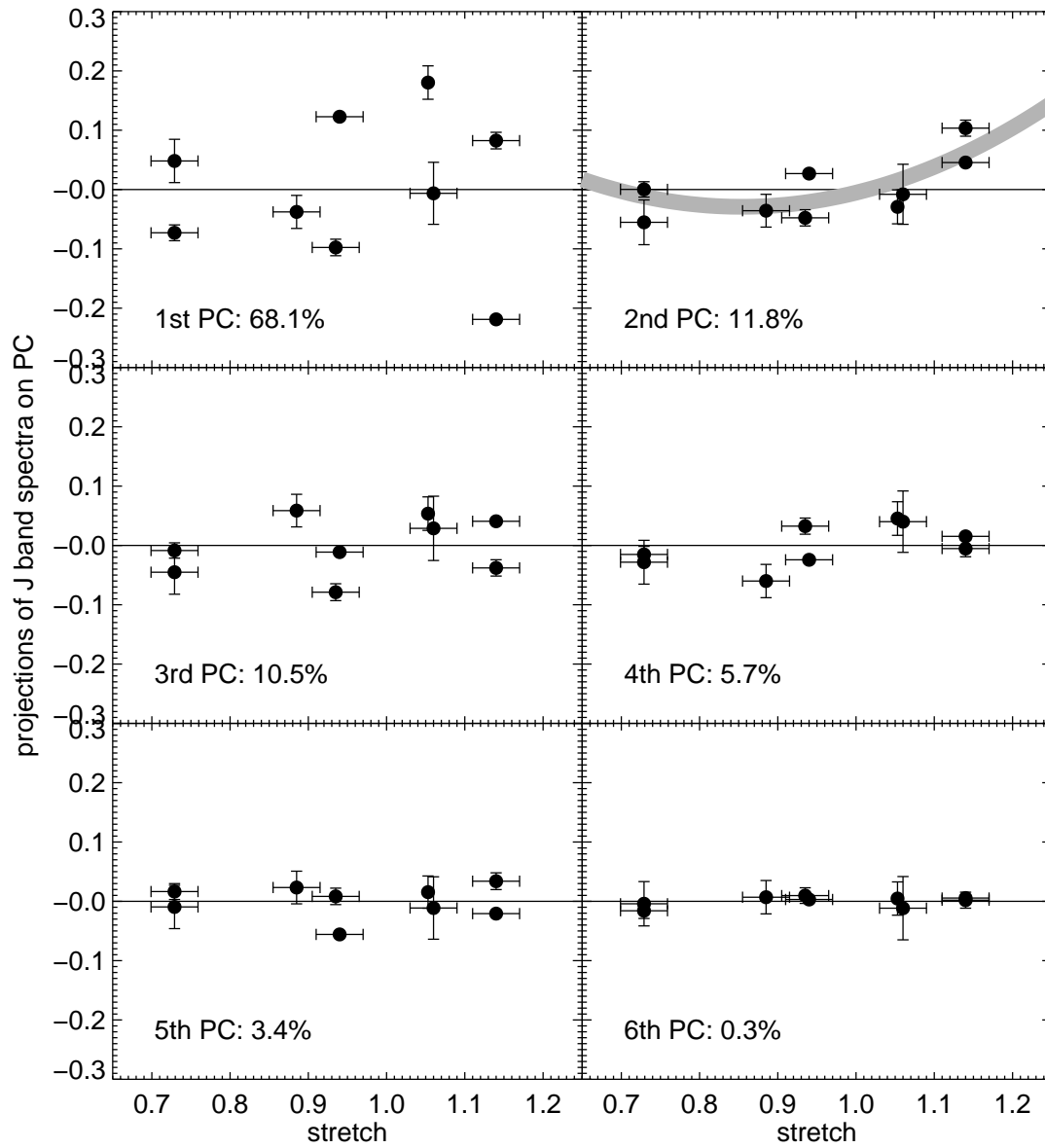
Figure 7.14: Same as Figure 7.13 in the *J* band.
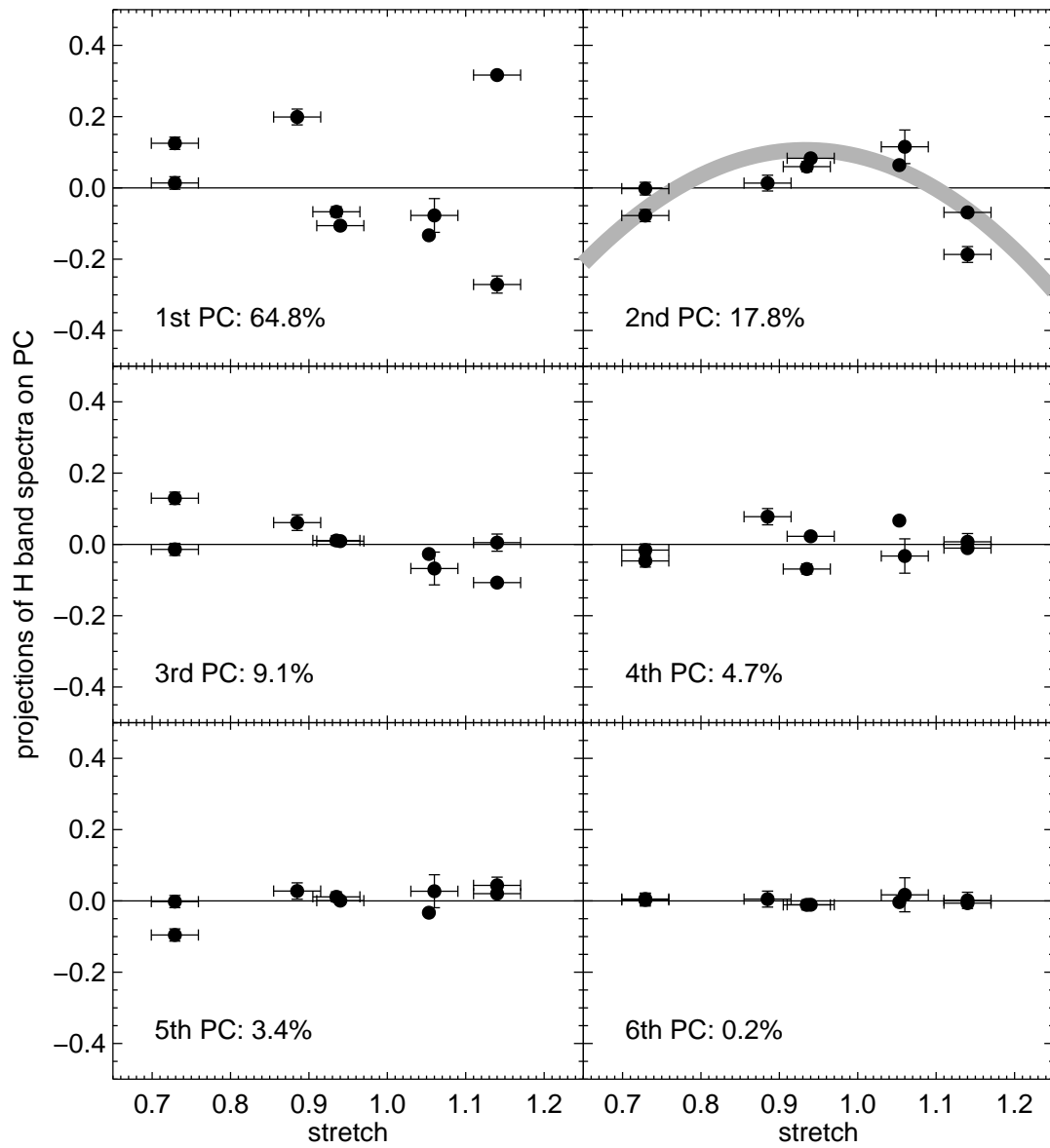
Figure 7.15: Same as Figure 7.13 in the *H* band.
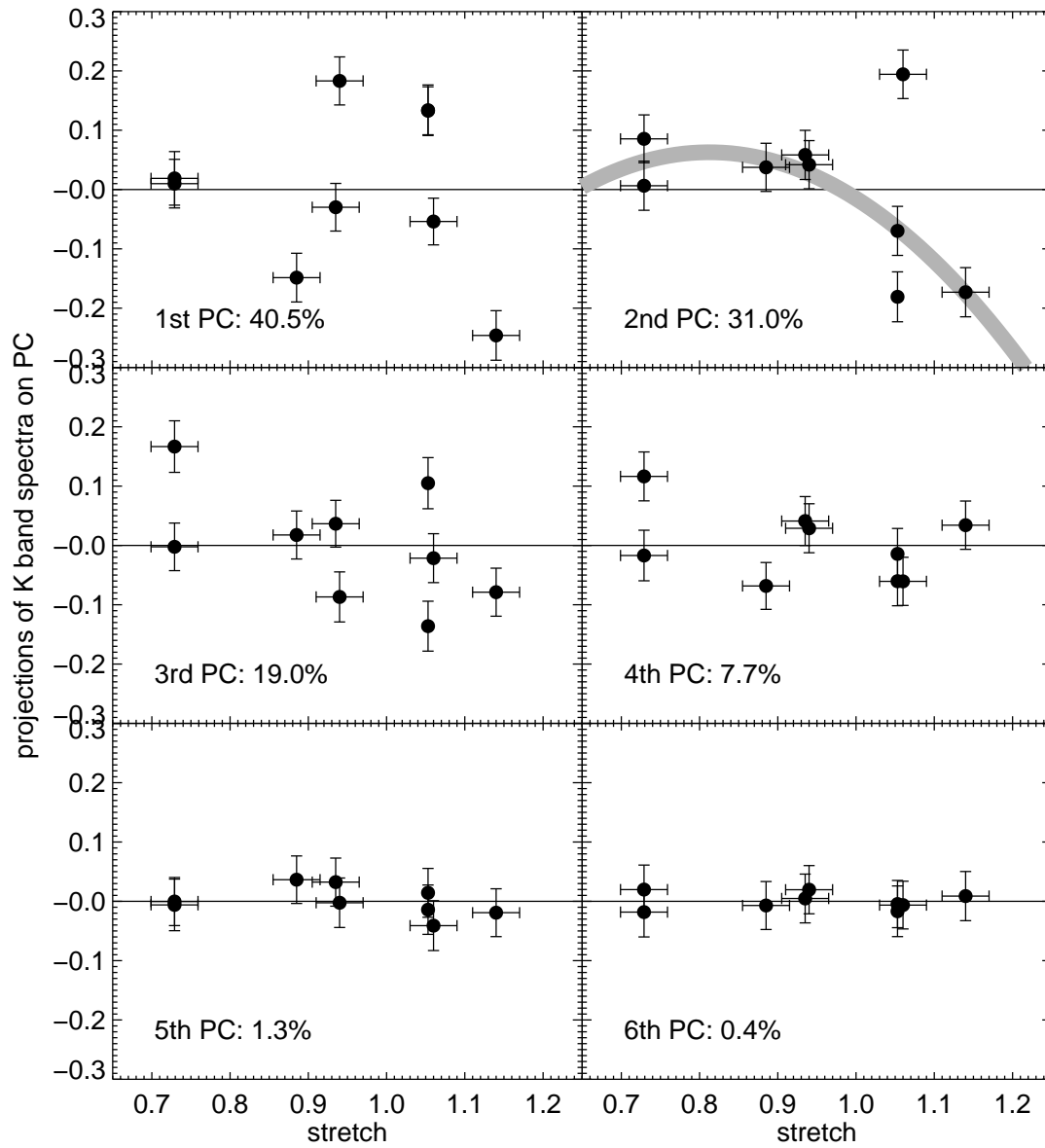
Figure 7.16: Same as Figure 7.13 in the *K* band.

template sequences using the method used to build a mean spectral template described by Hsiao et al. (2007a), and in Section 4.6. The resulting template sequences are plotted in Figure 7.17, Figure 7.18, Figure 7.19 and Figure 7.20, for the Y, J, H and K wavelength regions, respectively.

For each template sequence, the amount of spectral variation accounted for in this epoch range is tabulated in Table 7.2. Note that these values depend on the epoch range. A larger epoch interval can include more spectra, but stretch would have diminishing influence.

The template sequence in the Y band shows a slight deepening of the Mg II feature as stretch decreases. The sequence is detected by the first PC which constitutes over 40% of the observed diversity, but scatter around this relation is large. For both the J and H bands, the template sequences describe slight velocity shifts of the dominant features in the bands. These sequences are described by the second PCs which only constitute $\sim 10 - 20\%$ of the overall variation. For these two bands, time is the main driver and is responsible for the strengthening of the features (first PCs). For the specified epoch range, the time-dependent variation accounts for over 60% of the diversity in the data set. The K-band region is probing the ends of the spectra, and can include larger uncertainties as a result. More data points are needed in Figure 7.16 to see if they form scatter plots. Because the spectra in this epoch range are already quite uniform, the variations described by these spectroscopic sequences are indeed very small. We caution that these relations are formed by a small number of data points. More NIR spectra with complementary light curves are required to confirm or refute these correlations.

7.8 Spectroscopic sequence in the prominent H-band feature

At the second evolutionary stage described in Section 7.4, NIR spectra of SNe Ia are dominated by the prominent H-band feature caused by Fe II/Co II/Ni II line blanketing. In Section 7.5, we noted a spectral feature which lies at the center of this feature (~ 1.66 μm) and displays significant diversity among our sample of SNe Ia. For some spectra, it appears to be an emission-like feature, while absorption-like features are observed in others at the same wavelengths. The variation cannot be described by the temporal evolution of the mean spectral templates. We examine whether the diversity forms a spectroscopic sequence.

PCA is performed on spectra within the epoch range between 3 to 15 days past B-band
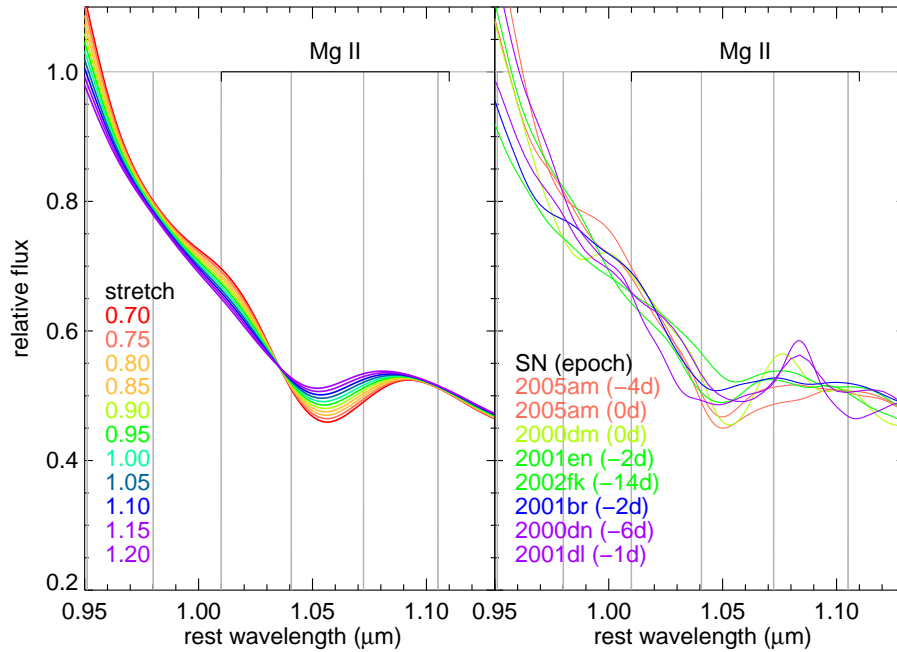
Figure 7.17: The template sequence in the *Y* band from the first PC for the epoch range between -15 and 3 days past *B*-band maximum. The left panel shows the template sequence, and the right panel shows the Gaussian smoothed library spectra. Each spectrum is color coded by stretch. The names and the epochs of the library spectra are noted. The narrowband filters used to quantify the features are plotted as gray lines. The dominant species responsible for each spectral feature in the region is also noted.

maximum, as assigned for the second evolutionary stage. Five narrowband measurements are used covering the region of the entire *H*-band structure. The projections of the library spectra on the resulting PCs are again plotted against both epoch and stretch to separate the two effects. The projections with respect to epoch and stretch are plotted in Figure 7.21 and Figure 7.22, respectively.

The prominent *H*-band feature has been shown to strengthen rapidly during the epoch range considered. The first PC detects the strengthening of this structure, but shows large scatter in its temporal evolution (Figure 7.21). This is again the large scatter shown in the second evolutionary stage in Figure 7.4, suggesting that the time evolution of this feature can be quite different between SNe Ia. Because of the abrupt nature of the evolution, the uncertainties in the epoch determinations may also play a role.

The second PC also shows little time dependence, but shows a significant trend with stretch. A linear fit is performed through this apparent spectroscopic sequence. The tem-
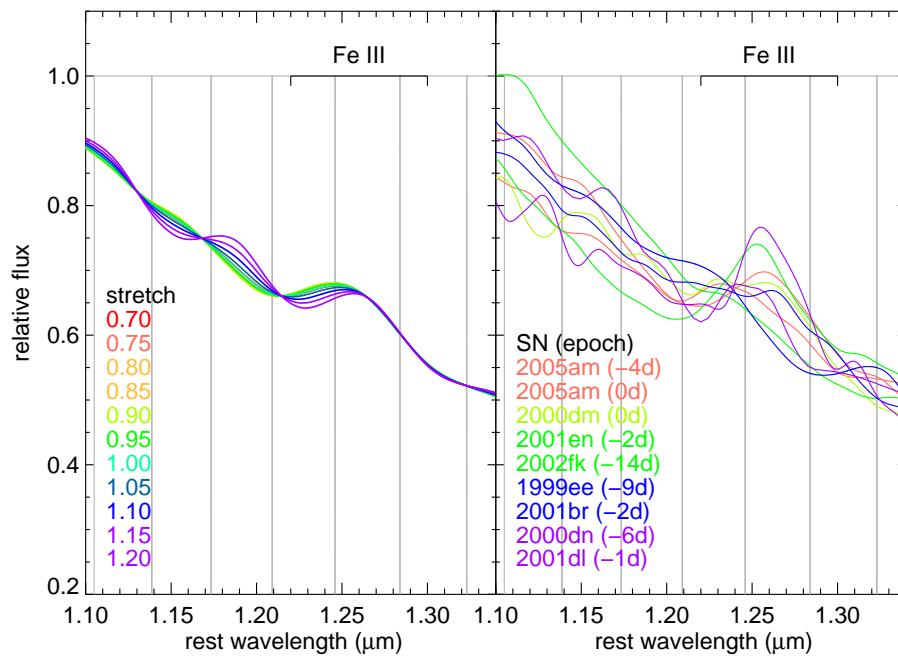
Figure 7.18: Same as Figure 7.17 in the *J* band from the second PC.
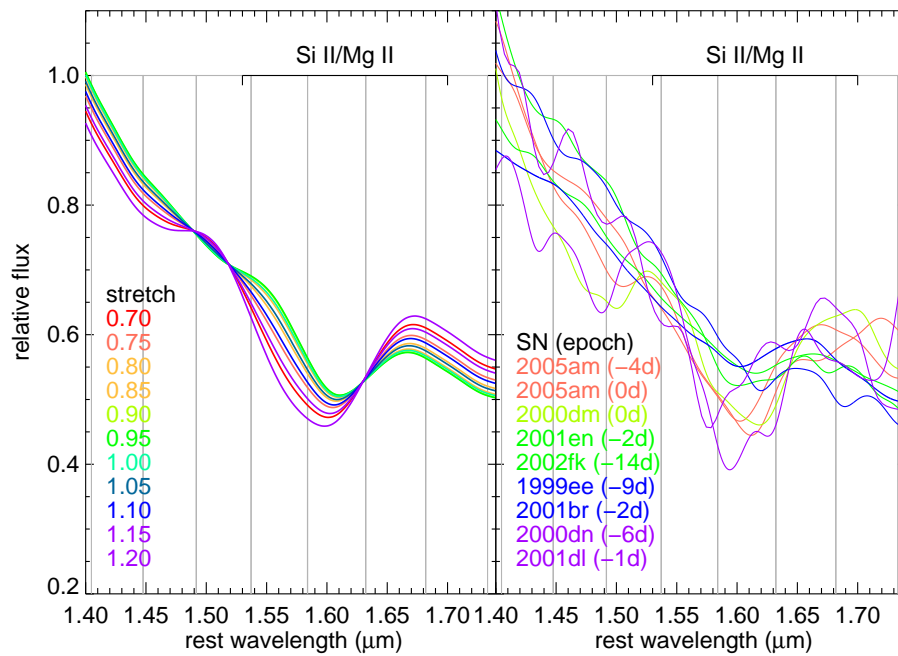
Figure 7.19: Same as Figure 7.17 in the *H* band from the second PC.
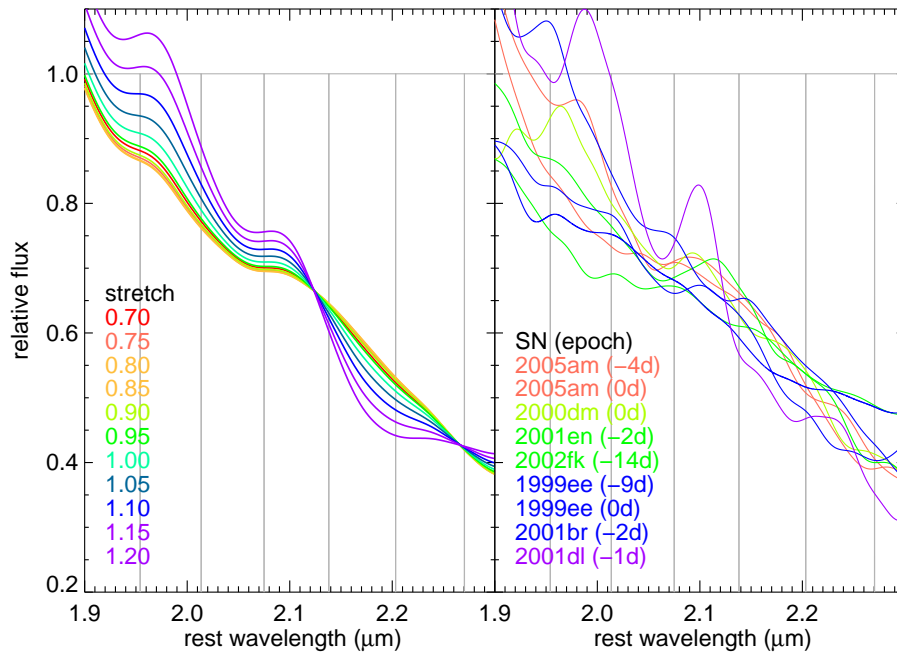
Figure 7.20: Same as Figure 7.17 in the *K* band from the second PC.

plate sequence from the linear fit is presented in Figure 7.23. The second PC indeed picks up the diversity of the spectral feature at 1.66 *μm*. The sequence associates the emission-like shapes to low-stretch objects and the absorption-like shapes to high-stretch objects. The emission-like features are found in two low-stretch objects, SN 2000dk and SN 2005am. Both SNe Ia have stretch values below 0.8, and the spectra are taken at $6 - 7$ days past *B*-band maximum.

By visual inspection, this emission-like feature is also observed in the spectrum of SN 2002fb at eight days past *B*-band maximum. If this spectral feature is exclusively associated with low-stretch objects, as suggested by our limited data set, SN 2002fb should also be a low-stretch object. There is no complementary photometry available for this SN Ia to derive a stretch parameter. The host galaxy, NGC 759, of SN 2002fb is classified as an elliptical galaxy by van den Bergh et al. (2003). The spectroscopic identification done by the CfA Supernova Group classified the optical spectrum as 1991bg-like (Matheson et al. 2002). These two pieces of information are consistent with our inference that SN 2002fb is a subluminous, low-stretch object. From the linear relation between the spectral features and stretch dictated by the second PC, a stretch value of $s = 0.60$ is deduced for SN 2002fb. This value is consistent with the stretch values of subluminous objects, such as SN 1991bg ($s = 0.54$) and SN 1999by ($s = 0.61$).

The emission-like features at 1.66 μm, associated with low-stretch objects, are all observed in a narrow epoch range, $6 - 8$ days past B-band maximum. It is uncertain from our data whether this characteristic only exists during this narrow range or persists through later epochs.

Höflich et al. (2002) noted a similar feature in their subluminous model. The emission feature originates from the innermost Ni-rich region. Their synthetic spectrum at six days past V-band maximum does not show a clear emission-like feature, but shows the lack of a local minimum, common in most other spectra and also in models of normal luminosity SNe Ia (e.g., Wheeler et al. 1998). This lends support to our observation that the emission-like feature at 1.66 μm is associated exclusively with low-stretch objects. However, Höflich et al. (2002) also reported that the peculiar and low-stretch SN 1999by does not exhibit this feature in its unusually weak Fe II/Co II/Ni II structure. Thus, the one-parameter description of this spectral feature is far from definitive. More spectroscopic data in the NIR is required to confirm this trend and to determine whether or not the peculiar NIR spectral feature of SN 1999by is an isolated occurrence for subluminous objects.

7.9 Conclusion

The spectroscopic properties of NIR spectra before around 3 days past B-band maximum are shown to be exceptionally uniform with very slow temporal evolution. This epoch range centers approximately on the time of the NIR primary maximum which occurs a few days before B-band maximum. The observation is consistent with the photometric observations of the uniformity in the peak NIR absolute magnitudes (e.g., Krisciunas et al. 2004a; Wood-Vasey et al. 2008). From the standpoint of K-corrections, this epoch range is excellent for cosmology, as uncertainties associated with using an assumed spectral energy distribution are very small.

The first mean spectral template time series of SNe Ia in the NIR is presented. K-corrections calculated using individual spectra are shown to incur significant systematic errors. The mean spectral template presented here is specifically designed to minimize these systematic errors. The K-correction errors around the NIR primary maximum have also been shown to be exceptionally small.

Around the NIR primary maximum, a spectroscopic sequence is detected in each of the NIR Y, J, H and K bands. Because the spectra in this epoch range are already quite uniform, the variations described by these spectroscopic sequences are very small. In the Y band, there is evidence for the slight increase in strength of the Mg II feature as stretch
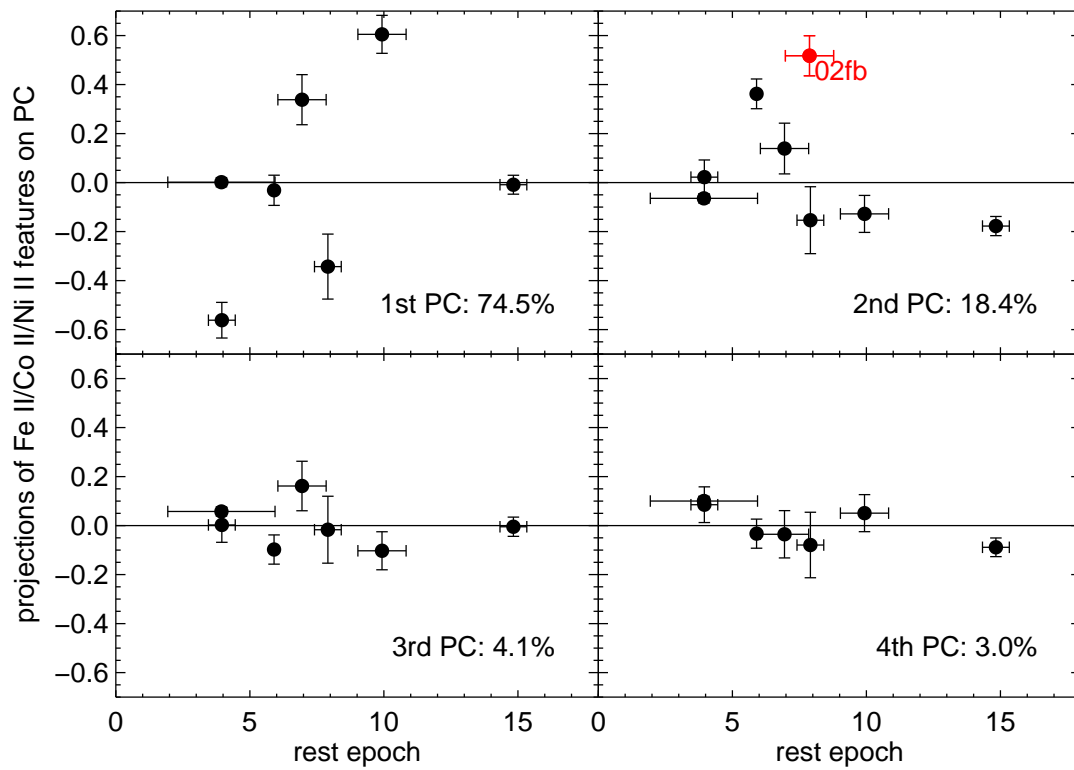
Figure 7.21: The projections of the prominent *H*-band spectral feature on the PCs with respect to epoch. The epochs are corrected for time dilation and are with respect to *B*-band maximum. The projection of SN 2002fb is marked as red in the second PC. SN 2002fb has no available stretch and is not included in the PCA.
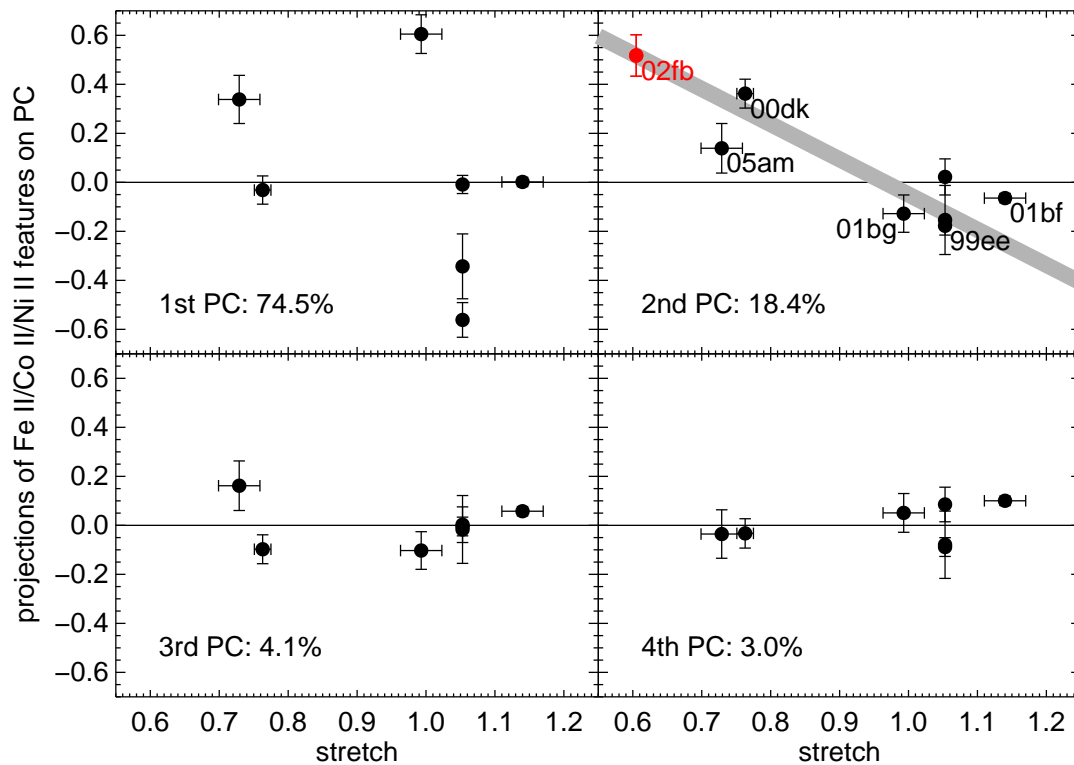
Figure 7.22: The projections of the prominent *H*-band spectral feature on the PCs with respect to stretch. The linear fit through the sequence in the second PC is plotted as a gray line. SN 2002fb has no available stretch and is not included in the PCA. A stretch value for SN 2002fb is derived using the linear fit, and the projection is marked as red in the second PC.
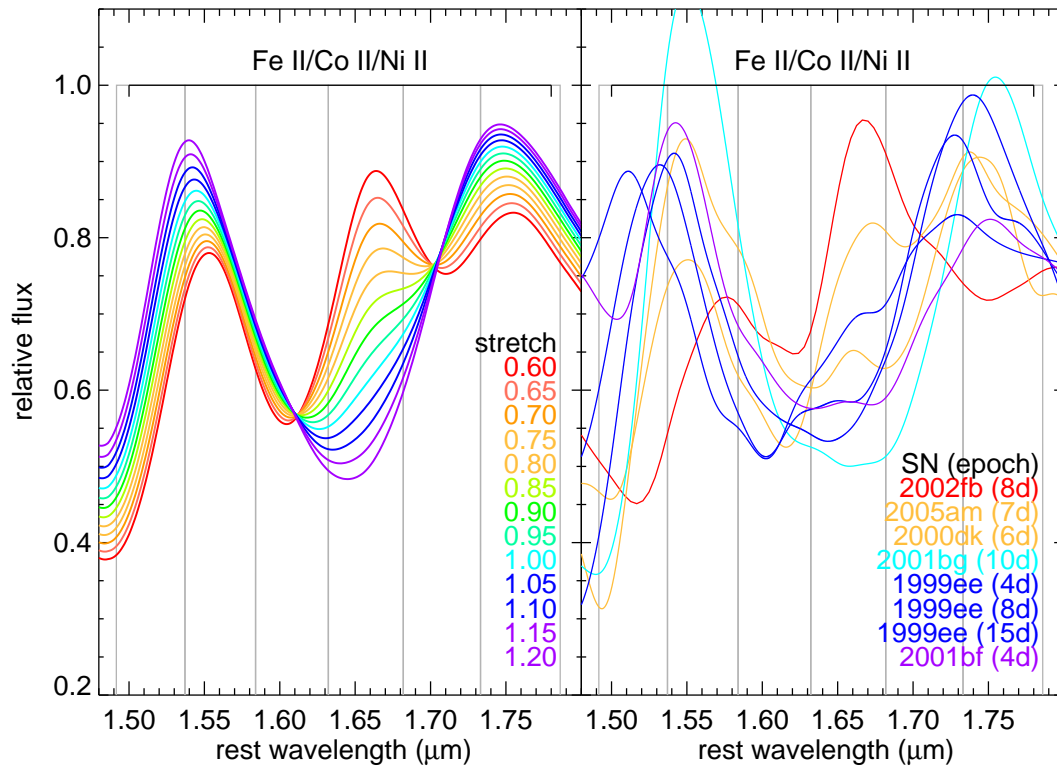
Figure 7.23: The template sequence of the prominent *H*-band feature from the second PC for the epoch range between 3 and 15 days past *B*-band maximum. The left panel shows the template sequence, and the right panel shows the smoothed library spectra. SN 2002fb has no available stretch and is not included in the PCA. Each spectrum is color coded by stretch. The names and the epochs of the library spectra are noted. The narrowband filters used to quantify the features are plotted as gray lines. The dominant species responsible for each spectral feature in the region is also noted.

decreases. In the *J* and *H*, the sequences describe small velocity shifts of the spectral features. The correlations between the NIR spectral features and light-curve widths are formed using only $8-9$ data points in each band. More data is required to confirm or refute these trends. The NIR absolute magnitudes of SNe Ia have been shown to have little or no dependence on light-curve widths (Krisciunas et al. 2004a). The variations described by the spectroscopic sequences are perhaps too small to enter into broadband photometric observations.

In the epoch range between 3 to 15 days past *B*-band maximum, the NIR spectra are dominated by the rapid formation of the wide *H*-band feature, attributed to the line blanketing by Fe II, Co II and Ni II. An emission-like feature is found at the center of the wide *H*-band structure and is associated only with low-stretch objects in our data set. This feature yields evidence of another spectroscopic sequence in the NIR. However, Höflich et al. (2002) reported that the low-stretch SN 1999by does not exhibit this feature in its unusually weak Fe II/Co II/Ni II structure, indicating that perhaps the one-parameter description of spectroscopic variations is incomplete.

Chapter 8

Conclusion

The path to improving the use of Type Ia supernovae (SNe Ia) as standard candles in cosmological studies and the path to the understanding of the origins of the observed properties of SNe Ia are one and the same. In this work, a large library of spectroscopic data is constructed to study the effect of the observed spectroscopic diversity on cosmological studies and to search for the origins of the observed diversity.

Before this work, the inhomogeneity in the SN Ia spectra had not been dealt with adequately, and the K-correction calculations were a major source of systematic errors in SN Ia cosmology. New methods have been developed here to consistently quantify observed spectral features and the K-correction errors associated with the diversity. A mean spectral template time series is built to have the mean spectroscopic properties of SNe Ia and is shown to largely obviate systematic errors caused by assuming the SED of a particular supernova.

The remaining statistical errors are shown to be redshift dependent, with minima at redshifts where the rest-frame filter band and the observed filter bands are aligned. These errors are attributed to the inhomogeneity in the observed spectral features. As these errors directly affect the magnitudes of the SNe Ia, it is important to incorporate the redshift-dependent effect in cosmology. The statistical errors can be reduced if the spectroscopic differences from the mean of individual SNe Ia can be predicted from their photometric properties.

Principal component analysis (PCA) has been adopted to search for the global trends in the variations of spectral features in the sample of nearby SNe Ia. At maximum light, significant correlations between the light-curve width and the spectral features are found for every spectral feature from U band to I band, even for features which have been previously reported to show little or no correlation. The result in turn suggests that the SN Ia intrinsic

luminosity is the main driver of the observed variation in the spectral features. Template spectroscopic sequences are built to illustrate in detail how the features vary with light-curve width. The methods presented here also provide ways to use the spectral features as independent indicators of intrinsic luminosity and color.

Beyond maximum light, there is also evidence of the persistence of the spectroscopic sequences throughout other epochs. The effect is attributed to the more rapid spectroscopic temporal evolution of fainter objects than that of their brighter counterparts. This observation provides the first justification for selecting the stretch-adjusted epochs of a spectral template time series for the use in cosmological studies. It also supports the theory that the width-luminosity relation (WLR) is primarily a spectroscopic phenomenon, rather than a bolometric one, and points to the speed of the ionization evolution of iron-peak elements as the origin of the WLR (Kasen & Woosley 2007).

In the near-infrared (NIR), the spectroscopic properties of SNe Ia are found to be remarkably uniform, especially around the NIR primary maximum. The spectroscopic homogeneity is consistent with the photometric observation that SNe Ia are true standard candles in the NIR. Within the homogeneous spectral features, PCA detected correlations between the small variations and light-curve width. The correlations at the NIR maximum are barely discernable. Stronger evidence of a spectroscopic sequence is provided for the prominent *H*-band feature which appears abruptly at approximately a week past maximum light and is attributed to the line blanketing by iron-group elements. The center of the feature appears as an emission feature for low-stretch objects and as an absorption feature for high-stretch objects. However, more spectroscopic data in the NIR is required to confirm or refute this finding.

Exquisitely detailed spectroscopic observations of high-redshift SNe Ia are beginning to detect systematic differences between the spectroscopic properties of nearby and distant SNe Ia (Foley et al. 2008a; Sullivan et al. 2009). As the cosmic star formation density increases with redshift, the mean light-curve width of SNe Ia, which depends on the star formation rate of the host galaxy, also increases with redshift. It is thus unclear whether the observed differences are due to the demographic shift of the host galaxies or true evolution in SN Ia properties, such as a different width-luminosity relation at high-redshift. The relations between spectral features and light-curve width established here will be able to disentangle the variations driven by the shift in average light-curve width and by other factors.

PCA and other methods developed here also have potential application in spectroscopic typing of supernovae. Current tools for spectroscopic typing involve the comparison be-

tween the spectrum in question and individual observed spectra covering a large range of supernova types, epochs and wavelengths (Howell et al. 2005; Blondin & Tonry 2007). Problems can arise for this approach when large gaps exist in the parameter space. Unpublished spectroscopic data can also make the distribution of the tool difficult. PCA can be used to search for patterns in the spectra instigated by type, epoch, redshift, galaxy light. The established relations can then be used to determine the information without the aid of any photometric information. This approach also provides a statistical indicator of the database spectrum which most closely resembles an observed spectrum. The deviation from the established relations can also be used to identify exotic objects.

In summary, the current measures of the K-correction error contributions caused by the spectroscopic diversity of SNe Ia are tabulated in Table 8.1. The broadband colors are still the largest component. With adequate filter coverage and the careful treatment of the broadband colors of the spectral templates, this component can be largely eliminated. The intrinsic dispersion in the spectral features contributes errors on the order of 10^{-2} mag. The spectroscopic sequences established here have the potential to account for a large fraction of the intrinsic dispersion at maximum light. With better spectroscopic observations of high-redshift SNe Ia and the spectroscopic sequences established here by low-redshift SNe Ia, there is real hope that a more certain constraint on the SN Ia evolution can be determined in the near future.

Table 8.1: Sources of K-correction errors from spectroscopic diversity

Contributions	Δmag
broadband colors	10^{-1}
spectral features	10^{-2}
spectroscopic sequences	10^{-2}
evolution	?

Appendix A

List of library spectra

Table A.1: The full list of library spectra. The stretch parameters are obtained from *B*-band light curves. The references marked as M. M. Phillips and D. A. Howell are spectra obtained through private communications. The references marked as CSP and SNLS are spectra from the Carnegie Supernova Project (Hamuy et al. 2006) and the Supernova Legacy Survey (Howell et al. 2005; Bronder et al. 2008; Baumont et al. 2008), respectively. Some of the spectra from these collaborations are not yet published.

Name	Number of spectra	Stretch	Redshift	References
1981B	8	0.902	0.0060	Branch et al. (1983)
1986G	19	0.696	0.0026	Phillips et al. (1987)
1989B	25	0.902	0.0024	Barbon et al. (1990); Wells et al. (1994)
1990G	1		0.0358	Gomez et al. (1996)
1990M	1		0.0090	Gomez et al. (1996)
1990N	13	1.027	0.0034	Mazzali et al. (1993)
1990O	7	1.088	0.0303	Gomez et al. (1996); M. M. Phillips
1990R	3		0.0161	Gomez et al. (1996)
1990T	2	1.028	0.0404	M. M. Phillips

Table A.1 – Continued

Name	Number of spectra	Stretch	Redshift	References
1990af	1	0.747	0.0506	M. M. Phillips
1991F	2		0.0060	Gomez et al. (1996)
1991M	3	0.971	0.0072	Gomez et al. (1996)
1991S	2	1.052	0.0546	Gomez et al. (1996); M. M. Phillips
1991T	19	1.080	0.0058	Mazzali et al. (1995)
1991U	1	1.088	0.0317	M. M. Phillips
1991X	1		0.0088	Gomez et al. (1996)
1991ad	1		0.0700	Gomez et al. (1996)
1991ag	2	1.125	0.0141	M. M. Phillips
1991bc	1		0.0214	Gomez et al. (1996)
1991bd	1		0.0127	Gomez et al. (1996)
1991bg	28	0.536	0.0035	Turatto et al. (1996)
1991bj	1		0.0182	Gomez et al. (1996)
1992A	15	0.798	0.0063	Kirshner et al. (1993)
1992G	4	1.014	0.0053	Gomez et al. (1996)
1992J	2	0.831	0.0446	M. M. Phillips
1992K	1		0.0103	M. M. Phillips
1992P	1	1.092	0.0252	M. M. Phillips
1992ac	2		0.0523	Gomez et al. (1996)
1992ae	1	0.957	0.0752	M. M. Phillips
1992ag	1	1.066	0.0249	M. M. Phillips
1992ah	1		0.0250	Gomez et al. (1996)
1992al	2	0.950	0.0146	M. M. Phillips
1992aq	1	0.840	0.1018	M. M. Phillips
1992au	1		0.0614	M. M. Phillips
1992bc	3	1.033	0.0202	M. M. Phillips
1992bg	1	1.014	0.0352	M. M. Phillips
1992bh	1	1.012	0.0450	M. M. Phillips
1992bk	2	0.790	0.0581	M. M. Phillips

Continued on the next page...

Table A.1 – Continued

Name	Number of spectra	Stretch	Redshift	References
1992bl	1	0.813	0.0437	M. M. Phillips
1992bo	1	0.751	0.0189	M. M. Phillips
1992bp	1	0.887	0.0793	M. M. Phillips
1992br	1	0.627	0.0882	M. M. Phillips
1992bs	1	1.017	0.0637	M. M. Phillips
1993B	1	0.983	0.0696	M. M. Phillips
1993H	3	0.714	0.0239	M. M. Phillips
1993O	2	0.908	0.0510	M. M. Phillips
1994D	42	0.798	0.0015	Patat et al. (1996)
1994M	1	0.854	0.0232	Gomez et al. (1996)
1994Q	2	1.126	0.0296	Gomez et al. (1996)
1994S	1	0.990	0.0152	Gomez et al. (1996)
1994U	1		0.0044	Gomez et al. (1996)
1994ae	18	1.007	0.0043	D. A. Howell
1996X	20	0.911	0.0069	Salvo et al. (2001)
1997br	9	1.057	0.0053	Li et al. (1999)
1997cn	1	0.890	0.0162	Turatto et al. (1998)
1997do	12	0.978	0.0105	Matheson et al. (2008)
1997dt	7	0.969	0.0073	Matheson et al. (2008)
1998V	8	1.016	0.0172	Matheson et al. (2008)
1998ab	10	0.967	0.0279	Matheson et al. (2008)
1998aq	54	0.985	0.0043	Branch et al. (2003); Matheson et al. (2008)
1998bp	11	0.646	0.0102	Matheson et al. (2008)
1998bu	65	1.006	0.0042	Cappellaro et al. (2001); Matheson et al. (2008)
1998de	7	0.604	0.0156	Matheson et al. (2008)
1998dh	10	0.871	0.0090	Matheson et al. (2008)
1998dk	10	0.963	0.0132	Matheson et al. (2008)

Continued on the next page…

Table A.1 – Continued

Name	Number of spectra	Stretch	Redshift	References
1998dm	10	0.952	0.0065	Matheson et al. (2008)
1998ec	6	0.946	0.0199	Matheson et al. (2008)
1998eg	6	0.971	0.0235	Matheson et al. (2008)
1998es	26	1.135	0.0096	Matheson et al. (2008)
1999X	6	0.930	0.0252	Matheson et al. (2008)
1999aa	43	1.131	0.0153	Garavini et al. (2004);
				Matheson et al. (2008)
1999ac	33	0.973	0.0098	Garavini et al. (2004);
				Matheson et al. (2008)
1999aw	8	1.205	0.0380	Strolger et al. (2002)
1999by	18	0.612	0.0027	Garnavich et al. (2004);
				Matheson et al. (2008)
1999cc	7	0.808	0.0315	Matheson et al. (2008)
1999cl	11	0.964	0.0087	Matheson et al. (2008)
1999dq	18	1.111	0.0135	Matheson et al. (2008)
1999ee	37	1.053	0.0114	Hamuy et al. (2002)
1999ej	5	0.797	0.0137	Matheson et al. (2008)
1999gd	5	0.942	0.0193	Matheson et al. (2008)
1999gh	15	0.702	0.0077	Matheson et al. (2008)
1999gp	10	1.146	0.0260	Matheson et al. (2008)
2000B	7	0.778	0.0198	Matheson et al. (2008)
2000E	5	1.030	0.0044	Valentini et al. (2003)
2000cf	6	0.933	0.0365	Matheson et al. (2008)
2000cn	10	0.778	0.0232	Matheson et al. (2008)
2000cx	42	1.090	0.0081	Li et al. (2001a); Matheson et al. (2008)
2000dk	9	0.763	0.0165	Marion et al. (2003);
				Matheson et al. (2008)
2000dm	1	0.885	0.0150	Marion et al. (2003)
2000dn	1	1.140	0.0321	Marion et al. (2003)

Continued on the next page...

Table A.1 – Continued

Name	Number of spectra	Stretch	Redshift	References
2000do	1		0.0109	Marion et al. (2009)
2000fa	14	1.053	0.0218	Marion et al. (2003);
				Matheson et al. (2008)
2001ay	6	1.500	0.0302	Howell & Nugent (2004)
2001ba	5	1.018	0.0305	M. M. Phillips
2001bf	3	1.140	0.0155	Marion et al. (2003); M. M. Phillips
2001bg	1	0.993	0.0071	Marion et al. (2003)
2001br	1	1.060	0.0206	Marion et al. (2003)
2001bt	1	0.900	0.0144	M. M. Phillips
2001cn	2	0.978	0.0154	M. M. Phillips
2001dl	1	1.140	0.0207	Marion et al. (2003)
2001el	10	0.981	0.0039	Wang et al. (2003)
2001en	2	0.935	0.0159	Marion et al. (2009)
2001ex	6		0.0264	D. A. Howell
2001hc	1		0.3500	Lidman et al. (2005)
2002bo	15	0.922	0.0042	Benetti et al. (2004);
				Marion et al. (2009)
2002cr	1		0.0095	Marion et al. (2009)
2002ef	1		0.0240	Marion et al. (2009)
2002er	25	0.922	0.0086	Kotak et al. (2005)
2002fb	1		0.0156	Marion et al. (2009)
2002fk	2	0.940	0.0071	Marion et al. (2003)
2002ha	1		0.0140	Marion et al. (2003)
2002hw	1		0.0175	Marion et al. (2003)
2002iu	1		0.1100	Matheson et al. (2005)
2003W	2		0.0201	Marion et al. (2009)
2003bf	6		0.0336	D. A. Howell
2003bs	3		0.0500	D. A. Howell
2003bt	2		0.0266	D. A. Howell

Continued on the next page. . .

Table A.1 – Continued

Name	Number of spectra	Stretch	Redshift	References
2003bu	1		0.0201	D. A. Howell
2003cg	1		0.0041	Marion et al. (2009)
2003du	10	1.056	0.0064	Anupama et al. (2005);
				Marion et al. (2009)
2004E	1		0.0298	Marion et al. (2009)
2004S	8		0.0091	Krisciunas et al. (2007)
2004ab	1		0.0058	Marion et al. (2009)
2004bk	1		0.0231	Marion et al. (2009)
2004bl	1		0.0173	Marion et al. (2009)
2004bv	2		0.0106	Marion et al. (2009)
2004bw	1		0.0212	Marion et al. (2009)
2004ca	1		0.0178	Marion et al. (2009)
2004da	4		0.0159	Marion et al. (2009)
2004ef	7	0.791	0.0310	CSP
2004eo	3	0.788	0.0157	CSP
2004ey	4	1.016	0.0158	CSP
2004gs	2	0.685	0.0266	CSP
2005M	8	1.060	0.0220	CSP
2005al	7	0.929	0.0124	CSP
2005am	11	0.729	0.0079	CSP; Marion et al. (2009)
2005cg	6	1.070	0.0313	Quimby et al. (2006)
2005el	4	0.811	0.0149	CSP
2005eq	2	1.144	0.0290	CSP
2005hc	1	0.989	0.0459	CSP
2005iq	2	0.861	0.0340	CSP
2005kc	2	0.879	0.0151	CSP
2005ke	6	0.601	0.0049	CSP
2005ki	3	0.866	0.0196	CSP
2005na	3	1.014	0.0263	CSP

Continued on the next page...

Table A.1 – Continued

Name	Number of spectra	Stretch	Redshift	References
2006D	11	0.789	0.0085	CSP
2006ax	8	1.003	0.0168	CSP
2006bh	2	0.750	0.0109	CSP
03D1au	1	1.119	0.5040	Ellis et al. (2008); SNLS
03D1aw	1	1.076	0.5820	Ellis et al. (2008); SNLS
03D1dj	1	1.123	0.4000	Ellis et al. (2008); SNLS
03D3ay	1	1.064	0.3710	Ellis et al. (2008); SNLS
03D3bb	1		0.2440	Ellis et al. (2008); SNLS
03D3bl	1	0.989	0.3550	Ellis et al. (2008); SNLS
03D3cc	1	1.013	0.4630	Ellis et al. (2008); SNLS
03D3cd	1	1.099	0.4610	Ellis et al. (2008); SNLS
03D4ag	1	1.049	0.2850	Ellis et al. (2008); SNLS
03D4cj	1	1.039	0.2700	Ellis et al. (2008); SNLS
03D4dh	1	1.053	0.6270	Ellis et al. (2008); SNLS
03D4gl	1	0.931	0.5710	Ellis et al. (2008); SNLS
04D1hd	1		0.3690	Ellis et al. (2008); SNLS
04D1jg	1		0.5840	Ellis et al. (2008); SNLS
04D1rh	1	0.965	0.4350	Ellis et al. (2008); SNLS
04D2gc	1	1.096	0.5220	Ellis et al. (2008); SNLS
04D2kr	1	1.069	0.7440	Ellis et al. (2008); SNLS
04D3ez	1	0.935	0.2630	Ellis et al. (2008); SNLS
04D3fk	1	0.963	0.3580	Ellis et al. (2008); SNLS
04D3nq	1	1.035	0.2200	Howell et al. (2005); SNLS
04D4in	1	1.045	0.5160	Ellis et al. (2008); SNLS
04D4jr	1	1.182	0.4820	Ellis et al. (2008); SNLS
05D1hk	1	1.060	0.2630	Ellis et al. (2008); SNLS
05D1hn	1	0.981	0.1490	Ellis et al. (2008); SNLS
05D1if	1	1.039	0.7630	Ellis et al. (2008); SNLS
05D1ix	1	0.950	0.4900	Ellis et al. (2008); SNLS

Continued on the next page. . .

Table A.1 – Continued

Name	Number of spectra	Stretch	Redshift	References
05D1iy	1	0.814	0.2480	Ellis et al. (2008); SNLS
05D2le	1	1.144	0.7000	Ellis et al. (2008); SNLS
05D2mp	1	1.138	0.3540	Ellis et al. (2008); SNLS
05D3kx	1	1.051	0.2190	SNLS
05D3mq	1	0.868	0.2400	SNLS
05D3ne	1	0.823	0.1692	SNLS
06D2fb	1	0.976	0.1242	SNLS
06D2ez	1		0.0822	SNLS
06D3cn	1		0.2320	SNLS

Appendix B

Plaskett Spectroscopic Supernova Survey

The Plaskett Spectroscopic Supernova Survey (PSSS)[1] is an ongoing observing program initiated and led by the author. It uses the 1.82-m Plaskett Telescope of the Dominion Astrophysical Observatory (DAO) in Victoria to obtain spectroscopic data of nearby supernovae. The survey began in the latter half of 2007 and is now run by five graduate students. A large fraction of nights on the Plaskett Telescope has been allocated to this survey, on average between one to two nights a week. The main goals of the survey are to spectroscopically confirm and classify newly discovered nearby supernovae and to expand the current library of spectra.

Because the supernova spectral features are broad, the lowest dispersion setting for the Cassegrain spectrograph is used to maximize the amount of light received at each wavelength. The spectrograph at the Plaskett telescope is designed to observe objects down to 16th magnitude. With long exposure times, spectra for supernovae down to 17th magnitude are consistently obtained. From the known telescope limits of hour angle, declination and magnitude, an IDL program is written to automatically generate a list of targets from the astronomical circulars for each observing night. On average $2 - 3$ spectra can be obtained on a clear night, with unclassified supernovae given priority. During the first six quarters, the survey has produced 37 spectra and published 13 astronomical circulars for spectroscopic classifications. The publications and their Central Bureau Electronic Telegrams (CBET) numbers are listed in Table B.1. During this time the survey has observed spectra for some very interesting objects. A sample of them is described as follows:

---

[1]http://www.astro.uvic.ca/~hsiao/psss/

SN 2007gk   SN 2007gk has been classified as a Type Ia supernova by the PSSS (Hsiao et al. 2007b). The two spectra of SN 2007gk observed by the PSSS resemble those of peculiar SN 2002bo (Benetti et al. 2004), characterized by their unusually large expansion veloc-ities of the Si II features. The expansion velocity for the Si II 6355Å line of SN 2007gk is measured to be approximately $14\,500\,\mathrm{km\,s^{-1}}$, much higher than those of normal Type Ia supernovae (Figure B.1). The high velocity suggests that the burning to intermediate mass elements has reached the outermost region. The Si II 5972Å line is one of the best indicators of intrinsic luminosity (Chapter 6). The depth of the Si II 5972Å of SN 2007gk is quite typical. A PCA projection analysis of this feature infers a stretch value of $s = 1.0$. The higher than usual expansion velocities are therefore not driven by an extreme amount of ^{56}Ni. Benetti et al. (2004) argued that the one-parameter description is inadequate for the Si II expansion velocities, as there exists a wide range of velocities for supernovae with similar light-curve widths.

SN 2008A   The two spectra of SN 2008A obtained by the PSSS resemble those of pecu-liar SN 2002cx (Li et al. 2003) and SN 2005hk (Phillips et al. 2007). SN 2002cx has been called "the most peculiar known Type Ia supernova," because it has premaximum spectra resembling overluminous 1991T-like objects, yet its low peak luminosity resembles un-derluminous 1991bg-like objects. The reported discovery magnitude of SN 2008A is 17.6 (Nakano et al. 2008) and corresponds to an absolute magnitude of -16.6, assuming that it is in the Hubble flow and suffers from no dust extinction. This is consistent with an underlu-minous object. Its premaximum spectrum is also reported to show high ionization features characteristic of overluminous objects (Blondin & Berlind 2008). The PSSS spectra of SN 2008A are taken approximately three weeks past maximum light and exhibit unusually narrow features (Figure B.2), present in both SN 2002cx and SN 2005hk. These narrow features show evidence of well-mixed unprocessed carbon, supporting a pure deflagration burning front. As more of these 2002cx-like objects are discovered, it is clear that they are not isolated events.

SN 2008fz   The PSSS obtained an early spectrum of SN 2008fz approximately one day past discovery. The spectrum is quite featureless (Figure B.3) and is classified as a Type Ic (Hsiao et al. 2008a). Hydrogen Balmer lines are reported to be present in a later spectrum of SN 2008fz, and the supernova is re-classified as Type IIn (Benetti et al. 2008). The redshift from the Balmer lines is measured to be $z = 0.133$ and suggests that this object is quite distant and luminous. Benetti et al. (2008) derived an absolute magnitude of -

22.1, which makes it one of the brightest supernovae observed. There is some controversy over the explosion mechanism of some of the Type IIn supernovae, such as SN 2002ic (Hamuy et al. 2003; Benetti et al. 2006). Our classification of Type Ic appears to favor SN 2008fz being a core-collapse supernova. However, the early spectrum of SN 2008fz is quite featureless, making the classification less secure.

SN 2008hp   SN 2008hp is classified by the PSSS as a Type Ia supernova (Hsiao et al. 2008b), approximately four days past discovery. The spectrum matches that of a normal Type Ia supernova at approximately 10 days past maximum light. The host galaxy is found to have a very low luminosity, with an absolute magnitude of approximately -12.4 (Drake et al. 2008). This luminosity is at the low end of the population, even among dwarf galaxies. A supernova like SN 2008hp would probably have been missed in galaxy-targeted searches, creating a sampling bias towards brighter hosts.

There are plans to keep the survey going because of the interest in observing generated among young graduate students. At the time of writing, the survey is ongoing and run mostly by students who do not have previous experience in observing or supernova science. Although the lack of complementary photometry and the survey's inability to make time series observations will probably continue to limit the scientific goals, the PSSS has been shown to be a good facility for students to gain valuable hands-on observing experience.

Table B.1: Astronomical circulars published by the PSSS

CBET number	Supernova name	Supernova type	Host redshift	Days past discovery
1025	2007gk	Ia	0.02663	1.4
1219	2008L	Ia	0.01940	8.1
1224	2008P	II	0.01214	1.0
1267	2008ak	II	0.00793	7.9
1429	2008dx	Ia	0.02303	3.6
1434	2008dw	II	0.01244	5.5
1434	2008ea	II	0.01426	1.8
1436	2008eb	Ic	0.00761	1.5
1502	2008fn	Ibc	0.02984	36.5
1524	2008fz	II		0.5
1547	2008gl	Ia	0.03402	1.8
1551	2008gm	IIn	0.01173	6.6
1589	2008hp	Ia	0.02700	3.5
1804	2009en	Ia	0.04674	6.3
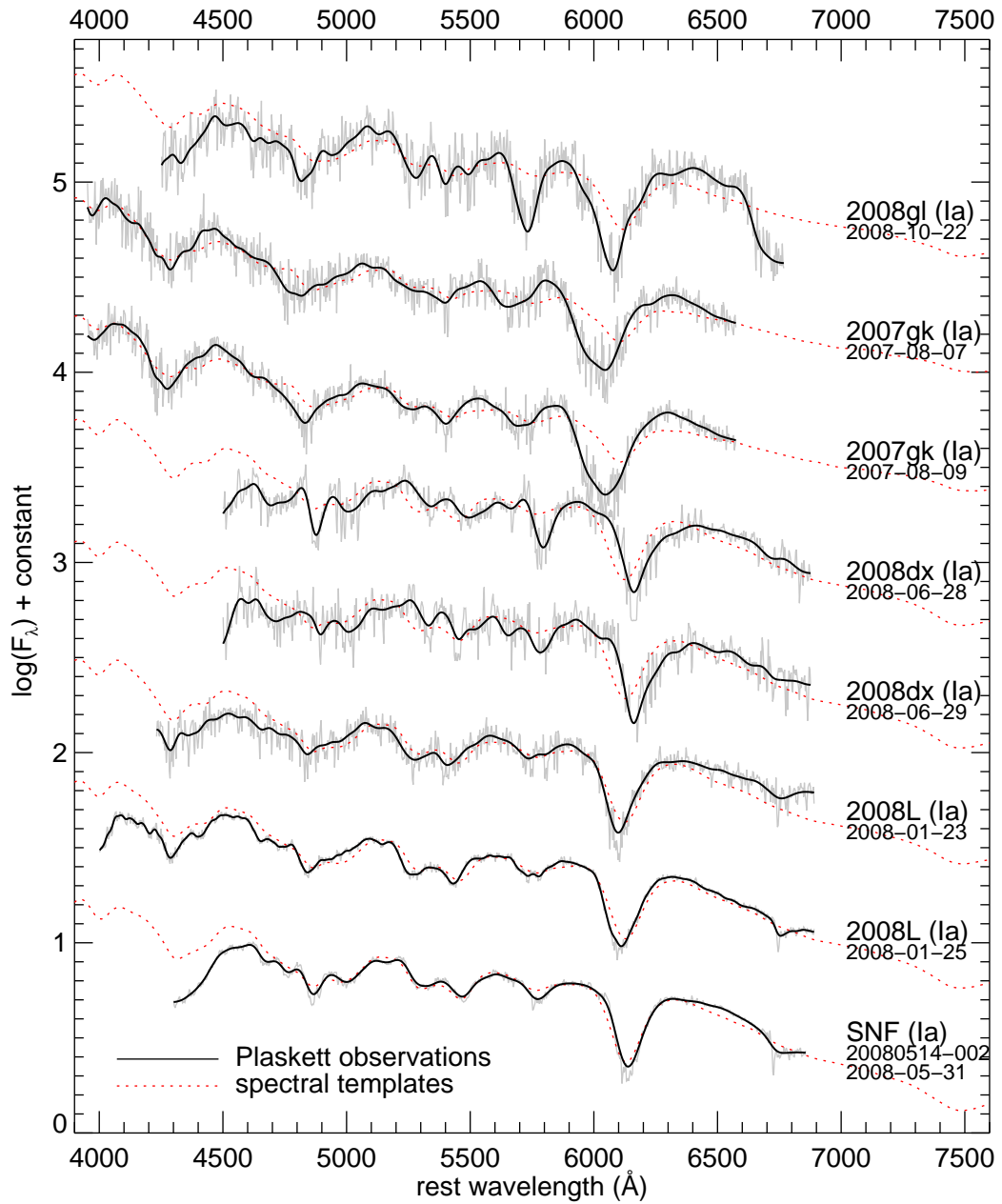
Figure B.1: The spectra of Type Ia supernovae near peak brightness obtained by the PSSS. The spectra have been de-redshifted to the rest frame using the redshifts of the host galaxies. For the cases where the host redshifts are not available, the redshifts which yield best fits to the spectral templates are used. The PSSS spectra and template spectra are plotted as solid gray and dotted red curves, respectively. Smoothed PSSS spectra are plotted as black curves to aid the comparison.
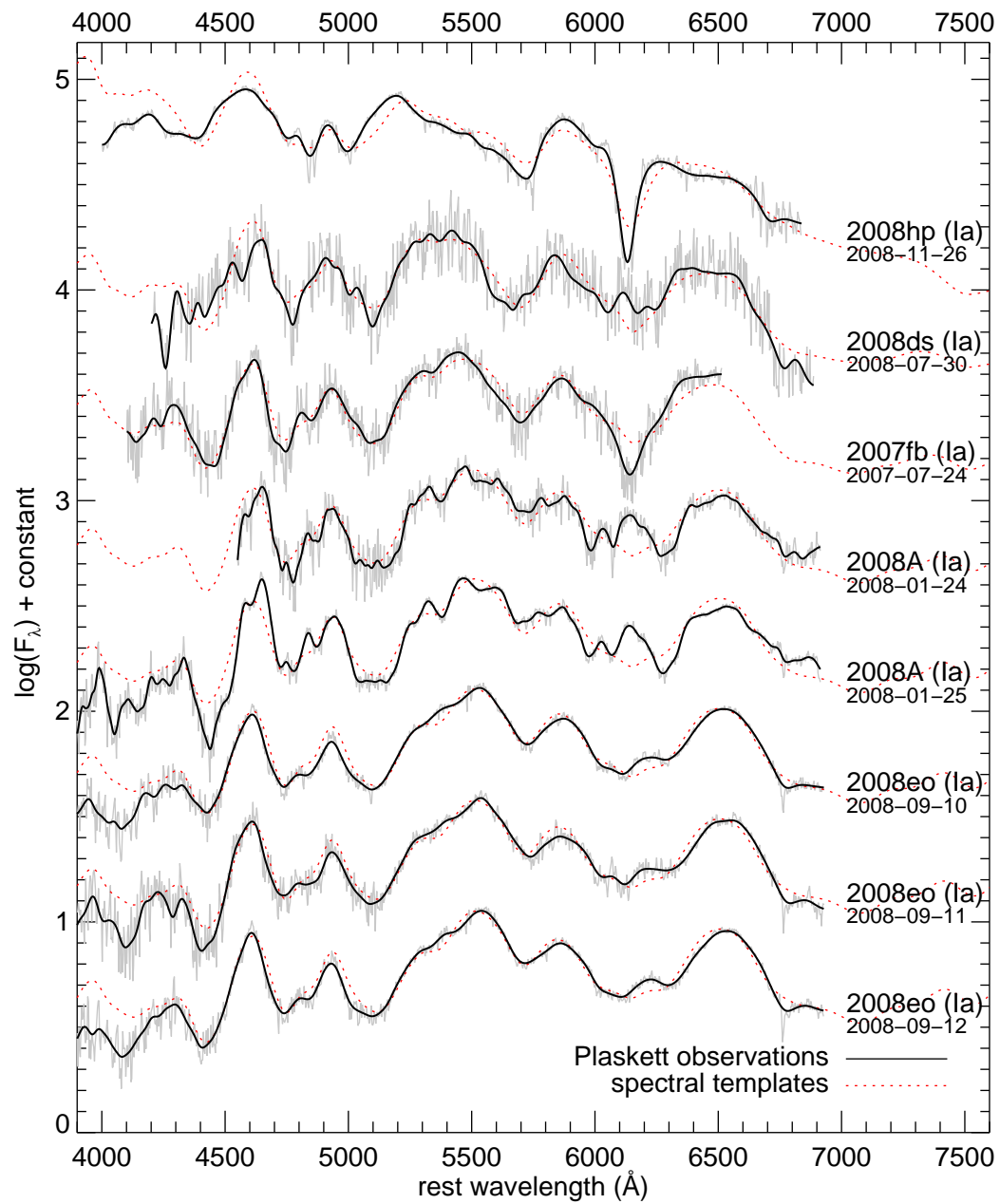
Figure B.2: Same as Figure B.1 for Type Ia supernovae at postmaximum epochs.
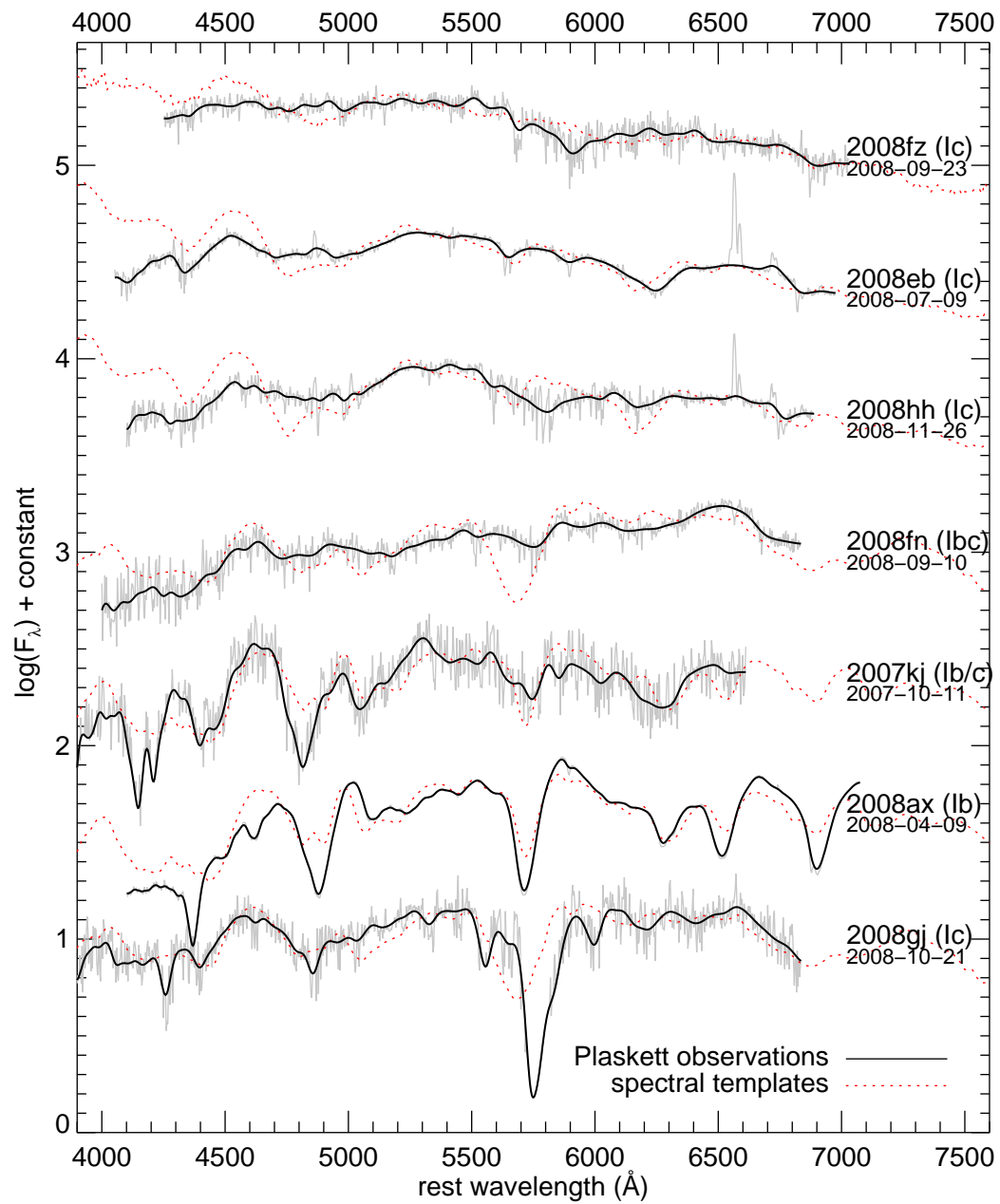
Figure B.3: Same as Figure B.1 for Type Ibc supernovae.
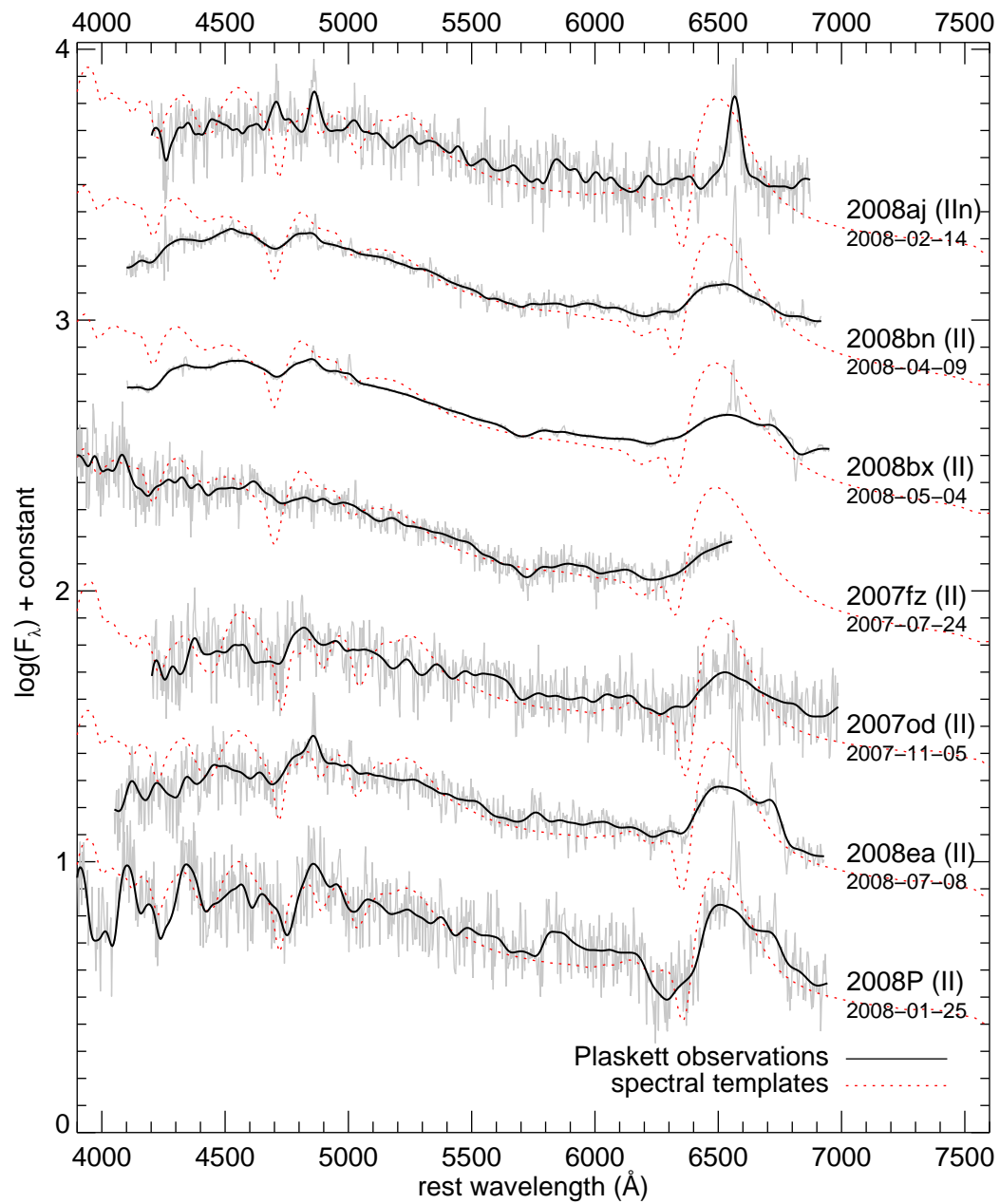
Figure B.4: Same as Figure B.1 for Type II supernovae.
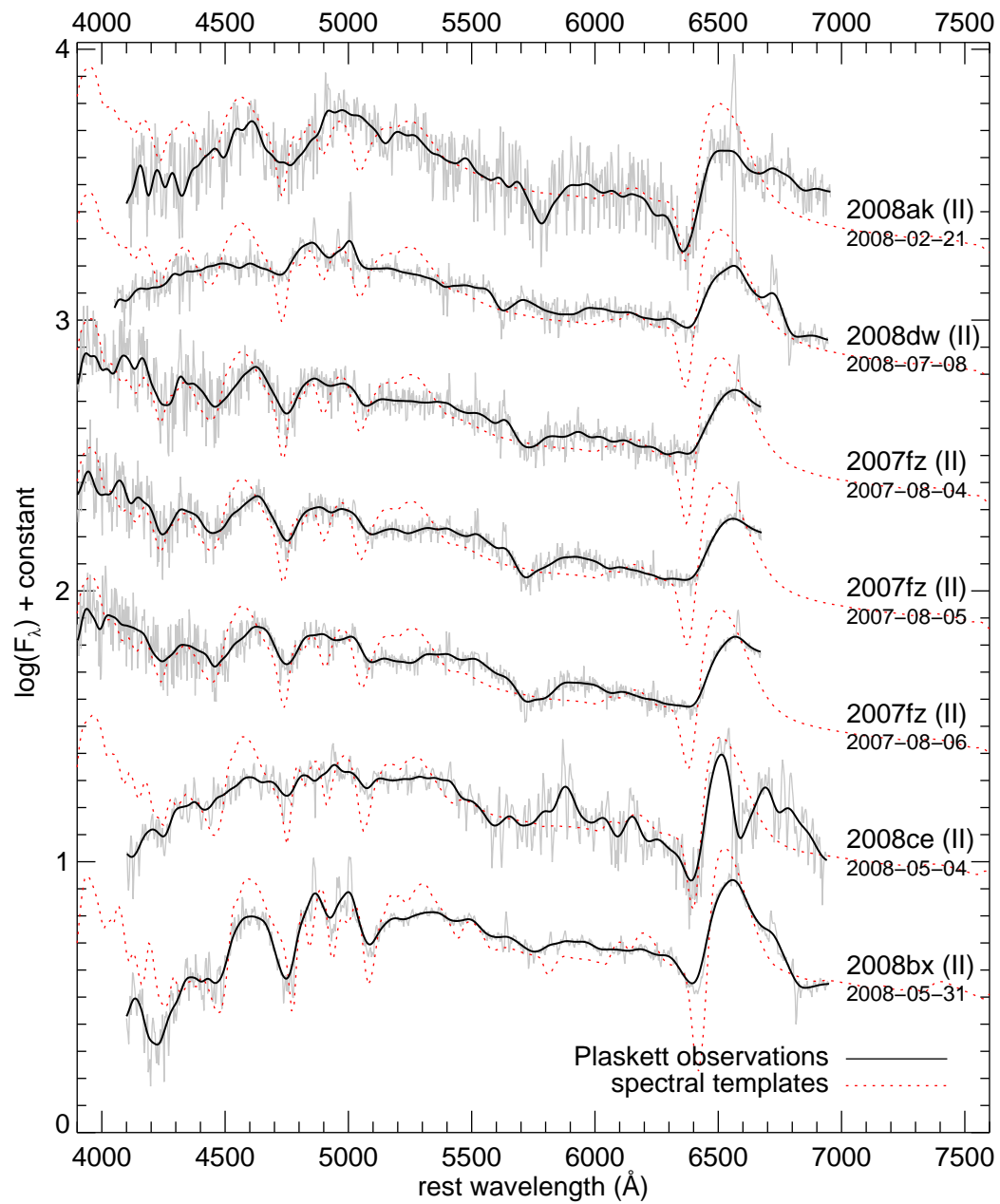
Figure B.5: Same as Figure B.1 for Type II supernovae.

Bibliography

Aguirre, A., **Intergalactic Dust and Observations of Type IA Supernovae**, *ApJ*, 1999a, 525, 583

Aguirre, A. N., **Dust versus Cosmic Acceleration**, *ApJ*, 1999b, 512, L19

Aldering, G., Antilogus, P., Bailey, S., Baltay, C., Bauer, A., Blanc, N., Bongard, S., Copin, Y., Gangler, E., Gilles, S., Kessler, R., Kocevski, D., Lee, B. C., Loken, S., Nugent, P., Pain, R., Pécontal, E., Pereira, R., Perlmutter, S., Rabinowitz, D., Rigaudier, G., Scalzo, R., Smadja, G., Thomas, R. C., Wang, L., & Weaver, B. A., **Nearby Supernova Factory Observations of SN 2005gj: Another Type Ia Supernova in a Massive Circumstellar Envelope**, *ApJ*, 2006, 650, 510

Allen, S. W., Rapetti, D. A., Schmidt, R. W., Ebeling, H., Morris, R. G., & Fabian, A. C., **Improved constraints on dark energy from Chandra X-ray observations of the largest relaxed galaxy clusters**, *MNRAS*, 2008, 383, 879

Altavilla, G., Ruiz-Lapuente, P., Balastegui, A., Méndez, J., Irwin, M., España-Bonet, C., Ellis, R. S., Folatelli, G., Goobar, A., Hillebrandt, W., McMahon, R. M., Nobili, S., Stanishev, V., & Walton, N. A., **Type Ia SNe Along Redshift: The $\mathcal{R}$(Si II) Ratio and the Expansion Velocities in Intermediate-z Supernovae**, *ApJ*, 2009, 695, 135

Anupama, G. C., Sahu, D. K., & Jose, J., **Type Ia supernova SN 2003du: Optical observations**, *A&A*, 2005, 429, 667

Arnett, W. D., **On the theory of Type I supernovae**, *ApJ*, 1979, 230, L37

Arnett, W. D., **Type I supernovae. I - Analytic solutions for the early part of the light curve**, *ApJ*, 1982, 253, 785

Arsenijevic, V., Fabbro, S., Mourão, A. M., & Rica da Silva, A. J., **Diversity of supernovae Ia determined using equivalent widths of Si II 4000**, *A&A*, 2008, 492, 535

Astier, P., Guy, J., Regnault, N., Pain, R., Aubourg, E., Balam, D., Basa, S., Carlberg, R. G., Fabbro, S., Fouchez, D., Hook, I. M., Howell, D. A., Lafoux, H., Neill, J. D., Palanque-Delabrouille, N., Perrett, K., Pritchet, C. J., Rich, J., Sullivan, M., Taillet, R., Aldering, G., Antilogus, P., Arsenijevic, V., Balland, C., Baumont, S., Bronder, J., Courtois, H., Ellis, R. S., Filiol, M., Gonçalves, A. C., Goobar, A., Guide, D., Hardin, D., Lusset, V., Lidman, C., McMahon, R., Mouchet, M., Mourao, A., Perlmutter, S., Ripoche, P., Tao, C., & Walton, N., **The Supernova Legacy Survey: measurement of Ω_M, Ω_Λ and w from the first year data set**, *A&A*, 2006, 447, 31

Baade, W., **The Absolute Photographic Magnitude of Supernovae.**, *ApJ*, 1938, 88, 285

Baade, W., **The Crab Nebula.**, *ApJ*, 1942, 96, 188

Bailey, S., Aldering, G., Antilogus, P., Aragon, C., Baltay, C., Bongard, S., Buton, C., Childress, M., Chotard, N., Copin, Y., Gangler, E., Loken, S., Nugent, P., Pain, R., Pecontal, E., Pereira, R., Perlmutter, S., Rabinowitz, D., Rigaudier, G., Runge, K., Scalzo, R., Smadja, G., Swift, H., Tao, C., Thomas, R. C., & Wu, C., **Using Spectral Flux Ratios to Standardize SN Ia Luminosities**, 2009, arXiv:0905.0340

Barbon, R., Benetti, S., Rosino, L., Cappellaro, E., & Turatto, M., **Type IA supernova 1989B in NGC 3627**, *A&A*, 1990, 237, 79

Barris, B. J., Tonry, J. L., Blondin, S., Challis, P., Chornock, R., Clocchiatti, A., Filippenko, A. V., Garnavich, P., Holland, S. T., Jha, S., Kirshner, R. P., Krisciunas, K., Leibundgut, B., Li, W., Matheson, T., Miknaitis, G., Riess, A. G., Schmidt, B. P., Smith, R. C., Sollerman, J., Spyromilio, J., Stubbs, C. W., Suntzeff, N. B., Aussel, H., Chambers, K. C., Connelley, M. S., Donovan, D., Henry, J. P., Kaiser, N., Liu, M. C., Martín, E. L., & Wainscoat, R. J., **Twenty-Three High-Redshift Supernovae from the Institute for Astronomy Deep Survey: Doubling the Supernova Sample at z > 0.7**, *ApJ*, 2004, 602, 571

Baumont, S., Balland, C., Astier, P., Guy, J., Hardin, D., Howell, D. A., Lidman, C., Mouchet, M., Pain, R., & Regnault, N., **PHotometry Assisted Spectral Extraction (PHASE) and identification of SNLS supernovae**, *A&A*, 2008, 491, 567

Benetti, S., Meikle, P., Stehle, M., Altavilla, G., Desidera, S., Folatelli, G., Goobar, A., Mattila, S., Mendez, J., Navasardyan, H., Pastorello, A., Patat, F., Riello, M., Ruiz-Lapuente, P., Tsvetkov, D., Turatto, M., Mazzali, P., & Hillebrandt, W., **Supernova 2002bo: inadequacy of the single parameter description**, *MNRAS*, 2004, 348, 261

Benetti, S., Cappellaro, E., Mazzali, P. A., Turatto, M., Altavilla, G., Bufano, F, Elias-Rosa, N., Kotak, R., Pignata, G., Salvo, M., & Stanishev, V., **The Diversity of Type Ia Supernovae: Evidence for Systematics?**, *ApJ*, 2005, 623, 1011

Benetti, S., Cappellaro, E., Turatto, M., Taubenberger, S., Harutyunyan, A., & Valenti, S., **Supernova 2002ic: The Collapse of a Stripped-Envelope, Massive Star in a Dense Medium?**, *ApJ*, 2006, 653, L129

Benetti, S., Harutyunyan, A., Agnoletto, I., Valenti, S., Pastorello, A., & Lorenzi, V., **Supernova 2008fz**, *Central Bureau Electronic Telegrams*, 2008, 1533, 1

Bessell, M. S., **UBVRI passbands**, *PASP*, 1990, 102, 1181

Blinnikov, S. I., Röpke, F. K., Sorokina, E. I., Gieseler, M., Reinecke, M., Travaglio, C., Hillebrandt, W., & Stritzinger, M., **Theoretical light curves for deflagration models of type Ia supernova**, *A&A*, 2006, 453, 229

Blondin, S., & Berlind, P., **Supernova 2008A in NGC 634**, *Central Bureau Electronic Telegrams*, 2008, 1198, 1

Blondin, S., & Tonry, J. L., **Determining the Type, Redshift, and Age of a Supernova Spectrum**, *ApJ*, 2007, 666, 1024

Blondin, S., Dessart, L., Leibundgut, B., Branch, D., Höflich, P., Tonry, J. L., Matheson, T., Foley, R. J., Chornock, R., Filippenko, A. V., Sollerman, J., Spyromilio, J., Kirshner, R. P., Wood-Vasey, W. M., Clocchiatti, A., Aguilera, C., Barris, B., Becker, A. C., Challis, P., Covarrubias, R., Davis, T. M., Garnavich, P., Hicken, M., Jha, S., Krisciunas, K., Li, W., Miceli, A., Miknaitis, G., Pignata, G., Prieto, J. L., Rest, A., Riess, A. G., Salvo, M. E., Schmidt, B. P., Smith, R. C., Stubbs, C. W., & Suntzeff, N. B., **Using Line Profiles to Test the Fraternity of Type Ia Supernovae at High and Low Redshifts**, *AJ*, 2006, 131, 1648

Blondin, S., Davis, T. M., Krisciunas, K., Schmidt, B. P., Sollerman, J., Wood-Vasey, W. M., Becker, A. C., Challis, P., Clocchiatti, A., Damke, G., Filippenko, A. V., Foley, R. J., Garnavich, P. M., Jha, S. W., Kirshner, R. P., Leibundgut, B., Li, W., Matheson, T., Miknaitis, G., Narayan, G., Pignata, G., Rest, A., Riess, A. G., Silverman, J. M., Smith, R. C., Spyromilio, J., Stritzinger, M., Stubbs, C. W., Suntzeff, N. B., Tonry, J. L., Tucker, B. E., & Zenteno, A., **Time Dilation in Type Ia Supernova Spectra at High Redshift**, *ApJ*, 2008, 682, 724

Blondin, S., Prieto, J. L., Patat, F., Challis, P., Hicken, M., Kirshner, R. P., Matheson, T., & Modjaz, M., **A Second Case of Variable Na I D Lines in a Highly Reddened Type Ia Supernova**, *ApJ*, 2009, 693, 207

Boisseau, J. R., & Wheeler, J. C., **The effect of background galaxy contamination on the absolute magnitude and light curve speed class of type IA supernovae**, *AJ*, 1991, 101, 1281

Bongard, S., Baron, E., Smadja, G., Branch, D., & Hauschildt, P. H., **Type Ia Supernova Spectral Line Ratios as Luminosity Indicators**, *ApJ*, 2006, 647, 513

Bowers, E. J. C., Meikle, W. P. S., Geballe, T. R., Walton, N. A., Pinto, P. A., Dhillon, V. S., Howell, S. B., & Harrop-Allin, M. K., **Infrared and optical spectroscopy of Type IA supernovae in the nebular phase**, *MNRAS*, 1997, 290, 663

Branch, D., & Bettis, C., **The Hubble diagram for supernovae**, *AJ*, 1978, 83, 224

Branch, D., & Miller, D. L., **Type IA supernovae as standard candles**, *ApJ*, 1993, 405, L5

Branch, D., Lacy, C. H., McCall, M. L., Sutherland, P. G., Uomoto, A., Wheeler, J. C., & Wills, B. J., **The Type I supernova 1981b in NGC 4536 - The first 100 days**, *ApJ*, 1983, 270, 123

Branch, D., Fisher, A., & Nugent, P., **On the relative frequencies of spectroscopically normal and peculiar type IA supernovae**, *AJ*, 1993, 106, 2383

Branch, D., Garnavich, P., Matheson, T., Baron, E., Thomas, R. C., Hatano, K., Challis, P., Jha, S., & Kirshner, R. P., **Optical Spectra of the Type Ia Supernova 1998aq**, *AJ*, 2003, 126, 1489

Branch, D., **Spectroscopically Peculiar Type Ia Supernovae and Implications for Progenitors**, *PASP*, 2001, 113, 169

Bronder, T. J., Hook, I. M., Astier, P., Balam, D., Balland, C., Basa, S., Carlberg, R. G., Conley, A., Fouchez, D., Guy, J., Howell, D. A., Neill, J. D., Pain, R., Perrett, K., Pritchet, C. J., Regnault, N., Sullivan, M., Baumont, S., Fabbro, S., Filliol, M., Perlmutter, S., & Ripoche, P., **SNLS spectroscopy: testing for evolution in type Ia supernovae**, *A&A*, 2008, 477, 717

Buta, R. J., & Turner, A., **The photometric properties of the bright Type I supernova 1981b in NGC 4536**, *PASP*, 1983, 95, 72

Candia, P., Krisciunas, K., Suntzeff, N. B., González, D., Espinoza, J., Leiton, R., Rest, A., Smith, R. C., Cuadra, J., Tavenner, T., Logan, C., Snider, K., Thomas, M., West, A. A., González, G., González, S., Phillips, M. M., Hastings, N. C., & McMillan, R., **Optical and Infrared Photometry of the Unusual Type Ia Supernova 2000cx**, *PASP*, 2003, 115, 277

Capaccioli, M., Cappellaro, E., della Valle, M., D'Onofrio, M., Rosino, L., & Turatto, M., **Distances of the Virgo and Coma clusters of galaxies through novae and supernovae**, *ApJ*, 1990, 350, 110

Cappellaro, E., Patat, F., Mazzali, P. A., Benetti, S., Danziger, J. I., Pastorello, A., Rizzi, L., Salvo, M., & Turatto, M., **Detection of a Light Echo from SN 1998BU**, *ApJ*, 2001, 549, L215

Cardelli, J. A., Clayton, G. C., & Mathis, J. S., **The relationship between infrared, optical, and ultraviolet extinction**, *ApJ*, 1989, 345, 245

Chandrasekhar, S., **The Maximum Mass of Ideal White Dwarfs**, *ApJ*, 1931, 74, 81

Chugai, N. N., & Danziger, I. J., **Supernova 1988Z - Low-Mass Ejecta Colliding with the Clumpy Wind**, *MNRAS*, 1994, 268, 173

Clifton, T., Ferreira, P. G., & Land, K., **Living in a Void: Testing the Copernican Principle with Distant Supernovae**, *Physical Review Letters*, 2008, 101, 131302

Colgate, S. A., & McKee, C., **Early Supernova Luminosity**, *ApJ*, 1969, 157, 623

Conley, A., Howell, D. A., Howes, A., Sullivan, M., Astier, P., Balam, D., Basa, S., Carlberg, R. G., Fouchez, D., Guy, J., Hook, I., Neill, J. D., Pain, R., Perrett, K., Pritchet, C. J., Regnault, N., Rich, J., Taillet, R., Aubourg, E., Bronder, J., Ellis, R. S., Fabbro, S., Filiol, M., Le Borgne, D., Palanque-Delabrouille, N., Perlmutter, S., & Ripoche, P., **The Rise Time of Type Ia Supernovae from the Supernova Legacy Survey**, *AJ*, 2006, 132, 1707

Conley, A., Sullivan, M., Hsiao, E. Y., Guy, J., Astier, P., Balam, D., Balland, C., Basa, S., Carlberg, R. G., Fouchez, D., Hardin, D., Howell, D. A., Hook, I. M., Pain, R., Perrett,

K., Pritchet, C. J., & Regnault, N., **SiFTO: An Empirical Method for Fitting SN Ia Light Curves**, *ApJ*, 2008, 681, 482

Contardo, G., Leibundgut, B., & Vacca, W. D., **Epochs of maximum light and bolometric light curves of type Ia supernovae**, *A&A*, 2000, 359, 876

Cooray, A., & Caldwell, R. R., **Large-scale bulk motions complicate the Hubble diagram**, *Phys. Rev. D*, 2006, 73, 103002

Cushing, M. C., Vacca, W. D., & Rayner, J. T., **Spextool: A Spectral Extraction Package for SpeX, a 0.8-5.5 Micron Cross-Dispersed Spectrograph**, *PASP*, 2004, 116, 362

Davis, T. M., Schmidt, B. P., & Kim, A. G., **Ideal Bandpasses for Type Ia Supernova Cosmology**, *PASP*, 2006, 118, 205

Drake, A. J., Williams, R., Mahabal, A., Djorgovski, S. G., Graham, M. J., Catelan, M., Beshore, E. C., Larson, S. M., Boattini, A., & Christensen, E., **Supernova 2008hp**, *Central Bureau Electronic Telegrams*, 2008, 1589, 1

Dyson, F. W., Eddington, A. S., & Davidson, C., **A Determination of the Deflection of Light by the Sun's Gravitational Field, from Observations Made at the Total Eclipse of May 29, 1919**, *Royal Society of London Philosophical Transactions Series A*, 1920, 220, 291

Einstein, A., **Die Feldgleichungen der Gravitation**, *Sitzungsberichte der Königlich Preußischen Akademie der Wissenschaften (Berlin), Seite 844-847.*, 1915, 844

Einstein, A., **Die Grundlage der allgemeinen Relativitätstheorie**, *Annalen der Physik*, 1916, 354, 769

Elias, J. H., Frogel, J. A., Hackwell, J. A., & Persson, S. E., **Infrared light curves of Type I supernovae**, *ApJ*, 1981, 251, L13

Elias, J. H., Matthews, K., Neugebauer, G., & Persson, S. E., **Type I supernovae in the infrared and their use as distance indicators**, *ApJ*, 1985, 296, 379

Elias-Rosa, N., Benetti, S., Cappellaro, E., Turatto, M., Mazzali, P. A., Patat, F., Meikle, W. P. S., Stehle, M., Pastorello, A., Pignata, G., Kotak, R., Harutyunyan, A., Altavilla, G., Navasardyan, H., Qiu, Y., Salvo, M., & Hillebrandt, W., **Anomalous extinction behaviour towards the Type Ia SN 2003cg**, *MNRAS*, 2006, 369, 1880

Elias-Rosa, N., Benetti, S., Turatto, M., Cappellaro, E., Valenti, S., Arkharov, A. A., Beckman, J. E., di Paola, A., Dolci, M., Filippenko, A. V., Foley, R. J., Krisciunas, K., Larionov, V. M., Li, W., Meikle, W. P. S., Pastorello, A., Valentini, G., & Hillebrandt, W., **SN 2002cv: a heavily obscured Type Ia supernova**, *MNRAS*, 2008, 384, 107

Ellis, R. S., Sullivan, M., Nugent, P. E., Howell, D. A., Gal-Yam, A., Astier, P., Balam, D., Balland, C., Basa, S., Carlberg, R. G., Conley, A., Fouchez, D., Guy, J., Hardin, D., Hook, I., Pain, R., Perrett, K., Pritchet, C. J., & Regnault, N., **Verifying the Cosmological Utility of Type Ia Supernovae: Implications of a Dispersion in the Ultraviolet Spectra**, *ApJ*, 2008, 674, 51

Ferreras, I., Pasquali, A., de Carvalho, R. R., de la Rosa, I. G., & Lahav, O., **A principal component analysis approach to the star formation history of elliptical galaxies in compact groups**, *MNRAS*, 2006, 370, 828

Filippenko, A. V., & Sargent, W. L. W., **A peculiar supernova in the spiral galaxy NGC4618**, *Nature*, 1985, 316, 407

Filippenko, A. V., Richmond, M. W., Branch, D., Gaskell, M., Herbst, W., Ford, C. H., Treffers, R. R., Matheson, T., Ho, L. C., Dey, A., Sargent, W. L. W., Small, T. A., & van Breugel, W. J. M., **The subluminous, spectroscopically peculiar type IA supernova 1991bg in the elliptical galaxy NGC 4374**, *AJ*, 1992a, 104, 1543

Filippenko, A. V., Richmond, M. W., Matheson, T., Shields, J. C., Burbidge, E. M., Cohen, R. D., Dickinson, M., Malkan, M. A., Nelson, B., Pietz, J., Schlegel, D., Schmeer, P., Spinrad, H., Steidel, C. C., Tran, H. D., & Wren, W., **The peculiar Type IA SN 1991T - Detonation of a white dwarf?**, *ApJ*, 1992b, 384, L15

Filippenko, A. V., **Supernova 1987K - Type II in youth, type Ib in old age**, *AJ*, 1988, 96, 1941

Filippenko, A. V., **Optical Spectra of Supernovae**, *ARA&A*, 1997, 35, 309

Folatelli, G., **Spectral homogeneity of type Ia supernovae**, *New Astronomy Review*, 2004, 48, 623

Foley, R. J., Filippenko, A. V., Leonard, D. C., Riess, A. G., Nugent, P., & Perlmutter, S., **A Definitive Measurement of Time Dilation in the Spectral Evolution of the Moderate-Redshift Type Ia Supernova 1997ex**, *ApJ*, 2005, 626, L11

Foley, R. J., Filippenko, A. V., Aguilera, C., Becker, A. C., Blondin, S., Challis, P., Cloc-chiatti, A., Covarrubias, R., Davis, T. M., Garnavich, P. M., Jha, S. W., Kirshner, R. P., Krisciunas, K., Leibundgut, B., Li, W., Matheson, T., Miceli, A., Miknaitis, G., Pig-nata, G., Rest, A., Riess, A. G., Schmidt, B. P., Smith, R. C., Sollerman, J., Spyromilio, J., Stubbs, C. W., Suntzeff, N. B., Tonry, J. L., Wood-Vasey, W. M., & Zenteno, A., **Constraining Cosmic Evolution of Type Ia Supernovae**, *ApJ*, 2008a, 684, 68

Foley, R. J., Filippenko, A. V., & Jha, S. W., **Luminosity Indicators in the Ultraviolet Spectra of Type Ia Supernovae**, *ApJ*, 2008b, 686, 117

Foley, R. J., Chornock, R., Filippenko, A. V., Ganeshalingam, M., Kirshner, R. P., Li, W., Cenko, S. B., Challis, P. J., Friedman, A. S., Modjaz, M., Silverman, J. M., & Wood-Vasey, W. M., **SN 2008ha: An Extremely Low Luminosity and Exceptionally Low Energy Supernova**, *AJ*, 2009, 138, 376

Freedman, W. L., **The Carnegie Supernova Project**, *Observing Dark Energy*, 2005, 339, 50

Friedman, A., **Über die Krümmung des Raumes**, *Zeitschrift für Physik* , 1922, 10, 377

Frieman, J. A., Bassett, B., Becker, A., Choi, C., Cinabro, D., DeJongh, F., Depoy, D. L., Dilday, B., Doi, M., Garnavich, P. M., Hogan, C. J., Holtzman, J., Im, M., Jha, S., Kessler, R., Konishi, K., Lampeitl, H., Marriner, J., Marshall, J. L., McGinnis, D., Mik-naitis, G., Nichol, R. C., Prieto, J. L., Riess, A. G., Richmond, M. W., Romani, R., Sako, M., Schneider, D. P., Smith, M., Takanashi, N., Tokita, K., van der Heyden, K., Yasuda, N., Zheng, C., Adelman-McCarthy, J., Annis, J., Assef, R. J., Barentine, J., Bender, R., Blandford, R. D., Boroski, W. N., Bremer, M., Brewington, H., Collins, C. A., Crotts, A., Dembicky, J., Eastman, J., Edge, A., Edmondson, E., Elson, E., Eyler, M. E., Filippenko, A. V., Foley, R. J., Frank, S., Goobar, A., Gueth, T., Gunn, J. E., Harvanek, M., Hopp, U., Ihara, Y., Ivezić, Ž., Kahn, S., Kaplan, J., Kent, S., Ketzeback, W., Kleinman, S. J., Kollatschny, W., Kron, R. G., Krzesiński, J., Lamenti, D., Leloudas, G., Lin, H., Long, D. C., Lucey, J., Lupton, R. H., Malanushenko, E., Malanushenko, V., McMillan, R. J., Mendez, J., Morgan, C. W., Morokuma, T., Nitta, A., Ostman, L., Pan, K., Rockosi, C. M., Romer, A. K., Ruiz-Lapuente, P., Saurage, G., Schlesinger, K., Snedden, S. A., Sollerman, J., Stoughton, C., Stritzinger, M., Subba Rao, M., Tucker, D., Vaisanen, P., Watson, L. C., Watters, S., Wheeler, J. C., Yanny, B., & York, D., **The Sloan Digital Sky Survey-II Supernova Survey: Technical Summary**, *AJ*, 2008, 135, 338

Frogel, J. A., Gregory, B., Kawara, K., Laney, D., Phillips, M. M., Terndrup, D., Vrba, F., & Whitford, A. E., **Infrared photometry and spectroscopy of supernova 1986g in NGC 5128-Centaurus A**, *ApJ*, 1987, 315, L129

Fukugita, M., Ichikawa, T., Gunn, J. E., Doi, M., Shimasaku, K., & Schneider, D. P., **The Sloan Digital Sky Survey Photometric System**, *AJ*, 1996, 111, 1748

Gallagher, J. S., Garnavich, P. M., Berlind, P., Challis, P., Jha, S., & Kirshner, R. P., **Chemistry and Star Formation in the Host Galaxies of Type Ia Supernovae**, *ApJ*, 2005, 634, 210

Gallagher, J. S., Garnavich, P. M., Caldwell, N., Kirshner, R. P., Jha, S. W., Li, W., Ganeshalingam, M., & Filippenko, A. V., **Supernovae in Early-Type Galaxies: Directly Connecting Age and Metallicity with Type Ia Luminosity**, *ApJ*, 2008, 685, 752

Gamezo, V. N., Khokhlov, A. M., Oran, E. S., Chtchelkanova, A. Y., & Rosenberg, R. O., **Thermonuclear Supernovae: Simulations of the Deflagration Stage and Their Implications**, *Science*, 2003, 299, 77

Gamezo, V. N., Khokhlov, A. M., & Oran, E. S., **Three-dimensional Delayed-Detonation Model of Type Ia Supernovae**, *ApJ*, 2005, 623, 337

Gamow, G., **My world line: An informal autobiography.**, *My world line: An informal autobiography., by Gamow, G.. New York, NY (USA): Viking Press, 178 p.*, 1970,

Garavini, G., Folatelli, G., Goobar, A., Nobili, S., Aldering, G., Amadon, A., Amanullah, R., Astier, P., Balland, C., Blanc, G., Burns, M. S., Conley, A., Dahlén, T., Deustua, S. E., Ellis, R., Fabbro, S., Fan, X., Frye, B., Gates, E. L., Gibbons, R., Goldhaber, G., Goldman, B., Groom, D. E., Haissinski, J., Hardin, D., Hook, I. M., Howell, D. A., Kasen, D., Kent, S., Kim, A. G., Knop, R. A., Lee, B. C., Lidman, C., Mendez, J., Miller, G. J., Moniez, M., Mourão, A., Newberg, H., Nugent, P. E., Pain, R., Perdereau, O., Perlmutter, S., Prasad, V., Quimby, R., Raux, J., Regnault, N., Rich, J., Richards, G. T., Ruiz-Lapuente, P., Sainton, G., Schaefer, B. E., Schahmaneche, K., Smith, E., Spadafora, A. L., Stanishev, V., Walton, N. A., Wang, L., & Wood-Vasey, W. M., **Spectroscopic Observations and Analysis of the Peculiar SN 1999aa**, *AJ*, 2004, 128, 387

Garavini, G., Aldering, G., Amadon, A., Amanullah, R., Astier, P., Balland, C., Blanc, G., Conley, A., Dahlén, T., Deustua, S. E., Ellis, R., Fabbro, S., Fadeyev, V., Fan, X., Folatelli, G., Frye, B., Gates, E. L., Gibbons, R., Goldhaber, G., Goldman, B., Goobar,

A., Groom, D. E., Haissinski, J., Hardin, D., Hook, I., Howell, D. A., Kent, S., Kim, A. G., Knop, R. A., Kowalski, M., Kuznetsova, N., Lee, B. C., Lidman, C., Mendez, J., Miller, G. J., Moniez, M., Mouchet, M., Mourão, A., Newberg, H., Nobili, S., Nugent, P. E., Pain, R., Perdereau, O., Perlmutter, S., Quimby, R., Regnault, N., Rich, J., Richards, G. T., Ruiz-Lapuente, P., Schaefer, B. E., Schahmaneche, K., Smith, E., Spadafora, A. L., Stanishev, V., Thomas, R. C., Walton, N. A., Wang, L., & Wood-Vasey, W. M., **Spectroscopic Observations and Analysis of the Unusual Type Ia SN 1999ac**, *AJ*, 2005, 130, 2278

Garavini, G., Folatelli, G., Nobili, S., Aldering, G., Amanullah, R., Antilogus, P., Astier, P., Blanc, G., Bronder, T., Burns, M. S., Conley, A., Deustua, S. E., Doi, M., Fabbro, S., Fadeyev, V., Gibbons, R., Goldhaber, G., Goobar, A., Groom, D. E., Hook, I., Howell, D. A., Kashikawa, N., Kim, A. G., Kowalski, M., Kuznetsova, N., Lee, B. C., Lidman, C., Mendez, J., Morokuma, T., Motohara, K., Nugent, P. E., Pain, R., Perlmutter, S., Quimby, R., Raux, J., Regnault, N., Ruiz-Lapuente, P., Sainton, G., Schahmaneche, K., Smith, E., Spadafora, A. L., Stanishev, V., Thomas, R. C., Walton, N. A., Wang, L., Wood-Vasey, W. M., & Yasuda, N., **Quantitative comparison between type Ia supernova spectra at low and high redshifts: a case study**, *A&A*, 2007, 470, 411

Garnavich, P. M., Kirshner, R. P., Challis, P., Tonry, J., Gilliland, R. L., Smith, R. C., Clocchiatti, A., Diercks, A., Filippenko, A. V., Hamuy, M., Hogan, C. J., Leibundgut, B., Phillips, M. M., Reiss, D., Riess, A. G., Schmidt, B. P., Schommer, R. A., Spyromilio, J., Stubbs, C., Suntzeff, N. B., & Wells, L., **Constraints on Cosmological Models from Hubble Space Telescope Observations of High-z Supernovae**, *ApJ*, 1998, 493, L53

Garnavich, P., Jha, S., Kirshner, R., Challis, P., & Calkins, M., **Supernova 1999cl in NGC 4501**, *IAU Circ.*, 1999, 7190, 2

Garnavich, P. M., Bonanos, A. Z., Krisciunas, K., Jha, S., Kirshner, R. P., Schlegel, E. M., Challis, P., Macri, L. M., Hatano, K., Branch, D., Bothun, G. D., & Freedman, W. L., **The Luminosity of SN 1999by in NGC 2841 and the Nature of "Peculiar" Type Ia Supernovae**, *ApJ*, 2004, 613, 1120

Goldhaber, G., Groom, D. E., Kim, A., Aldering, G., Astier, P., Conley, A., Deustua, S. E., Ellis, R., Fabbro, S., Fruchter, A. S., Goobar, A., Hook, I., Irwin, M., Kim, M., Knop, R. A., Lidman, C., McMahon, R., Nugent, P. E., Pain, R., Panagia, N., Pennypacker, C. R., Perlmutter, S., Ruiz-Lapuente, P., Schaefer, B., Walton, N. A., & York, T.,

Timescale Stretch Parameterization of Type Ia Supernova B-Band Light Curves, *ApJ*, 2001, 558, 359

Gomez, G., Lopez, R., & Sanchez, F., **The Canaris Type IA Supernovae Archive (I)**, *AJ*, 1996, 112, 2094

Guth, A. H., **Inflationary universe: A possible solution to the horizon and flatness problems**, *Phys. Rev. D*, 1981, 23, 347

Guy, J., Astier, P., Nobili, S., Regnault, N., & Pain, R., **SALT: a spectral adaptive light curve template for type Ia supernovae**, *A&A*, 2005, 443, 781

Guy, J., Astier, P., Baumont, S., Hardin, D., Pain, R., Regnault, N., Basa, S., Carlberg, R. G., Conley, A., Fabbro, S., Fouchez, D., Hook, I. M., Howell, D. A., Perrett, K., Pritchet, C. J., Rich, J., Sullivan, M., Antilogus, P., Aubourg, E., Bazin, G., Bronder, J., Filiol, M., Palanque-Delabrouille, N., Ripoche, P., & Ruhlmann-Kleider, V., **SALT2: using distant supernovae to improve the use of type Ia supernovae as distance indicators**, *A&A*, 2007, 466, 11

Hachinger, S., Mazzali, P. A., & Benetti, S., **Exploring the spectroscopic diversity of Type Ia supernovae**, *MNRAS*, 2006, 370, 299

Hachinger, S., Mazzali, P. A., Tanaka, M., Hillebrandt, W., & Benetti, S., **Spectral luminosity indicators in Type Ia supernovae. Understanding the (SiII) line-strength ratio and beyond**, *MNRAS*, 2008, 389, 1087

Hachisu, I., Kato, M., & Nomoto, K., **A New Model for Progenitor Systems of Type IA Supernovae**, *ApJ*, 1996, 470, L97

Hamuy, M., Phillips, M. M., Wells, L. A., & Maza, J., **K Corrections for type IA supernovae**, *PASP*, 1993, 105, 787

Hamuy, M., Phillips, M. M., Maza, J., Suntzeff, N. B., Schommer, R. A., & Aviles, R., **A Hubble diagram of distant type IA supernovae**, *AJ*, 1995, 109, 1

Hamuy, M., Phillips, M. M., Suntzeff, N. B., Schommer, R. A., Maza, J., Antezan, A. R., Wischnjewsky, M., Valladares, G., Muena, C., Gonzales, L. E., Aviles, R., Wells, L. A., Smith, R. C., Navarrete, M., Covarrubias, R., Williger, G. M., Walker, A. R., Layden, A. C., Elias, J. H., Baldwin, J. A., Hernandez, M., Tirado, H., Ugarte, P., Elston, R., Saavedra, N., Barrientos, F., Costa, E., Lira, P., Ruiz, M. T., Anguita, C., Gomez, X.,

Ortiz, P., della Valle, M., Danziger, J., Storm, J., Kim, Y.-C., Bailyn, C., Rubenstein, E. P., Tucker, D., Cersosimo, S., Mendez, R. A., Siciliano, L., Sherry, W., Chaboyer, B., Koopmann, R. A., Geisler, D., Sarajedini, A., Dey, A., Tyson, N., Rich, R. M., Gal, R., Lamontagne, R., Caldwell, N., Guhathakurta, P., Phillips, A. C., Szkody, P., Prosser, C., Ho, L. C., McMahan, R., Baggley, G., Cheng, K.-P., Havlen, R., Wakamatsu, K., Janes, K., Malkan, M., Baganoff, F., Seitzer, P., Shara, M., Sturch, C., Hesser, J., Hartig, A. N. P., Hughes, J., Welch, D., Williams, T. B., Ferguson, H., Francis, P. J., French, L., Bolte, M., Roth, J., Odewahn, S., Howell, S., & Krzeminski, W., **BVRI Light Curves for 29 Type IA Supernovae**, *AJ*, 1996a, 112, 2408

Hamuy, M., Phillips, M. M., Suntzeff, N. B., Schommer, R. A., Maza, J., & Aviles, R., **The Absolute Luminosities of the Calan/Tololo Type IA Supernovae**, *AJ*, 1996b, 112, 2391

Hamuy, M., Phillips, M. M., Suntzeff, N. B., Schommer, R. A., Maza, J., & Aviles, R., **The Hubble Diagram of the Calan/Tololo Type IA Supernovae and the Value of HO**, *AJ*, 1996c, 112, 2398

Hamuy, M., Trager, S. C., Pinto, P. A., Phillips, M. M., Schommer, R. A., Ivanov, V., & Suntzeff, N. B., **A Search for Environmental Effects on Type IA Supernovae**, *AJ*, 2000, 120, 1479

Hamuy, M., Maza, J., Pinto, P. A., Phillips, M. M., Suntzeff, N. B., Blum, R. D., Olsen, K. A. G., Pinfield, D. J., Ivanov, V. D., Augusteijn, T., Brillant, S., Chadid, M., Cuby, J.-G., Doublier, V., Hainaut, O. R., Le Floc'h, E., Lidman, C., Petr-Gotzens, M. G., Pompei, E., & Vanzi, L., **Optical and Infrared Spectroscopy of SN 1999ee and SN 1999ex**, *AJ*, 2002, 124, 417

Hamuy, M., Phillips, M. M., Suntzeff, N. B., Maza, J., González, L. E., Roth, M., Krisciunas, K., Morrell, N., Green, E. M., Persson, S. E., & McCarthy, P. J., **An asymptotic-giant-branch star in the progenitor system of a type Ia supernova**, *Nature*, 2003, 424, 651

Hamuy, M., Folatelli, G., Morrell, N. I., Phillips, M. M., Suntzeff, N. B., Persson, S. E., Roth, M., Gonzalez, S., Krzeminski, W., Contreras, C., Freedman, W. L., Murphy, D. C., Madore, B. F., Wyatt, P., Maza, J., Filippenko, A. V., Li, W., & Pinto, P. A., **The Carnegie Supernova Project: The Low-Redshift Survey**, *PASP*, 2006, 118, 2

Harrison, E. R., **Fluctuations at the Threshold of Classical Cosmology**, *Phys. Rev. D*, 1970, 1, 2726

Hatano, K., Branch, D., Lentz, E. J., Baron, E., Filippenko, A. V., & Garnavich, P. M., **On the Spectroscopic Diversity of Type IA Supernovae**, *ApJ*, 2000, 543, L49

Hawking, S. W., **The development of irregularities in a single bubble inflationary universe**, *Physics Letters B*, 1982, 115, 295

Hernandez, M., Meikle, W. P. S., Aparicio, A., Benn, C. R., Burleigh, M. R., Chrysostomou, A. C., Fernandes, A. J. L., Geballe, T. R., Hammersley, P. L., Iglesias-Paramo, J., James, D. J., James, P. A., Kemp, S. N., Lister, T. A., Martinez-Delgado, D., Oscoz, A., Pollacco, D. L., Rozas, M., Smartt, S. J., Sorensen, P., Swaters, R. A., Telting, J. H., Vacca, W. D., Walton, N. A., & Zapatero-Osorio, M. R., **An early-time infrared and optical study of the Type Ia Supernova 1998bu in M96**, *MNRAS*, 2000, 319, 223

Hicken, M., Garnavich, P. M., Prieto, J. L., Blondin, S., DePoy, D. L., Kirshner, R. P., & Parrent, J., **The Luminous and Carbon-rich Supernova 2006gz: A Double Degenerate Merger?**, *ApJ*, 2007, 669, L17

Hicken, M., Challis, P., Jha, S., Kirshner, R. P., Matheson, T., Modjaz, M., Rest, A., & Wood-Vasey, W. M., **CfA3: 185 Type Ia Supernova Light Curves from the CfA**, 2009, arXiv:0901.4787

Höflich, P., Khokhlov, A., Wheeler, J. C., Phillips, M. M., Suntzeff, N. B., & Hamuy, M., **Maximum Brightness and Postmaximum Decline of Light Curves of Type IA Supernovae: A Comparison of Theory and Observations**, *ApJ*, 1996, 472, L81

Höflich, P., Wheeler, J. C., & Thielemann, F. K., **Type IA Supernovae: Influence of the Initial Composition on the Nucleosynthesis, Light Curves, and Spectra and Consequences for the Determination of Omega M and Lambda**, *ApJ*, 1998, 495, 617

Höflich, P., Gerardy, C. L., Fesen, R. A., & Sakai, S., **Infrared Spectra of the Subluminous Type Ia Supernova SN 1999by**, *ApJ*, 2002, 568, 791

Hogg, D. W., Baldry, I. K., Blanton, M. R., & Eisenstein, D. J., **The K correction**, 2002, arXiv:astro-ph/0210394

Hogg, D. W., **Distance measures in cosmology**, 1999, arXiv:astro-ph/9905116

Holz, D. E., & Linder, E. V., **Safety in Numbers: Gravitational Lensing Degradation of the Luminosity Distance-Redshift Relation**, *ApJ*, 2005, 631, 678

Hook, I. M., Howell, D. A., Aldering, G., Amanullah, R., Burns, M. S., Conley, A., Deustua, S. E., Ellis, R., Fabbro, S., Fadeyev, V., Folatelli, G., Garavini, G., Gibbons, R., Goldhaber, G., Goobar, A., Groom, D. E., Kim, A. G., Knop, R. A., Kowalski, M., Lidman, C., Nobili, S., Nugent, P. E., Pain, R., Pennypacker, C. R., Perlmutter, S., Ruiz-Lapuente, P., Sainton, G., Schaefer, B. E., Smith, E., Spadafora, A. L., Stanishev, V., Thomas, R. C., Walton, N. A., Wang, L., & Wood-Vasey, W. M., **Spectra of High-Redshift Type Ia Supernovae and a Comparison with Their Low-Redshift Counterparts**, *AJ*, 2005, 130, 2788

Howell, A., & Nugent, P., **Broad lightcurve SNe Ia: asymmetry or something else?**, *Cosmic explosions in three dimensions*, 2004, 151

Howell, D. A., Sullivan, M., Perrett, K., Bronder, T. J., Hook, I. M., Astier, P., Aubourg, E., Balam, D., Basa, S., Carlberg, R. G., Fabbro, S., Fouchez, D., Guy, J., Lafoux, H., Neill, J. D., Pain, R., Palanque-Delabrouille, N., Pritchet, C. J., Regnault, N., Rich, J., Taillet, R., Knop, R., McMahon, R. G., Perlmutter, S., & Walton, N. A., **Gemini Spectroscopy of Supernovae from the Supernova Legacy Survey: Improving High-Redshift Supernova Selection and Classification**, *ApJ*, 2005, 634, 1190

Howell, D. A., Sullivan, M., Nugent, P. E., Ellis, R. S., Conley, A. J., Le Borgne, D., Carlberg, R. G., Guy, J., Balam, D., Basa, S., Fouchez, D., Hook, I. M., Hsiao, E. Y., Neill, J. D., Pain, R., Perrett, K. M., & Pritchet, C. J., **The type Ia supernova SNLS-03D3bb from a super-Chandrasekhar-mass white dwarf star**, *Nature*, 2006, 443, 308

Howell, D. A., Sullivan, M., Conley, A., & Carlberg, R., **Predicted and Observed Evolution in the Mean Properties of Type Ia Supernovae with Redshift**, *ApJ*, 2007, 667, L37

Howell, D. A., Sullivan, M., Brown, E. F., Conley, A., LeBorgne, D., Hsiao, E. Y., Astier, P., Balam, D., Balland, C., Basa, S., Carlberg, R. G., Fouchez, D., Guy, J., Hardin, D., Hook, I. M., Pain, R., Perrett, K., Pritchet, C. J., Regnault, N., Baumont, S., LeDu, J., Lidman, C., Perlmutter, S., Suzuki, N., Walker, E. S., & Wheeler, J. C., **The Effect of Progenitor Age and Metallicity on Luminosity and ^{56}Ni Yield in Type Ia Supernovae**, *ApJ*, 2009, 691, 661

Howell, D. A., **The Progenitors of Subluminous Type Ia Supernovae**, *ApJ*, 2001, 554, L193

Hoyle, F., & Fowler, W. A., **Nucleosynthesis in Supernovae.**, *ApJ*, 1960, 132, 565

Hsiao, E. Y., Conley, A., Howell, D. A., Sullivan, M., Pritchet, C. J., Carlberg, R. G., Nugent, P. E., & Phillips, M. M., **K-Corrections and Spectral Templates of Type Ia Supernovae**, *ApJ*, 2007a, 663, 1187

Hsiao, E. Y., Graham, M., Balam, D., & Howell, D. A., **Supernova 2007gk in MCG +11-20-27**, *Central Bureau Electronic Telegrams*, 2007b, 1025, 1

Hsiao, E. Y., Graham, M. L., Pritchet, C. J., & Balam, D., **Supernova 2008fz**, *Central Bureau Electronic Telegrams*, 2008a, 1524, 2

Hsiao, E. Y., Graham, M. L., Pritchet, C. J., Parker, A., Sadavoy, S., & Balam, D., **Supernova 2008hp**, *Central Bureau Electronic Telegrams*, 2008b, 1589, 2

Hubble, E., **A Relation between Distance and Radial Velocity among Extra-Galactic Nebulae**, *Proceedings of the National Academy of Science*, 1929, 15, 168

Hubble, E., **Effects of Red Shifts on the Distribution of Nebulae**, *ApJ*, 1936, 84, 517

Hui, L., & Greene, P. B., **Correlated fluctuations in luminosity distance and the importance of peculiar motion in supernova surveys**, *Phys. Rev. D*, 2006, 73, 123526

Humason, M. L., Mayall, N. U., & Sandage, A. R., **Redshifts and magnitudes of extra-galactic nebulae.**, *AJ*, 1956, 61, 97

Huterer, D., & Turner, M. S., **Probing dark energy: Methods and strategies**, *Phys. Rev. D*, 2001, 64, 123527

Iben, I., Jr., & Tutukov, A. V., **Supernovae of type I as end products of the evolution of binaries with components of moderate initial mass (M not greater than about 9 solar masses)**, *ApJS*, 1984, 54, 335

Ivanov, V. D., Hamuy, M., & Pinto, P. A., **On the Relation between Peak Luminosity and Parent Population of Type IA Supernovae: A New Tool for Probing the Ages of Distant Galaxies**, *ApJ*, 2000, 542, 588

Iwamoto, K., Mazzali, P. A., Nomoto, K., Umeda, H., Nakamura, T., Patat, F., Danziger, I. J., Young, T. R., Suzuki, T., Shigeyama, T., Augusteijn, T., Doublier, V., Gonzalez, J.-F., Boehnhardt, H., Brewer, J., Hainaut, O. R., Lidman, C., Leibundgut, B., Cappellaro, E., Turatto, M., Galama, T. J., Vreeswijk, P. M., Kouveliotou, C., van Paradijs, J., Pian, E., Palazzi, E., & Frontera, F., **A hypernova model for the supernova associated with the gamma-ray burst of 25 April 1998**, *Nature*, 1998, 395, 672

Jha, S., Garnavich, P. M., Kirshner, R. P., Challis, P., Soderberg, A. M., Macri, L. M., Huchra, J. P., Barmby, P., Barton, E. J., Berlind, P., Brown, W. R., Caldwell, N., Calkins, M. L., Kannappan, S. J., Koranyi, D. M., Pahre, M. A., Rines, K. J., Stanek, K. Z., Stefanik, R. P., Szentgyorgyi, A. H., Väisänen, P., Wang, Z., Zajac, J. M., Riess, A. G., Filippenko, A. V., Li, W., Modjaz, M., Treffers, R. R., Hergenrother, C. W., Grebel, E. K., Seitzer, P., Jacoby, G. H., Benson, P. J., Rizvi, A., Marschall, L. A., Goldader, J. D., Beasley, M., Vacca, W. D., Leibundgut, B., Spyromilio, J., Schmidt, B. P., & Wood, P. R., **The Type IA Supernova 1998BU in M96 and the Hubble Constant**, *ApJS*, 1999, 125, 73

Jha, S., Kirshner, R. P., Challis, P., Garnavich, P. M., Matheson, T., Soderberg, A. M., Graves, G. J. M., Hicken, M., Alves, J. F., Arce, H. G., Balog, Z., Barmby, P., Barton, E. J., Berlind, P., Bragg, A. E., Briceño, C., Brown, W. R., Buckley, J. H., Caldwell, N., Calkins, M. L., Carter, B. J., Concannon, K. D., Donnelly, R. H., Eriksen, K. A., Fabricant, D. G., Falco, E. E., Fiore, F., Garcia, M. R., Gómez, M., Grogin, N. A., Groner, T., Groot, P. J., Haisch, K. E., Jr., Hartmann, L., Hergenrother, C. W., Holman, M. J., Huchra, J. P., Jayawardhana, R., Jerius, D., Kannappan, S. J., Kim, D.-W., Kleyna, J. T., Kochanek, C. S., Koranyi, D. M., Krockenberger, M., Lada, C. J., Luhman, K. L., Luu, J. X., Macri, L. M., Mader, J. A., Mahdavi, A., Marengo, M., Marsden, B. G., McLeod, B. A., McNamara, B. R., Megeath, S. T., Moraru, D., Mossman, A. E., Muench, A. A., Muñoz, J. A., Muzerolle, J., Naranjo, O., Nelson-Patel, K., Pahre, M. A., Patten, B. M., Peters, J., Peters, W., Raymond, J. C., Rines, K., Schild, R. E., Sobczak, G. J., Spahr, T. B., Stauffer, J. R., Stefanik, R. P., Szentgyorgyi, A. H., Tollestrup, E. V., Väisänen, P., Vikhlinin, A., Wang, Z., Willner, S. P., Wolk, S. J., Zajac, J. M., Zhao, P., & Stanek, K. Z., **UBVRI Light Curves of 44 Type Ia Supernovae**, *AJ*, 2006, 131, 527

Jha, S., Riess, A. G., & Kirshner, R. P., **Improved Distances to Type Ia Supernovae with Multicolor Light-Curve Shapes: MLCS2k2**, *ApJ*, 2007, 659, 122

Johnson, H. L., & Morgan, W. W., **Fundamental stellar photometry for standards of spectral type on the revised system of the Yerkes spectral atlas**, *ApJ*, 1953, 117, 313

Kahabka, P., & van den Heuvel, E. P. J., **Luminous Supersoft X-Ray Sources**, *ARA&A*, 1997, 35, 69

Karp, A. H., Lasher, G., Chan, K. L., & Salpeter, E. E., **The opacity of expanding media - The effect of spectral lines**, *ApJ*, 1977, 214, 161

Kasen, D., & Woosley, S. E., **On the Origin of the Type Ia Supernova Width-Luminosity Relation**, *ApJ*, 2007, 656, 661

Kasen, D., Nugent, P., Wang, L., Howell, D. A., Wheeler, J. C., Höflich, P., Baade, D., Baron, E., & Hauschildt, P. H., **Analysis of the Flux and Polarization Spectra of the Type Ia Supernova SN 2001el: Exploring the Geometry of the High-Velocity Ejecta**, *ApJ*, 2003, 593, 788

Kasen, D., **Secondary Maximum in the Near-Infrared Light Curves of Type Ia Supernovae**, *ApJ*, 2006, 649, 939

Kawabata, K. S., Maeda, K., Nomoto, K., Taubenberger, S., Tanaka, M., Hattori, T., & Itagaki, K., **A unique core-collapse supernova in an elliptical galaxy**, 2009, arXiv:0906.2811

Kerzendorf, W. E., Schmidt, B. P., Asplund, M., Nomoto, K., Podsiadlowski, P., Frebel, A., Fesen, R. A., & Yong, D., **Subaru high-resolution spectroscopy of Star G in the Tycho supernova remnant**, 2009, arXiv:0906.0982

Khokhlov, A. M., **Delayed detonation model for type IA supernovae**, *A&A*, 1991, 245, 114

Kidger, M., Casares, J., Garcia-Lario, P., Mampaso, A., Manteiga, M., Jones, D., Ellis, R., Allington-Smith, J., Charles, P., Ruiz-Lapuente, P., Lopez, R., Canal, R., Wheeler, J. C., Thompson, K., & Goodrich, R., **Supernovae 1989A in NGC 3687 and 1989B in NGC 3627**, *IAU Circ.*, 1989, 4740, 1

Kim, A., Goobar, A., & Perlmutter, S., **A Generalized K Correction for Type IA Supernovae: Comparing R-band Photometry beyond z=0.2 with B, V, and R-band Nearby Photometry**, *PASP*, 1996, 108, 190

Kirkman, D., Tytler, D., Suzuki, N., O'Meara, J. M., & Lubin, D., **The Cosmological Baryon Density from the Deuterium-to-Hydrogen Ratio in QSO Absorption Systems: D/H toward Q1243+3047**, *ApJS*, 2003, 149, 1

Kirshner, R. P., Jeffery, D. J., Leibundgut, B., Challis, P. M., Sonneborn, G., Phillips, M. M., Suntzeff, N. B., Smith, R. C., Winkler, P. F., Winge, C., Hamuy, M., Hunter, D. A., Roth, K. C., Blades, J. C., Branch, D., Chevalier, R. A., Fransson, C., Panagia, N., Wagoner, R. V., Wheeler, J. C., & Harkness, R. P., **SN 1992A: Ultraviolet and Optical Studies Based on HST, IUE, and CTIO Observations**, *ApJ*, 1993, 415, 589

Knop, R. A., Aldering, G., Amanullah, R., Astier, P., Blanc, G., Burns, M. S., Conley, A., Deustua, S. E., Doi, M., Ellis, R., Fabbro, S., Folatelli, G., Fruchter, A. S., Garavini, G., Garmond, S., Garton, K., Gibbons, R., Goldhaber, G., Goobar, A., Groom, D. E., Hardin, D., Hook, I., Howell, D. A., Kim, A. G., Lee, B. C., Lidman, C., Mendez, J., Nobili, S., Nugent, P. E., Pain, R., Panagia, N., Pennypacker, C. R., Perlmutter, S., Quimby, R., Raux, J., Regnault, N., Ruiz-Lapuente, P., Sainton, G., Schaefer, B., Schahmaneche, K., Smith, E., Spadafora, A. L., Stanishev, V., Sullivan, M., Walton, N. A., Wang, L., Wood-Vasey, W. M., & Yasuda, N., **New Constraints on Ω_M, Ω_Λ, and w from an Independent Set of 11 High-Redshift Supernovae Observed with the Hubble Space Telescope**, *ApJ*, 2003, 598, 102

Kong, X., & Cheng, F. Z., **Principal component analysis for spectral indices of stellar populations**, *MNRAS*, 2001, 323, 1035

Kotak, R., Meikle, W. P. S., Pignata, G., Stehle, M., Smartt, S. J., Benetti, S., Hillebrandt, W., Lennon, D. J., Mazzali, P. A., Patat, F., & Turatto, M., **Spectroscopy of the type Ia supernova SN 2002er: Days -11 to +215**, *A&A*, 2005, 436, 1021

Kowal, C. T., **Absolute magnitudes of supernovae.**, *AJ*, 1968, 73, 1021

Krisciunas, K., Hastings, N. C., Loomis, K., McMillan, R., Rest, A., Riess, A. G., & Stubbs, C., **Uniformity of (V-Near-Infrared) Color Evolution of Type Ia Supernovae and Implications for Host Galaxy Extinction Determination**, *ApJ*, 2000, 539, 658

Krisciunas, K., Phillips, M. M., Stubbs, C., Rest, A., Miknaitis, G., Riess, A. G., Suntzeff, N. B., Roth, M., Persson, S. E., & Freedman, W. L., **Optical and Infrared Photometry of the Type Ia Supernovae 1999da, 1999dk, 1999gp, 2000bk, and 2000ce**, *AJ*, 2001, 122, 1616

Krisciunas, K., Suntzeff, N. B., Candia, P., Arenas, J., Espinoza, J., Gonzalez, D., Gonzalez, S., Höflich, P. A., Landolt, A. U., Phillips, M. M., & Pizarro, S., **Optical and Infrared Photometry of the Nearby Type Ia Supernova 2001el**, *AJ*, 2003, 125, 166

Krisciunas, K., Phillips, M. M., & Suntzeff, N. B., **Hubble Diagrams of Type Ia Supernovae in the Near-Infrared**, *ApJ*, 2004a, 602, L81

Krisciunas, K., Phillips, M. M., Suntzeff, N. B., Persson, S. E., Hamuy, M., Antezana, R., Candia, P., Clocchiatti, A., DePoy, D. L., Germany, L. M., Gonzalez, L., Gonzalez, S., Krzeminski, W., Maza, J., Nugent, P. E., Qiu, Y., Rest, A., Roth, M., Stritzinger, M., Strolger, L.-G., Thompson, I., Williams, T. B., & Wischnjewsky, M., **Optical and Infrared Photometry of the Nearby Type Ia Supernovae 1999ee, 2000bh, 2000ca, and 2001ba**, *AJ*, 2004b, 127, 1664

Krisciunas, K., Suntzeff, N. B., Phillips, M. M., Candia, P., Prieto, J. L., Antezana, R., Chassagne, R., Chen, H.-W., Dickinson, M., Eisenhardt, P. R., Espinoza, J., Garnavich, P. M., González, D., Harrison, T. E., Hamuy, M., Ivanov, V. D., Krzemiński, W., Kulesa, C., McCarthy, P., Moro-Martín, A., Muena, C., Noriega-Crespo, A., Persson, S. E., Pinto, P. A., Roth, M., Rubenstein, E. P., Stanford, S. A., Stringfellow, G. S., Zapata, A., Porter, A., & Wischnjewsky, M., **Optical and Infrared Photometry of the Type Ia Supernovae 1991T, 1991bg, 1999ek, 2001bt, 2001cn, 2001cz, and 2002bo**, *AJ*, 2004c, 128, 3034

Krisciunas, K., Prieto, J. L., Garnavich, P. M., Riley, J.-L. G., Rest, A., Stubbs, C., & McMillan, R., **Photometry of the Type Ia Supernovae 1999cc, 1999cl, and 2000cf**, *AJ*, 2006, 131, 1639

Krisciunas, K., Garnavich, P. M., Stanishev, V., Suntzeff, N. B., Prieto, J. L., Espinoza, J., Gonzalez, D., Salvo, M. E., Elias de la Rosa, N., Smartt, S. J., Maund, J. R., & Kudritzki, R.-P., **The Type Ia Supernova 2004S, a Clone of SN 2001el, and the Optimal Photometric Bands for Extinction Estimation**, *AJ*, 2007, 133, 58

Landolt, A. U., **UBVRI photometric standard stars in the magnitude range 11.5-16.0 around the celestial equator**, *AJ*, 1992, 104, 340

Leith, B. M., Ng, S. C. C., & Wiltshire, D. L., **Gravitational Energy as Dark Energy: Concordance of Cosmological Tests**, *ApJ*, 2008, 672, L91

Lentz, E. J., Baron, E., Branch, D., Hauschildt, P. H., & Nugent, P. E., **Metallicity Effects in Non-LTE Model Atmospheres of Type IA Supernovae**, *ApJ*, 2000, 530, 966

Li, W. D., Qiu, Y. L., Qiao, Q. Y., Zhu, X. H., Hu, J. Y., Richmond, M. W., Filippenko, A. V., Treffers, R. R., Peng, C. Y., & Leonard, D. C., **The Type IA Supernova 1997BR in ESO 576-G40**, *AJ*, 1999, 117, 2709

Li, W. D., Filippenko, A. V., Treffers, R. R., Friedman, A., Halderson, E., Johnson, R. A., King, J. Y., Modjaz, M., Papenkova, M., Sato, Y., & Shefler, T., **The Lick Observatory Supernova Search**, *American Institute of Physics Conference Series*, 2000, 522, 103

Li, W., Filippenko, A. V., Gates, E., Chornock, R., Gal-Yam, A., Ofek, E. O., Leonard, D. C., Modjaz, M., Rich, R. M., Riess, A. G., & Treffers, R. R., **The Unique Type Ia Supernova 2000cx in NGC 524**, *PASP*, 2001a, 113, 1178

Li, W., Filippenko, A. V., Treffers, R. R., Riess, A. G., Hu, J., & Qiu, Y., **A High Intrinsic Peculiarity Rate among Type IA Supernovae**, *ApJ*, 2001b, 546, 734

Li, W., Filippenko, A. V., Chornock, R., Berger, E., Berlind, P., Calkins, M. L., Challis, P., Fassnacht, C., Jha, S., Kirshner, R. P., Matheson, T., Sargent, W. L. W., Simcoe, R. A., Smith, G. H., & Squires, G., **SN 2002cx: The Most Peculiar Known Type Ia Supernova**, *PASP*, 2003, 115, 453

Lidman, C., Howell, D. A., Folatelli, G., Garavini, G., Nobili, S., Aldering, G., Amanullah, R., Antilogus, P., Astier, P., Blanc, G., Burns, M. S., Conley, A., Deustua, S. E., Doi, M., Ellis, R., Fabbro, S., Fadeyev, V., Gibbons, R., Goldhaber, G., Goobar, A., Groom, D. E., Hook, I., Kashikawa, N., Kim, A. G., Knop, R. A., Lee, B. C., Mendez, J., Morokuma, T., Motohara, K., Nugent, P. E., Pain, R., Perlmutter, S., Prasad, V., Quimby, R., Raux, J., Regnault, N., Ruiz-Lapuente, P., Sainton, G., Schaefer, B. E., Schahmaneche, K., Smith, E., Spadafora, A. L., Stanishev, V., Walton, N. A., Wang, L., Wood-Vasey, W. M., Yasuda, N., & The Supernova Cosmology Project, **Spectroscopic confirmation of high-redshift supernovae with the ESO VLT.**, *A&A*, 2005, 430, 843

Livio, M., & Riess, A. G., **Have the Elusive Progenitors of Type Ia Supernovae Been Discovered?**, *ApJ*, 2003, 594, L93

Livio, M., **The Progenitors of Type Ia Supernovae**, *Type Ia Supernovae, Theory and Cosmology*, 2000, 33

Livio, M., **Type Ia supernovae and their implications for cosmology**, *Supernovae and Gamma-Ray Bursts: the Greatest Explosions since the Big Bang*, 2001, 334

Lundmark, K., **Nebulæ, The motions and the distances of spiral**, *MNRAS*, 1925, 85, 865

Madgwick, D. S., Hewett, P. C., Mortlock, D. J., & Wang, L., **Spectroscopic Detection of Type Ia Supernovae in the Sloan Digital Sky Survey**, *ApJ*, 2003, 599, L33

Maiolino, R., Rieke, G. H., & Rieke, M. J., **Correction of the Atmospheric Transmission in Infrared Spectroscopy**, *AJ*, 1996, 111, 537

Malmquist, G., *Lund Medd. Ser. II*, 1920, 22, 1

Mannucci, F., Della Valle, M., Panagia, N., Cappellaro, E., Cresci, G., Maiolino, R., Petrosian, A., & Turatto, M., **The supernova rate per unit mass**, *A&A*, 2005, 433, 807

Mannucci, F., Della Valle, M., & Panagia, N., **Two populations of progenitors for Type Ia supernovae?**, *MNRAS*, 2006, 370, 773

Marion, G. H., Höflich, P., Vacca, W. D., & Wheeler, J. C., **Near-Infrared Spectra of Type Ia Supernovae**, *ApJ*, 2003, 591, 316

Marion, G. H., Höflich, P., Wheeler, J. C., Robinson, E. L., Gerardy, C. L., & Vacca, W. D., **Low Carbon Abundance in Type Ia Supernovae**, *ApJ*, 2006, 645, 1392

Marion, G. H., Höflich, P., Gerardy, C. L., Vacca, W. D., Wheeler, J. C., & Robinson, E. L., **A Catalog of Near Infrared Spectra from Type Ia Supernovae**, 2009, arXiv:0906.4085

Markwardt, C. B., **Non-linear Least Squares Fitting in IDL with MPFIT**, 2009, arXiv:0902.2850

Matheson, T., Challis, P., Kirshner, R., & Calkins, M., **Supernovae 2002ez, 2002fa, and 2002fb**, *IAU Circ.*, 2002, 7967, 2

Matheson, T., Blondin, S., Foley, R. J., Chornock, R., Filippenko, A. V., Leibundgut, B., Smith, R. C., Sollerman, J., Spyromilio, J., Kirshner, R. P., Clocchiatti, A., Aguilera, C., Barris, B., Becker, A. C., Challis, P., Covarrubias, R., Garnavich, P., Hicken, M., Jha, S., Krisciunas, K., Li, W., Miceli, A., Miknaitis, G., Prieto, J. L., Rest, A., Riess, A. G., Salvo, M. E., Schmidt, B. P., Stubbs, C. W., Suntzeff, N. B., & Tonry, J. L., **Spectroscopy**

of High-Redshift Supernovae from the ESSENCE Project: The First 2 Years, *AJ*, 2005, 129, 2352

Matheson, T., Kirshner, R. P., Challis, P., Jha, S., Garnavich, P. M., Berlind, P., Calkins, M. L., Blondin, S., Balog, Z., Bragg, A. E., Caldwell, N., Dendy Concannon, K., Falco, E. E., Graves, G. J. M., Huchra, J. P., Kuraszkiewicz, J., Mader, J. A., Mahdavi, A., Phelps, M., Rines, K., Song, I., & Wilkes, B. J., **Optical Spectroscopy of Type ia Supernovae**, *AJ*, 2008, 135, 1598

Mayya, Y. D., Puerari, I., & Kuhn, O., **Supernova 1998bu in NGC 3368**, *IAU Circ.*, 1998, 6907, 2

Mazzali, P. A., Lucy, L. B., Danziger, I. J., Gouiffes, C., Cappellaro, E., & Turatto, M., **Models for the early-time spectral evolution of the 'standard' type IA supernova 1990 N**, *A&A*, 1993, 269, 423

Mazzali, P. A., Danziger, I. J., & Turatto, M., **A study of the properties of the peculiar SN IA 1991T through models of its evolving early-time spectrum.**, *A&A*, 1995, 297, 509

Mazzali, P. A., Nomoto, K., Cappellaro, E., Nakamura, T., Umeda, H., & Iwamoto, K., **Can Differences in the Nickel Abundance in Chandrasekhar-Mass Models Explain the Relation between the Brightness and Decline Rate of Normal Type IA Supernovae?**, *ApJ*, 2001, 547, 988

Mazzali, P. A., Benetti, S., Altavilla, G., Blanc, G., Cappellaro, E., Elias-Rosa, N., Garavini, G., Goobar, A., Harutyunyan, A., Kotak, R., Leibundgut, B., Lundqvist, P., Mattila, S., Mendez, J., Nobili, S., Pain, R., Pastorello, A., Patat, F., Pignata, G., Podsiadlowski, P., Ruiz-Lapuente, P., Salvo, M., Schmidt, B. P., Sollerman, J., Stanishev, V., Stehle, M., Tout, C., Turatto, M., & Hillebrandt, W., **High-Velocity Features: A Ubiquitous Property of Type Ia Supernovae**, *ApJ*, 2005a, 623, L37

Mazzali, P. A., Benetti, S., Stehle, M., Branch, D., Deng, J., Maeda, K., Nomoto, K., & Hamuy, M., **High-velocity features in the spectra of the Type Ia supernova SN 1999ee: a property of the explosion or evidence of circumstellar interaction?**, *MNRAS*, 2005b, 357, 200

Meikle, W. P. S., Cumming, R. J., Geballe, T. R., Lewis, J. R., Walton, N. A., Balcells, M., Cimatti, A., Croom, S. M., Dhillon, V. S., Economou, F., Jenkins, C. R., Knapen, J. H.,

Meadows, V. S., Morris, P. W., Perez-Fournon, I., Shanks, T., Smith, L. J., Tanvir, N. R., Veilleux, S., Vilchez, J., Wall, J. V., & Lucey, J. R., **An early-time infrared and optical study of the Type IA supernovae SN 1994D and 1991T**, *MNRAS*, 1996, 281, 263

Meikle, W. P. S., **The absolute infrared magnitudes of type Ia supernovae**, *MNRAS*, 2000, 314, 782

Miknaitis, G., Pignata, G., Rest, A., Wood-Vasey, W. M., Blondin, S., Challis, P., Smith, R. C., Stubbs, C. W., Suntzeff, N. B., Foley, R. J., Matheson, T., Tonry, J. L., Aguilera, C., Blackman, J. W., Becker, A. C., Clocchiatti, A., Covarrubias, R., Davis, T. M., Filippenko, A. V., Garg, A., Garnavich, P. M., Hicken, M., Jha, S., Krisciunas, K., Kirshner, R. P., Leibundgut, B., Li, W., Miceli, A., Narayan, G., Prieto, J. L., Riess, A. G., Salvo, M. E., Schmidt, B. P., Sollerman, J., Spyromilio, J., & Zenteno, A., **The ESSENCE Supernova Survey: Survey Optimization, Observations, and Supernova Photometry**, *ApJ*, 2007, 666, 674

Minkowski, R., **Spectra of Supernovae**, *PASP*, 1941, 53, 224

Mustapha, N., Hellaby, C., & Ellis, G. F. R., **Large-scale inhomogeneity versus source evolution - Can we distinguish them observationally?**, *MNRAS*, 1997, 292, 817

Nakano, S., Ichimura, Y., Itagaki, K., Kadota, K., & Hirose, Y., **Supernova 2008A in NGC 634**, *Central Bureau Electronic Telegrams*, 2008, 1193, 1

Napiwotzki, R., Yungelson, L., Nelemans, G., Marsh, T. R., Leibundgut, B., Renzini, R., Homeier, D., Koester, D., Moehler, S., Christlieb, N., Reimers, D., Drechsel, H., Heber, U., Karl, C., & Pauli, E.-M., **Double degenerates and progenitors of supernovae type Ia**, *Spectroscopically and Spatially Resolving the Components of the Close Binary Stars*, 2004, 318, 402

Narlikar, J. V., & Padmanabhan, T., **Standard Cosmology and Alternatives: A Critical Appraisal**, *ARA&A*, 2001, 39, 211

Neill, J. D., Hudson, M. J., & Conley, A., **The Peculiar Velocities of Local Type Ia Supernovae and Their Impact on Cosmology**, *ApJ*, 2007, 661, L123

Nobili, S., Amanullah, R., Garavini, G., Goobar, A., Lidman, C., Stanishev, V., Aldering, G., Antilogus, P., Astier, P., Burns, M. S., Conley, A., Deustua, S. E., Ellis, R., Fabbro,

S., Fadeyev, V., Folatelli, G., Gibbons, R., Goldhaber, G., Groom, D. E., Hook, I., Howell, D. A., Kim, A. G., Knop, R. A., Nugent, P. E., Pain, R., Perlmutter, S., Quimby, R., Raux, J., Regnault, N., Ruiz-Lapuente, P., Sainton, G., Schahmaneche, K., Smith, E., Spadafora, A. L., Thomas, R. C., Wang, L., & The Supernova Cosmology Project, **Restframe I-band Hubble diagram for type Ia supernovae up to redshift z ∼ 0.5**, *A&A*, 2005, 437, 789

Nomoto, K., & Kondo, Y., **Conditions for accretion-induced collapse of white dwarfs**, *ApJ*, 1991, 367, L19

Nomoto, K., & Sugimoto, D., **Rejuvenation of Helium White Dwarfs by Mass Accretion**, *PASJ*, 1977, 29, 765

Nomoto, K., Thielemann, F.-K., & Yokoi, K., **Accreting white dwarf models of Type I supernovae. III - Carbon deflagration supernovae**, *ApJ*, 1984, 286, 644

Nomoto, K. I., Iwamoto, K., & Suzuki, T., **The evolution and explosion of massive binary stars and Type Ib-Ic-IIb-IIL supernovae.**, *Phys. Rep.*, 1995, 256, 173

Nomoto, K., **Accreting white dwarf models for type I supernovae. I - Presupernova evolution and triggering mechanisms**, *ApJ*, 1982, 253, 798

Nugent, P., Phillips, M., Baron, E., Branch, D., & Hauschildt, P., **Evidence for a Spectroscopic Sequence among Type 1a Supernovae**, *ApJ*, 1995, 455, L147

Nugent, P., Baron, E., Branch, D., Fisher, A., & Hauschildt, P. H., **Synthetic Spectra of Hydrodynamic Models of Type IA Supernovae**, *ApJ*, 1997, 485, 812

Nugent, P., Kim, A., & Perlmutter, S., **K-Corrections and Extinction Corrections for Type Ia Supernovae**, *PASP*, 2002, 114, 803

Oke, J. B., & Sandage, A., **Energy Distributions, K Corrections, and the Stebbins-Whitford Effect for Giant Elliptical Galaxies**, *ApJ*, 1968, 154, 21

Paczynski, B., **Evolution of cataclysmic binaries**, *Cataclysmic Variables and Low-Mass X-ray Binaries*, 1985, 113, 1

Padmanabhan, T., **Dark Energy: Mystery of the Millennium**, *Albert Einstein Century International Conference*, 2006, 861, 179

Panagia, N., Sramek, R. A., & Weiler, K. W., **Subluminous, radio emitting Type I supernovae**, *ApJ*, 1986, 300, L55

Panagia, N., Van Dyk, S. D., Weiler, K. W., Sramek, R. A., Stockdale, C. J., & Murata, K. P., **A Search for Radio Emission from Type Ia Supernovae**, *ApJ*, 2006, 646, 369

Parodi, B. R., Saha, A., Sandage, A., & Tammann, G. A., **Supernova Type Ia Luminosities, Their Dependence on Second Parameters, and the Value of H¡SUB¿0¡/SUB¿**, *ApJ*, 2000, 540, 634

Parthasarathy, M., Branch, D., Jeffery, D. J., & Baron, E., **Progenitors of type Ia supernovae: Binary stars with white dwarf companions**, *New Astronomy Review*, 2007, 51, 524

Pastorello, A., Mazzali, P. A., Pignata, G., Benetti, S., Cappellaro, E., Filippenko, A. V., Li, W., Meikle, W. P. S., Arkharov, A. A., Blanc, G., Bufano, F., Derekas, A., Dolci, M., Elias-Rosa, N., Foley, R. J., Ganeshalingam, M., Harutyunyan, A., Kiss, L. L., Kotak, R., Larionov, V. M., Lucey, J. R., Napoleone, N., Navasardyan, H., Patat, F., Rich, J., Ryder, S. D., Salvo, M., Schmidt, B. P., Stanishev, V., Székely, P., Taubenberger, S., Temporin, S., Turatto, M., & Hillebrandt, W., **ESC and KAIT observations of the transitional Type Ia SN 2004eo**, *MNRAS*, 2007a, 377, 1531

Pastorello, A., Taubenberger, S., Elias-Rosa, N., Mazzali, P. A., Pignata, G., Cappellaro, E., Garavini, G., Nobili, S., Anupama, G. C., Bayliss, D. D. R., Benetti, S., Bufano, F., Chakradhari, N. K., Kotak, R., Goobar, A., Navasardyan, H., Patat, F., Sahu, D. K., Salvo, M., Schmidt, B. P., Stanishev, V., Turatto, M., & Hillebrandt, W., **ESC observations of SN 2005cf - I. Photometric evolution of a normal Type Ia supernova**, *MNRAS*, 2007b, 376, 1301

Patat, F., Benetti, S., Cappellaro, E., Danziger, I. J., della Valle, M., Mazzali, P. A., & Turatto, M., **The type IA supernova 1994D in NGC 4526: the early phases**, *MNRAS*, 1996, 278, 111

Patat, F., Chandra, P., Chevalier, R., Justham, S., Podsiadlowski, P., Wolf, C., Gal-Yam, A., Pasquini, L., Crawford, I. A., Mazzali, P. A., Pauldrach, A. W. A., Nomoto, K., Benetti, S., Cappellaro, E., Elias-Rosa, N., Hillebrandt, W., Leonard, D. C., Pastorello, A., Renzini, A., Sabbadin, F., Simon, J. D., & Turatto, M., **Detection of Circumstellar Material in a Normal Type Ia Supernova**, *Science*, 2007, 317, 924

Percival, W. J., Cole, S., Eisenstein, D. J., Nichol, R. C., Peacock, J. A., Pope, A. C., & Szalay, A. S., **Measuring the Baryon Acoustic Oscillation scale using the Sloan Digital Sky Survey and 2dF Galaxy Redshift Survey**, *MNRAS*, 2007, 381, 1053

Perlmutter, S. A., & et al., **Scheduled discovery of 7+ high-redshift SNe: first cosmology results and bounds on** q_0, *NATO ASIC Proc. 486: Thermonuclear Supernovae*, 1997, 749

Perlmutter, S., Gabi, S., Goldhaber, G., Goobar, A., Groom, D. E., Hook, I. M., Kim, A. G., Kim, M. Y., Lee, J. C., Pain, R., Pennypacker, C. R., Small, I. A., Ellis, R. S., McMahon, R. G., Boyle, B. J., Bunclark, P. S., Carter, D., Irwin, M. J., Glazebrook, K., Newberg, H. J. M., Filippenko, A. V., Matheson, T., Dopita, M., Couch, W. J., & The Supernova Cosmology Project, **Measurements of the Cosmological Parameters Omega and Lambda from the First Seven Supernovae at Z >= 0.35**, *ApJ*, 1997, 483, 565

Perlmutter, S., Aldering, G., della Valle, M., Deustua, S., Ellis, R. S., Fabbro, S., Fruchter, A., Goldhaber, G., Groom, D. E., Hook, I. M., Kim, A. G., Kim, M. Y., Knop, R. A., Lidman, C., McMahon, R. G., Nugent, P., Pain, R., Panagia, N., Pennypacker, C. R., Ruiz-Lapuente, P., Schaefer, B., & Walton, N., **Discovery of a supernova explosion at half the age of the universe**, *Nature*, 1998, 391, 51

Perlmutter, S., Aldering, G., Goldhaber, G., Knop, R. A., Nugent, P., Castro, P. G., Deustua, S., Fabbro, S., Goobar, A., Groom, D. E., Hook, I. M., Kim, A. G., Kim, M. Y., Lee, J. C., Nunes, N. J., Pain, R., Pennypacker, C. R., Quimby, R., Lidman, C., Ellis, R. S., Irwin, M., McMahon, R. G., Ruiz-Lapuente, P., Walton, N., Schaefer, B., Boyle, B. J., Filippenko, A. V., Matheson, T., Fruchter, A. S., Panagia, N., Newberg, H. J. M., Couch, W. J., & The Supernova Cosmology Project, **Measurements of Omega and Lambda from 42 High-Redshift Supernovae**, *ApJ*, 1999, 517, 565

Persson, S. E., Murphy, D. C., Gunnels, S. M., Birk, C., Bagish, A., & Koch, E., **The Las Campanas Infrared Survey Camera**, *AJ*, 2002, 124, 619

Petric, A., Telis, G. A., Paerels, F., & Helfand, D. J., **A Direct Upper Limit on the Density of Cosmological Dust from the Absence of an X-Ray Scattering Halo around the z=4.3 Quasar QSO 1508+5714**, *ApJ*, 2006, 651, 41

Phillips, M. M., Phillips, A. C., Heathcote, S. R., Blanco, V. M., Geisler, D., Hamilton, D., Suntzeff, N. B., Jablonski, F. J., Steiner, J. E., Cowley, A. P., Schmidtke, P., Wyckoff, S.,

Hutchings, J. B., Tonry, J., Strauss, M. A., Thorstensen, J. R., Honey, W., Maza, J., Ruiz, M. T., Landolt, A. U., Uomoto, A., Rich, R. M., Grindlay, J. E., Cohn, H., Smith, H. A., Lutz, J. H., Lavery, R. J., & Saha, A., **The type 1a supernova 1986G in NGC 5128 - Optical photometry and spectra**, *PASP*, 1987, 99, 592

Phillips, M. M., Wells, L. A., Suntzeff, N. B., Hamuy, M., Leibundgut, B., Kirshner, R. P., & Foltz, C. B., **SN 1991T - Further evidence of the heterogeneous nature of type IA supernovae**, *AJ*, 1992, 103, 1632

Phillips, M. M., Krisciunas, K., Suntzeff, N. B., Abraham, R. G., Beckett, M. G., Bonati, M., Candia, P., Corwin, T. M., Depoy, D. L., Espinoza, J., Firth, A. E., Freedman, W. L., Galaz, G., Germany, L., Gonzalez, D., Hamuy, M., Hastings, N. C., Hungerford, A. L., Ivanov, V. D., Labbé, E., Marzke, R. O., McCarthy, P. J., McMahon, R. G., McMillan, R., Muena, C., Persson, S. E., Roth, M., Ruiz, M. T., Smith, R. C., Smith, R., Strolger, L.-G., & Stubbs, C., **Optical and Near-Infrared Observations of the Peculiar Type ia Supernova 1999ac**, *AJ*, 2006, 131, 2615

Phillips, M. M., Li, W., Frieman, J. A., Blinnikov, S. I., DePoy, D., Prieto, J. L., Milne, P., Contreras, C., Folatelli, G., Morrell, N., Hamuy, M., Suntzeff, N. B., Roth, M., González, S., Krzeminski, W., Filippenko, A. V., Freedman, W. L., Chornock, R., Jha, S., Madore, B. F., Persson, S. E., Burns, C. R., Wyatt, P., Murphy, D., Foley, R. J., Ganeshalingam, M., Serduke, F. J. D., Krisciunas, K., Bassett, B., Becker, A., Dilday, B., Eastman, J., Garnavich, P. M., Holtzman, J., Kessler, R., Lampeitl, H., Marriner, J., Frank, S., Marshall, J. L., Miknaitis, G., Sako, M., Schneider, D. P., van der Heyden, K., & Yasuda, N., **The Peculiar SN 2005hk: Do Some Type Ia Supernovae Explode as Deflagrations?**, *PASP*, 2007, 119, 360

Phillips, M. M., **The absolute magnitudes of Type IA supernovae**, *ApJ*, 1993, 413, L105

Phillips, M. M., **Type Ia Supernovae as Distance Indicators**, *1604-2004: Supernovae as Cosmological Lighthouses*, 2005, 342, 211

Pignata, G., Benetti, S., Mazzali, P. A., Kotak, R., Patat, F., Meikle, P., Stehle, M., Leibundgut, B., Suntzeff, N. B., Buson, L. M., Cappellaro, E., Clocchiatti, A., Hamuy, M., Maza, J., Mendez, J., Ruiz-Lapuente, P., Salvo, M., Schmidt, B. P., Turatto, M., & Hillebrandt, W., **Optical and infrared observations of SN 2002dj: some possible common properties of fast-expanding Type Ia supernovae**, *MNRAS*, 2008, 388, 971

Pinto, P. A., & Eastman, R. G., **The Physics of Type IA Supernova Light Curves. I. Analytic Results and Time Dependence**, *ApJ*, 2000a, 530, 744

Pinto, P. A., & Eastman, R. G., **The Physics of Type IA Supernova Light Curves. II. Opacity and Diffusion**, *ApJ*, 2000b, 530, 757

Pinto, P. A., & Eastman, R. G., **The type Ia supernova width-luminosity relation**, *New Astronomy*, 2001, 6, 307

Pound, R. V., & Rebka, G. A., **Gravitational Red-Shift in Nuclear Resonance**, *Physical Review Letters*, 1959, 3, 439

Pound, R. V., & Rebka, G. A., **Apparent Weight of Photons**, *Physical Review Letters*, 1960, 4, 337

Pound, R. V., & Snider, J. L., **Effect of Gravity on Nuclear Resonance**, *Physical Review Letters*, 1964, 13, 539

Press, W. H., Teukolsky, S. A., Vetterling, W. T., & Flannery, B. P., **Numerical recipes in C. The art of scientific computing**, *Cambridge: University Press, —c1992, 2nd ed.*, 1992,

Prieto, J. L., Rest, A., & Suntzeff, N. B., **A New Method to Calibrate the Magnitudes of Type Ia Supernovae at Maximum Light**, *ApJ*, 2006, 647, 501

Prieto, J. L., Garnavich, P. M., Phillips, M. M., DePoy, D. L., Parrent, J., Pooley, D., Dwarkadas, V. V., Baron, E., Bassett, B., Becker, A., Cinabro, D., DeJongh, F., Dilday, B., Doi, M., Frieman, J. A., Hogan, C. J., Holtzman, J., Jha, S., Kessler, R., Konishi, K., Lampeitl, H., Marriner, J., Marshall, J. L., Miknaitis, G., Nichol, R. C., Riess, A. G., Richmond, M. W., Romani, R., Sako, M., Schneider, D. P., Smith, M., Takanashi, N., Tokita, K., van der Heyden, K., Yasuda, N., Zheng, C., Wheeler, J. C., Barentine, J., Dembicky, J., Eastman, J., Frank, S., Ketzeback, W., McMillan, R. J., Morrell, N., Folatelli, G., Contreras, C., Burns, C. R., Freedman, W. L., Gonzalez, S., Hamuy, M., Krzeminski, W., Madore, B. F., Murphy, D., Persson, S. E., Roth, M., & Suntzeff, N. B., **A Study of the Type Ia/IIn Supernova 2005gj from X-ray to the Infrared: Paper I**, 2007, arXiv:0706.4088

Pritchet, C. J., Howell, D. A., & Sullivan, M., **The Progenitors of Type Ia Supernovae**, *ApJ*, 2008, 683, L25

Pskovskii, Y. P., **Phase Dependence of the Colors of Type I and II Supernovae.**, *Soviet Astronomy*, 1968, 11, 570

Pskovskii, I. P., **Light curves, color curves, and expansion velocity of type I supernovae as functions of the rate of brightness decline**, *Soviet Astronomy*, 1977, 21, 675

Pskovskii, Y. P., **Photometric classification and basic parameters of type I supernovae**, *Soviet Astronomy*, 1984, 28, 658

Quimby, R., Höflich, P., Kannappan, S. J., Rykoff, E., Rujopakarn, W., Akerlof, C. W., Gerardy, C. L., & Wheeler, J. C., **SN 2005cg: Explosion Physics and Circumstellar Interaction of a Normal Type Ia Supernova in a Low-Luminosity Host**, *ApJ*, 2006, 636, 400

Rayner, J. T., Toomey, D. W., Onaka, P. M., Denault, A. J., Stahlberger, W. E., Watanabe, D. Y., & Wang, S.-I., **SpeX: a medium-resolution IR spectrograph for IRTF**, *Proc. SPIE*, 1998, 3354, 468

Riess, A. G., Press, W. H., & Kirshner, R. P., **A Precise Distance Indicator: Type IA Supernova Multicolor Light-Curve Shapes**, *ApJ*, 1996, 473, 88

Riess, A. G., Filippenko, A. V., Leonard, D. C., Schmidt, B. P., Suntzeff, N., Phillips, M. M., Schommer, R., Clocchiatti, A., Kirshner, R. P., Garnavich, P., Challis, P., Leibundgut, B., Spyromilio, J., & Smith, R. C., **Time Dilation from Spectral Feature Age Measurements of Type IA Supernovae.**, *AJ*, 1997, 114, 722

Riess, A. G., Filippenko, A. V., Challis, P., Clocchiatti, A., Diercks, A., Garnavich, P. M., Gilliland, R. L., Hogan, C. J., Jha, S., Kirshner, R. P., Leibundgut, B., Phillips, M. M., Reiss, D., Schmidt, B. P., Schommer, R. A., Smith, R. C., Spyromilio, J., Stubbs, C., Suntzeff, N. B., & Tonry, J., **Observational Evidence from Supernovae for an Accelerating Universe and a Cosmological Constant**, *AJ*, 1998, 116, 1009

Riess, A. G., Kirshner, R. P., Schmidt, B. P., Jha, S., Challis, P., Garnavich, P. M., Esin, A. A., Carpenter, C., Grashius, R., Schild, R. E., Berlind, P. L., Huchra, J. P., Prosser, C. F., Falco, E. E., Benson, P. J., Briceño, C., Brown, W. R., Caldwell, N., dell'Antonio, I. P., Filippenko, A. V., Goodman, A. A., Grogin, N. A., Groner, T., Hughes, J. P., Green, P. J., Jansen, R. A., Kleyna, J. T., Luu, J. X., Macri, L. M., McLeod, B. A., McLeod, K. K., McNamara, B. R., McLean, B., Milone, A. A. E., Mohr, J. J., Moraru, D., Peng,

C., Peters, J., Prestwich, A. H., Stanek, K. Z., Szentgyorgyi, A., & Zhao, P., **BVRI Light Curves for 22 Type IA Supernovae**, *AJ*, 1999, 117, 707

Riess, A. G., Strolger, L.-G., Tonry, J., Casertano, S., Ferguson, H. C., Mobasher, B., Challis, P., Filippenko, A. V., Jha, S., Li, W., Chornock, R., Kirshner, R. P., Leibundgut, B., Dickinson, M., Livio, M., Giavalisco, M., Steidel, C. C., Benítez, T., & Tsvetanov, Z., **Type Ia Supernova Discoveries at z > 1 from the Hubble Space Telescope: Evidence for Past Deceleration and Constraints on Dark Energy Evolution**, *ApJ*, 2004, 607, 665

Riess, A. G., Strolger, L.-G., Casertano, S., Ferguson, H. C., Mobasher, B., Gold, B., Challis, P. J., Filippenko, A. V., Jha, S., Li, W., Tonry, J., Foley, R., Kirshner, R. P., Dickinson, M., MacDonald, E., Eisenstein, D., Livio, M., Younger, J., Xu, C., Dahlén, T., & Stern, D., **New Hubble Space Telescope Discoveries of Type Ia Supernovae at z >= 1: Narrowing Constraints on the Early Behavior of Dark Energy**, *ApJ*, 2007, 659, 98

Ritter, H., & Burkert, A., **The mass spectrum of the white dwarfs in cataclysmic binaries**, *A&A*, 1986, 158, 161

Robertson, H. P., **Kinematics and World-Structure**, *ApJ*, 1935, 82, 284

Robertson, H. P., **The apparent luminosity of a receding nebula. Mit 3 Abbildungen.**, *Zeitschrift für Astrophysik*, 1938, 15, 69

Ronen, S., Aragon-Salamanca, A., & Lahav, O., **Principal component analysis of synthetic galaxy spectra**, *MNRAS*, 1999, 303, 284

Röpke, F. K., & Hillebrandt, W., **Full-star type Ia supernova explosion models**, *A&A*, 2005, 431, 635

Rudy, R. J., Lynch, D. K., Mazuk, S., Venturini, C. C., Puetter, R. C., Höflich, P., **Early-Time Infrared Spectra of the Type Ia Supernova 2000cx**, *ApJ*, 2002, 565, 413

Ruiz-Lapuente, P., Comeron, F., Méndez, J., Canal, R., Smartt, S. J., Filippenko, A. V., Kurucz, R. L., Chornock, R., Foley, R. J., Stanishev, V., & Ibata, R., **The binary progenitor of Tycho Brahe's 1572 supernova**, *Nature*, 2004, 431, 1069

Saio, H., & Nomoto, K., **Off-Center Carbon Ignition in Rapidly Rotating, Accreting Carbon-Oxygen White Dwarfs**, *ApJ*, 2004, 615, 444

Sako, M., Bassett, B., Becker, A., Cinabro, D., DeJongh, F., Depoy, D. L., Dilday, B., Doi, M., Frieman, J. A., Garnavich, P. M., Hogan, C. J., Holtzman, J., Jha, S., Kessler, R., Konishi, K., Lampeitl, H., Marriner, J., Miknaitis, G., Nichol, R. C., Prieto, J. L., Riess, A. G., Richmond, M. W., Romani, R., Schneider, D. P., Smith, M., Subba Rao, M., Takanashi, N., Tokita, K., van der Heyden, K., Yasuda, N., Zheng, C., Barentine, J., Brewington, H., Choi, C., Dembicky, J., Harnavek, M., Ihara, Y., Im, M., Ketzeback, W., Kleinman, S. J., Krzesiński, J., Long, D. C., Malanushenko, E., Malanushenko, V., McMillan, R. J., Morokuma, T., Nitta, A., Pan, K., Saurage, G., & Snedden, S. A., **The Sloan Digital Sky Survey-II Supernova Survey: Search Algorithm and Follow-Up Observations**, *AJ*, 2008, 135, 348

Salvo, M. E., Cappellaro, E., Mazzali, P. A., Benetti, S., Danziger, I. J., Patat, F., & Turatto, M., **The template type Ia supernova 1996X**, *MNRAS*, 2001, 321, 254

Sandage, A., & Tammann, G. A., **Steps toward the Hubble constant. VIII - The global value**, *ApJ*, 1982, 256, 339

Sandage, A., & Tammann, G. A., **The Hubble diagram in V for supernovae of Type IA and the value of H(0) therefrom**, *ApJ*, 1993, 415, 1

Sandage, A. R., Kron, R. G., Longair, M. S., Binggeli, B., & Buser, R., **The Deep Universe**, *Saas-Fee Advanced Course 23. Lecture Notes 1993. Swiss Society for Astrophysics and Astronomy, XIV, 526 pp. 204 figs.. Springer-Verlag Berlin Heidelberg New York*, 1995,

Scannapieco, E., & Bildsten, L., **The Type Ia Supernova Rate**, *ApJ*, 2005, 629, L85

Schlegel, E. M., **A new subclass of Type II supernovae?**, *MNRAS*, 1990, 244, 269

Schmidt, B. P., Suntzeff, N. B., Phillips, M. M., Schommer, R. A., Clocchiatti, A., Kirshner, R. P., Garnavich, P., Challis, P., Leibundgut, B., Spyromilio, J., Riess, A. G., Filippenko, A. V., Hamuy, M., Smith, R. C., Hogan, C., Stubbs, C., Diercks, A., Reiss, D., Gilliland, R., Tonry, J., Maza, J., Dressler, A., Walsh, J., & Ciardullo, R., **The High-Z Supernova Search: Measuring Cosmic Deceleration and Global Curvature of the Universe Using Type IA Supernovae**, *ApJ*, 1998, 507, 46

Shapiro, I. I., **Fourth Test of General Relativity**, *Physical Review Letters*, 1964, 13, 789

Smith, J. A., Tucker, D. L., Kent, S., Richmond, M. W., Fukugita, M., Ichikawa, T., Ichikawa, S.-i., Jorgensen, A. M., Uomoto, A., Gunn, J. E., Hamabe, M., Watanabe, M., Tolea, A., Henden, A., Annis, J., Pier, J. R., McKay, T. A., Brinkmann, J., Chen, B., Holtzman, J., Shimasaku, K., & York, D. G., **The u'g'r'i'z' Standard-Star System**, *AJ*, 2002, 123, 2121

Spergel, D. N., Bean, R., Doré, O., Nolta, M. R., Bennett, C. L., Dunkley, J., Hinshaw, G., Jarosik, N., Komatsu, E., Page, L., Peiris, H. V., Verde, L., Halpern, M., Hill, R. S., Kogut, A., Limon, M., Meyer, S. S., Odegard, N., Tucker, G. S., Weiland, J. L., Wollack, E., & Wright, E. L., **Three-Year Wilkinson Microwave Anisotropy Probe (WMAP) Observations: Implications for Cosmology**, *ApJS*, 2007, 170, 377

Stevenson, C. C., **Penetrating the Fog - Correcting Groundbased CCD Spectroscopy for Telluric Absorption**, *MNRAS*, 1994, 267, 904

Stritzinger, M., & Sollerman, J., **Late-time emission of type Ia supernovae: optical and near-infrared observations of SN 2001el**, *A&A*, 2007, 470, L1

Stritzinger, M., Leibundgut, B., Walch, S., & Contardo, G., **Constraints on the progenitor systems of type Ia supernovae**, *A&A*, 2006a, 450, 241

Stritzinger, M., Mazzali, P. A., Sollerman, J., & Benetti, S., **Consistent estimates of ^{56}Ni yields for type Ia supernovae**, *A&A*, 2006b, 460, 793

Strolger, L.-G., Smith, R. C., Suntzeff, N. B., Phillips, M. M., Aldering, G., Nugent, P., Knop, R., Perlmutter, S., Schommer, R. A., Ho, L. C., Hamuy, M., Krisciunas, K., Germany, L. M., Covarrubias, R., Candia, P., Athey, A., Blanc, G., Bonacic, A., Bowers, T., Conley, A., Dahlén, T., Freedman, W., Galaz, G., Gates, E., Goldhaber, G., Goobar, A., Groom, D., Hook, I. M., Marzke, R., Mateo, M., McCarthy, P., Méndez, J., Muena, C., Persson, S. E., Quimby, R., Roth, M., Ruiz-Lapuente, P., Seguel, J., Szentgyorgyi, A., von Braun, K., Wood-Vasey, W. M., & York, T., **The Type Ia Supernova 1999aw: A Probable 1999aa-like Event in a Low-Luminosity Host Galaxy**, *AJ*, 2002, 124, 2905

Strovink, M., **Diversity of Decline Rate-corrected Type Ia Supernova Rise Times: One Mode or Two?**, *ApJ*, 2007, 671, 1084

Sullivan, M., Ellis, R. S., Aldering, G., Amanullah, R., Astier, P., Blanc, G., Burns, M. S., Conley, A., Deustua, S. E., Doi, M., Fabbro, S., Folatelli, G., Fruchter, A. S., Garavini, G., Gibbons, R., Goldhaber, G., Goobar, A., Groom, D. E., Hardin, D., Hook, I., Howell,

D. A., Irwin, M., Kim, A. G., Knop, R. A., Lidman, C., McMahon, R., Mendez, J., Nobili, S., Nugent, P. E., Pain, R., Panagia, N., Pennypacker, C. R., Perlmutter, S., Quimby, R., Raux, J., Regnault, N., Ruiz-Lapuente, P., Schaefer, B., Schahmaneche, K., Spadafora, A. L., Walton, N. A., Wang, L., Wood-Vasey, W. M., & Yasuda, N., **The Hubble diagram of type Ia supernovae as a function of host galaxy morphology**, *MNRAS*, 2003, 340, 1057

Sullivan, M., Le Borgne, D., Pritchet, C. J., Hodsman, A., Neill, J. D., Howell, D. A., Carlberg, R. G., Astier, P., Aubourg, E., Balam, D., Basa, S., Conley, A., Fabbro, S., Fouchez, D., Guy, J., Hook, I., Pain, R., Palanque-Delabrouille, N., Perrett, K., Regnault, N., Rich, J., Taillet, R., Baumont, S., Bronder, J., Ellis, R. S., Filiol, M., Lusset, V., Perlmutter, S., Ripoche, P., & Tao, C., **Rates and Properties of Type Ia Supernovae as a Function of Mass and Star Formation in Their Host Galaxies**, *ApJ*, 2006, 648, 868

Sullivan, M., Ellis, R. S., Howell, D. A., Riess, A., Nugent, P. E., & Gal-Yam, A., **The Mean Type Ia Supernova Spectrum Over the Past Nine Gigayears**, *ApJ*, 2009, 693, L76

Suzuki, N., **Quasar Spectrum Classification with Principal Component Analysis (PCA): Emission Lines in the Lyα Forest**, *ApJS*, 2006, 163, 110

Tammann, G. A., & Leibundgut, B., **Supernova studies. IV - The global value of H0 from supernovae IA and the peculiar motion of field galaxies**, *A&A*, 1990, 236, 9

Taubenberger, S., Hachinger, S., Pignata, G., Mazzali, P. A., Contreras, C., Valenti, S., Pastorello, A., Elias-Rosa, N., Bärnbantner, O., Barwig, H., Benetti, S., Dolci, M., Fliri, J., Folatelli, G., Freedman, W. L., Gonzalez, S., Hamuy, M., Krzeminski, W., Morrell, N., Navasardyan, H., Persson, S. E., Phillips, M. M., Ries, C., Roth, M., Suntzeff, N. B., Turatto, M., & Hillebrandt, W., **The underluminous Type Ia supernova 2005bl and the class of objects similar to SN 1991bg**, *MNRAS*, 2008, 385, 75

Thomas, R. C., Aldering, G., Antilogus, P., Aragon, C., Bailey, S., Baltay, C., Baron, E., Bauer, A., Buton, C., Bongard, S., Copin, Y., Gangler, E., Gilles, S., Kessler, R., Loken, S., Nugent, P., Pain, R., Parrent, J., Pécontal, E., Pereira, R., Perlmutter, S., Rabinowitz, D., Rigaudier, G., Runge, K., Scalzo, R., Smadja, G., Wang, L., & Weaver, B. A., **Nearby Supernova Factory Observations of SN 2006D: On Sporadic Carbon Signatures in Early Type Ia Supernova Spectra**, *ApJ*, 2007, 654, L53

Timmes, F. X., Brown, E. F., & Truran, J. W., **On Variations in the Peak Luminosity of Type Ia Supernovae**, *ApJ*, 2003, 590, L83

Tonry, J. L., Schmidt, B. P., Barris, B., Candia, P., Challis, P., Clocchiatti, A., Coil, A. L., Filippenko, A. V., Garnavich, P., Hogan, C., Holland, S. T., Jha, S., Kirshner, R. P., Krisciunas, K., Leibundgut, B., Li, W., Matheson, T., Phillips, M. M., Riess, A. G., Schommer, R., Smith, R. C., Sollerman, J., Spyromilio, J., Stubbs, C. W., & Suntzeff, N. B., **Cosmological Results from High-z Supernovae**, *ApJ*, 2003, 594, 1

Totani, T., Morokuma, T., Oda, T., Doi, M., & Yasuda, N., **Delay Time Distribution Measurement of Type Ia Supernovae by the Subaru/XMM-Newton Deep Survey and Implications for the Progenitor**, *PASJ*, 2008, 60, 1327

Tripp, R., & Branch, D., **Determination of the Hubble Constant Using a Two-Parameter Luminosity Correction for Type IA Supernovae**, *ApJ*, 1999, 525, 209

Tripp, R., **A two-parameter luminosity correction for Type IA supernovae**, *A&A*, 1998, 331, 815

Truran, J. W., Arnett, W. D., & Cameron, A. G. W., **Nucleosynthesis in supernova shock waves**, *Canadian Journal of Physics*, 1967, 45, 2315

Turatto, M., Benetti, S., Cappellaro, E., Danziger, I. J., Della Valle, M., Gouiffes, C., Mazzali, P. A., & Patat, F., **The properties of the peculiar type Ia supernova 1991bg. I. Analysis and discussion of two years of observations.**, *MNRAS*, 1996, 283, 1

Turatto, M., Piemonte, A., Benetti, S., Cappellaro, E., Mazzali, P. A., Danziger, I. J., & Patat, F., **A New Faint Type IA Supernova: SN 1997CN in NGC 5490**, *AJ*, 1998, 116, 2431

Turatto, M., **Classification of Supernovae**, *Supernovae and Gamma-Ray Bursters*, 2003, 598, 21

Uomoto, A., & Kirshner, R. P., **Peculiar Type I supernovas**, *A&A*, 1985, 149, L7

Vacca, W. D., Cushing, M. C., & Rayner, J. T., **A Method of Correcting Near-Infrared Spectra for Telluric Absorption**, *PASP*, 2003, 115, 389

Valenti, S., Pastorello, A., Cappellaro, E., Benetti, S., Mazzali, P. A., Manteca, J., Taubenberger, S., Elias-Rosa, N., Ferrando, R., Harutyunyan, A., Hentunen, V. P., Nissinen,

M., Pian, E., Turatto, M., Zampieri, L., & Smartt, S. J., **A low-energy core-collapse supernova without a hydrogen envelope**, *Nature*, 2009, 459, 674

Valentini, G., Di Carlo, E., Massi, F., Dolci, M., Arkharov, A. A., Larionov, V. M., Pastorello, A., Di Paola, A., Benetti, S., Cappellaro, E., Turatto, M., Pedichini, F., D'Alessio, F., Caratti o Garatti, A., Li Causi, G., Speziali, R., Danziger, I. J., & Tornambé, A., **Optical and Near-Infrared Photometry of the Type Ia Supernova 2000E in NGC 6951**, *ApJ*, 2003, 595, 779

van den Bergh, S., Li, W., & Filippenko, A. V., **Classifications of the Host Galaxies of Supernovae**, *PASP*, 2002, 114, 820

van den Bergh, S., Li, W., & Filippenko, A. V., **Classifications of the Host Galaxies of Supernovae, Set II**, *PASP*, 2003, 115, 1280

van den Bergh, S., Li, W., & Filippenko, A. V., **Classifications of the Host Galaxies of Supernovae, Set III**, *PASP*, 2005, 117, 773

Wang, L., Höflich, P., & Wheeler, J. C., **Supernovae and Their Host Galaxies**, *ApJ*, 1997, 483, L29

Wang, L., Baade, D., Höflich, P., Khokhlov, A., Wheeler, J. C., Kasen, D., Nugent, P. E., Perlmutter, S., Fransson, C., & Lundqvist, P., **Spectropolarimetry of SN 2001el in NGC 1448: Asphericity of a Normal Type Ia Supernova**, *ApJ*, 2003, 591, 1110

Wang, X., Li, W., Filippenko, A. V., Krisciunas, K., Suntzeff, N. B., Li, J., Zhang, T., Deng, J., Foley, R. J., Ganeshalingam, M., Li, T., Lou, Y., Qiu, Y., Shang, R., Silverman, J. M., Zhang, S., & Zhang, Y., **Optical and Near-Infrared Observations of the Highly Reddened, Rapidly Expanding Type Ia Supernova SN 2006X in M100**, *ApJ*, 2008, 675, 626

Wang, X., Li, W., Filippenko, A. V., Foley, R. J., Kirshner, R. P., Modjaz, M., Bloom, J., Brown, P. J., Carter, D., Friedman, A. S., Gal-Yam, A., Ganeshalingam, M., Hicken, M., Krisciunas, K., Milne, P., Silverman, J. M., Suntzeff, N. B., Wood-Vasey, W. M., Cenko, S. B., Challis, P., Fox, D. B., Kirkman, D., Li, J. Z., Li, T. P., Malkan, M. A., Moore, M. R., Reitzel, D. B., Rich, R. M., Serduke, F. J. D., Shang, R. C., Steele, T. N., Swift, B. J., Tao, C., Wong, D. S., & Zhang, S. N., **The Golden Standard Type Ia Supernova 2005cf: Observations from the Ultraviolet to the Near-Infrared Wavebands**, *ApJ*, 2009a, 697, 380

Wang, X., Filippenko, A. V., Ganeshalingam, M., Li, W., Silverman, J. M., Wang, L., Chornock, R., Foley, R. J., Gates, E. L., Macomber, B., Serduke, F. J. D., Steele, T. N., & Wong, D. S., **Improved Distances to Type Ia Supernovae with Two Spectroscopic Subclasses**, 2009b, arXiv:0906.1616

Webbink, R. F., **Double white dwarfs as progenitors of R Coronae Borealis stars and Type I supernovae**, *ApJ*, 1984, 277, 355

Weinberg, S., **Anthropic bound on the cosmological constant**, *Physical Review Letters*, 1987, 59, 2607

Weinberg, S., **The cosmological constant problem**, *Reviews of Modern Physics*, 1989, 61, 1

Wells, L. A., Phillips, M. M., Suntzeff, B., Heathcote, S. R., Hamuy, M., Navarrete, M., Fernandez, M., Weller, W. G., Schommer, R. A., Kirshner, R. P., Leibundgut, B., Willner, S. P., Peletier, R. P., Schlegel, E. M., Wheeler, J. C., Harkness, R. P., Bell, D. J., Matthews, J. M., Filippenko, A. V., Shields, J. C., Richmond, M. W., Jewitt, D., Luu, J., Tran, H. D., Appleton, P. N., Robson, E. I., Tyson, J. A., Guhathakurta, P., Eder, J. A., Bond, H. E., Potter, M., Veilleux, S., Porter, A. C., Humphreys, R. M., Janes, K. A., Williams, T. B., Costa, E., Ruiz, M. T., Lee, J. T., Lutz, J. H., Rich, R. M., Winkler, P. F., & Tyson, N. D., **The Type IA supernova 1989B in NGC 3627 (M66)**, *AJ*, 1994, 108, 2233

Wheeler, J. C., & Levreault, R., **The peculiar Type I supernova in NGC 991**, *ApJ*, 1985, 294, L17

Wheeler, J. C., Höflich, P., Harkness, R. P., & Spyromilio, J., **Explosion Diagnostics of Type IA Supernovae from Early Infrared Spectra**, *ApJ*, 1998, 496, 908

Whelan, J., & Iben, I. J., **Binaries and Supernovae of Type I**, *ApJ*, 1973, 186, 1007

Wood-Vasey, W. M., Aldering, G., Lee, B. C., Loken, S., Nugent, P., Perlmutter, S., Siegrist, J., Wang, L., Antilogus, P., Astier, P., Hardin, D., Pain, R., Copin, Y., Smadja, G., Gangler, E., Castera, A., Adam, G., Bacon, R., Lemonnier, J.-P., Pécontal, A., Pécontal, E., & Kessler, R., **The Nearby Supernova Factory**, *New Astronomy Review*, 2004, 48, 637

Wood-Vasey, W. M., Miknaitis, G., Stubbs, C. W., Jha, S., Riess, A. G., Garnavich, P. M., Kirshner, R. P., Aguilera, C., Becker, A. C., Blackman, J. W., Blondin, S., Challis, P., Clocchiatti, A., Conley, A., Covarrubias, R., Davis, T. M., Filippenko, A. V., Foley, R. J., Garg, A., Hicken, M., Krisciunas, K., Leibundgut, B., Li, W., Matheson, T., Miceli, A., Narayan, G., Pignata, G., Prieto, J. L., Rest, A., Salvo, M. E., Schmidt, B. P., Smith, R. C., Sollerman, J., Spyromilio, J., Tonry, J. L., Suntzeff, N. B., & Zenteno, A., **Observational Constraints on the Nature of Dark Energy: First Cosmological Results from the ESSENCE Supernova Survey**, *ApJ*, 2007, 666, 694

Wood-Vasey, W. M., Friedman, A. S., Bloom, J. S., Hicken, M., Modjaz, M., Kirshner, R. P., Starr, D. L., Blake, C. H., Falco, E. E., Szentgyorgyi, A. H., Challis, P., Blondin, S., Mandel, K. S., & Rest, A., **Type Ia Supernovae Are Good Standard Candles in the Near Infrared: Evidence from PAIRITEL**, *ApJ*, 2008, 689, 377

Woosley, S. E., & Weaver, T. A., **The physics of supernova explosions**, *ARA&A*, 1986, 24, 205

Woosley, S. E., & Weaver, T. A., **Sub-Chandrasekhar mass models for Type IA supernovae**, *ApJ*, 1994, 423, 371

Woosley, S. E., Weaver, T. A., & Taam, R. E., **Models for Type I supernovae**, *Texas Workshop on Type I Supernovae*, 1980, 96

Woosley, S. E., Eastman, R. G., & Schmidt, B. P., **Gamma-Ray Bursts and Type IC Supernova SN 1998BW**, *ApJ*, 1999, 516, 788

Yamaoka, H., Nomoto, K., Shigeyama, T., & Thielemann, F.-K., **Late detonation models for the type IA supernovae SN 1991T and SN 1990N**, *ApJ*, 1992, 393, L55

Yoon, S.-C., & Langer, N., **The first binary star evolution model producing a Chandrasekhar mass white dwarf**, *A&A*, 2003, 412, L53

Zeldovich, Y. B., **A hypothesis, unifying the structure and the entropy of the Universe**, *MNRAS*, 1972, 160, 1P Query Results from the ADS DatabaseRetrieved 162 abstracts, starting with number 1. Total number selected: 162.

Zingale, M., & Dursi, L. J., **Propagation of the First Flames in Type Ia Supernovae**, *ApJ*, 2007, 656, 333